A Fundamental Understanding of Al-Ni-Mn alloys: Microstructure, Mechanical Properties, Solidification and Minor Alloying

A thesis submitted for the degree of

Doctor of Philosophy

By

Jiao Fang

Department of Mechanical and Aerospace Engineering

College of Engineering, Design and Physical Sciences

Brunel University London, Uxbridge, UB8 3PH

United Kingdom

May 2022

Supervision: Prof. Shouxun Ji

Prof. Zhongyun Fan

Abstract

The development of aluminium alloys for applications at elevated temperatures has become an important topic for several decades. Since the application temperatures of Al-Si based alloys are limited because of the deterioration of mechanical properties at high temperatures, the development of new aluminium alloys is increasingly attractive. The Al-Ni-Mn alloys are potentially good candidates because the eutectic temperature (640 ℃) is higher than that of Al-Si systems (577 ℃), and the Al_3Ni phase is stable up to 600 ℃. However, there is limited research in the existing literatures and the understanding of Al-Ni based alloys is not sufficient to draw solid conclusions either from fundamental theory or from applicable evidences. Therefore, the aim of present study is to fill the knowledgegap to enhance the understanding of Al-Ni-Mn alloys from the microstructural characteristics and mechanical properties at ambient and elevated temperatures, in association with the solidification process and the effect of minor elements in alloy systems.

The effect of Mn on the microstructure and mechanical properties of hypoeutectic, eutectic and hypereutectic Al-Ni alloys was thoroughly studied. The microstructural characteristics of Al-4Ni-xMn, Al-6Ni-xMn and Al-8Ni-xMn (x=0, 2 ,3 ,4) alloys revealed that 2% Mn addition could transform the eutectic structure from α-Al+Al_3Ni to α-Al+$Al_9(Ni, Mn)_2$. For Al-6Ni and Al-8Ni alloys, Mn also transformed the primary phase from Al_3Ni to $Al_9(Ni, Mn)_2$. The κ-phase (Al-15.6Mn-4.8Ni (at.%)), O-phase (Al-12.6Mn-7.0Ni (at.%)) and Al_6Mn were formed with increasing Mn content to the level of 3.0% and 4.0%. Moreover, the addition of Mn in Al-Ni alloys improved the tensile strength at both ambient temperature and 250 °C. The best tensile strength was obtained by the Al-6Ni-4Mn alloy. It offered yield strength of 164 MPa, ultimate tensile strength (UTS) of 256 MPa at 25 °C, and the yield strength of 134 MPa, UTS of 176 MPa at 250 °C.

The significant progresses have also been made for the understanding in the microstructural evolution of Al-4Ni-2Mn alloy under different cooling rates. The eutectic structure was α-

$Al+Al_9(Ni, Mn)_2$ in PMC alloy and then became α-$Al+Al_9(Ni, Mn)_2$+O and a mixture of α-$Al+Al_9(Ni, Mn)_2$+O+Al_3Ni as the cooling rates decreased to 20 K/min and 0.5 K/min, respectively. The primary α-Al phase was the only primary phase in the alloy processed byPMC. When the cooling rate decreased to 5 K/min and 0.2 K/min, the O-phase and Al_6Mn phase began to form, respectively.

The evaluation of the thermal stability of the eutectic $Al_9(Ni, Mn)_2$ phase in Al-Ni-Mn alloys was not foreseen in previous researches. The eutectic $Al_9(Ni, Mn)_2$ phase showed excellent thermal stability at 250 °C. No coarsening of eutectic rods was observed after 2000 h isothermal holding at 250 °C. However, after 720 h at 300 °C or 20 h at 400 °C, the κ-phase was observed at α-$Al/Al_9(Ni, Mn)_2$ interphase boundaries and segmented eutectic $Al_9(Ni, Mn)_2$ rods was clear in the microstructure, which are responsible for the deterioration of mechanical properties at elevated temperatures.

The effect of Cu and Ce on the microstructure and mechanical properties were firstly studied in Al-Ni-Mn alloys. The Cu addition in the Al-5Ni-2Mn alloy could increase the strength under as-cast condition. When Cu content was increased from 0 to 2.0 wt.% Cu, the yield strength increased from 109 MPa to 130 MPa and the UTS increased from 228 MPa to 248 MPa , respectively. However, T6 heat treatment was found to be able to provide very limited strengthening effect for the Cu addition. The main reason is attributed to the dissolution of Cu in the $Al_9(Ni, Mn)_2$ phase. On the other hand, the Ce addition was found to introduce eutectic $Al_{11}Ce_3$ phase when Ce content reached 0.5% and to form primary $Al_{10}Mn_2Ce$ phase when Ce reached 5.0%. The morphology of the eutectic $Al_9(Ni, Mn)_2$ phase was completely changed from rod-like shapes to fibrous morphologies in the alloy with 2.0% Ce addition. It is interesting to find that the hardness of the Al-5Ni-2Mn alloy increased significantly with increasing the Ce contents but the tensile strength was not significantly improved. It is mainly due to the morphological change of the eutectic $Al_9(Ni, Mn)_2$ phase from well aligned rods to fibrous structures, which provides weaker strengthening effect of the eutectic $Al_{11}Ce_3$ phase compared with the $Al_9(Ni, Mn)_2$ phase.

Key words: Aluminium alloys; Microstructure; Mechanical properties; Al-Ni-Mn; Cooling rate; Thermal stability; Rare earth elements

Acknowledgement

Firstly, I would like to express my gratitude to my supervisors, Professor Shouxun Ji and Professor Zhongyun Fan, for offering me this opportunity and for their continuous support during my PhD study and related research. Their encouragement and guidance helped me in all the time of study at Brunel University London.

I would like to thank my Research Development Advisor, Dr Yan Huang. He gave me very good instructions for presenting skills and constructive comments in analysing experimental results. Also, I would like to thank the members of my review panels, Dr Yun Wang, Dr Chamini Mends and Dr Brian McKay. They provided lots of suggestions for thesis plan and organisation.

Special thanks go to Dr Xiangzhen Zhu for his tremendous help in planning experiments and analysing unexpected results. I also want to thank Dr Feng Wang for the help in TEM operation, Dr Guangyu Liu, Dr Dan Luo and Dr Xixi Dong for their support in experiments and writing.

I would like to thank all lab members for stimulating discussions, sleepless nights and restless weekends we were working together. All happy moments we had together will be always remembered.

I would express my sincere thanks to my family. Thanks my parents for their encouragement and all the good personalities they have given me. Special thanks goes to my husband, Liuxun Li. His patience, support and accompany encouraged me in the hard time during PhD study.

The last word goes for Ellie, my baby girl, who has been the light of my life and who has given me the extra strength and motivation to get a PhD. This thesis is dedicated to her.

Table of Contents

Abbreviations

Abbreviations	Meaning
DSC	Differential scanning calorimetry
EDS	Energy-dispersive X-ray analyser
EL	Elongation
EPMA	Electron probe micro-analyser
GDC	Gravity die casting
HPDC	High pressure die casting
OES	Optical emission spectrometry
LPDC	Low pressure die casting
OM	Optical microscopy
PIPs	Precision ion polishing system
PMC	Permanent mould casting
SAED	Selected area electron diffraction
SDAS	Secondary dendrite arm spacing
SEM	Scanning electron microscopy
TEM	Transmission electron microscopy
UTS	Ultimate tensile strength
WDS	Wavelength dispersive spectroscopy
XRD	X-ray diffraction
YS	Yield strength

List of Publications

[1] Jiao Fang, Xixi Dong, Shouxun Ji. Effect of Mn on Microstructure and Mechanical Properties of Al-4Ni Alloy. *JOM*,2021. https://doi.org/10.1007/s11837-021-04908-3.

Chapter 1: Introduction

1.1 Background and Motivation

The development of aluminium alloys for applications at elevated temperatures has become an important topic [1]. Considerable efforts have been carried out to increase the application temperature for aluminium alloys. Numerous studies have attempted to modify conventional Al-Si based alloys with heat-resistant Al_3X dispersoids and precipitates, using transition metals such as Sc [2–5], Zr [6–9], Ti [10–12], V [13,14], Ni [7,8,15] and rare earth elements such as Er, Gd, Hf, Y, Yb, Tm [16–23]. However, only a very limited volume fraction of Al_3X phases can be precipitated to strengthen aluminium alloys at elevated temperatures. Some of these elements can be very expensive, resulting in the devaluation of practical application in Al-Si based alloys. Other attempts were the development of new aluminium alloys, notables including Al-Fe-V-Si [24], Al-Fe-Gd [25] and Al-Co-Cr-Fe-Ni [26]. However, many of the newly developed aluminium alloys required rapid solidification during processing, such as powder atomization, melt spinning and spray casting. These processes are high-cost and thus cause technical difficulties in producing large parts with complex shapes. Based on the aforementioned work, the development of novel aluminium alloys needs to primarily deliver the improved mechanical properties at higher temperatures. Also, the new alloys should have excellent castability, which is preferably suitable for sand casting, permanent mould casting (PMC), or high pressure die casting (HPDC) because of the economic advantages in manufacturing.

The Al-Ni binary system has a higher eutectic temperature (640 ℃) than the Al-Si system (577 ℃). The Al_3Ni phase is stable at up to 600 ℃, which shows great potential for the applications at higher temperatures. Mn was found effective in improving mechanical properties at elevated temperatures [8,27]. Recently, the Al-Ni-Mn alloys attracted increasing attention in development [28–30]. It was reported that Al-Ni-Mn alloys possess

good castability and can be produced by conventional casting such as sand casting and/or PMC [30]. An Al-6Ni-4Mn alloy was reported to offer the yield strength of 130 MPa at 300 ℃ [28]. It is much higher than that offered by Al-Si based alloys. Therefore, Al-Ni-Mn alloys can be potential candidates for the applications at elevated temperatures.

However, the publications about Al-Ni-Mn alloys are limited and scientific understanding from process to microstructure and mechanical properties are still unclear. The microstructures of Al-Ni-Mn alloys under controlled solidification rates of 90 K/s and 5 K/s were reported, but the microstructures with PMC are missed. The effect of Ni and Mn contents on the microstructure and mechanical properties have also not been characterized systematically. Moreover, there are no sufficient reports for the mechanical properties at elevated temperatures. Also, the effect of cooling rates on microstructure is important to be studied systematically. Since Al-Ni-Mn alloys are mainly developed for the applications at elevated temperatures, the evaluation of thermal stability is essential. Up to now, limited research was found. Additionally, studies on the minor element additions to Al-Ni-Mn alloys are also very important but lacking the information in the literatures. Therefore, the present study aims to develop comprehensive understandings for Al-Ni-Mn alloys and explore the technical approaches to modify Al-Ni-Mn alloys with the additions of minor alloying elements.

1.2 Research Objectives

The major objectives of the present study are:

1. To study the effect of Mn on the microstructure and mechanical properties of Al-4Ni, Al-6Ni, and Al-8Ni alloys.
2. To explore the relationship between the microstructure and the mechanical properties of Al-Ni-Mn alloys and to finalise the optimal composition.
3. To study the effect of cooling rates on the microstructure of Al-4Ni-2Mn alloy.
4. To investigate the size and distribution of primary intermetallic phases at different pouring temperatures.

5. To assess the thermal stability of eutectic $Al_9(Ni, Mn)_2$ phase at 250 °C, 300 °C, and 400 °C.
6. To modify the Al-Ni-Mn alloys with minor additions of alloying elements (Cu, Ce).

1.3 Thesis Outline

Following the introduction in Chapter 1, the literature review will be presented in Chapter 2. The history of aluminium alloy application in automotive engines and the performance of commonly used Al-Si based alloys are summarised. The limitations of Al-Si based alloys are presented, and the approaches to improve the mechanical performance at elevated temperatures are described. Then, the demand for developing a novel aluminium alloy is introduced and the attention is focused on the Al-Ni and Al-Ni-Mn alloys. Additionally, the available phase diagram information of the Al-Ni-Mn system, and the microstructure and mechanical properties of Al-Ni-Mn alloys are reviewed. Especially, the potential of Al-Ni-Mn alloys for the applications at elevated temperatures is evaluated. Finally, scientific and technical gaps for further development of Al-Ni-Mn alloys are presented according to the literature of available publications.

In Chapter 3, the research methodologies used in the present study are listed. Moreover, the equipment and techniques parameters of casting process, heat treatment, microstructure characterization and mechanical property testing are given.

Chapter 4 investigates the effect of Mn on the microstructure and mechanical properties of Al-4Ni alloy. The microstructure was characterized by Scan Electron Microscopy (SEM). Phase identification was conducted using Transmission Electron Microscopy (TEM) and X-Ray Diffraction (XRD). The tensile properties were tested at both ambient temperature and the elevated temperature of 250 °C. Lastly, the microstructure, the mechanical properties and the fractural morphology were analysed and described.

Chapter 5 investigates the effect of Mn on the microstructure and mechanical properties of Al-6Ni and Al-8Ni alloys. The primary intermetallic phases, the tensile properties were

reported at ambient temperature and 250 °C. Finally, the optimum composition for Al-Ni-Mn alloy was described.

Chapter 6 presents the microstructural characteristics of Al-4Ni-2Mn alloy under different cooling rates. The cooling rates were controlled by Differential Scanning Calorimetry (DSC). The eutectic structural evolution with the different cooling rates was studied using SEM and TEM to identify different phases. Moreover, the effect of pouring temperature on the microstructure of Al-Ni-Mn alloys was investigated. Four different pouring temperatures (780 °C, 765 °C, 750 °C, 740 °C) were chosen and the size and distribution of the primary intermetallic phases were characterized.

Chapter 7 studies the thermal stability of Al-Ni-Mn alloy at elevated temperatures (250 °C, 300 °C and 400 °C). The coarsening of eutectic $Al_9(Ni, Mn)_2$ phase was investigated and the transformation of eutectic phases from $Al_9(Ni, Mn)_2$ to κ-phase was characterized. Also, the precipitates were studied for the size and distribution at elevated temperatures. Additionally, the hardness response after long term isothermal holding at 250 °C, 300 °C and 400 °C were measured for Al-NI-Mn alloys. The discussion focuses on the thermal stability of eutectic α-Al+$Al_9(Ni, Mn)_2$ structure and the suitable temperature for the application of Al-Ni-Mn alloys.

Chapter 8 investigates the improvement of the mechanical properties of Al-Ni-Mn alloy using minor elements. Cu and Ce elements were used as addition in Al-5Ni-2Mn alloy. The microstructures of Al-5Ni-2Mn-xCu (x=0, 1, 2) and Al-5Ni-2Mn-xCe (x=0, 0.5, 2, 5) were characterized in association with heat treatment. The mechanical properties including the hardness and tensile properties at ambient temperature and 250 °C were studied and discussed.

Chapter 9 presents the main conclusions of the present study. And Chapter 10 provides suggestions for future works in relevant areas.

Chapter 2: Literature review

2.1 Introduction

This chapter focuses on the literature review, in which the history of alloy materials used in automotive engines and the mechanical properties of common commercial aluminium alloys at elevated temperatures are summarised. The latest attempts and the limits of different technical approaches are discussed. Lastly, the potential of Al-Ni-Mn alloys is presented and research gaps are identified.

2.2 The history of materials used in automotive engines

In automotive industry, the applications of aluminium engine parts (such as engine blocks, cylinders and pistons) started in gasoline engines in the late 1970s [31,32] to replace the grey cast iron [33,34]. Compared to grey cast iron, aluminium alloys present advantages in many aspects, such as lightweight, good castability, high thermal conductivity, low thermal expansion and easy recycling. As a substitute for the traditional grey cast iron, aluminium casting alloys show consistent increasing share in automotive engines nowadays. The European Aluminium Association published production numbers of engine blocks in Western Europe from 1997 to 2005 [35]. In 2005, the market share of aluminium engine blocks exceeded that of grey iron for the first time, which reached over 50%. Now, the share of aluminium engine blocks reaches 80%. The global market size for engine blocks was valued at USD 54.81 billion in 2018 and is anticipated to rise up to USD 68.04 billion by 2025 [36]. The engine blocks market in terms of production is expected to be 98,184 thousand units in 2018 and is expected to reach 1,25,989 thousand units in 2025. Growing vehicle production in developing economies is anticipated to drive the automotive engine block market growth. Besides, demand for light weighting vehicle to meet the specific requirements with stringent emission norms is predicted to boost the demand for lighter engine blocks.

Today, engine blocks, cylinder heads and pistons are mainly made from aluminium alloys [31,37–40]. The engine block is the basic framework of a car engine. It supports and holds all the other engine parts. Considering the working circumstance, aluminium alloys for manufacturing engine blocks should meet the following requirements: (1) 200 MPa YS at ambient temperature, 150 MPa YS at 250 °C and elongation more than 2% at ambient temperature, (2) Good thermal conductivity, (3) Good fatigue strength and (4) Low cost. The engine blocks are usually produced by A319 [41–46], A380 [47–50] or A354 alloys [7,8,51,52]. A319 alloy contains 5.0-7.0% Si, 3-5% Cu, and minor additions of Mn, Mg, Ni, Zn, Ti etc. A380 alloy contains 7.5-9.5% Si, 2.0-3.5% Cu, and minor additions of Mn, Mg, Ni, Zn, Ti, Zr etc. A354 alloy contains 8.6-9.4% Si, 1.6-2.0% Cu, 0.40-0.60% Mg, and minor additions of Mn, Zn, Ti, etc. The pistons move up and down within the cylinders and drive the wheels. With the development of engines, the working temperature and cylinder pressure of pistons also increases. For piston alloys, special requirements such as good wear resistance and high thermal fatigue resistance are essential. The eutectic Al-Si alloys are most widely used for pistons [53–60]. The main composition ranges are 11-14% Si, 3-4% Cu, 1-3% Ni and less than 1% Mg. Most pistons are produced by gravity die casting [57,59–64] and some are produced by forging [65–67].

2.3 The performance of Al-Si alloys and modification attempts

2.3.1 The strength loss of commonly used Al-Si alloys at elevated temperatures

Al-Si-Cu based alloys are widely used aluminium alloys for engine blocks. In practice, a wide range of optimized alloys have been developed to achieve specific requirements. Here, the mechanical performance of typical Al-Si-Cu alloys are analysed.

The statistical mechanical properties of 319, 380 and 354 alloys at various temperatures were found in ref [68], as listed in Table 2.1, Table 2.2 and Table 2.3. The mechanical properties at different temperatures provide a glance at softening behaviour at elevated temperatures.

The tensile strength data with different times varying from 0.5 h to 10000 h at each temperature was obtained. Here we focus on strength data after 100 h at elevated temperatures, as shown in Figure 2.1. The 319 alloy presented a yield strength of 180 MPa and ultimate tensile strength of 205 MPa at 25 °C after T5 heat treatment. At 177 °C, the yield strength was 160 MPa and the UTS was 185 MPa. At 230 °C, the yield strength and UTS were 110 MPa and 140 MPa, respectively. When temperature increased to 260 °C, the yield strength decreased to 85 MPa and UTS decreased to 105 MPa. When temperature increased to 315 °C, the yield strength and UTS decreased dramatically to 52 MPa and 66 MPa, respectively. Strength loss is a important factor to evaluate softening resistance, which is calculated by dividing the strength at room temperature by the strength difference between room and elevated temperatures. The 319 alloy experienced 39% yield strength loss at 230 °C and 53% yield strength loss at 260 °C. Therefore, the 319 alloy cannot be used at 260 °C and above.

The 380 alloy presented yield strength of 165 MPa and and UTS of 330 MPa at 25 °C. At 177 °C, the yield strength was 150 MPa and the UTS was 230 MPa, which were slightly decreased. When the temperature was increased to 260 °C, the yield strength and ultimate tensile strength decreased significantly to 90 MPa and 145 MPa, respectively. At a temperature of 315 °C and above, the yield strength and ultimate tensile strength decreased to extremely low levels. The 380 alloy showed 45% yield strength loss at 260 °C, which is better than 319 alloy. But it only presented yield strength of 90 MPa after 100 h at 260 °C, which is unsatisfied for application at this temperature.The 354 alloy with T6 heat treatment presented yield strength of 285 MPa and UTS of 380 MPa at 25 °C. At 177 °C, the yield strength was 260 MPa and UTS was 290 MPa, demonstrated a slight decrease. When temperature was increased to 230 °C, the yield strength and UTS were 95 MPa and 125 MPa, respectively, which was a remarkable decrease. When temperature was increased to 260 °C, the yield strength and UTS decreased dramatically to 66 MPa and 85 MPa, respectively. The 354 alloy presented yield strength loss of 67% at 230 °C and 77% at 260 °C. Clearly, it is not suitable for application at 230 °C and above.

All these alloys showed dramatic decrease at 230°C and above, which demonstrates limitations of applications at elevated temperatures.

Table 2.1 Typical tensile properties of 319-T5 sand castings [68].

Temperature, °C	Time at temperature, h	Yield Strength, MPa	Tensile strength, MPa	Elongation in 50 mm, %
25	…	180	205	1.5
100	0.5	170	195	1.5
	10	170	195	1.5
	100	170	195	1.5
	1000	180	200	1.5
	10000	200	215	1.5
150	0.5	160	180	1
	10	180	200	1
	100	180	200	1
	1000	170	195	1
	10000	165	185	1
177	0.5	150	170	1
	10	165	195	1
	100	160	185	1
	1000	150	180	1
	10000	130	160	1
230	0.5	140	150	1
	10	130	150	1.5
	100	110	140	1.5
	1000	95	125	2.5
	10000	90	115	3.5
260	0.5	115	130	1.5
	10	105	125	2
	100	85	105	2.5
	1000	75	105	3.5
	10000	70	95	4.5
315	0.5	75	90	3
	10	59	75	5
	100	52	66	5.5
	1000	48	66	5.5
	10000	45	66	5.5
370	0.5	41	48	8
	10	38	48	11
	100	38	48	11
	1000	38	48	11
	10000	38	48	11

Table 2.2 Typical tensile properties of 380-F permanent mould castings [68].

Temperature, °C	Time at temperature, h	Yield Strength, MPa	Tensile strength, MPa	Elongation in 50 mm, %
25	…	165	330	4
100	0.5	165	315	7
	10	165	315	7
	100	165	315	7
	1000	185	330	7
	10000	200	325	7
150	0.5	160	275	10
	10	165	290	10
	100	170	260	10
	1000	165	250	10
	10000	160	235	10
177	0.5	150	250	11
	10	160	255	11
	100	150	230	12
	1000	145	220	12
	10000	130	215	13
205	0.5	145	220	13
	10	140	200	13
	100	130	195	14
	1000	115	185	15
	10000	110	180	16
260	0.5	105	150	17
	10	95	145	18
	100	90	145	20
	1000	70	115	30
	10000	59	83	31
315	0.5	62	90	26
	10	55	85	29
	100	45	66	31
	1000	32	48	45
	10000	26	48	45
370	0.5	28	45	45
	10	22	38	46
	100	17	31	47
	1000	17	31	50
	10000	17	31	50

Table 2.3 Typical tensile properties of 354-T6 permanent mould castings [68].

Temperature, °C	Time at temperature, h	Yield Strength, MPa	Tensile strength, MPa	Elongation in 4D, %
25	…	285	380	6
100	0.5	285	345	6
	10	285	350	6
	100	290	360	6
	1000	310	370	6
	10000	340	415	6
150	0.5	275	325	6
	10	295	345	6
	100	315	350	
	1000	305	340	6
	10000	240	290	6
177	0.5	270	310	6
	10	290	325	6
	100	260	295	8
	1000	195	230	13
	10000	95	130	24
205	0.5	270	290	6
	10	250	270	9
	100	180	205	17
	1000	105	130	30
	10000	75	105	45
230	0.5	240	255	9
	10	170	195	15
	100	95	125	25
	1000	75	95	40
	10000	59	85	55
260	0.5	170	195	16
	10	105	115	22
	100	66	85	35
	1000	52	66	50
	10000	41	59	65
315	0.5	85	90	29
	10	48	59	60
	100	34	41	85
	1000	-	-	-
	10000	-	-	-

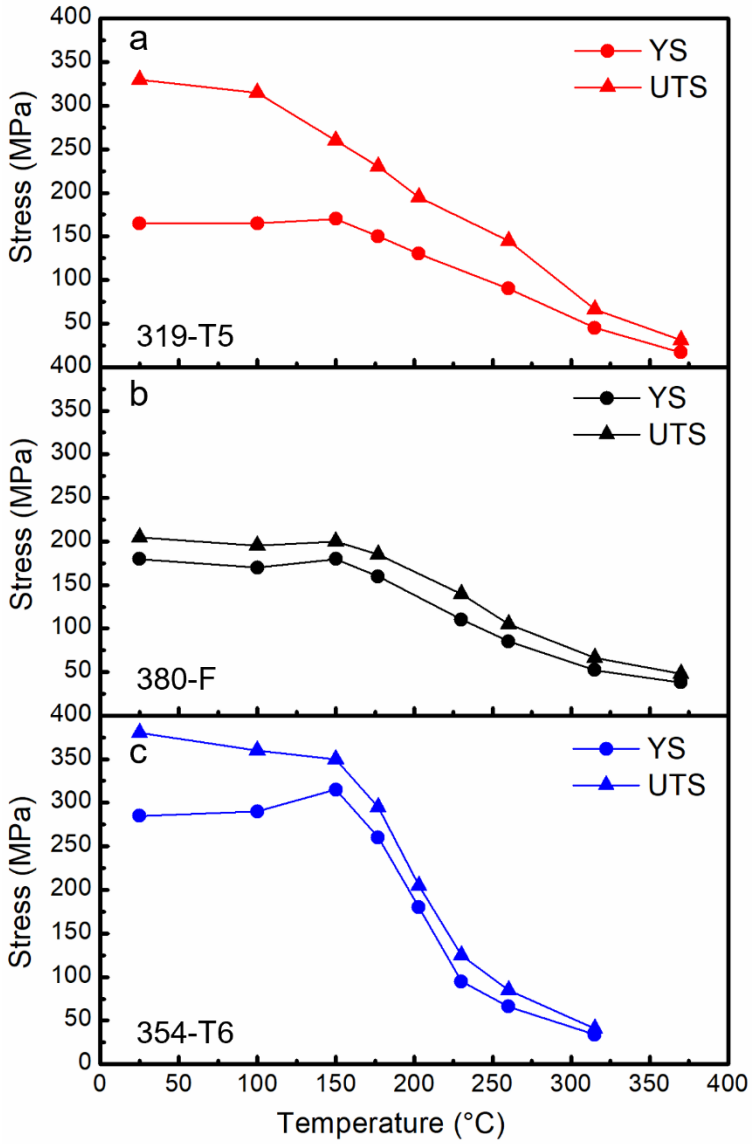

Figure 2.1 The tensile strength of (a) 319 alloy with T5 heat treatment, (b) as-cast 380 alloy and (c) 354 alloy with T6 heat treatment after 100 h at elevated temperatures.

2.3.2 The modification of Al-Si alloys with minor alloying elements

The development of a new generation of automotive engines requires better strength at higher temperatures. Many researchers have been working on it, and several approaches have been attempted. The most common attempt is to modify the Al-Si based alloys with minor elements. Mg [69–71] is a widely used alloying element. Especially, transition metals like zirconium [6–9], scandium [4,5,72–77], nickel [7,8,15], manganese [8], rare-earth metals [18,78–80], molybdenum [81] and combination of zirconium, vanadium and

titanium [82–86] are promising for improving mechanical properties at elevated temperatures.

The effects of Mg on the microstructure and mechanical properties of A319 alloys was investigated [71]. 0.45% Mg addition in A319 resulted in a increasement of as-cast strength from 140 MPa to 175 MPa. After ageing at 150 °C, the peak yield strength increased from 337 MPa to 415 MPa with 0.45% Mg. The significant improvement was achieved through cooperative precipitation of Al_2Cu and Mg_2Si precipitates. Figure 2.2 displays the yield strength after ageing at different temperatures. It was observed that the peak came earlier with increasing ageing temperatures. When the temperature reached 220 °C, softening was observed after 8 h. And when the temperature increased to 250 °C, an immediate softening was observed. Softening behaviour of A319.2 alloy with Mg addition alloy indicates that both Al_2Cu and Mg_2Si precipitates started to lose strengthening effect at 220 °C and above in a very short time.

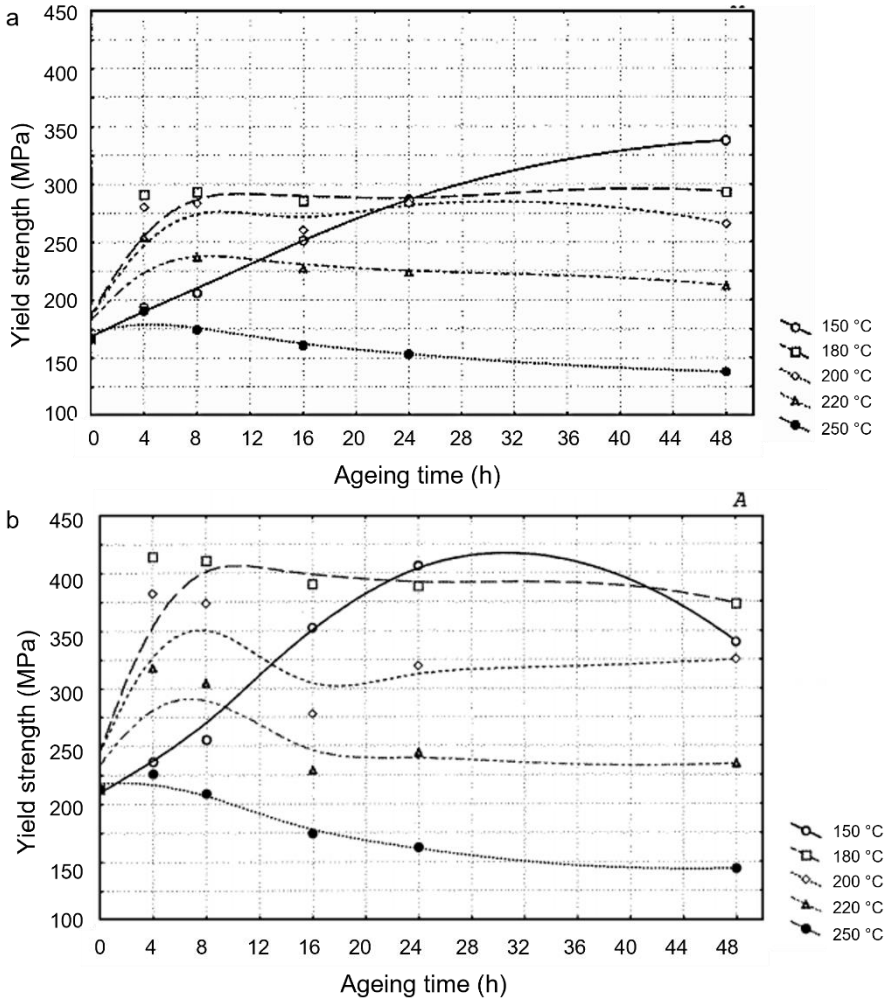

Figure 2.2 Variation in the yield strength of (a) alloy 319.2 and (b) alloy 319.2 with 0.45% Mg in the T6 condition [71].

Zr exhibits potential in improving mechanical properties at elevated temperatures. In the Al-rich corner of the Al-Zr binary phase diagram [87], the eutectic Al_3Zr phase and Al_3Zr precipitate exist. The Al_3Zr has a stable $D0_{23}$ structure and a metastable $L1_2$ structure, which is the same structure as the Ni_3Al phase in Ni-based superalloys [88]. The maximum solubility of Zr in Al is 0.083 at.%. Knipling [89] investigated the Al-0.1Zr and Al-0.2Zr alloys. The nanometre-scale $L1_2$ Al_3Zr precipitates formed after ageing. Figure 2.3 displays the Vickers microhardness after ageing, which indicates a strong strengthening effect of the Al_3Zr precipitates. The hardness after ageing increased significantly with increasing Zr contents. Moreover, the ageing temperatures were at 375°, 400 °C and 425 °C, which are

much higher than the range of 150 °C to 200 °C for the Al-Si-Cu-Mg alloys. More significantly, the Al_3Zr precipitates commence at 420 °C and above. Based on this, the Al_3Zr precipitate is more heat resistant than the Al_2Cu and Mg_2Si phases at elevated temperatures.

The effect of Zr on the Al-Si-Cu-Mg-Ni alloy have been investigated. In one study, the yield strength at 350 °C increased from 72 MPa to 82 MPa with 2.5% Zr. [6]. In another study [9], 0.14% Zr addition increased the yield strength from 218 MPa to 293 MPa at ambient temperature and from 160 MPa to 232 MPa at 200 °C. Additionally, the effect of Zr on A354 alloy was also studied. The yield strength increased by 40 MPa with 0.3% Zr [8]. Another study showed the yield strength at 190 °C increased from 248 MPa to 261 MPa with 0.4% Zr [7].

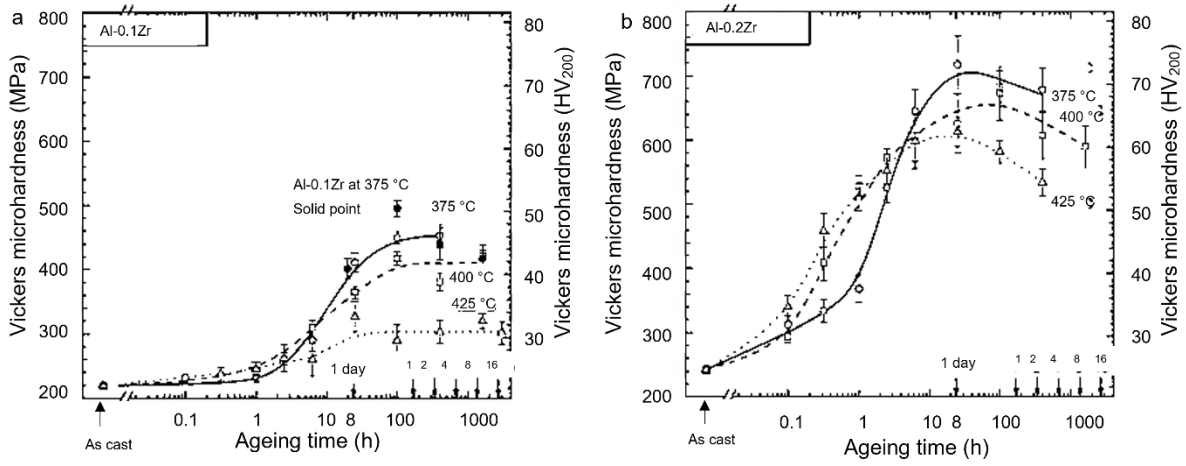

Figure 2.3 Vickers microhardness vs ageing time at 375 °C, 400 °C and 425 °C for (a) Al–0.1 Zr, (b) Al–0.2 Zr [89].

Sc has attracted growing attention during the past two decades. The lattice constant of $L1_2$-type Al_3Sc particles (a=0.4103 nm) is very close to that of α-Al (a=0.405 nm) [73], which presents a lattice mismatch of only 1.5% with aluminium. Therefore, the Al_3Sc phase has very strong strengthening effect. The Sc was also found to be effective in grain refinement [90].

As reported in references [3,91–93], Al–Sc alloys have good performance at ambient as well as elevated temperatures. According to the Al-Sc binary phase diagram [94], in the Al-rich corner, the maximum solubility of Sc in Al is 0.23 at.%, and the eutectic concentration is 0.31 at.%. The Al_3Sc precipitate forms from supersaturated solid solution during the ageing process [95]. The $L1_2$ structure Al_3Sc precipitate is coherent with the matrix and exhibits a high number density, a low coarsening rate, and good thermal stability at elevated temperatures [76,96].

The effect of Sc contents on the microstructure and mechanical properties have been studied by many researchers [75,97]. A study [75] investigated the Al-Sc alloys, and three main points were obtained, (1) increasing amount of Sc is effective to improve the mechanical performance of Al-Sc alloys; (2) for different Sc contents, the peak hardness reaches at different ageing time. Alloys with higher Sc contents reaches peak value earlier than the alloys with less Sc; (3) for a specific amount of Sc addition, the maximum hardness is obtained at an ageing temperature around 325 ℃; lower or higher ageing temperatures lead to reduced hardness. It was apparent from Figure 2.4 [98] that the Al_3Sc ($L1_2$) started to precipitate when temperature reached 250 ℃. And an ageing peak of 429 MPa was achieved at about 325 ℃. However, hardness decreased from 448 MPa to 295 MPa after 400 h at 400 ℃, which indicates softening at this temperature.

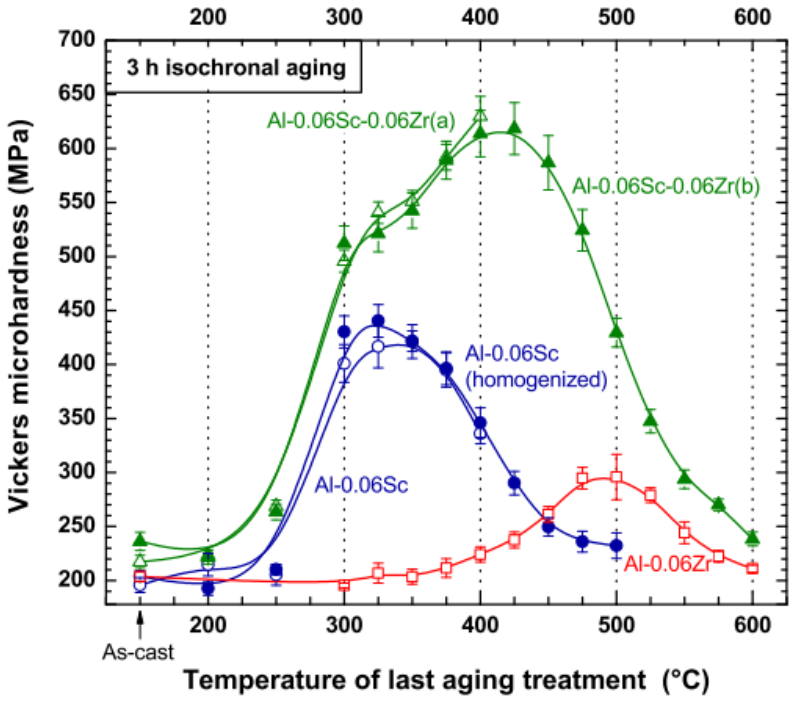

Figure 2.4 Vickers microhardness evolution during isochronal ageing of Al-0.06Sc, Al-0.06Zr and Al-0.06Sc-0.06Zr [98].

Ramli [99] investigated the effect of Sc on microstructure and mechanical properties of Al-Si alloy and concluded that the hardness and tensile strength increased with increasing Sc levels. The effect of Sc contents on mechanical properties of Al-Si-Mg-Cu-Ti alloy was studied and the tensile strength was plotted in Figure 2.5 [77]. It was seen that the tensile strength increased from 281 MPa to 304 MPa with 0.2% Sc addition.

Figure 2.4 also demonstrates the combined effect of Zr and Sc. The Al-0.06Sc-0.06Zr alloy showed a peak microhardness of 618 MPa, which was much higher than the Al-0.06Sc alloy and the Al-0.06Zr alloy as well. The the combination of Zr and Sc provides better performance.

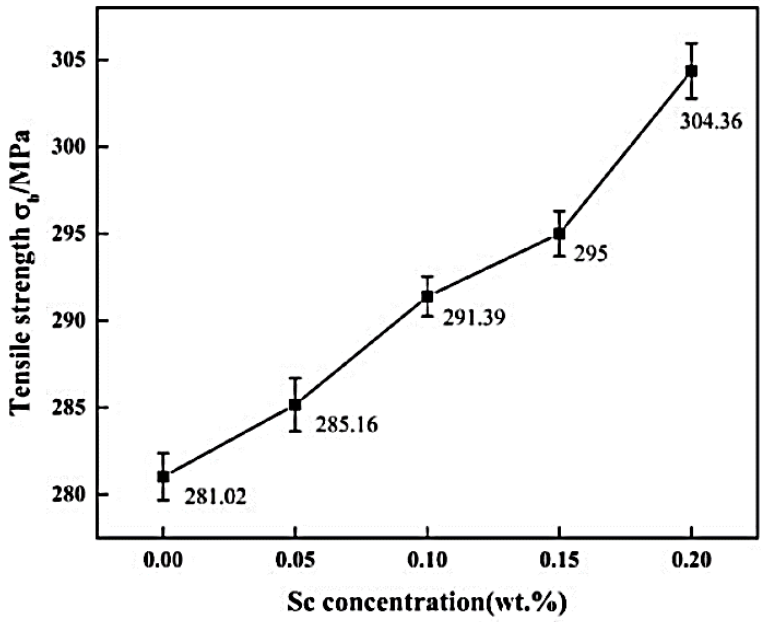

Figure 2.5 The effect of Sc content on tensile strength of Al-Si-Mg-Cu-Ti alloy with T6 heat treatment [77].

The intermetallic compound Al_3Ti is also attractive as a high-temperature strengthening phase due to its high melting point, lightweight, and good oxidation resistance [100]. But the tetragonal D_{022} structure makes Al_3Ti very brittle at room temperature. Some efforts have been made to transfer the D_{022} structure to those of higher symmetry [101].

Ni is also a common element addition in aluminium alloys for improved performance at elevated temperatures. A study reported that 0.5% Ni addition to A354 improved yield strength at 190 °C from 248 MPa to 261 MPa [7]. The effect of Ni on A354 was also found in another ref [8]. At ambient temperature, 2% Ni addition increased yield strength by 20 MPa. However, the yield strength decreased significantly when Ni content was further increased to 4%. At 250 °C, the yield strength increased from 218 MPa to 224 MPa with 2% Ni and 254 MPa with 4% Ni.

The effects of Mn on A354 alloy was also displayed in ref [8]. Mn improved the tensile strength at both ambient and elevated temperatures. The yield strength at ambient temperature increased from 325 MPa to 355 MPa with 0.75% Mn. And the yield strength at

250 °C increased from 214 MPa to 246 MPa. Moreover, the effect of Mn on Al-12.6Si alloy was investigated [27], and the results are plotted in Figure 2.6. It was seen that 1% Mn addition significantly improved both the yield strength and ultimate tensile strength. However, high Mn contents (2% or more) decreased tensile strength dramatically. The best yield strength and ultimate tensile strength obtained with Mn additions were 133 MPa and 198 MPa, respectively, which showed 75% and 54% improvements compared to the Mn-free alloy.

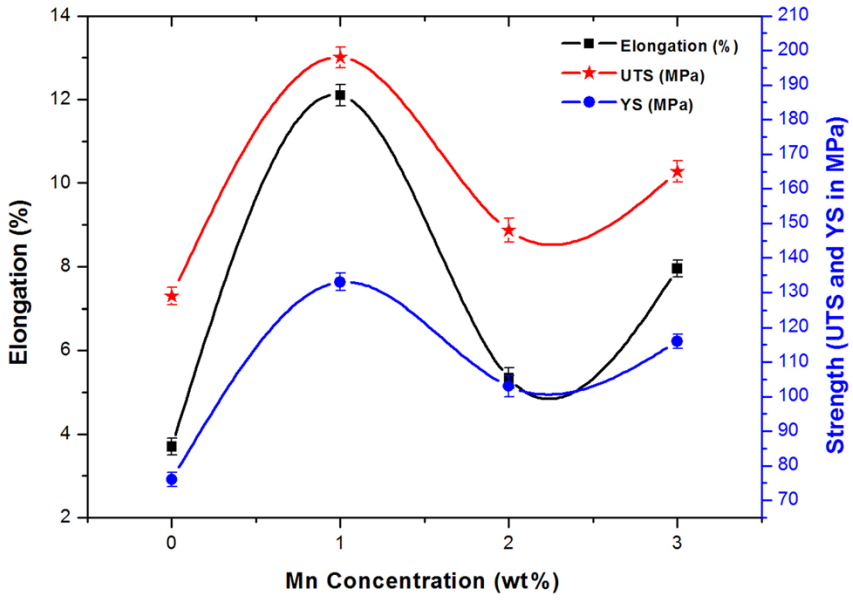

Figure 2.6 Graphical representation of ultimate tensile strength, yield strength, and percentage elongation as a function of Mn concentration in Al-12.6Si alloy [27].

Rare earth elements have attracted increasing attentions. It was reported effective in modifying the morphology of eutectic Si particles in Al-Si alloys [19,20,23,79]. Among all the rare earth elements, Ce and La are the most commonly used elements. Figure 2.7 presents the effect of Ce on mechanical properties of an Al-Si-Cu-Mg alloy [63]. The tensile strength increased from 204 MPa to 238 MPa with 0.1% Ce. However, with further increase of Ce additions, the tensile strength decreased. The hardness, increased constantly from 74.6 HV to 80.8 HV with increasing Ce contents. Another study focused on effect of Ce on an Al-Zn-Mg alloy [102]. The tensile strength increased by 81 MPa and 191 MPa with 0.15

and 0.3% Ce, respectively. Additionally, Ce additions to Al-Cu-Mg-Ag alloy was investigated [103]. The yield strength increased by 41 MPa, 30 MPa, 60 MPa and 76 MPa with 0.2% Ce at ambient temperature, 200 ℃, 300 ℃ and 350 ℃, respectively. Based on these results, it was deduced that Ce is effective in improving performance at elevated temperatures.

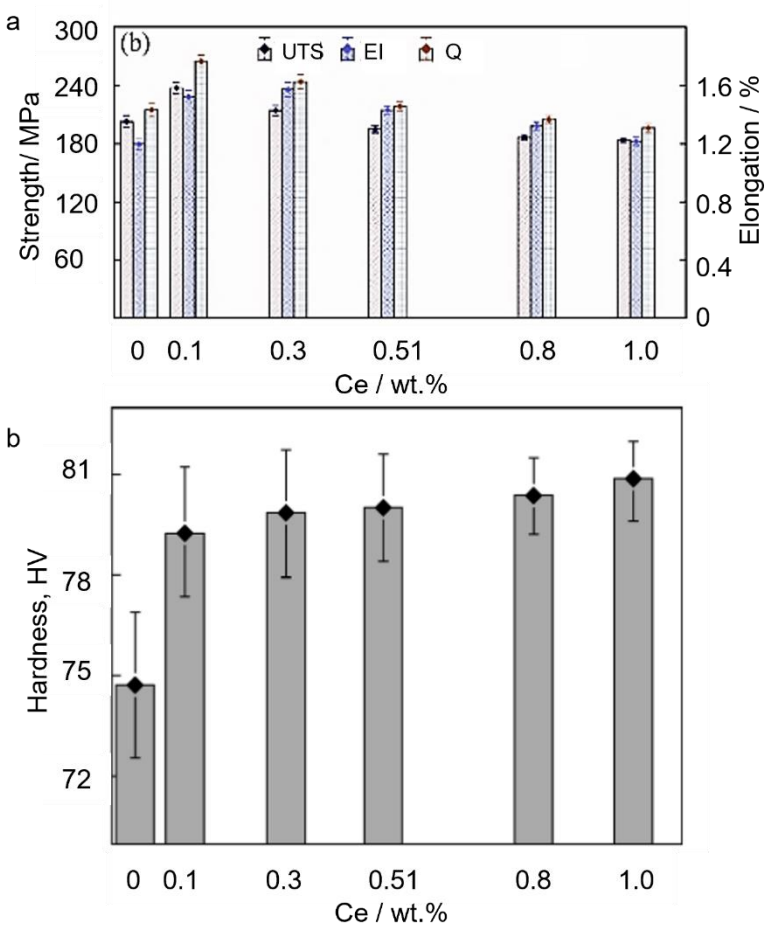

Figure 2.7 (a) Tensile strength test results composed of the UTS, El, and Q of the base alloy with different concentrations of Ce, (b) Hardness values for base Al-11Si-Cu-Mg with different Ce levels [60].

Several elements have been studied and three main mechanisms to provide strengthening effect are summarised. Firstly, producing precipitates to improve strength, such as Al_2Cu, Mg_2Si, Al_3Sc and Al_3Zr. Secondly, modifying microstructure to improve strength. For instance, modify the morphology of Si particle or decrease the secondary dendrite arm

spacing (SDAS) to improve strength. Thirdly, introducing secondary phases to improve strength, such as Ni-rich phase, $Al_{15}(Mn, Fe)_3Si_2$ phase etc.

2.4 Development of novel aluminium alloys for application at elevated temperatures

The temperature in a combustion chamber of an engine can reach up to 1500 °C. While the working temperature of the engine blocks, heads and pistons are normally within a range from 150 °C to 300 °C which is achieved by a cooling system. Circulating coolant liquid takes heat and maintains temperatures of all engine parts within durable temperature ranges. According to this, there are two approaches to increase engine efficiency; increasing heat dissipation efficiency and improving the heat resistance of engine parts. As mentioned, cast iron was commonly used engine materials before aluminium alloys. The thermal conductivity of cast iron is 55 W/(m·K). While the thermal conductivity of pure aluminium and aluminium alloys are 220 W/(m·K) and 120-180 W/(m·K) [104], respectively. Aluminium alloys show a huge advantage in thermal conductivity. A higher thermal conductivity coefficient leads to quick heat dissipation. Hence, engine parts can be protected from high temperature by a cooling system and work properly. The other important and promising approach to increase engine efficiency is to improve the heat resistance of engine material.

2.4.1 Al-Cu-Mn-Zr alloys

Apart from modifying Al-Si based alloys, developing new aluminium alloys with improved mechanical properties at higher temperatures has become more attractive. Some attempts are developments of Al-Fe-V-Si [24], Al-Fe-Gd [25], and Al-Co-Cr-Fe-Ni [26] alloys. However, these alloys require rapid solidification processing, such as powder atomization, melt spinning or spray casting. These are costly technologies, which may encounter difficulties in producing large size and complex shape parts.

Another promising direction is developing novel Al-Cu based alloys. The metastable θ′ (tetragonal Al_2Cu) precipitates provide strong strengthening effect and lead to high strength. Furthermore, the metastable θ′ phase was able to be stabilized by microalloying with Mn

and Zr [105,106], and therefore stay stable to a temperature of up to 350 °C. Due to the role of Zr and Mn stabilizing the metastable θ′ phase, the Al-Cu-Mn-Zr alloys were referred as ACMZ alloys [107]. ACMZ alloys are newly created by Nemak. An ACMZ alloy in reference [107,108] demonstrated half of the YS of Al5CuMg alloy at 25 °C but doubled at 300 °C, which indicates good performance at elevated temperatures. They have the following important properties: (1) High conductivity, improving the thermal management of higher power density engines; (2) Low thermal expansion, which significantly increases the dimensional stability of the component within the engine; (3) High resistance to thermal fatigue allowing greater engine safety design limits. Hot tearing is a key issue encountered in aluminium alloys with high Cu levels. Nemak claimed it has been solved by a newly-developed liquid metal processing method (Rotacast®). Now the hot tear resistance of the ACMZ alloy is superior.

RR350 alloy is a good representative of ACMZ alloys, which was designed especially for creep resistance [107,108]. In addition to Mn and Zr, the RR350 alloy has Ni and Co alloying additions, which form particles on grain boundaries and reduce creep rate at elevated temperatures. RR350 contains about 5% Cu, 0.2% Mn, 0.15% Zr, 1.5% Ni and 0.25% Co. The metastable θ′ precipitates in RR350 alloy is maintained up to 300 °C and evolution of θ′ to θ is not observed [109,110]. In comparison to the A319 alloy, the coarsening of θ′ precipitates is reduced, leading to significantly improved elevated temperature mechanical properties. The tensile strength is listed in Table 2.3.

Another ACMZ alloy with composition of Al-6.5Cu-0.2Mn-0.15Zr-0.10Ti was investigated [111], named as ACMZ01 alloy in this thesis. The tensile strength displayed YS of 200 MPa, UTS of 356 MPa at 25 °C and YS of 105 MPa, UTS of 134 MPa at 300 °C, which is higher than the RR350 alloy, as shown in Table 2.4. A complex shape cylinder head was cast with this new alloy, as shown in Figure 2.8, demonstrating good castability of the ACMZ alloys.

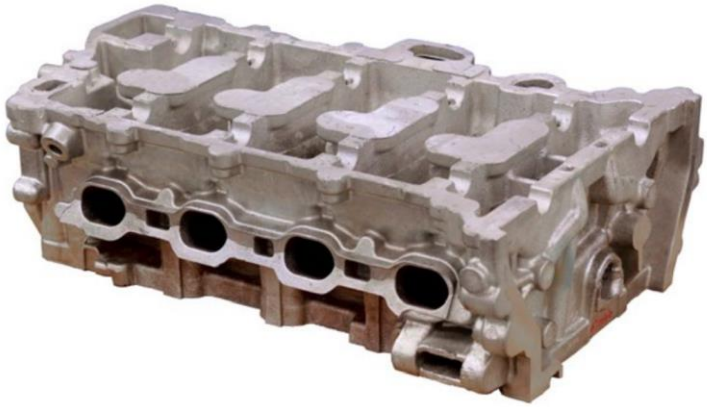

Figure 2.8 Cylinder head produced with the new ACMZ alloy [112].

Table 2.4 Tensile strength of RR350 and ACMZ01 alloy [111].

Alloy	25 °C		300 °C	
	YS	UTS	YS	UTS
RR350[a]	171	286	98	124
ACMZ01[b]	200	356	105	134

2.4.2 Al-Ce based alloys

Another promising attempt to improve mechanical properties at high temperatures is Al-Ce based alloys. The Al-Ce alloy was firstly studied using powder metallurgy, which provided good mechanical strength at high temperature [113]. However, powder metallurgy technology limited the capability of producing complex shape components. Belov [114] studied the Al-Ce-Ni alloys. Fine eutectic Al_4Ce and Al_3Ni particles provided high mechanical properties at room and elevated temperatures. Recently, the Al-Ce based alloy attracts increasing attention, which presents several advantages. Firstly, the eutectic $Al_{11}Ce_3$ phase remains stable to above 500 °C [115]. Figure 2.9 displays the eutectic Si phase in the Al-12.6Si alloy and eutectic $Al_{11}Ce_3$ phase in the Al-12.5Ce alloy after ageing at 400 °C

[116]. The eutectic Si phase coarsened and spheroidized after 751 h at 400 °C, while the eutectic $Al_{11}Ce_3$ phase remained the same morphology after 12 weeks. It is expected that stable $Al_{11}Ce_3$ phase improves performance at elevated temperatures. The Al-Ce alloy was reported to retain over 60% of the room temperature yield strength and more than 40% UTS at 300° C [115].

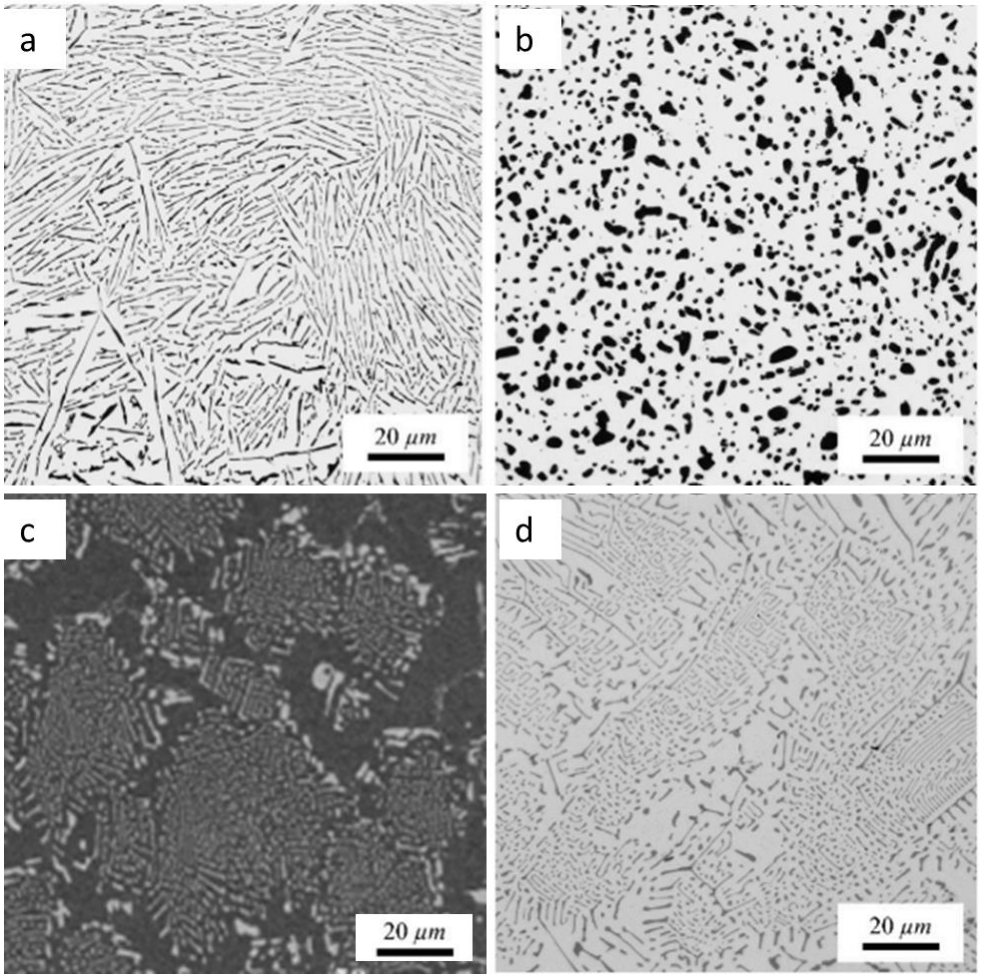

Figure 2.9 Microstructures of (a) as-cast Al-12.6Si alloy, (b) Al-12.6Si alloy after ageing for 751 h at 400 °C, (c) as-cast Al-12.5Ce alloy, (d) Al-12.5Ce alloy after ageing 12 weeks at 400 °C [116].

Secondly, the Al-Ce alloys showed good castability, which allows for sand casting, permanent mould casting and squeeze casting. The hot tearing tendency was also tested to be very low. Figure 2.10 shows air-cooled cylinder head cast from Al-12Ce and Al-12Ce-0.4Mg alloys [113]. The complex shape of cylinder head confirmed the superior melt

fluidity of Al-Ce alloys. Thirdly, Al-Ce alloys shows superior elongation. Al-8Ce alloy displayed elongation of 19% and Al-12Ce alloy displayed elongation of 13.5% [117]. More tensile strength results list in Table 2.5. It is seen that binary Al-Ce alloys provided limited tensile strength. Therefore, other alloying elements are needed. Magnesium and Silicon are effective strengthening element for the aluminium matrix. When 10% Mg was added to the Al-8Ce alloy, the yield strength increased significantly from about 50 MPa to 162 MPa [118]. Another study investigated 0.4% Mg addition to Al-12Ce alloy. The as-cast yield strength increased from 58 MPa to 79 MPa. When Si was added to a Al-12Ce-0.4Mg alloy, a strong response to T6 heat treatment was presented. The yield strength increased from 75 MPa to 128 MPa and the UTS increased from 141 MPa to 252 MPa after heat treatment. The improvement is associated with formation of AlCeSi, AlSiMg, Al_3Mg_2 phase and precipitates. The Al-Ce based alloys have good castability as well as thermal stability, which is promising for lightweight high performance applications in the automotive, aerospace and other industrial sectors.

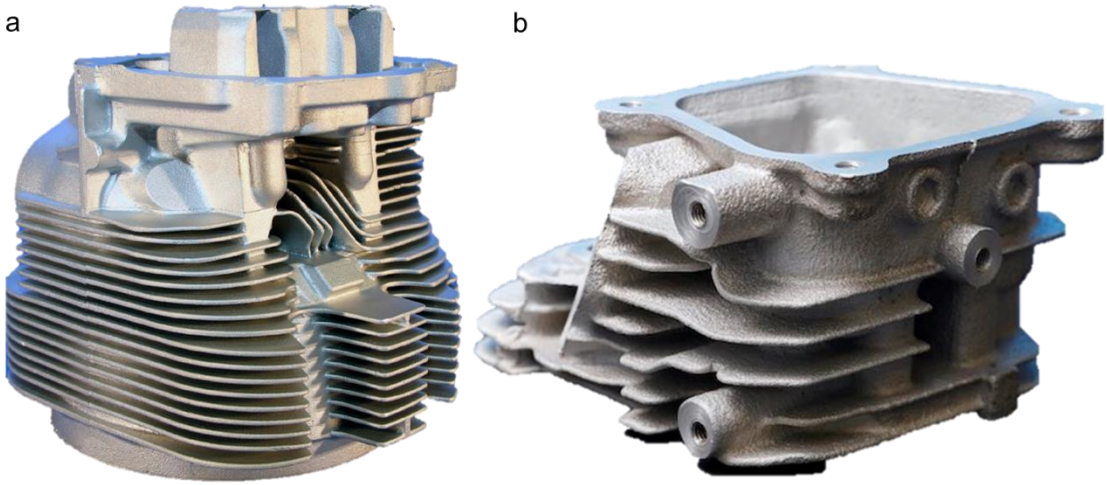

Figure 2.10 Air-cooled cylinder head cast from (a) Al-12Ce alloy and (b) Al-12Ce-0.4Mg alloy [113].

Table 2.5 Mechanical properties of Al-Ce and Al-Ce based alloys [113,117].

Alloy	As-Cast			T6 Heat-Treated		
	YS	UTS	EL	YS	UTS	EL
Al-6Ce	30	103	25	-	-	-
Al-8Ce	40	148	19	-	-	-
Al-10Ce	50	152	8	-	-	-
Al-12Ce	58	163	13.5	48	132	26.5
Al-16Ce	68	144	2.5	-	-	-
Al-12Ce-0.4Mg	79	201	6.0	62	224	8.5
Al-12Ce-4Si-0.4Mg	75	141	2.0	128	252	8.5

2.4.3 Al-Ni and Al-Ni-Mn alloys

Ni is a trace element added to Al-Si alloys. Moreover, the Al-Ni alloys attracted attention because its good thermal stability of the eutectic Al_3Ni phase [119], which provide the potential for applications at elevated temperatures. The Al-Ni phase diagram displays in Figure 2.11. In the Al-rich corner, the eutectic reaction $L \rightarrow \alpha Al + Al_3Ni$ happens at 639.9 °C. This eutectic temperature is much higher than the Al-Si eutectic temperature, indicating that the eutectic Al_3Ni phase is more stable at elevated temperatures. Also, because of the large portion of eutectic phases, the fluidity is good [120,121]. The eutectic Al_3Ni phase is a fine rods-like shape [119,122], therefore can hinder dislocation movement and provide good strength. The morphology of the eutectic Al_3Ni phase was revealed by deep etching and presented in Figure 2.12.

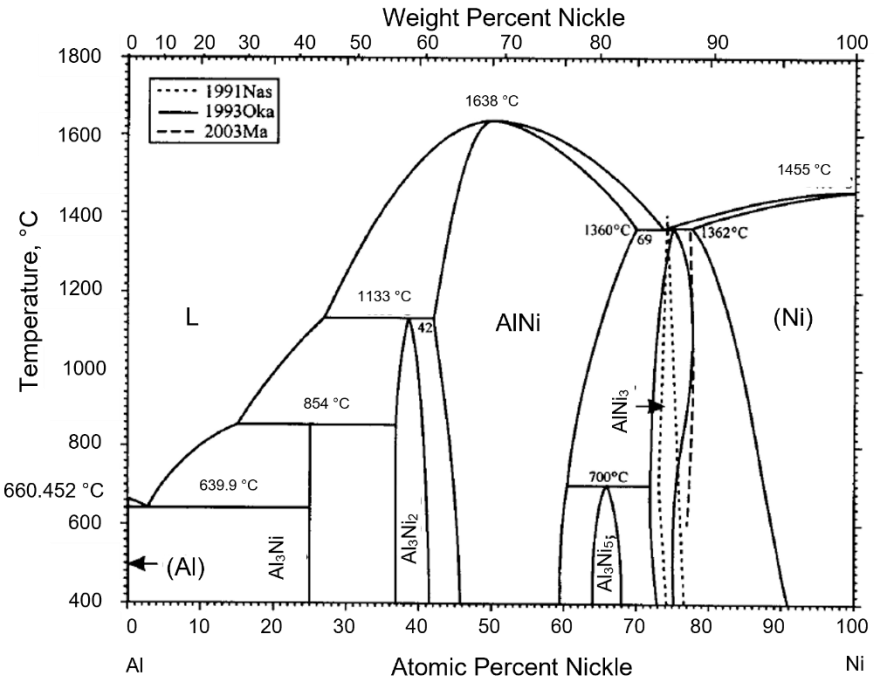

Figure 2.11 Al-Ni phase diagram [123].

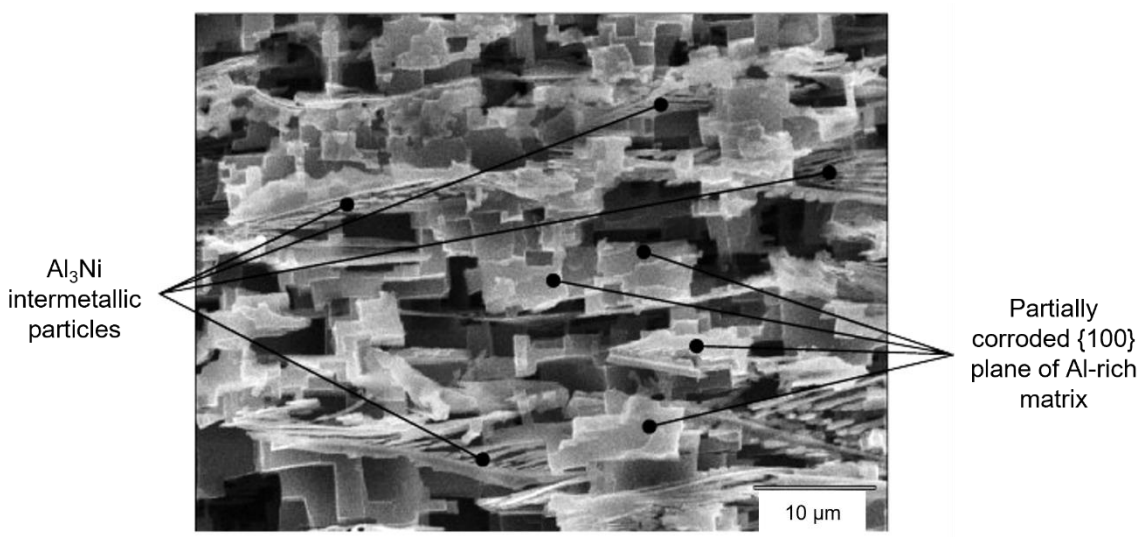

Figure 2.12 Typical SEM micrograph of Al-5% Ni alloy after deep etching [124].

The cooling rates affect eutectic Al_3Ni phase morphology and then affect the mechanical properties. The study on Al-5Ni alloy found that a high cooling rate leads to fine morphology and smaller secondary dendrite arm spacing [124]. The fine morphology offers yield strength of 85 MPa and UTS of 195 MPa, respectively, while the coarse morphology offers 60 MPa and 110 MPa, respectively. Though the room temperature strength of Al-Ni

alloy is relatively low, the heat resistance of Al-Ni alloys is higher than the Al-Si alloys. The hardness of Al-6Ni alloy and alloy A356 was tested at 300 °C and 350 °C, as shown in Figure 2.13 [125]. The hardness of A356 decreased dramatically after 1 h at 300 °C, while the Al-6Ni alloy remained at the same level after 36 h at 300 °C and 350 °C as well. It was confirmed that Al-Ni alloys present better heat resistance than Al-Si alloys.

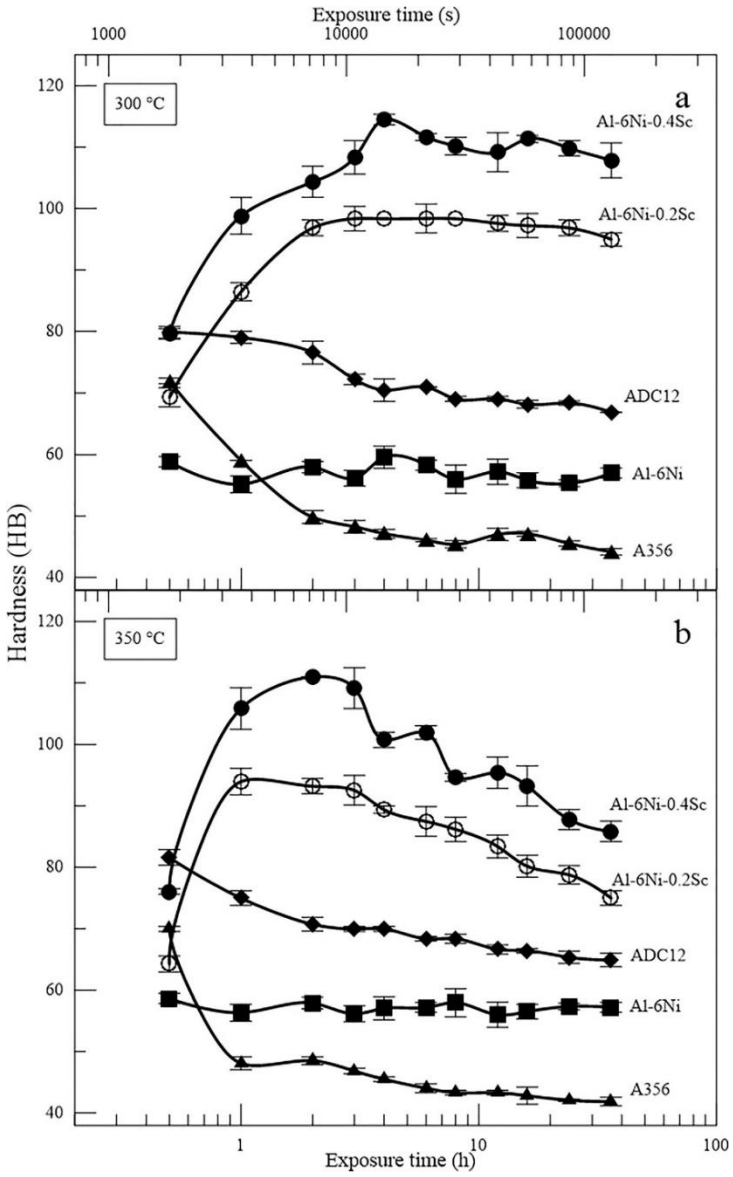

Figure 2.13 Hardness evolution of Al-Ni alloys after high-temperature exposure, compared with the commercial A356 alloys at (a) 300 °C and (b) 350 °C at different exposure time [125].

The Al-Ni-Mn alloys attracted increasing attention in the last two decades [30,126,127]. The traditional and widely used Al-Si-Cu alloys lose strength at elevated temperatures because of the coarsening of the Al_2Cu and Mg_2Si strengthening phases. It is necessary to develop new alloys which can work at 250 °C and above. The Al-Ni alloys, as described above, was believed to produce good strength and heat resistance. The eutectic Al_3Ni phase is the fine rod, which can hinder dislocation movement according to the Orowan mechanism. Moreover, Al_3Ni phase was confirmed very stable at elevated temperatures [119,122].

Mn is also considered an attractive alloying element to improve elevated temperature performance in aluminium alloys [8,10,27,128]. The Al_6Mn phase is thermal stable. The maximum solubility of Mn in Al at eutectic temperature is 1.8%, which can produce sufficient precipitates. Moreover, the diffusion rate of Mn is much lower than the Si, Mg and Cu. At 400 °C, the diffusion rate of Mn is 5.20×10^{-19} m^2/s, while the Cu is 2.31×10^{-15} m^2/s, the Mg is 1.1×10^{-14} m^2/s, and the Si = 3.68×10^{-15} m^2/s [129]. As a result, the coarsening of Al_6Mn at elevated temperatures is limited. The combination of the eutectic α-Al+Al_3Ni matrix and Al_6Mn phase is capable of providing promising application at elevated temperatures.

A few pieces of literature present phase equilibria of the Al-Ni-Mn system, and most of them focused on Ni and Mn-rich corners [130–133]. The phase equilibria in the Al-rich region was firstly investigated by Raynor in 1944 [134]. Apart from binary Al_3Ni, Al_6Mn ad Al_4Mn phases, a ternary phase termed X was found. The composition was about 14.5 at.% Mn, 5.3 at.% Ni and 80.1 at.% Al. The structural formula was $Ni_4Mn_{11}Al_{60}$. Robinson [135] firstly determined the crystal structure using image-seeking functions on Patterson projections and sections in 1954. The orthorhombic cell dimensions are: a = 23.8 Å, b = 12.5 Å, and c = 7.55 Å. In another reference in 1977 [136], the structural formula of $Ni_4Mn_{11}Al_{60}$ was determined as $Mn_6Ni_2Al_{31}$ or (Mn, Ni)$Al_{3.87}$. This phase was also termed Mn_3NiAl_{16} [137] and $Al_{16}Mn_3Ni$ [138] in some other literature. In later published papers, this phase was termed $Al_{60}Mn_{11}Ni_4$ and widely used and accepted by other researchers.

Another phase with almost the same composition of $Al_{60}Mn_{11}Ni_4$ but with different crystal parameters was found in 1988. It also has an orthorhombic structure, and the cell dimensions are a = 3.37 Å, b = 12.4 Å, and c = 2.40 Å. This phase was termed $C_{3,I}$-$Al_{60}Mn_{11}Ni_4$. The lattice parameters: a = 3.27, b = 12.5, and c = 2.38 Å were determined in another ref [139], through high resolution electron microscopy (HREM) images. Therefore, the $Al_{60}Mn_{11}Ni_4$ and $C_{3,I}$-$Al_{60}Mn_{11}Ni_4$ are almost the same with only one lattice parameter difference.

The experimental diagram of the Al-Ni-Mn system in the Al-rich corner was firstly published in 1976 [137] and updated in 2005 [138], as shown in Figure 2.14. There are Al_3Ni, Al_6Mn, Al_4Mn, $Al_{16}Mn_3Ni$ phases in this corner. A peritectoid reaction happens at 645 °C (P): L + Al_6Mn→(Al) + $Al_{16}Mn_3Ni$. At lower temperature of 637 °C (E), an eutectic reaction occurs: L → (Al) + Al_3Ni + $Al_{16}Mn_3Ni$. Besides, there are three mono variant reactions in this corner. The line e1-P represents L → (Al) + Al_6Mn, and the temperature range is between 658-645 °C. The line P-E represents L → (Al) + $Al_{16}Mn_3Ni$, and the temperature range is between 645-637 °C. The line e2-E represents L → (Al) + Al_3Ni, and the temperature range is between 640-637 °C. The solubility of Ni in Al_6Mn phase is neglectable, while the Mn in Al_3Ni is about 0.26%.

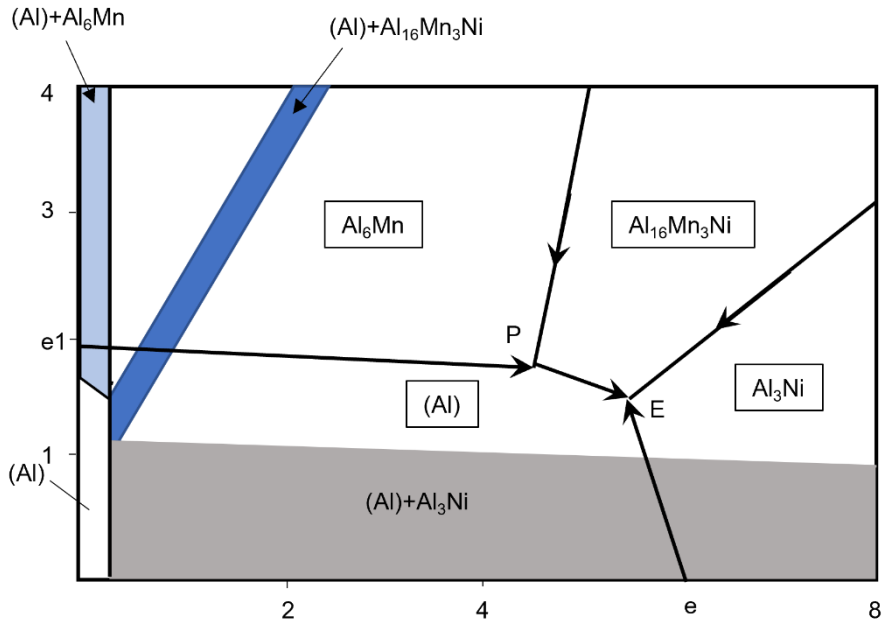

Figure 2.14 Phase diagram of Al-Mn-Ni system: projection of the solidification surface and distribution of phase regions in the solid-state at 627 ℃ [138].

The experimental phase diagram in the Al-rich corner was also found in other literature [140,141]. Massive alloys with varying Ni and Mn contents were obtained. Each sample weighed about 5 g and annealed and then water-quenched. The partial isothermal sections at 850 ℃, 750 ℃, 645 ℃ and 620 ℃ are presented in Figure 2.15. At 850 ℃, there is the only liquid phase when a small amount of Mn and Ni exists, while a series of phases (including β-AlNi phase, δ-Al_3Ni_2, γ-AlMn, γ_2-Al_8Mn_5, $Al_{11}Mn_4$, φ-phase and T phase) formed when high content of Ni and Mn appears. Adjacent to the liquid area, there are μ-Al_4Mn phase, κ-phase and Al_3Ni phase and their coexisting area. The κ-phase is a hexagonal phase with lattice parameters: a= 1.7625 nm, c = 1.2516 nm. It has the same structure as k-$Al_{14.4}Cr_{3.4}Ni_{1.1}$ in the Al-Cr-Ni system [142–144] and ζ-phase in the Al-Cr-Cu alloy [145,146].

When the temperature decreases to 750 ℃, an orthorhombic O-phase occurs. It is also known as $C_{3,I}$-$Al_{60}Mn_{11}Ni_4$. DTA results shows that this O-phase formed at 757 ℃. There are five coexisting areas adjacent to the liquid area: μ+L; κ+L; κ+O-phase+L; O-phase+Al_3Ni+L; Al_3Ni+L. At 645 ℃, the compositional region for liquid narrowed down to a minimal area. In the corner, apart from (Al) and liquid phases, the O-phase and κ-phase coexist with liquid, and the O-phase and Al_3Ni phase coexist with liquid. When the temperature decreased to 620 ℃, the liquid disappeared. The κ-phase coexists with Al_6Mn and (Al), and the O-phase coexists with Al_3Ni and (Al). The experimental maximum solubility of Mn in Al obtained is 0.7 at.%, and the maximum solubility of Ni in Al is 0.2 at.%.

According to the results described above, in the Al-rich corner, the (Al), Al_6Mn, κ -phase, O-phase and Al_3Ni phase form, and some can coexist in a specific compositional range.

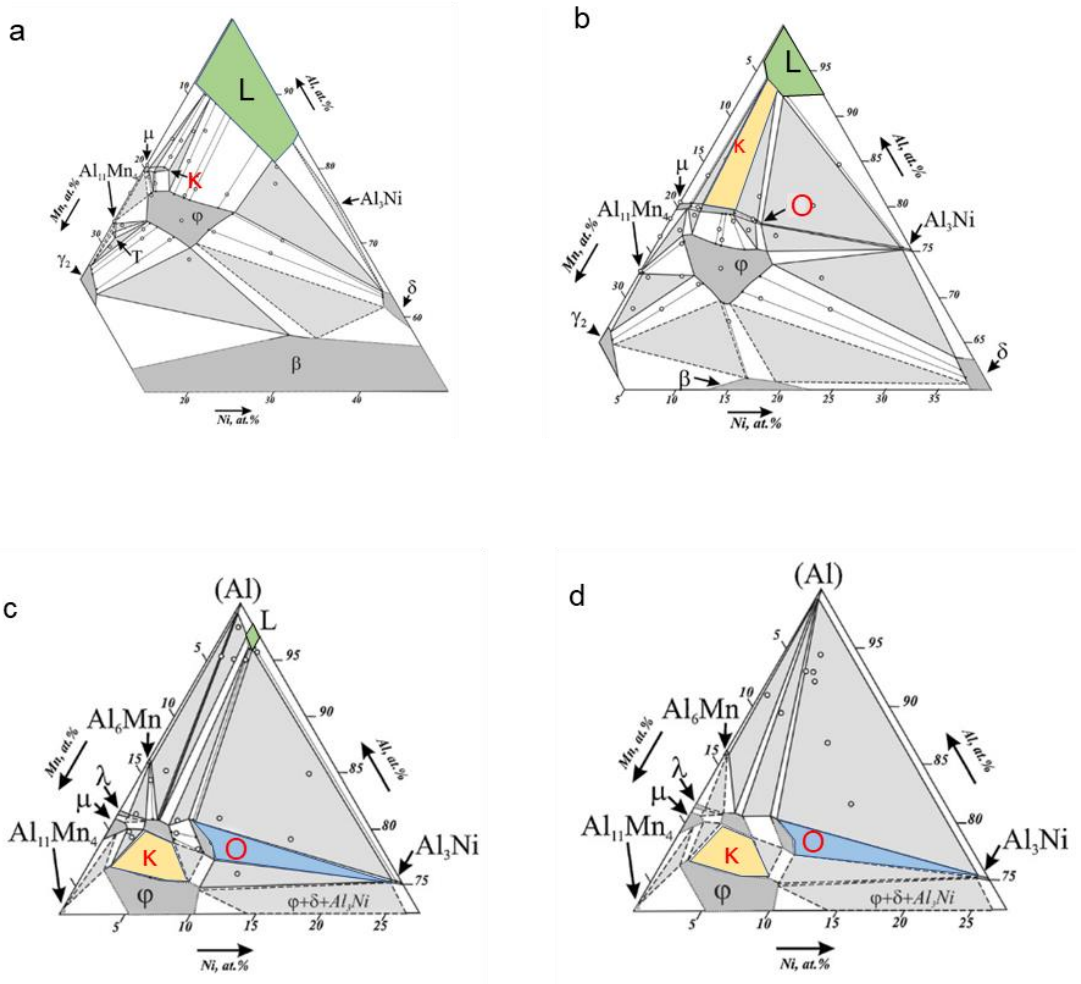

Figure 2.15 Partial isothermal section in the Al-rich corner at different temperatures. (a) κ-phase occurred at 850 °C, (b) O-phase occurred at 750 °C, (c) the compositional region for liquid narrowed down to a minimal area 645 °C, (d) liquid disappeared at 620 °C [141].

Lin [30,126,127] firstly investigated the mechanical properties of Al-Ni-Mn alloys. The main motivation of his study is to develop a novel alloy that can simplify the manufacturing process and hence reduce manufacturing costs. The new alloy can apply to aerospace and automotive casting parts. A non-heat-treatable alloy removes the time consuming and high-cost heat-treatment process. Even though removing only solution treatment and retaining the ageing process still reduce cost remarkably, the new alloy should be suitable for die casting, PMC, sand casting, squeeze casting and semi-solid metal forming.

Since the Al-Ni-Mn alloys are designed without post-treatment. The castability should be good enough to produce complex shape parts. The effect of Ni on the hot cracking index(HCI) was investigated. The results showed that when Ni content reaches 0.5% and above, the HCI is 4 mm, which is comparable to that of alloy A356.0.

The mechanical properties of Al-2Ni-2Mn alloy and Al-4Ni-2Mn alloy were tested. It was found that the further addition of 2% Ni in Al-2Ni-2Mn alloy increased the yield strength from 80 MPa to 98 MPa and ultimate tensile strength from 154 MPa to 174 MPa, respectively. The as-cast A356.0 alloy displayed yield strength of 101 MPa and ultimate tensile strength of 191 MPa. The strength of as-cast Al-4Ni-2Mn alloy and A356.0 are comparable. However, the A356 alloy with T6 treatment shows a yield strength of 210 MPa and ultimate tensile strength of 280 MPa. Therefore, the strength of Al-Ni-Mn alloys is relatively weak, and further modification is needed.

The Zr and Sc are very effective elements in improving the performance of Al-Si alloys at both room and elevated temperatures. Lin [30] also added Sc to improve the strength of Al-Ni-Mn alloy. The Al_3Zr and Al_3Sc precipitates formed in the T5 temper providing dispersion strengthening. When 0.3% Sc was added into Al-2Ni-2Mn alloy and aged at 300 °C for 3 h. The yield strength reached 189 MPa, which is 109 MPa higher than the Al-2Ni-2Mn alloy without Sc. The ultimate tensile strength also increased dramatically from 154 MPa to 243 MPa. The best strength achieved is then comparable to A356.0 alloy with T6 temper.

In the published papers [28,132,141,147,148], the eutectic phase in Al-Ni-Mn alloys was confirmed to be the Al_3Ni. However, another reference [29] reported that, in an Al-4Ni-2Mn alloy, the eutectic phase was confirmed to be the $Al_9(Ni, Mn)_2$. It has the same structure as monoclinic Al_9Co_2, and they both are Al_9TM_2-type structures. This Al_9TM_2-type structure was also reported in Al-Co alloy [149,150], Al-Ni-Fe [151–153] alloy and Al-Ni-Ru alloy [154]. The composition of the $Al_9(Ni, Mn)_2$ phase was reported to be $Al_{81.4}Mn_{3.4}Ni_{15.2}$ (at.%).

Another study [28] presents microstructure of Al-6Ni-4Mn and Al-4Ni-4Mn alloys with solidification rate of 90 °C/s and 5 °C/s , as shown in Figure 2.16. The primary phase was

the O-phase, and the eutectic intermetallic phase was reported to be the Al_3Ni phase. The κ-phase that occurred in the equilibria in literature [141,143] was not observed in all experimental alloys in this paper. Furthermore, increasing Mn content increased tensile strength. A maximum room temperature yield strength of 198 MPa was achieved by Al-6Ni-4Mn alloy. When tested at 300 °C, the Al-6Ni-4Mn alloy presented a yield strength of 130 MPa.

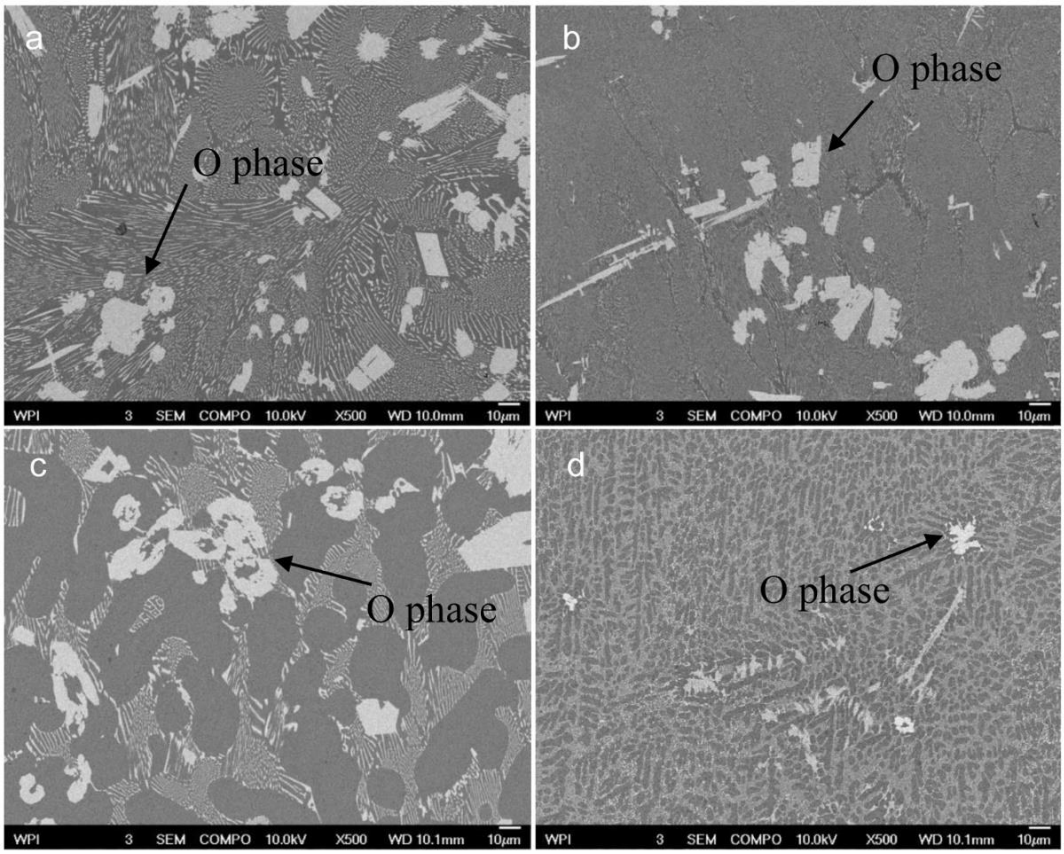

Figure 2.16 SEM micrographs of Al-6Ni-4Mn alloy cast with 5 °C/s (a) and 90 °C/s (b) and Al-4Ni-4Mn alloy cast with 5 °C/s (c) and 90 °C/s (d) [28].

2.4.4 Knowledge gap

According to the review of Al-Ni-Mn alloys above, the understanding of Al-Ni-Mn alloys is insufficient.

The effects of Ni and Mn contents on the microstructure and mechanical properties were not fully characterized. The mechanical properties of some Al-Ni-Mn alloys were tested [30],

but the microstructures were not presented. In another study [28], the microstructure of Al-6Ni and Al-4Ni alloys with 2, 3, and 4% Mn were presented. But only the Al-6Ni-4Mn alloy was tested at 300 °C. Therefore, an overall understanding of microstructures of Al-Ni-Mn alloys is lacking. The eutectic point of Al-Ni binary system in the Al-rich corner is 5.6% Ni. The hypoeutectic alloy (Al-4Ni), eutectic alloy (Al-6Ni) and hypereutectic alloy (Al-8Ni) with different Mn contents all need research. The microstructures are then characterized and summarized. Moreover, the eutectic phase in Al-Ni-Mn alloys is controversial. The Al_3Ni phase was claimed to be the eutectic phase in ref [28], while in other literature [29,140], it was claimed to be the $Al_9(Ni, Mn)_2$ phase. Hence, the identification of the eutectic phase in Al-Ni-Mn alloys is also demanded.

As for mechanical properties, few experimental data are available at elevated temperatures. In one reference [30], only tensile strength results at ambient temperature were displayed. And in another work [28], only one tensile strength result was obtained at 300 °C. It is important to obtain sufficient results and evaluate the performance of Al-Ni-Mn alloys at elevated temperatures. Therefore, more mechanical property results of Al-Ni-Mn alloys are needed at both ambient temperature and elevated temperatures.

Since the Al-Ni-Mn alloy is developed for elevated temperature applications, the thermal stability of the microstructure needs to be assessed and the suitable service temperature needs to be determined. No related research work has been published yet.

The effect of cooling rates on microstructure and mechanical properties of the Al-Ni-Mn alloys is another important research gap. It may change the phase constitution in the Al-Ni-Mn alloys and affect the distribution and size of phases. The microstructural evolution under different cooling rates is of great significance and yet to be studied in Al-Ni-Mn alloys.

Additionally, the approaches to improve mechanical properties of Al-Ni-Mn alloys are worth investigating. And minor elements addition is the most commonly applied method.

Exploration of minor element addition in Al-Ni-Mn alloys is an important puzzle to be solved.

2.4.5 Alloy design

According to the literature review, the potential of Al-Ni-Mn alloys appears but the study is insufficient. Here a alloy design plan is important to obtain comprehensive understanding of Al-Ni-Mn alloys and achieve expected strength at both ambient temperature and 250 °C. According to the Al-Ni binary system, the eutectic point is 5.6 wt.% Ni, hence three levels of Ni (4 wt.%, 6 wt.%, 8 wt.%) are chosen, which represent hypoeutectic, eutectic and hypereutectic alloys respectively. Three levels of Mn (2 wt.%, 3 wt.%, 4 wt.%) are chosen, which helps to explore the effect of Mn-rich phases on microstructure and mechanical properties. As for minor elements, Cu and Ce are chosen. Cu is widely used in Al-Si alloys as an effective strengthening element. The metastable θ′ (tetragonal Al_2Cu) precipitates provide a strong strengthening effect and lead to a high strength. Ce was reported being capable of improving elevated temperature strength by introducing heat resistant intermetallic phases. No research about the effects of Cu and Ce on Al-Ni-Mn alloys has been carried out yet.

2.5 Summary

The Al-Si based alloys are widely used for engine blocks, cylinder heads and pistons. However, with the development of new generations of engines, higher requirements have been put forward for engine materials. The materials should work at higher temperatures with improved strength. Since Al-Si alloys soften quickly at elevated temperatures (260 °C and above), attempts to improve Al-Si alloys with Zr, Sc and other minor elements have been tried. Sc and Zr did show effective improvement in the mechanical properties at elevated temperatures, but these element are expensive. More importantly, the improvement is limited because the Al-Si eutectic matrix still soften at elevated temperatures. Therefore, developing a new aluminium alloy suitable for elevated temperatures is very attractive.

The new aluminium alloy should meet following criteria: (1) Good castability allowing for HPDC or PMC. (2) 200 MPa YS at ambient temperature, 150 MPa YS at 250 °C and elongation more than 2% at ambient temperature. (3) Low cost to maintain the competitiveness of cast parts, so high cost elements should be avoided. (4) Being able to work well under as-cast condition or under the condition with minimised heat treatment, which saves cost of post processing.

Considering limited research work about Al-Ni-Mn alloys, a comprehensive understanding of Al-Ni-Mn alloys is highly desired. It should cover the following aspects: (1) The microstructures of Al-4Ni, Al-6Ni and Al-8Ni alloys with various Mn contents. All phases should be correctly identified. (2) Mechanical properties at room temperature and elevated temperatures as well. (3) The thermal stability of Al-Ni-Mn alloys. Microstructural evolution and hardness response at elevated temperatures will be obtained. (4) The effect of cooling rate on microstructure. Cooling rates affect solidified microstructure and consequently affect performance. (5) The effect of minor element addition on Al-Ni-Mn alloys. Minor elements addition is an effective method to improve mechanical properties.

Chapter 3: Methodology

3.1 Alloy casting

In the present study, Al-Ni, Al-Ni-Mn, Al-Ni-Mn-Cu, Al-Ni-Mn-Si, and Al-Ni-Mn-Ce alloys were prepared from commercial pure Al, pure Cu and four master alloys (Al-20 wt.% Ni master alloys; Al-20wt.%Mn master alloys; Al-50 wt.%Si master alloys and Al-20 wt.% Ce master alloy) (all compositions are in wt.% unless specified hereafter). The commercial pure Al billet was supplied by Coleshill Aluminium Limited, pure Cu was supplied by DS Metals Limited, Al-Ni alloy was supplied by Centaur Metals & Alloys Limited, Al-Mn and Al-Si alloys were supplied by Avon Metals Limited.

All alloys were prepared by PMC. For each casting, 7-8 kg melt was prepared in an A25 silicon carbide graphite crucible coated with boron nitride to prevent contamination. For each alloy, solidus and liquidus were calculated by Pandat, and the pouring temperature was set 100 °C above liquidus temperature; all were listed in Table 3.1.

The casting process is described below. Raw materials were put in an electric resistance furnace and were heated to 800-830 °C, which varies with different alloys. The melt was held at this temperature for 4 h and stirred several times to ensure compositional homogeneity. The melt was then degassed with N_2 using a rotary degassing machine (Figure 3.1) at a rotation rate of 350 r/min for 5-6 minutes. The dross on the melt surface was removed after degassing and flux was used after degassing to protect melt from absorbing gas. Then a thermal couple was used to monitor the melt temperature and adjust the melt temperature to pouring temperature. After holding for 10-15 mins, the melt was poured into mould. An ASTM-E8 standard steel mould coated with boron nitride was used (Figure 3.2a). It was preheated to 400 °C before use.

Table 3.1 Solidus, liquidus calculated by Pandat and corresponding pouring temperatures.

Alloy	Solidus	Liquidus	Pouring temperature
Al-4Ni	646 °C	651 °C	750 °C
Al-6Ni	646 °C	652 °C	750 °C
Al-8Ni	646 °C	670 °C	760 °C
Al-4Ni-2Mn	645 °C	659 °C	759 °C
Al-4Ni-3Mn	645 °C	683 °C	783 °C
Al-4Ni-4Mn	645 °C	704 °C	804 °C
Al-6Ni-2Mn	645 °C	661 °C	761 °C
Al-6Ni-3Mn	645 °C	685 °C	785 °C
Al-6Ni-4Mn	645 °C	708 °C	808 °C
Al-8Ni-2Mn	645 °C	676 °C	776 °C
Al-8Ni-3Mn	645 °C	687 °C	778 °C
Al-8Ni-4Mn	645 °C	713 °C	813 °C

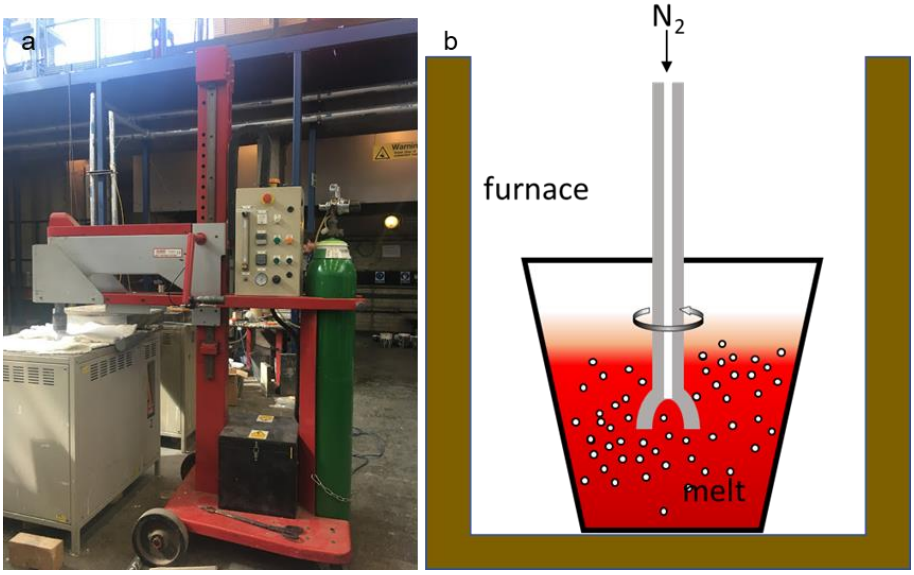

Figure 3.1 (a) Degassing machine and (b) schematic illustration of degassing process.

The castings obtained after solidification is shown in Figure 3.2b. Each casting weighted 1.1-1.3 kg, and two tensile test samples can be obtained from one casting as indicated in the rectangular area; the geometry of the tensile test sample is shown in Figure 3.3. Samples cut from casting are ready for the tensile test. 6-7 castings were obtained from each crucible, and hence 12-14 tensile test samples can be obtained. After three castings, a mushroom sample was obtained to test alloy composition, Aas shown in Figure 3.4a. The bottom surface of the mushroom sample was ground to get flat surface and 3 points were tested for each alloy. Then the FOUNDRY-MASTER PRO, as shown in Figure 3.4b, an optical emission spectrometry (OES) technology, was applied to test the actual compositions of all alloys. A high energy spark is discharged to the metal surface, burn it and plasma is generated. The plasma then enters the spectrometer. The incoming light is split into element-specific wavelengths by a diffraction grading in the spectrometer and the intensity of light for each element-specific wavelength is measured by a corresponding detector. Since the intensity is proportional to the concentration offset element in the sample, the composition is obtained. FOUNDRY-MASTER PRO covers all elements with wavelength range from 130 nm to 800 nm.

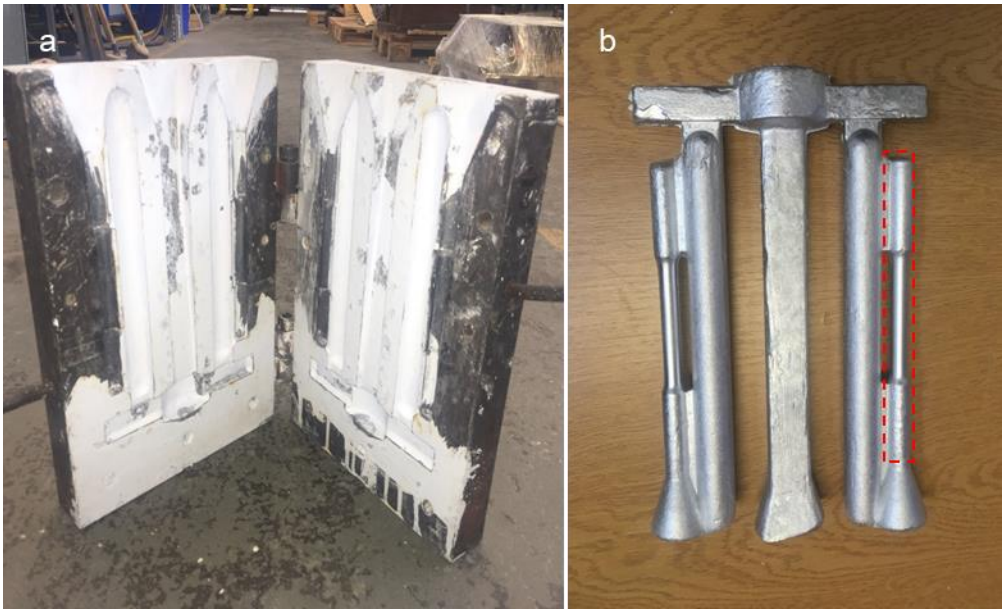

Figure 3.2 ASTM-E8 standard steel mould(a) and casting obtained(b).

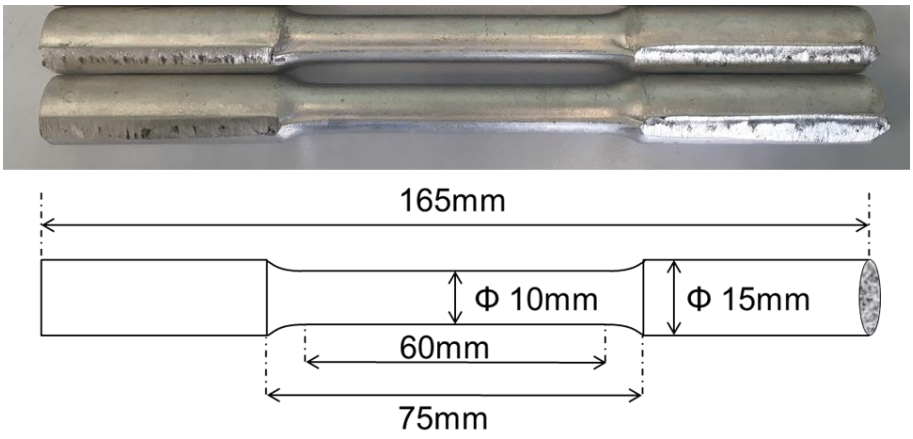

Figure 3.3 Tensile test samples and a schematic illustration showing the dimensions (in millimetres).

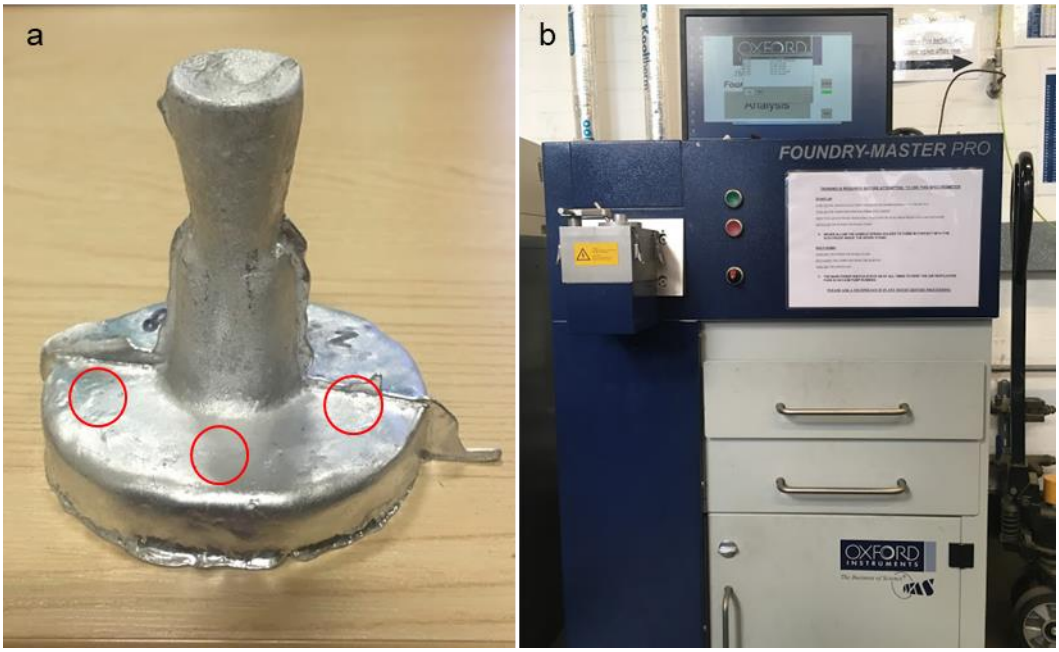

Figure 3.4 Mushroom sample (a) and FOUNDRY-MASTER PRO (b) for composition test.

3.2 Microstructure characterization

3.2.1 Metallographic Surface Preparation and deep etching

Samples for microstructure characterization and XRD were cut from the reduced section on tensile test bars obtained from castings. Each sample is a cylinder with a dimension of φ10*10 mm. These cylinders were then mounted with cross-sections exposed. The mounted samples were then ground and polished with a Buehler Automet ® 250 machine. SiC abrasive papers (400#, 800# and 2000#) were used with 10 N load to grind the sample. Each grinding process took 2-4 minutes. Then Silica suspension (OPS, 0.05 μm water-based SiO_2 suspension) was used to polish the samples with a load of 10 N for 6-10 minutes. Well prepared samples should show no scratches on the surface, which can be checked by an optical microscope.

Deep etching was performed to reveal morphologies of phases in this thesis. It removes the α-Al phase by corrosion and shows the remaining intermetallic phases. The solution used

was 10 vol.% HCl solution. Mounted samples were immersed in the solution for 10-20 min and needed to be taken out and checked regularly until α-Al was obviously removed. Then samples were flushed with water and then ethanol and dried out.

3.2.2 Optical microscope (OM)

Preliminary microstructure observation was conducted using an optical microscope. It is a Carl Zeiss AxioScope A1 optical microscope (OM), equipped with an AxioCam MRm digital camera and an image processing software AxioVision 4.9, as shown in Figure 3.5. Images at different magnifications (50x, 100x, 200x, and 500x) were obtained. The volume fraction of the primary α-Al phase, eutectic phases and primary intermetallic phase were obtained by processing OM images. At least ten images were analysed at a magnification of 50x, and an average area fraction was obtained. In this thesis, we assume the volume fraction equals the area fraction.

Figure 3.5 Carl Zeiss AxioScope A1 optical microscope

3.2.3 Scan electron microscope (SEM)

SEM was used to characterize microstructure at higher magnifications. There are two imaging modes: Secondary-Electron (SE) imaging and Backscattered-Electron (BSE) imaging. SE images reveal the topography of the sample's surface, while BSE images

provide information on composition. In this thesis, SE images were obtained to reveal morphologies of different phases and analyse fractured surfaces, and BSD images were used to present microstructure using phase contrast.

Microstructure characterization was conducted using ZEISS SUPRATM 35VP (Figure 3.6), and quantitative analysis was performed using Energy Dispersive X-ray Analyser (EDS). The voltage was set at 20 kV, and the working distance was 10 mm. Images at different magnifications (200x, 500x, 1000x, 2000x, 5000x and 10000x) were obtained. More accurate quantitative analysis was performed using a JEOL JXA−8230 electron probe micro-analyser (EPMA) coupled with wavelength dispersive spectroscopy (WDS) detectors operating at 15 kV.

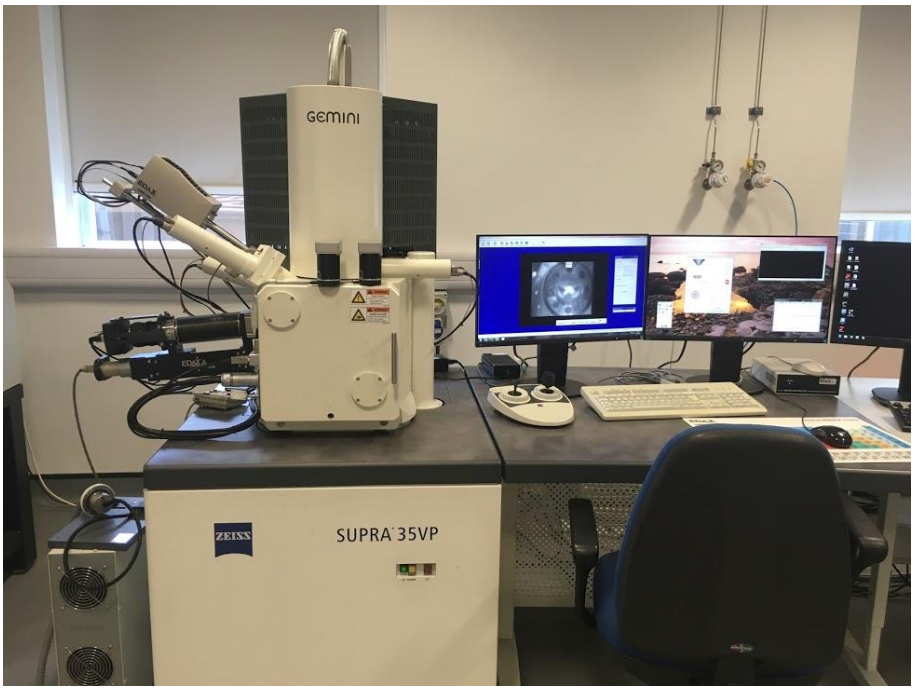

Figure 3.6 Scanning Electron Microscope (ZEISS SUPRATM 35VP).

3.2.4 Transmission electron microscope (TEM)

TEM was used to characterize microstructural evolution and precipitate at higher magnification and to obtain diffraction patterns which help to identify phases. Thin foils are needed for transmission electron microscope (TEM). Firstly, thin plates with 0.2-0.5 mm thickness were cut from reduce section of tensile test bars. Then, these plates were thinned

to 90-110 μm by grinding. Thirdly, these plates were punched into discs of approximately 3 mm diameter and thinned to 50-70 μm thickness also by grinding.

A Gatan Precision ion polishing system (PIPs) was used to further thin discs to perforation and obtain thin area, as shown in Figure 3.7a. Argon ion beam polisher is designed to produce high quality, TEM specimens with minimal effort. Ion polishing is done by two variable-angle, miniature Penning ion guns. The operating angles of the guns, ± 10 deg., are independent of one another. Both guns accurately center the beam onto the specimen at any angle within this range. The guns provide bright high current Argon ion beams and are capable of very high thinning rates. For Al-Ni-Mn samples. three steps were performed by adjusting angle and voltage. Firstly, a voltage of 5 keV and an angle of ±5° were applied till a hole was observed. Secondly, change the voltage to 4 keV and angle to ±4° till the large diameter of the oval hole reaches ¼ of the diameter of the disc (3 mm). Finally, the disc was further thinned with 3.5 keV and ±3° for about 20 minutes. Samples for TEM characterization were then well prepared. A plasma cleaning system was applied to clean TEM samples (Figure 3.7b), which removes the surface contaminations by oxygen or hydrogen plasma.

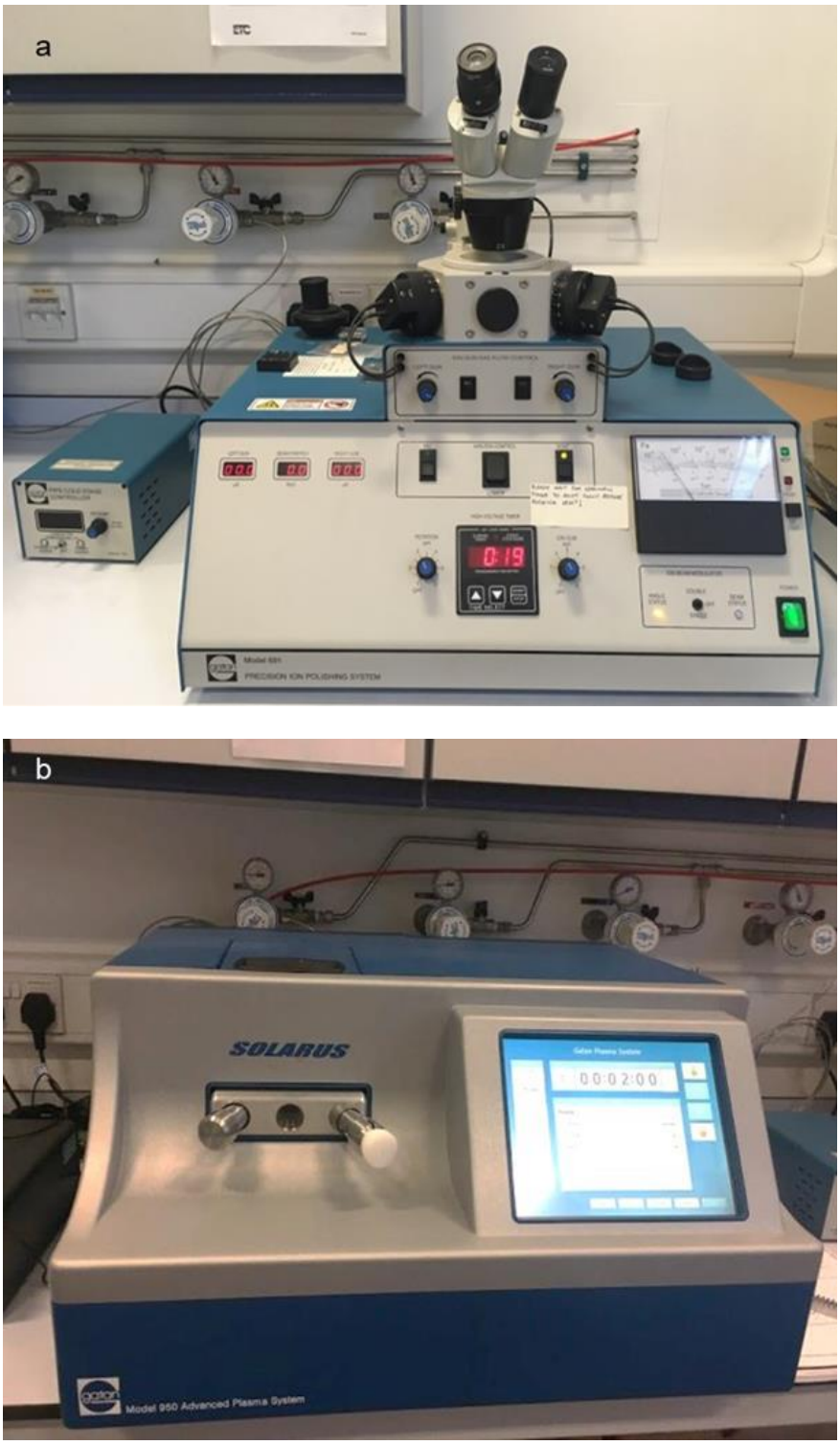

Figure 3.7 Gatan Precision ion polishing system (a) and Plasma Cleaning System (b).

TEM foils were characterized by JEOL JEM-2100F with a working voltage of 200 kV, as shown in Figure 3.8. Quantitative composition analysis was performed on JEOL JEM-

2100F equipped with a Thermo Fisher UltraDry energy disperse X-ray spectroscopy (EDS) detector. Observation and imaging were conducted at bright field mode, and Selected Area Electron Diffraction (SAED) patterns were also recorded from an area of interest. The diffraction patterns obtained were analysed. Firstly, the plane spacing was calculated. Secondly, the angles between different planes were measured. Thirdly, according to compositions and other information, lists all possible phases. Finally, compare obtained plane spacing and angles from diffraction patterns with lattice parameters of possible phases and identify the phases.

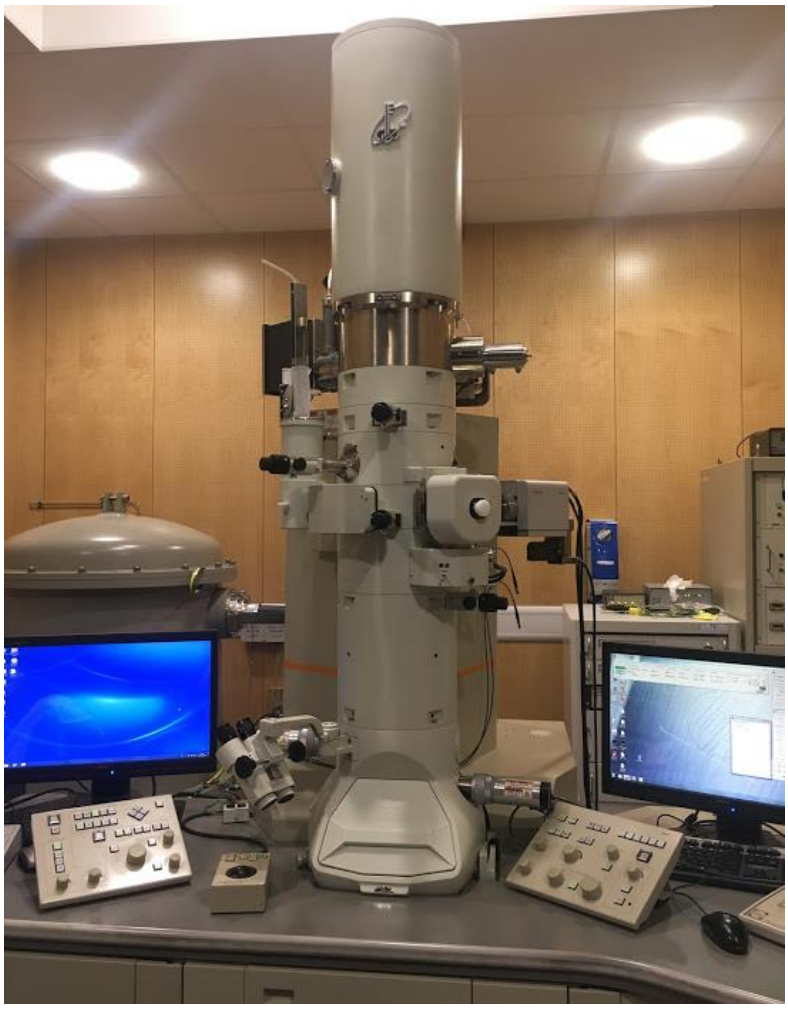

Figure 3.8 Transmission Electron Microscope (JEOL 2100F)

3.3 Differential Scanning Calorimetry

The solidification ranges and solidification sequences of alloys were measured by differential scanning calorimetry (DSC) Technology. DSC is a technique in which the difference in the amount of heat required to increase the temperature of a sample and reference are measured as function of temperature. Both the sample and reference are maintained at nearly the same temperature throughout the experiment. DSC enables the measurements of the transition such as the glass transition, melting, and crystallization. The NETZSCH STA 409 PC Luxx simultaneous thermal analyser, as shown in Figure 3.9, is equipped with a Julabo 5 E heating and cooling circulator bath, which helps the cooling process. There are two tiny crucibles in the chamber of the thermal analyser, one is for the sample, and the other one is for the reference. Al_2O_3 is the commonly used reference and was chosen in our experiments.

Samples for DSC were cut from bulk material and weighed about 40 mg. Samples were prepared flat to properly touch the bottom of crucibles, where there is a thermo-couple under it. Rough bottom may result in inaccurate temperature measurement. Samples were heated firstly to 850℃, holding for 20 minutes and then cooled at different cooling rates, during which temperature versus time data and heat flow (mW/mg) versus time data were recorded continuously at a rate of 12 points/K. Cooling rates used in this thesis vary from 20 k/min to 0.2 k/min. The slowest cooling rate is very close to equilibrium solidification. A heat flow (mW/mg) versus temperature plot was obtained by importing related data into Excel. Hence, the reaction temperature during solidification can be captured in a heat flow (mW/mg) versus temperature plot, which provides phase transformation reaction information. A typical solidification curve of Al-4Ni-2Mn alloy solidified at 10 k/min was presented in Figure 3.9b. There were two peaks observed which present two reactions. The first peak at 633 °C represents the formation of the primary α-Al phase from the melt. The second peak at 626 °C represents a eutectic reaction. Hence, the DSC curve provides clear information about phase formation reactions during solidification.

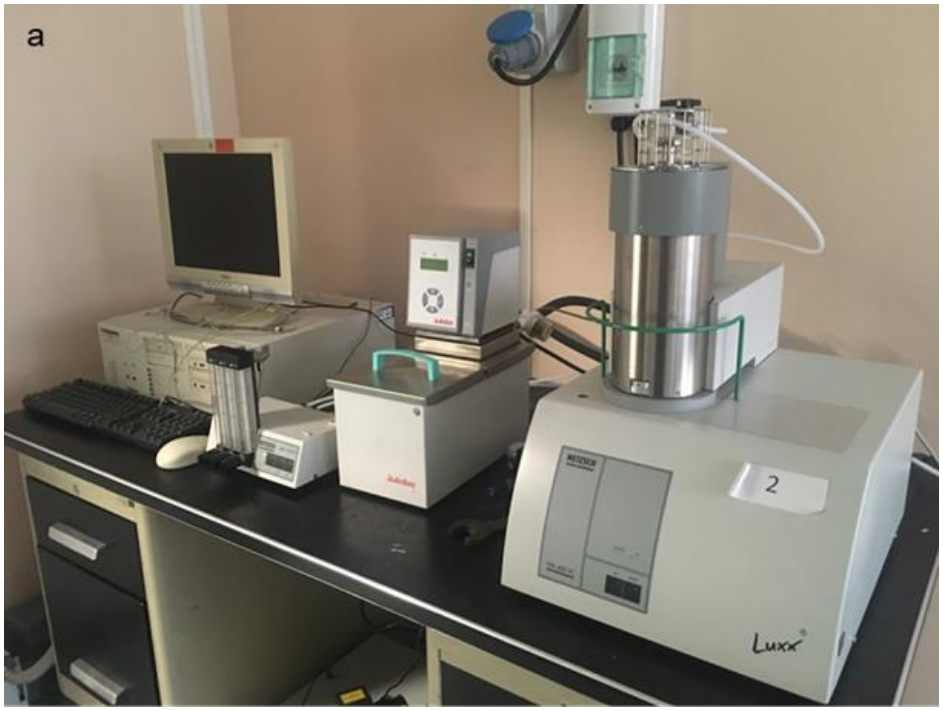
a
2
Luxx

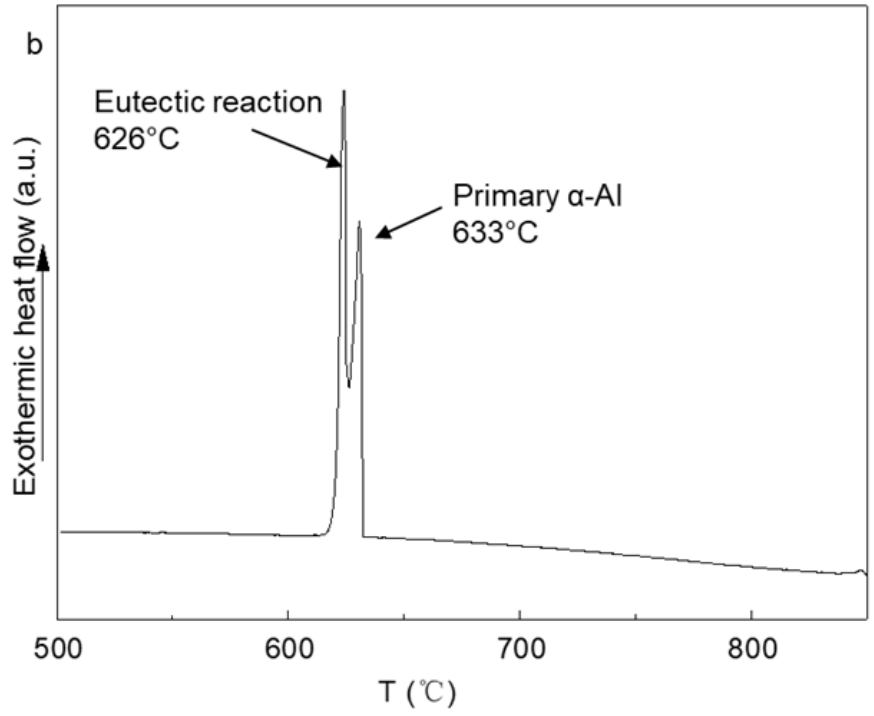
b
Eutectic reaction
626°C
Primary α-Al
633°C
Exothermic heat flow (a.u.)
500
600
700
800
T (℃)

Figure 3.9 Differential Scanning Calorimetry System (NETZSCH STA 409 PC Luxx)(a) and typical solidification curve of Al-4Ni-2Mn alloy (b).

3.4 X-ray diffraction (XRD)

Phase identification was carried out using X-ray diffraction (XRD) analysis on a Bruker D8 diffractometer equipped with a LynxEyeTM silicon strip detector and Cu Ka radiation (k = 0.15406 nm) (Figure 3.10). The 2θ angle of XRD analysis was set between 10° to 80° with the step size of 0.01°/s and an overall scan time of approximately 250 min for each sample. Cylinder samples were prepared with the Metallographic Surface Preparation process given in section 3.2. No mounting is needed. The analysis software DIFFRAC.EVA was used to identify phases with powder diffraction files.

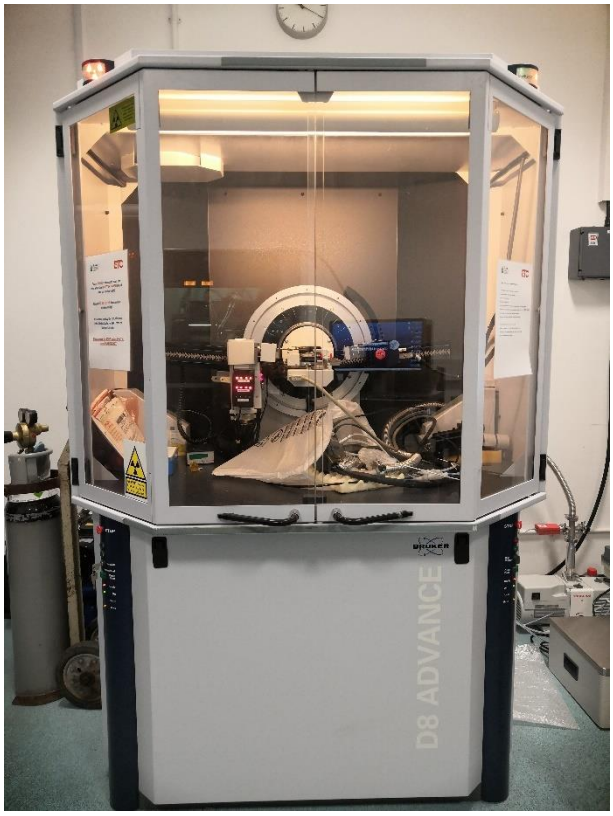

Figure 3.10 XRD facility (Bruker D8)

3.5 Mechanical property test

3.5.1 Hardness test

In the present study, Vickers hardness tests were conducted at room temperature using a 432 SVD digital auto turret macro Vickers Hardness Tester, as shown in Figure 3.11. A load of 10 kg and a dwell time of 10 s were set. A minimum of 8 measurements was taken for each sample. Average hardness and standard deviation were then calculated. Also, the Vickers number (HV) can be obtained using the following formula:

$$HV = 1.854(F/D^2),$$

with F being the applied load (measured in kilograms-force) and D^2 the area of the indentation (measured in square millimetres).

Figure 3.11 Wilson 432 SVD digital auto turret macro Vickers Hardness Tester.

3.5.2 Room temperature tensile test

Room temperature tensile property was tested by a table-mounted testing system (INSTRON 5569), as shown in Figure 3.12a. Elongation was obtained by Extensometer (Instron Static Axial Clip-on Extensometer, 2630-113). Sample cut from castings has a gauge length of 65 mm, and a diameter of 10 mm, and the extensometer has a gauge length of 50 mm, as shown in Figure 3.12b. It can record length change after a break and then calculate the elongation.

Room temperature tensile test was conducted at an extension rate of 1 mm/min. 0.2% offset yield strength, ultimate tensile strength and elongation were recorded after a single test. Each tensile test result reported in this thesis is based on the average results of at least 4 test results.

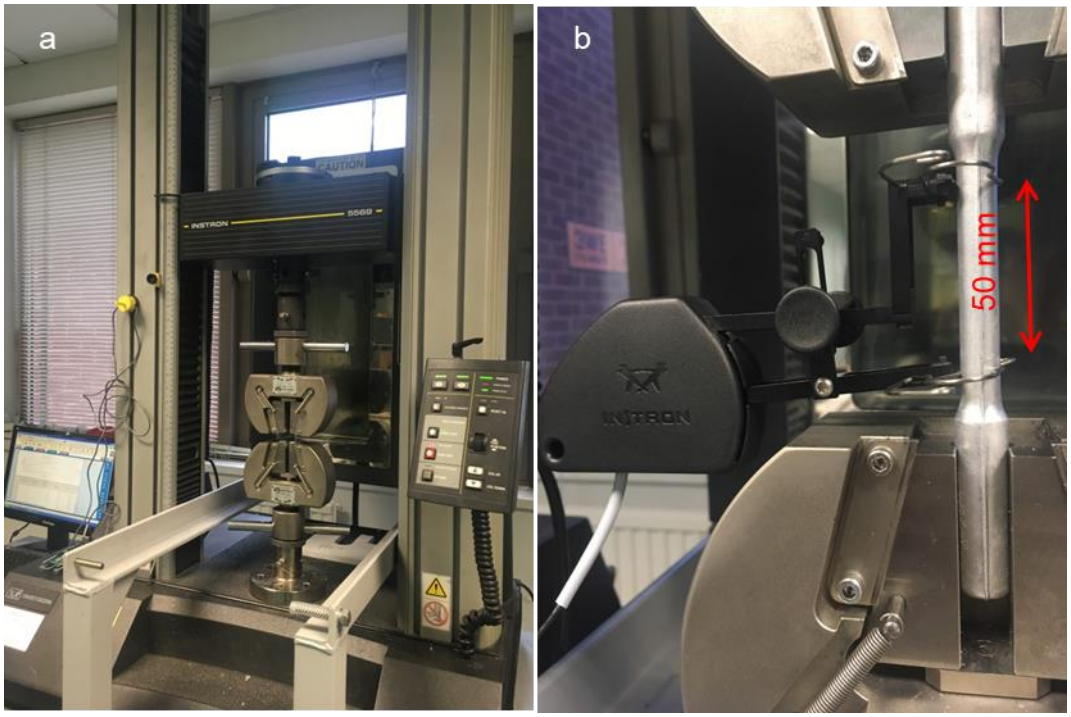

Figure 3.12 (a) Instron® 5569 universal materials testing machine, and (b) extensometer showing a gauge length of 50 mm.

3.5.3 High temperature tensile test

In the present study, tensile test was also conducted at 250 °C. A chamber is designed for it to achieve an elevated temperature environment, as shown in Figure 3.13a. Wedge Action Grips used for testing at room temperature cannot be used at 250 °C. Hence, a pair of buttonhead sample holders were designed, as shown in Figure 3.14a. There are threads on both sides of the sample holders, and hence samples also need thread, as shown in Figure 3.14b. The assembly in the chamber is presented in Figure 3.13b.

A fan was used to achieve a uniform temperature in the chamber during testing. The chamber was firstly heated to 250 °C. Then a sample was put in. Testing samples were held for 40 minutes in the chamber prior to testing. Finally, the testing started, and data was recorded till fracture. Extensometer for room temperature testing could not work at 250 °C. Hence, to measure the elongation, the movement of the crosshead is obtained, which is called extension. Then the elongation was calculated by dividing extension by the original gauge length (60 mm).

Figure 3.13 (a) Environmental chamber, and (b) sample inside the chamber.

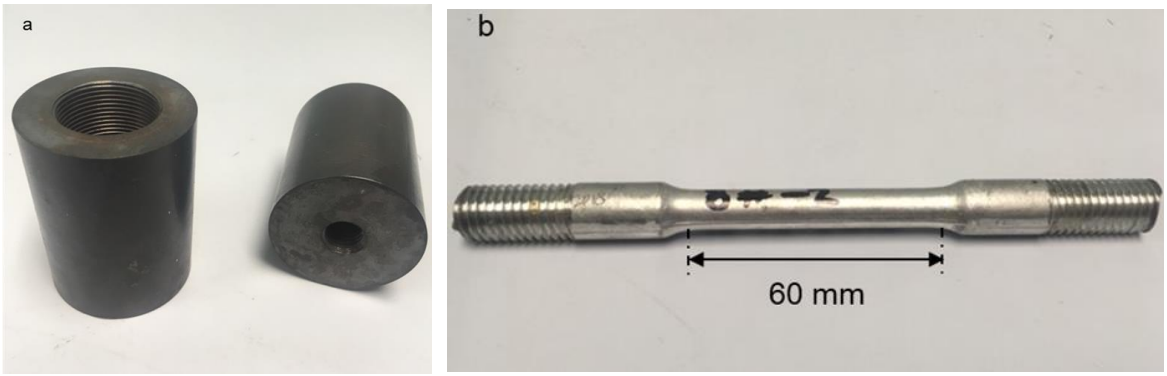

Figure 3.14 (a) Buttonhead sample holder and (b) sample with thread on shoulders for elevated temperature tensile test.

Chapter 4: The Effect of Mn on Microstructure and Mechanical Properties of Hypo-eutectic Al-4Ni Alloy

4.1 Introduction

In consideration of the lacking fundamental research of Al-Ni-Mn alloys described in the literature (Chapter 2), the effect of Mn on Al-Ni alloys, including hypo-eutectic Al-4Ni alloy, eutectic Al-6Ni alloy and hyper-eutectic Al-8Ni alloy, all need to be studied. Fundamental knowledge obtained then can be applied to evaluate the potential for elevated temperature applications and provide important guidance for alloy development. In this chapter, Mn addition to hypo-eutectic Al-4Ni alloys will be investigated. Whether the addition of Mn changes microstructure such as eutectic phases and introducing new intermetallic phases will be studied.

As such, four alloys, including Al-4Ni, Al-4Ni-2Mn, Al-4Ni-3Mn and Al-4Ni-4Mn alloys were prepared by PMC. The microstructure and mechanical properties of Al-Ni-Mn alloys with different compositions and at different temperatures were investigated. Emphasis is put on the microstructural evolution, performance at ambient temperature and 250 °C, the relevance between microstructure and mechanical properties, and fracture analysis.

4.2 Microstructures of as-cast Al-4Ni-(0-4)Mn alloys

The compositions of the experimental alloys obtained by optical emission spectrometry (OES) are listed in Table 4.1. It shows that actual composition is very close to designed nominal compositions, and the levels of impurity elements such as Si and Fe are controlled at very low.

Table 4.1 The actual composition of Al-Ni-Mn alloys measured by OES.

Alloy	Composition (wt.%)						
	Al	Ni	Mn	Fe	Si	Ti	Zr
Al-4Ni	Bal.	4.04	0.01	0.15	0.04	0.01	0.01
Al-4Ni-2Mn	Bal.	4.24	1.87	0.15	0.05	0.01	0.01
Al-4Ni-3Mn	Bal.	4.00	3.01	0.12	0.08	0.01	0.01
Al-4Ni-4Mn	Bal.	3.82	3.77	0.18	0.10	0.01	0.01

Typical microstructures of the Al-4Ni alloy are shown in Figure 4.1, which consist of α-Al dendrites and eutectic phases. Figure 4.2 displays microstructure of Al-4Ni-2Mn alloy. These two alloys display similar microstructure. In the Al-4Ni alloy, the primary α-Al contains 0.28% Ni. And in the Al-4Ni-2Mn alloy, the α-Al contained about 0.43% Ni and 1.6% Mn. The Ni has very limited solubility in Al [123] while the Mn has a maximum solubility of 1.8% in Al [155]. Hence, the concentration of Mn in α-Al is much higher than Ni. The eutectic intermetallic phase in Al-4Ni and Al-4Ni-2Mn alloys both showed a rod-like shape. The eutectic intermetallic phase in the Al-4Ni alloy showed the composition of Al-23.4 at.% Ni, which is a typical Al_3Ni phase according to the equilibrium phase diagram of Al-Ni binary alloys [123]. The eutectic intermetallic phase in the Al-4Ni-2Mn alloy, however, showed the composition of Al-13.5 at.% Ni -3.7 at.% Mn. Clearly, it is not Al_3Ni, but more close to $Al_9(Ni, Mn)_2$ phase, which was reported as monoclinic lattice structure of Al_9Co_2 phase and the structure parameters are a = 0.8585 nm, b = 0.6269 nm, c = 0.6205 nm, β= 95.34° [141].

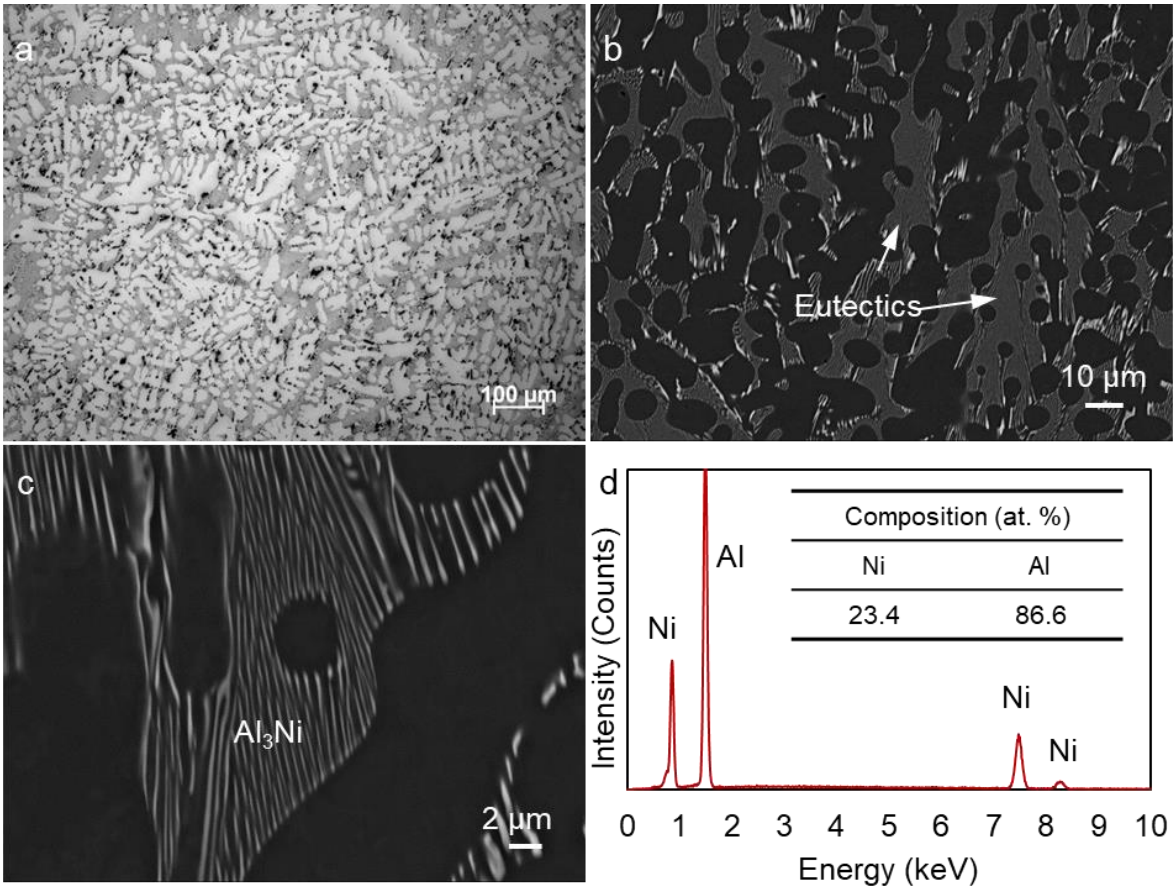

Figure 4.1 Optical image (a) and SEM images (b,c) showing the typical as-cast microstructure of the Al-4Ni alloy, and (d) the composition of eutectic intermetallic phase obtained by SEM-EDX.

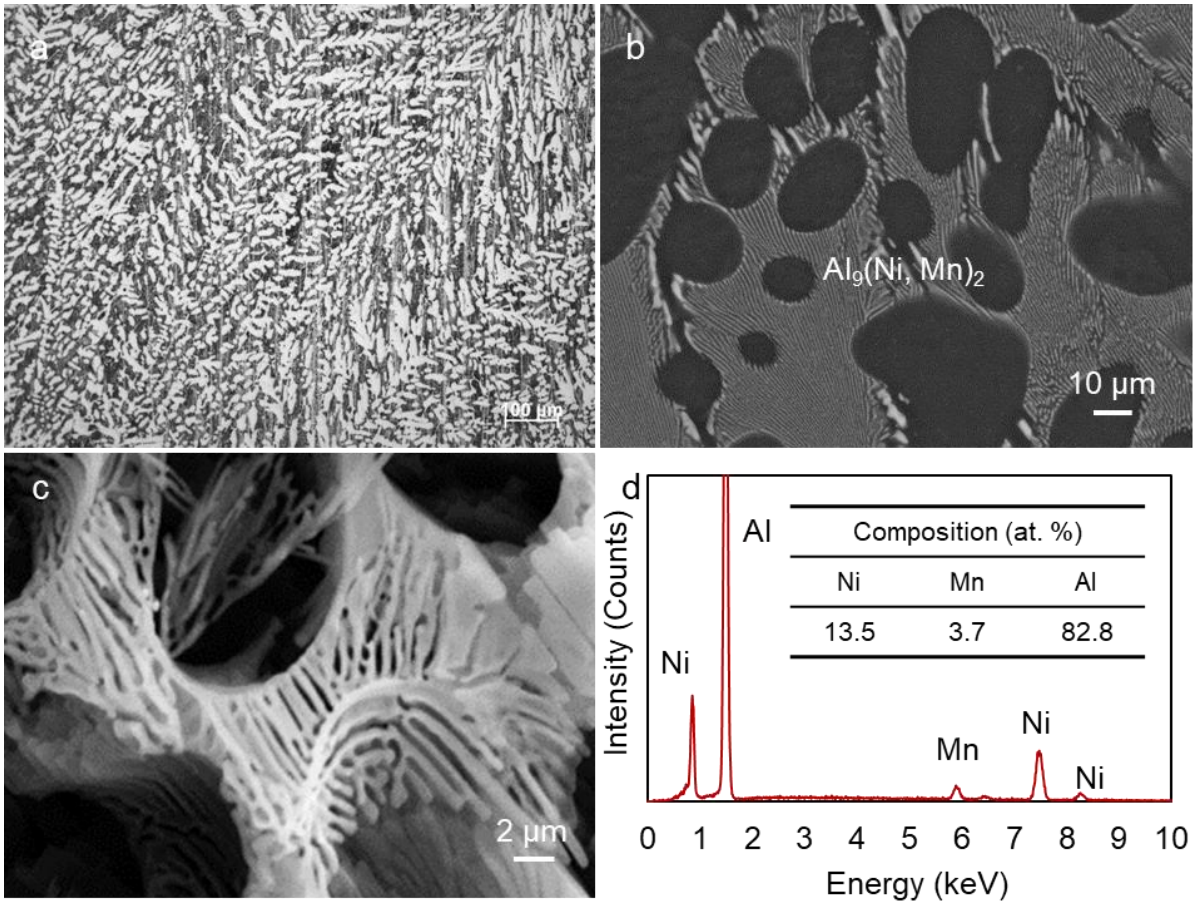

Figure 4.2 Optical image (a) and SEM images (b,c) showing the typical as-cast microstructure of the Al-4Ni-2Mn alloy, and (d) the composition of eutectic intermetallic phase obtained by SEM-EDX.

The XRD patterns for the Al-4Ni and Al-4Ni-2Mn alloys are shown in Figure 4.3. It shows that the eutectic intermetallic phase in Al-4Ni-2Mn alloy changed. The pattern showed good agreement with the XRD pattern of Al_9Co_2. TEM micrographs and diffraction patterns of the intermetallic phase are presented in Figure 4.4. The electron diffraction patterns were indexed as $Al_9(Ni, Mn)_2$ phase along zone axis [001] and [101]. Therefore, the eutectic intermetallic phase in the Al-4Ni-2Mn alloy was confirmed as $Al_9(Ni, Mn)_2$ phase. The addition of Mn to Al-4Ni alloy resulted in a transformation of the eutectic structure from α-Al+Al_3Ni to α-Al+$Al_9(Ni, Mn)_2$. This is different to the eutectic intermetallic phase identified by previous studies [18, 22], in which the eutectic Al_3Ni phase was reported in

Al-Ni-Mn alloys. The $Al_9(Ni, Mn)_2$ phase was also observed in Balanetskyy [141] and Yu[29]'s works. The $Al_9(Ni, Mn)_2$ phase has a Al_9Co_2-type lattice structure, which is similar to $Al_9(Fe, Ni)_2$ (or named as Al_9FeNi phase) [153]. For the $Al_9(Fe, Ni)_2$ phase, both Ni and Fe possibly appear on the sites which originally belonged to Co in Al_9Co_2 phase. It is most likely the same case for the $Al_9(Ni, Mn)_2$ phase. For each site of Co, both Ni and Mn are able to occupy it. Therefore, the concentration of Ni and Mn may not be fixed. Balanetskyy [141] reported a composition of Al-14.7 at.% Ni-2.8 at.% Mn while Yu [29] reported a composition of Al-16.5 at.% Ni-3.2 at.% Mn for the $Al_9(Ni, Mn)_2$ phase. In this paper, the composition for $Al_9(Ni, Mn)_2$ phase was measured as Al-13.5 at.% Ni -3.7 at.% Mn. Although the concentration of Ni and Mn may vary, the total amount of Ni and Mn is at a level of 18 at.%. As a result, it is clear that the addition of Mn to Al-4Ni alloy resulted in a transformation of the eutectic structure from α-Al+Al_3Ni to α-Al+$Al_9(Ni, Mn)_2$.

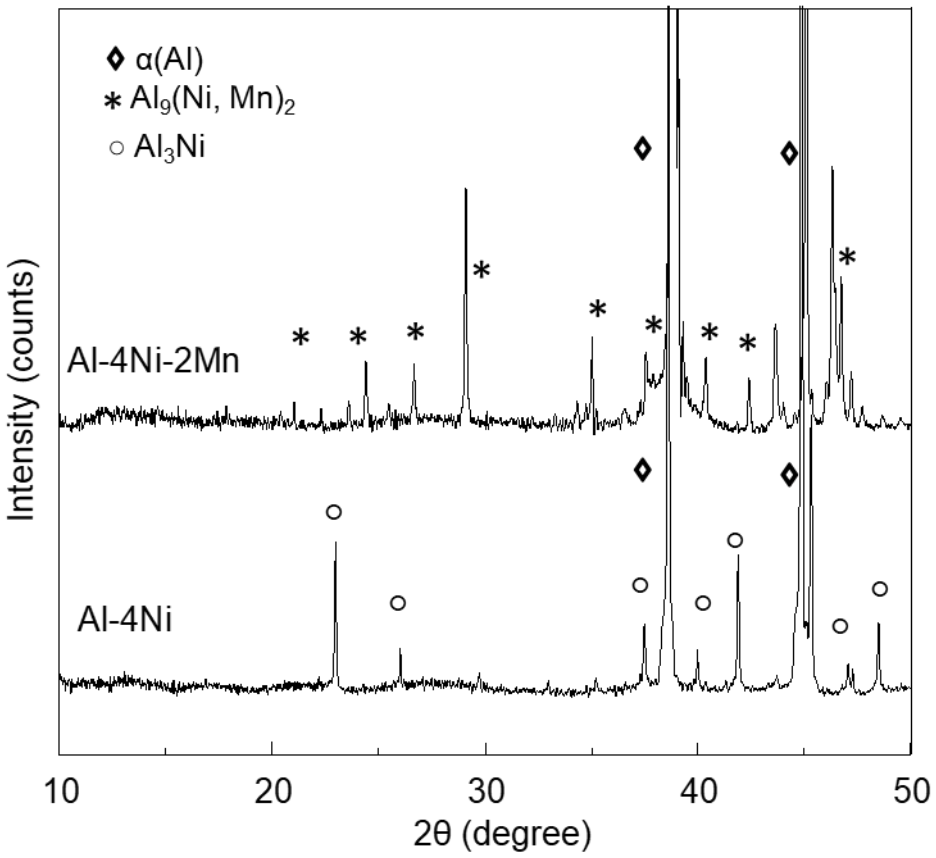

Figure 4.3 XRD patterns for the Al-4Ni and Al-4Ni-2Mn alloys.

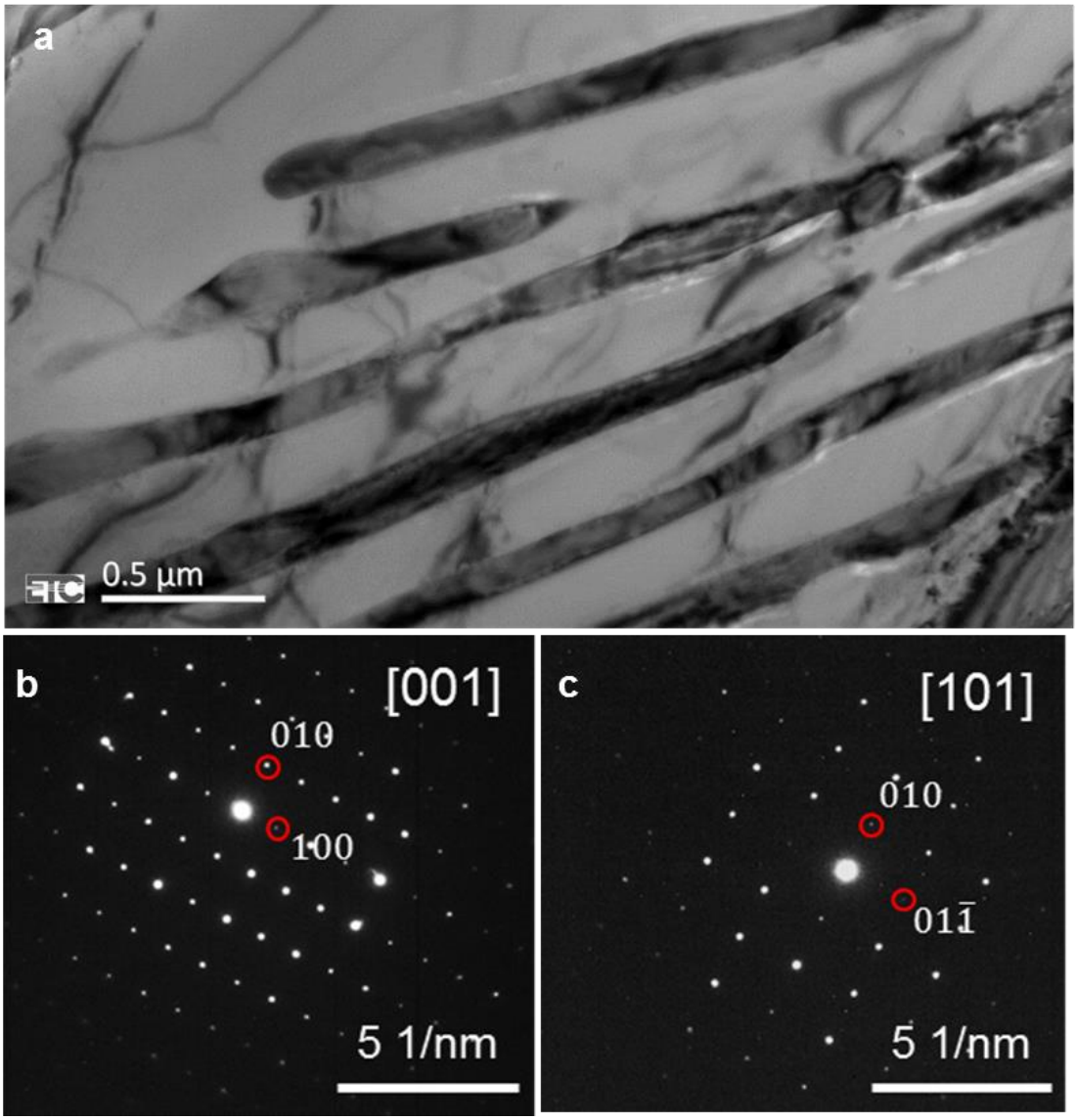

Figure 4.4 Transmission electron micrograph showing the eutectic $Al_9(Ni, Mn)_2$ rods. Electron diffraction pattern recorded along (b) zone axis [001], and (c) zone axis [101].

With increasing Mn content, some intermetallic phases appeared in the experimental alloys. For the Al-4Ni-3Mn alloy, on top of the α-Al dendrites and the α-Al+$Al_9(Ni, Mn)_2$ eutectic phases, two different primary intermetallic phases were observed. As shown in Figure 4.5a, the coarse grey particles show hexagonal shapes with black cores inside. The core inside contains 1.35% Mn and 0.37% Ni, which was confirmed to be α-Al. EPMA revealed the average composition of the the hexagonal phase and it was Al-15.6Mn-4.8Ni (at.%), which corresponds to the formula of $Al_{16.6}Mn_3Ni_1$. This hexagonal phase was identified as the κ-

phase, which has a composition range of Al-(14.7-18.9)Mn-(1.3-5.9)Ni (at.%) [140]. The κ-phase was reported as hexagonal lattice structure of $Al_{14.1}Cr_{3.4}Ni_{1.1}$ phase existing in Al-Cr-Ni and Al-Ni-Mn alloys [143]. Another phase with acicular morphology is shown in Figure 4.5b. The composition was measured as Al-12.6 at.% Mn-7.0 at.% Ni (at.%), which is close to the formula of $Al_{60}Mn_{11}Ni_4$. There are two lattice structures for the formula $Al_{60}Mn_{11}Ni_4$, which are $Al_{60}Mn_{11}Ni_4$ and $C_{3,I}$-$Al_{60}Mn_{11}Ni_4$, respectively. $Al_{60}Mn_{11}Ni_4$ phase is an orthorhombic structure with lattice parameters a=0.755 nm, b= 1.250 nm, c=2.380 nm while $C_{3,I}$-$Al_{60}Mn_{11}Ni_4$ is also a orthorhombic structure but with parameters a=3.27 nm, b=1.25 nm, c=2.38 nm. Obviously, both $C_{3,I}$-$Al_{60}Mn_{11}Ni_4$ and $Al_{60}Mn_{11}Ni_4$ are orthorhombic structures and the only difference is the lattice parameter a. Hence, it is not easy to distinguish $C_{3,I}$-$Al_{60}Mn_{11}Ni_4$ and $Al_{60}Mn_{11}Ni_4$ without detailed TEM diffraction patterns. $Al_{60}Mn_{11}Ni_4$ was referred to as X phase or R phase in Ref. [134,135] but referred as O-phase in Ref. [28]. Even earlier, Balanetskyy [141] referred the $C_{3,I}$-$Al_{60}Mn_{11}Ni_4$ as O-phase. Because of the uncertainty yet and these two phases are difficult to distinguish, we use O-phase for $Al_{60}Mn_{11}Ni_4$ phase in the present study.

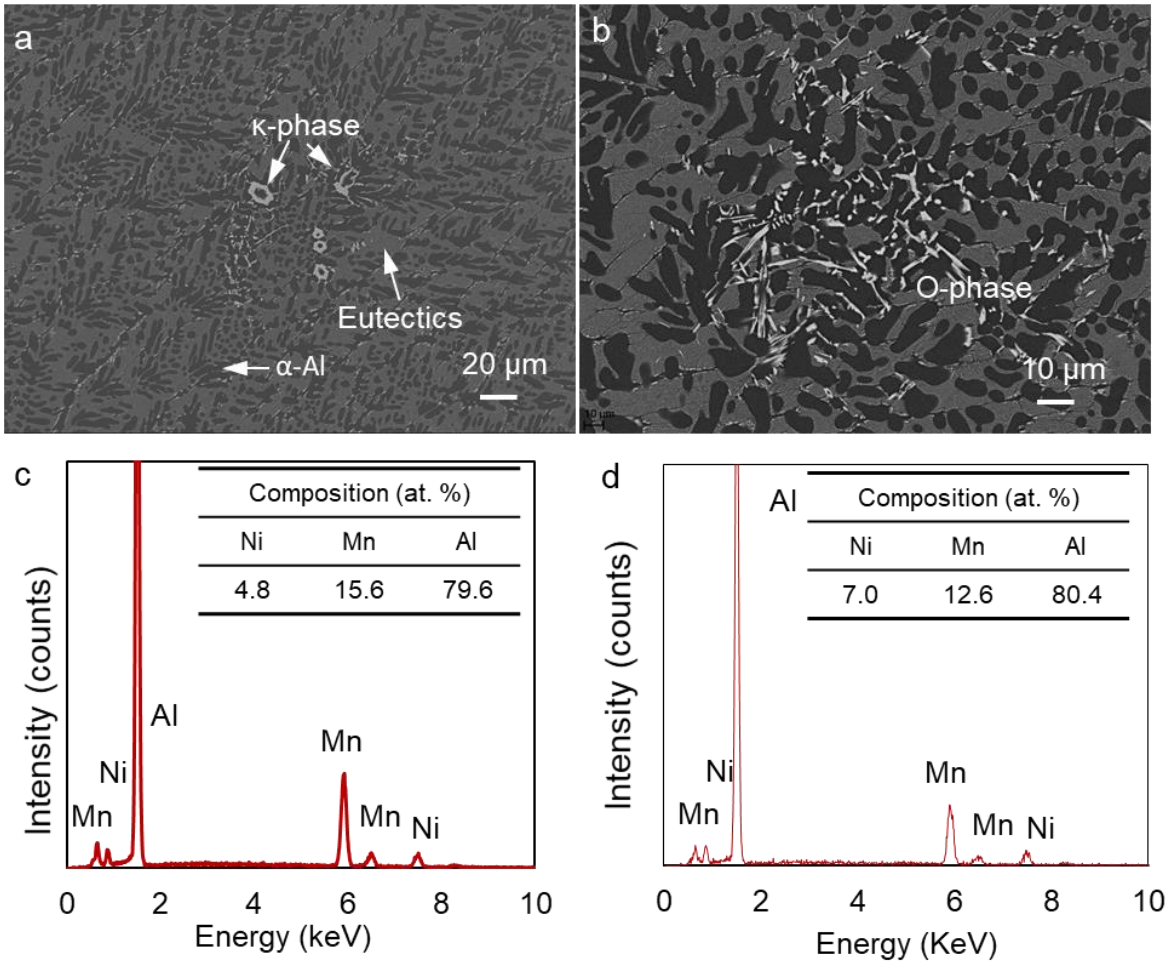

Figure 4.5 (a, b) Backscattered SEM micrographs showing primary intermetallic phase, and (c, d) SEM-EDX analysis of the composition of primary intermetallic phase in the Al-4Ni-3Mn alloy.

The deep etching reveals the morphology of the κ-phase in Figure 4.6a. It is a hexagonal particle displaying a hollow inside, which is caused by removal of the α-Al phase. The κ-phase is the only hexagonal phase observed in the Al-4Ni-3Mn alloy. The eutectic structure displayed in Figure 4.6b remains α-Al+$Al_9(Ni, Mn)_2$ structure and shows the same rod-like shape as in the Al-4Ni-2Mn alloy.

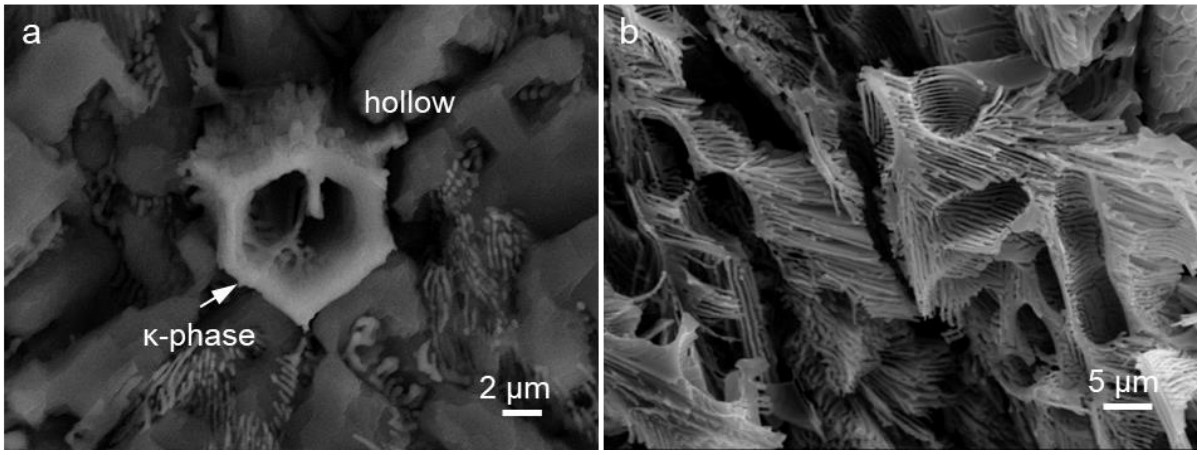

Figure 4.6 Morphologies of (a) κ-phase and (b) eutectic structure in Al-4Ni-3Mn alloy revealed by deep etching. The κ-phase showing hexagonal shape with a hollow inside.

Figure 4.7 displays the typical microstructure of as-cast Al-4Ni-4Mn alloy. The amount of intermetallic phases obviously increased with increasing Mn content. Large size κ-phase with branches was observed. Deep etching image in Figure 4.7b shows this complex morphology. Apart from the κ-phase, coarse Al_6Mn phase was also observed at a level of several hundred micrometres in the Al-4Ni-4Mn alloy, which displayed a well-developed dendritic morphology.

Images at higher magnification present more details of the microstructure. O-phase was observed in Figure 4.8a. Another small size dendritic phase displays in Figure 4.8b. TEM characterization was conducted to identify this phase, as shown in Figure 4.9. TEM-EDX shows a composition of $Al_{86.5}Mn_{13.3}Ni_{0.2}$ (at.%). Together with diffraction patterns, this phase was identified as the Al_6Mn phase. Therefore, when Mn content was further increased to 4%, the dendritic Al_6Mn phase appeared.

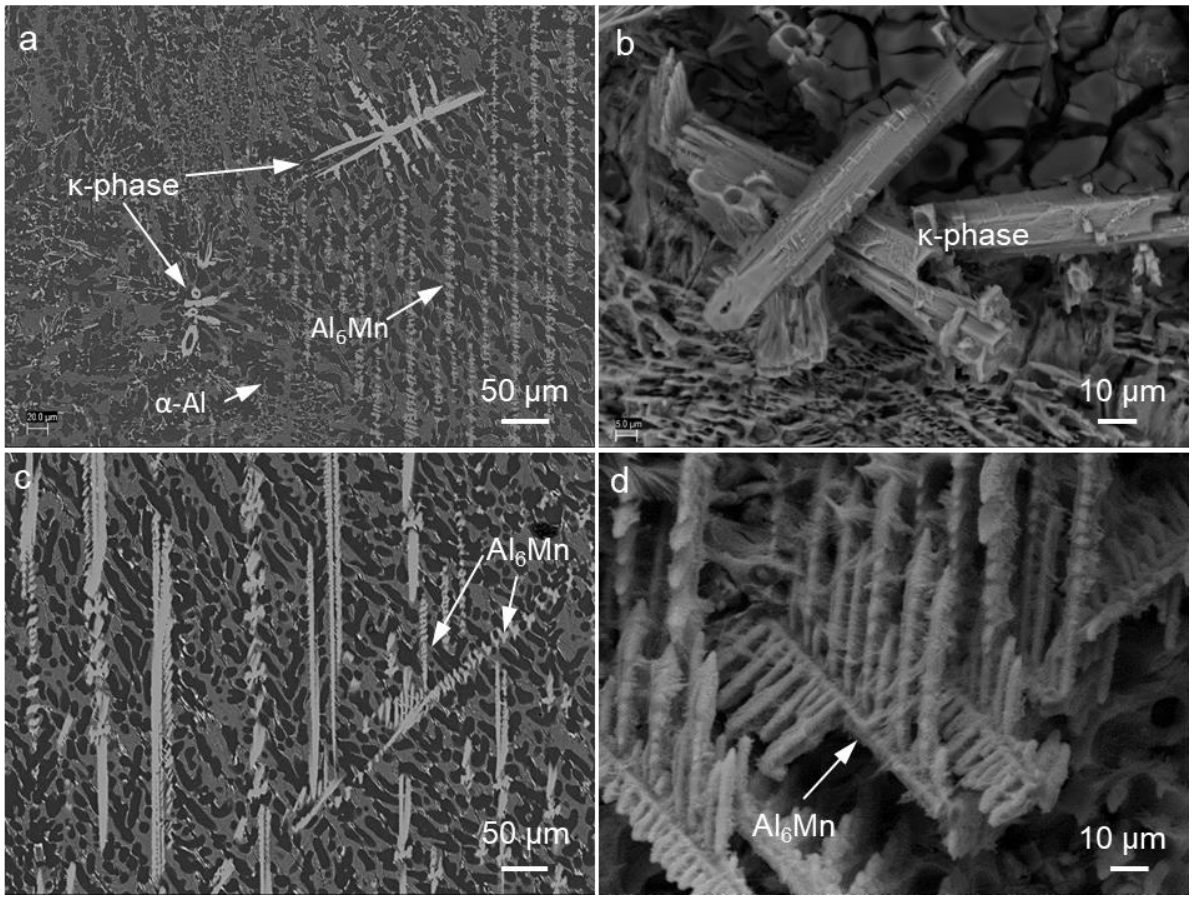

Figure 4.7 (a) Typical microstructure of the Al-4Ni-4Mn alloy, (b) morphology of κ-phase revealed by deep etching, (c, d) dendritic primary Al_6Mn phase.

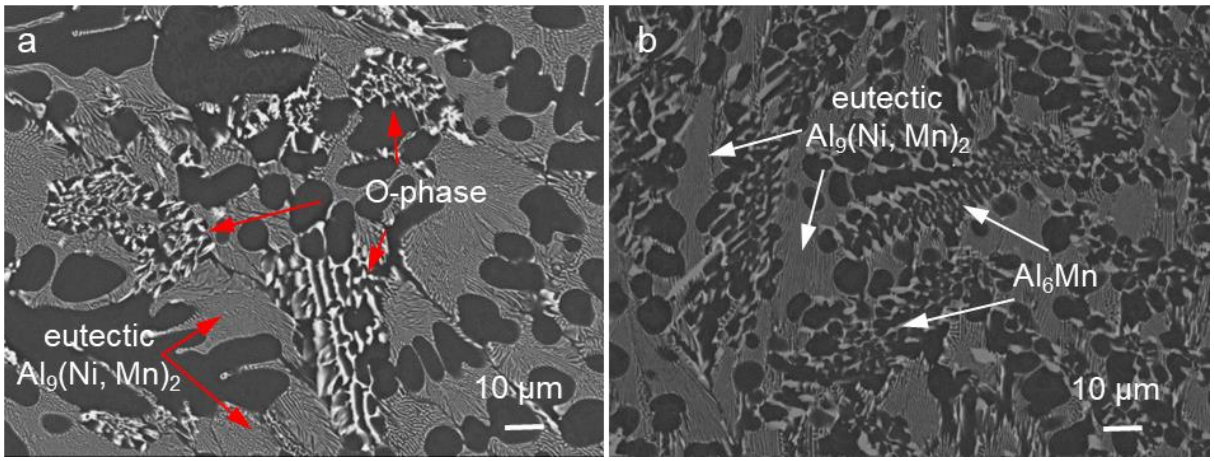

Figure 4.8 Higher magnification images showing (a) smaller size O-phase and (b) Al_6Mn phase.

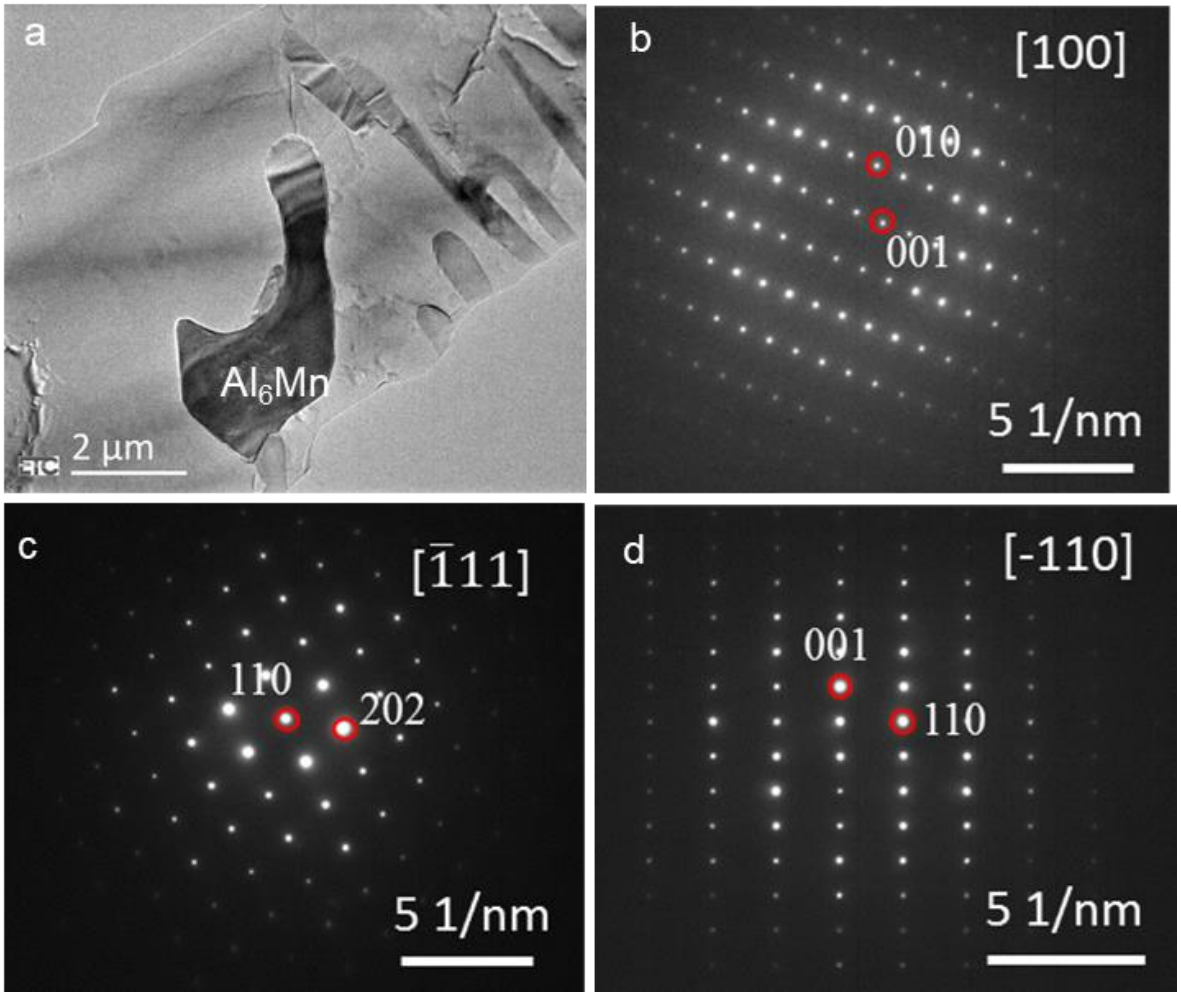

Figure 4.9 TEM image showing Al_6Mn phase and diffraction pattern obtained along zone axis [100], [-111] and [-110].

Microstructural evolution with increasing Mn level was revealed above, and the compositions of phases observed are listed in Table 4.2. The microstructure of Al-4Ni alloy simply consists of primary α-Al and eutectic α-Al+Al_3Ni phases. With 2% Mn addition, the eutectic structure transformed from α-Al+Al_3Ni to α-Al+$Al_9(Ni, Mn)_2$. The morphology of the eutectic $Al_9(Ni, Mn)_2$ phase is net shape, which is the same as the eutectic Al_3Ni phase. The microstructure of Al-4Ni-2Mn alloy simply consists of primary α-Al dendrites and eutectic α-Al+$Al_9(Ni, Mn)_2$ phases. With increasing Mn content to 3%, κ-phase and O-phase appeared. Microstructure of Al-4Ni-3Mn alloy consists of primary α-Al, κ-phase, O-phase and eutectic α-Al+$Al_9(Ni, Mn)_2$ phases. When Mn content increased to 4%, Al_6Mn

phase appeared and it showed dendritic morphology with huge size. Moreover, the amount and size of the κ-phase and O-phase also increased.

Table 4.2 Composition of different phases in Al-Ni-Mn alloys.

Phase	Composition (at. %)		
	Ni	Mn	Al
$Al_9(Ni, Mn)_2$[a]	13.5	3.7	82.8
K-phase[b]	4.8	15.6	79.8
$Al_{60}Mn_{11}Ni_4$[a]	7.0	12.6	80.4
Al_6Mn[a]	0.2	13.3	86.5
Al_6Mn[b]	0.7	13.5	85.2

[a] As measured by SEM/TEM-EDX

[b] As measured by EPMA

4.3 Mechanical property of Al-4Ni-(0-4)Mn alloys

4.3.1 Hardness

The hardness of Al-Ni-Mn alloys is shown in Figure 4.10 with different Mn levels. Clearly, the hardness increased linearly with the increase of Mn. The Al-4Ni alloy presents hardness of 42.3 HV10, while the Al-4Ni-2Mn alloy shows 53% increase to 64.5 HV10. When Mn content was further increased to 3% and 4%, the hardness increased to 67.2 HV10 and 69.9 HV10, respectively.

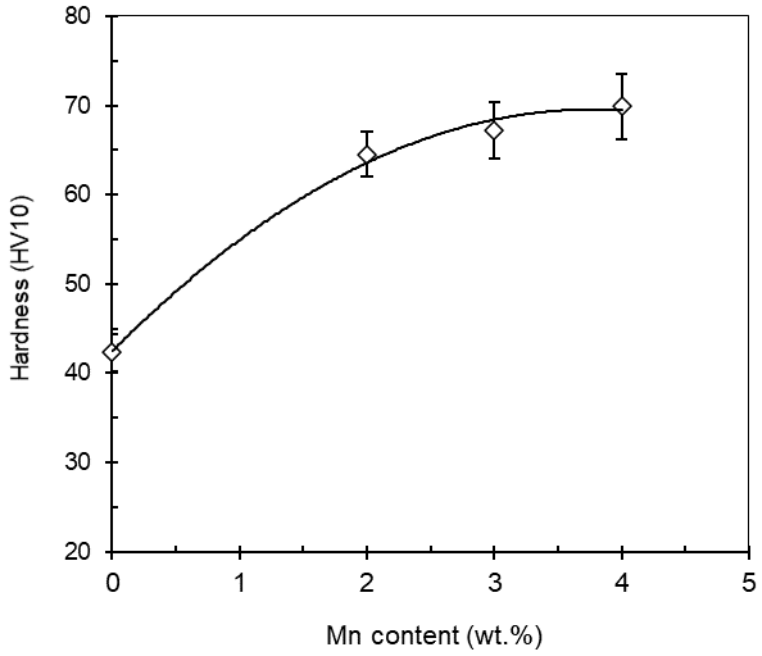

Figure 4.10 Effect of Mn contents on the Vickers hardness of the as-cast Al-4Ni alloy.

4.3.2 Tensile properties at ambient temperature

Figure 4.11 presents the tensile test results of Al-4Ni-(0-4)Mn alloys at ambient temperature (25 °C). It is seen that the yield strength exhibited a significant increase with increasing Mn content. The yield strength was 48 MPa for the Al-4Ni alloy, but it was 92 MPa for the Al-4Ni-2Mn alloy. When the Mn content increased to 3% and 4%, the yield strength continuously increased to 110 MPa and 117 MPa, respectively.

Strengthening of alloys are basically classified into five mechanisms, which are solid solution strengthening, second phase strengthening, grain boundary strengthening, precipitate strengthening and strain hardening. The maximum solubility of Ni in α-Al is 0.05% at 640 ^{o}C, which is negligible for solid solution strengthening, while Mn has a maximum solubility of 1.8% in α-Al at 658 ^{o}C [155]. The α-Al phase in experimental Al-4Ni-2Mn alloy contained 1.6% Mn. As the atomic radius for Mn is 1.40 Å and for Al is 1.25 Å [156], the solid solution with Mn in Al results in lattice distortion, which hinder dislocation motion under loading. Therefore, the addition of Mn contributes to solid solution strengthening in Al-Ni-Mn alloys.

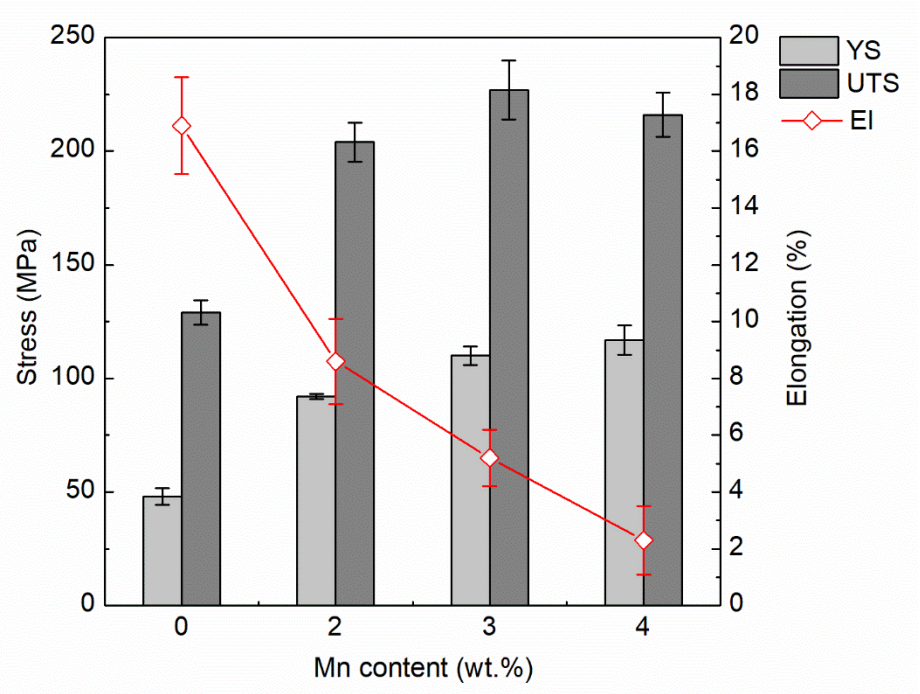

Figure 4.11 Effect of Mn contents on the tensile properties of as-cast Al-4Ni alloy at ambient temperature.

On the other hand, the increased Mn levels increased the amount of eutectic phases and primary intermetallic phases. The measured volume fractions of different phases in the experimental Al-4Ni-Mn alloys are listed in Table 4.3. As seen, the Al-4Ni alloy contained 44 vol.% of eutectic phases. With 2% Mn addition, the eutectic phases increased to 51 vol.%, while no primary intermetallic phase was found. With 3% Mn addition, the eutectic phases increased to 58 vol.%, and the primary intermetallic phase was found at a level of 1 vol.%. When Mn content increased to 4%, the eutectic phases increased to 60 vol.%, and the primary intermetallic phase increased to 5 vol.%. The increased eutectic phases and primary intermetallic phases can introduce second phase strengthening. Therefore, the improvement of yield strength by Mn addition was explained.

The UTS also displayed significant improvement with increasing the Mn content at ambient temperature. It increased dramatically from 129 MPa for the Al-4Ni alloy to 204 MPa for

the Al-4Ni-2Mn alloy. And then it reached peak strength of 227 MPa at 3% Mn. When Mn content increased to 4%, the UTS did not increase but decreased slightly to 225 MPa. As presented in Figure 4.7d, the dendritic Al_6Mn phase appeared in the Al-4Ni-4Mn alloy and it has size of several hundred micrometres. For this type of tough and large size intermetallic phase, the localized stress on the particle surface and especially in the dendrite corners and tips increases quickly and accelerates fracture of material. Therefore, the Al-4Ni-4Mn alloy presented lower UTS than the Al-4Ni-3Mn alloy. The elongation decreased dramatically with increasing Mn content. It was 18.0% for the Al-4Ni alloy and decreased to 8.6% and 5.2% for the Al-4Ni-2Mn and Al-4Ni-3Mn alloys respectively. For the Al-4Ni-4Mn alloy, the elongation was only 2.3%, which indicates brittle fracture. It provides corroboration for the decreased UTS of Al-4Ni-4Mn alloy.

Table 4.3. The volume fraction of different phases in the experimental Al-Ni-Mn alloys.

Alloy	Volume Fraction (vol.%)		
	Primary α-Al	Eutectic Phases	Intermetallic phases
Al-4Ni	56%	44%	--
Al-4Ni-2Mn	49%	51%	--
Al-4Ni-3Mn	41%	58%	1%
Al-4Ni-4Mn	35%	60%	5%

4.3.3 Tensile properties at 250 °C

Figure 4.12 shows the stress strain of Al-4Ni-2Mn alloy at 250 °C. The 0.2% offset yield strength was obtained. Tensile strength and elongation are shown in Figure 4.13. It was seen that Mn improved both the yield strength and the UTS of Al-4Ni-(0-4)Mn alloys at 250 °C. The yield strength was 35 MPa for the Al-4Ni alloy and 82 MPa for the Al-4Ni-2Mn alloy, increased by 134%. When Mn level was increased to 3% and 4%, the yield strength continuously increased to 96 MPa and 101 MPa, respectively. Meanwhile, the UTS increased from 51 MPa for the Al-4Ni alloy to 120 MPa for the Al-4Ni-2Mn alloy and then

increased to 143 MPa when Mn level increased to 4%. The elongation at 250 °C was much higher than that at ambient temperature but the addition of Mn decreased the elongation dramatically at 250 °C. The elongation was 49.0% for the Al-4Ni alloy and 17.9% for the Al-4Ni-2Mn alloy. It was further decreased to 11.9% and 3.7% for the Al-4Ni-3Mn alloy and Al-4Ni-4Mn alloy, respectively.

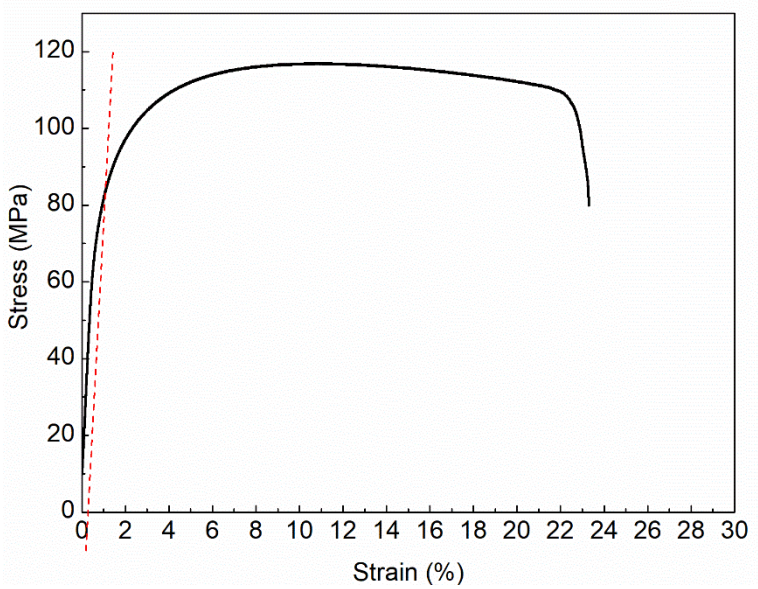

Figure 4.12 Stress-strain curve of Al-4Ni-2Mn alloy at 250 °C.

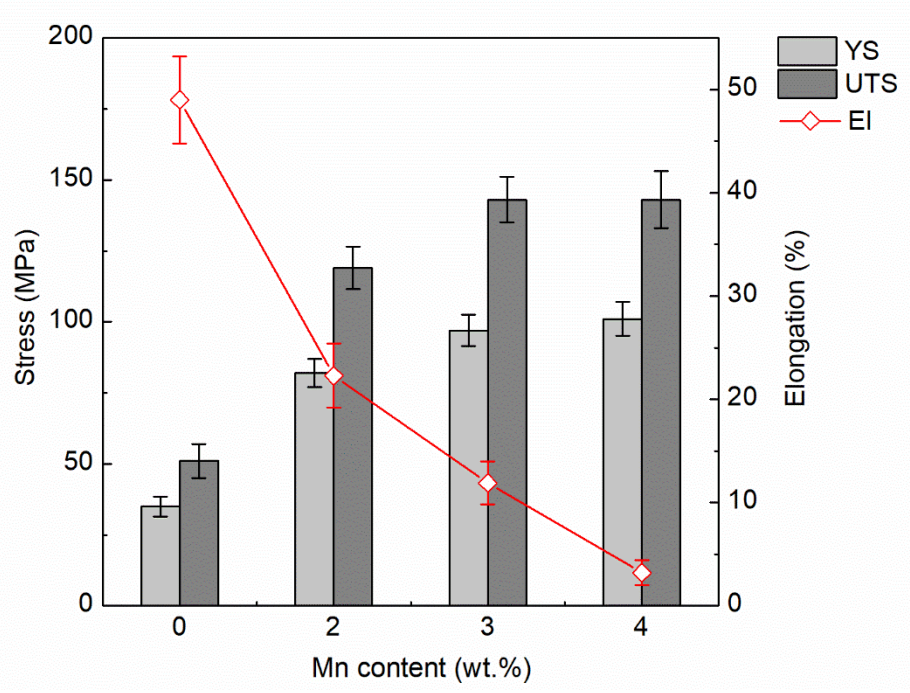

Figure 4.13 Effect of Mn contents on tensile properties of the as-cast Al-4Ni alloy at 250 °C.

Moreover, the alloys with Mn addition presented less strength loss when the temperature was increased to 250 °C. Table 4.4 lists the strength loss of experimental alloys. Clearly, the alloys with Mn addition presented less strength loss. The Al-4Ni alloy showed a reduction of 27% for the yield strength between 25 °C and 250 °C. However, the Al-4Ni-2Mn alloy showed only 10% yield strength loss. And the Al-4Ni-3Mn alloy and Al-4Ni-4Mn alloy presented 12% and 14% yield strength loss, respectively. Similarly, the ultimate tensile strength of Al-4Ni alloy showed 60% reduction while the Al-4Ni-2Mn alloy only showed 41%. The Al-4Ni-3Mn alloy and Al-4Ni-4Mn alloy presented 37% and 34% ultimate tensile strength loss respectively between 25 °C and 250 °C, which showed less strength loss than Al-4Ni alloy. Hence, it can be concluded that Mn addition can effectively improve the softening resistance of Al-4Ni alloys at evaluated temperatures.

Table 4.4 The strength loss of the Al-4Ni and Al-4Ni-xMn alloys at 250 °C.

Alloy	Strength Loss	
	Yield Strength	Ultimate Tensile Strength
Al-4Ni	27%	60%
Al-4Ni-2Mn	10%	41%
Al-4Ni-3Mn	12%	37%
Al-4Ni-4Mn	14%	34%

As mentioned above, the main difference between Al-4Ni and Al-4Ni-2Mn alloy is the eutectic structure. The eutectic structure was α-Al+Al_3Ni for the Al-4Ni alloy while it was α-Al+$Al_9(Ni, Mn)_2$ for the Al-4Ni-2Mn alloy. Hence, the difference may be related to different softening behaviour between $Al_9(Ni, Mn)_2$ and Al_3Ni phases. No data for $Al_9(Ni, Mn)_2$ phase was reported but Al_9FeNi phase was found. The microhardness of α-Al, Al_3Ni and Al_9FeNi phases were found in ref [53]. The Al_9FeNi phase [152] was also named as $Al_9(Fe, Ni)_2$. It shows the same monoclinic structure of Al_9Co_2 as $Al_9(Ni, Mn)_2$ phase. Also,

the composition of Al_9FeNi phase showed Al-13.4 at.% Ni-4.2 at.% Fe, which is close to the $Al_9(Ni, Mn)_2$ phase (Al-13.5 at.% Ni -3.7 at.% Mn). Moreover, Fe and Mn are next to each other in the periodic table. These two elements have very close atomic radius (R_{Mn}=1.40 Å, R_{Fe}=1.26 Å) and can replace each other in many intermetallic phases. In addition, the Al_9FeNi phase and $Al_9(Ni, Mn)_2$ contain a relatively low level of Fe and Mn respectively. It is then expected that Mn atoms replace Fe atoms. The Al_9FeNi and $Al_9(Ni, Mn)_2$ phase should present similar hardness and softening behaviour at elevated temperatures.

The microhardness of α-Al, Al_3Ni and Al_9FeNi phases were found in reference [53] and displayed in Figure 4.14. The microhardness of Al_9FeNi phase was reported to be 7.71 GPa at ambient temperature while Al_3Ni was only 5.95 GPa. When the temperature increased to 350 °C, the hardness of Al_9FeNi phase was 5.83 GPa while Al_3Ni was only 3.54 GPa. The Al_9FeNi phase showed higher hardness than the Al_3Ni phase at both ambient temperature and elevated temperatures. In addition, the hardness of the α-Al phase decreased dramatically from 1.45 GPa to 0.143 GPa when the temperature increased to 350 °C, which indicates the α-Al phase softens quickly at elevated temperatures. Figure 4.14b presents hardness retention at elevated temperatures for different phases. It is clear that the Al_9FeNi phase maintained higher hardness than the Al_3Ni phase. When the temperature increased to 350 °C, the Al_9FeNi phase maintained 75.6% of hardness while the Al_3Ni phase maintained only 59.5%. Hence, the Al_9FeNi phase showed better softening resistance than the Al_3Ni phase at elevated temperatures. Therefore, it is expected that the $Al_9(Ni, Mn)_2$ phase also presented higher softening resistance than the Al_3Ni phase. Similarly, the eutectic α-Al+$Al_9(Ni, Mn)_2$ structure displayed better softening resistance than the α-Al+Al_3Ni structure. Therefore, the transformation of the eutectic phase from Al_3Ni to $Al_9(Ni, Mn)_2$ improved the softening resistance at 250 °C.

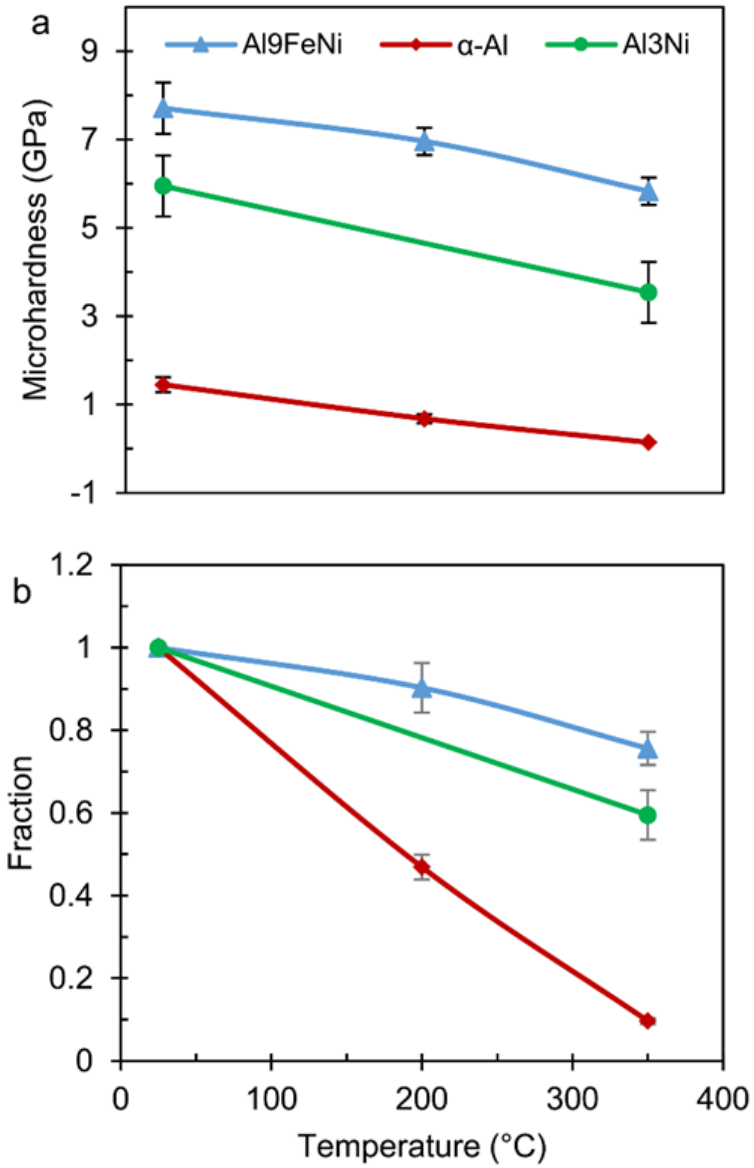

Figure 4.14 (a) The microhardness of α-Al, Al_3Ni and Al_9FeNi phases and (b) microhardness retention at different temperatures [53].

4.4 Fracture analysis

It is clear that the addition of Mn into Al-Ni alloys can significantly increase the yield strength and UTS with the scarification of elongation. In particular, the reduction of elongation is dramatic, in which the fracture mechanism should play a dominant role. Therefore, it is necessary to understand the mechanism of fracture in the alloys with different Mn levels and different temperatures. The study focuses on fractured surfaces and

microstructures adjacent to the fractured surface of Al-4Ni-(0-4)Mn at ambient temperature and 250 °C.

4.4.1 Fractured surface analysis at ambient temperature

Visual observation of the Al-4Ni alloy after ambient temperature tensile test shows a dull and fibrous appearance. The fracture surface obtained by SEM is shown in Figure 4.15. Fibrous features and small equiaxed dimples indicate ductile fracture. The Al-4Ni-2Mn alloy shows similar dull and fibrous appearance when examined visually. SEM images are shown in Figure 4.16. The fine and equiaxed dimples indicate that Al-4Ni-2Mn also shows ductile fracture. Both the Al-4Ni and Al-4Ni-2Mn alloy displayed typical ductile fracture.

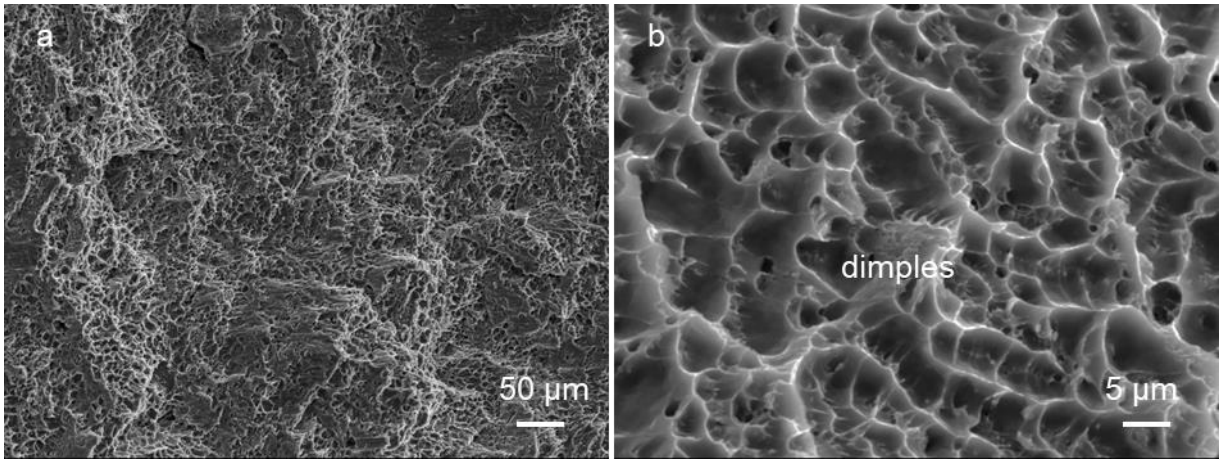

Figure 4.15 SEM micrographs showing the fracture surface of the Al-4Ni alloy after ambient temperature fracture. (a) fibrous morphology at low magnification and (b) dimples observed at high magnification.

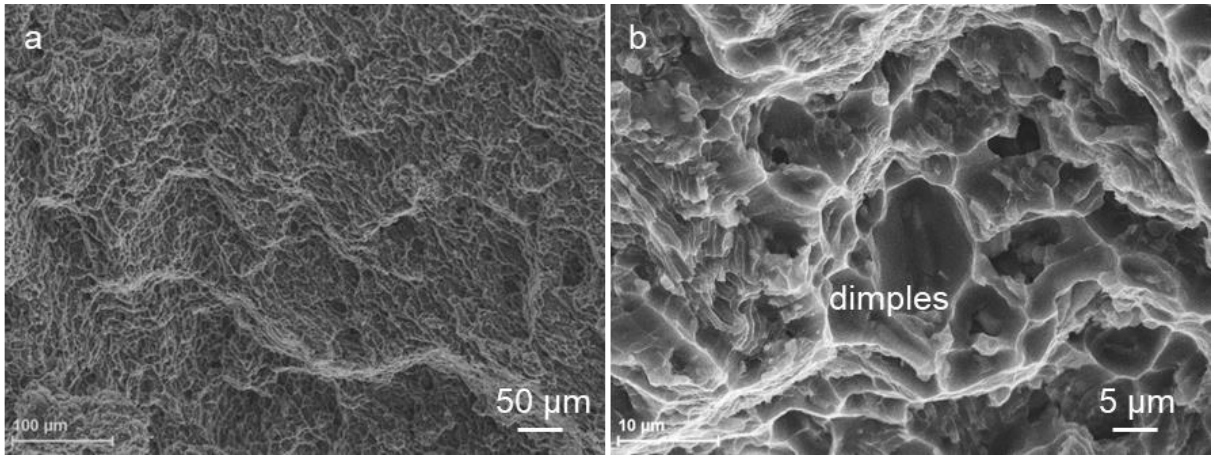

Figure 4.16 SEM micrographs showing the fracture surface of the Al-4Ni-2Mn after ambient temperature fracture. (a) fibrous morphology at low magnification and (b) dimples observed at high magnification.

Visual examination of Al-4Ni-4Mn alloy after tensile test shows granular and brighter appearance with some planes reflecting light. Figure 4.17 shows fracture surfaces under SEM. Clear cleavage facets are clear. Close examination showed that κ-phase and Al_6Mn phase were torn apart. Apart from the cleavage facets, dimples were also observed. In brief, the Al-4Ni-4Mn alloy shows quasi-cleavage fracture. The κ-phase cracked and tear ridges were observed. Therefore, the Al-4Ni-4Mn alloy presents mixed ductile and brittle fracture. In summary, the fracture mode shows a transformation from typical ductile fracture to mixed ductile and brittle fracture with increasing Mn level.

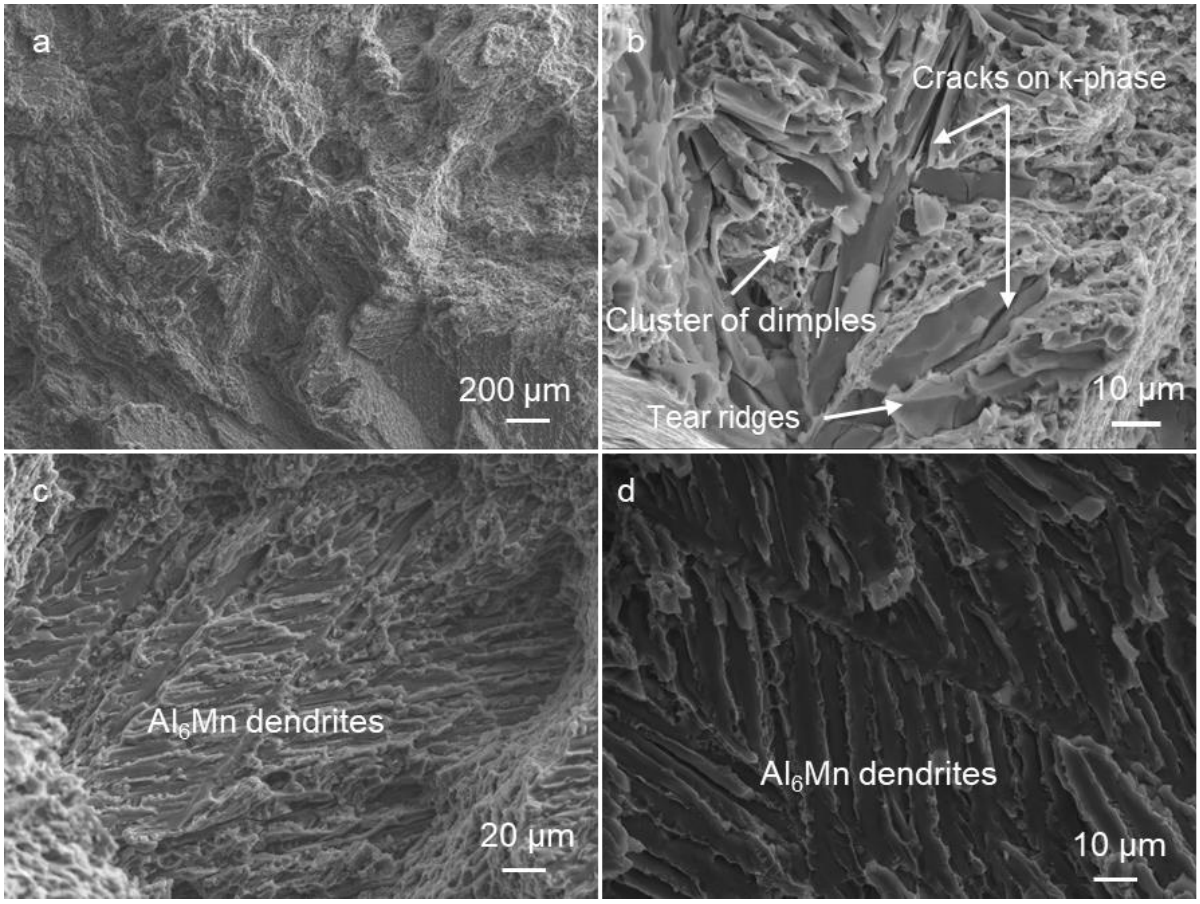

Figure 4.17 SEM micrographs showing the fracture surface of the Al-4Ni-4Mn after ambient temperature fracture.

Investigation of microstructure underneath fracture surfaces provides more details of the fracture process. The microstructure of Al-4Ni alloy beneath the fracture surface is shown in Figure 4.18. Cracks were on the interface of eutectic cell boundary/primary α-Al. Observation at higher magnification shows microstructure far away from the surfaces, as shown in Figure 4.18b. Crack initiation occurs on the eutectic Al_3Ni rods, and cracks are normal to tensile direction. Therefore, the cracks initiate on the eutectic Al_3Ni rods, and grew larger, which leads to fracture of Al-4Ni alloy.

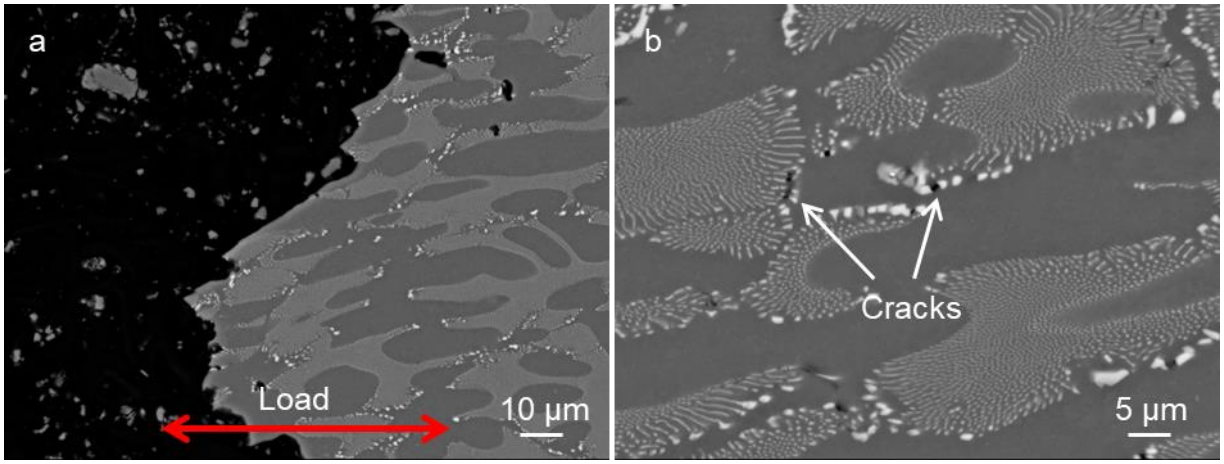

Figure 4.18 SEM micrographs showing microstructure of the Al-4Ni alloy beneath the fracture surface.

The microstructure of Al-4Ni-2Mn alloy near the fracture surface is shown in Figure 4.19a. It is clear that cracks propagate along the eutectic cell boundary, as shown in the oval. Figure 4.19b shows microstructure far away from the surface. It is seen that cracks initiate on the eutectic $Al_9(Ni, Mn)_2$ phase. Therefore, the Al-4Ni-2Mn alloy present similar crack initiation and propagation process as Al-4Ni alloy at ambient temperature.

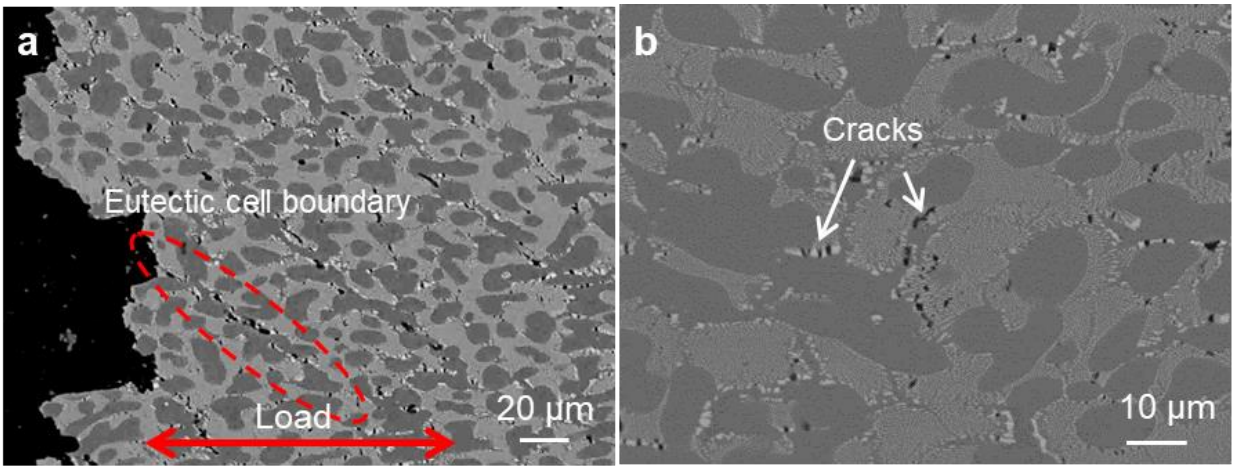

Figure 4.19 SEM micrographs showing microstructure of the Al-4Ni-2Mn alloy beneath the fracture surface.

The Al-4Ni-4Mn alloy, however, presents mixed ductile and brittle fracture. The microstructure near the fracture surface displays in Figure 4.20a. The Al_6Mn dendrites crack under tension stress and tear apart the α-Al matrix; thus, adjacent cracks join. As mentioned,

large Mn-rich phases (κ-phase and Al_6Mn phase) exists in Al-4Ni-4Mn alloy, which indicates a high cracking probability. Figure 4.20b shows a large crack on the κ-phase, which is far away from the fracture surface. And cracks are normal to tensile direction. In brief, crack initiates on large κ-phase and Al_6Mn phase and then tears apart α-Al matrix to connect together and leads to fracture of Al-4Ni-4Mn.

According to the observation of fracture surfaces and microstructure beneath fracture surfaces, it can be summarized that: (1) Both Al-4Ni and Al-4Ni-2Mn alloy present ductile fracture mode at ambient temperature. Dimples were observed on fracture surface. And they present similar crack initiation and propagation process. Crack initiates on the eutectic rods and then propagate along with eutectic cell/primary α-Al interface and finally leads to fracture; (2) with increasing Mn level, Al-4Ni-4Mn alloy displays a mixed ductile and brittle fracture. Cleavage facets were observed, and clusters of dimples were also found. Crack initiates on intermetallic phases (κ-phase and Al_6Mn), and then tears apart α-Al matrix and finally results in fracture.

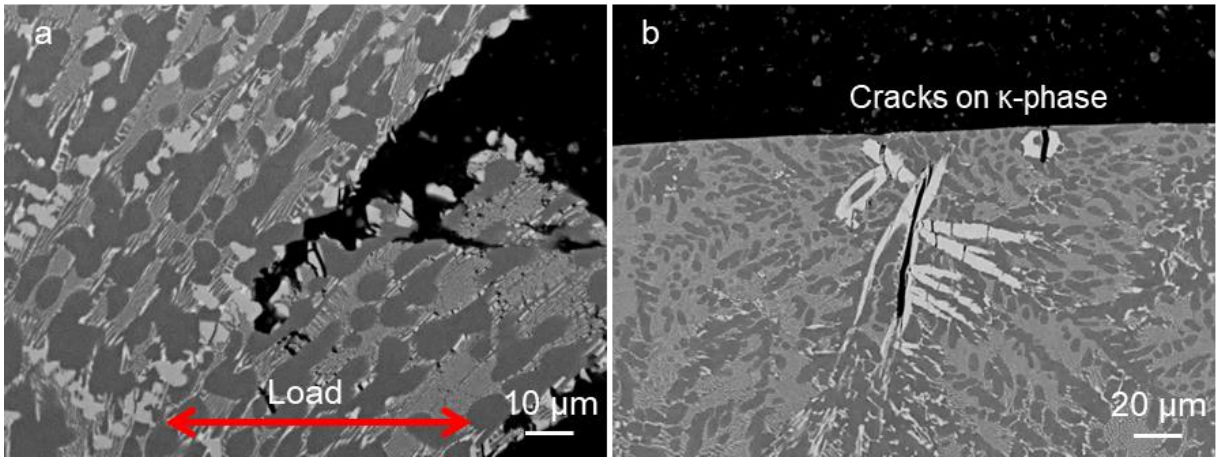

Figure 4.20 SEM micrographs showing microstructure of the Al-4Ni-4Mn alloy beneath the fracture surface. (a) crack propagation, (b) cracks on κ-phase particle.

4.4.2 Fractured surface analysis at elevated temperature

Fracture analysis was also conducted for Al-4Ni-(0-4) alloys when testing at 250 °C. The Al-4Ni alloy displays a typical cup and cone appearance when examining visually. Figure

4.21 shows the microstructure of the Al-4Ni alloy after fracture. A large amount of deformation was observed at the edge. The dendritic primary α-Al phase became elongated. Figure 4.21b shows crack initiation and propagation path. Porosities were observed and the irregular shape indicates shrinkage cavities. Shrinkage cavity was not observed in as-cast Al-4Ni sample. While during elevated temperature tensile test, shrinkage cavities can grow by diffusion. Crack initiates at the edge of a shrinkage cavity, where localised stress is concentrated. By observing α-Al dendrites near the surface, It is seen that crack propagates along the eutectic cell/primary α-Al interface. Some primary α-Al dendrites rotated and deboned. At elevated temperatures, Al-4Ni alloy experienced more deformation. Shrinkage cavities formed, and then cracks initiated from the cavity. Primary α-Al dendrites rotated and deboned from the eutectic area but did not tear apart, which is different from the ambient temperature tensile test. It shows higher ductility at elevated temperatures.

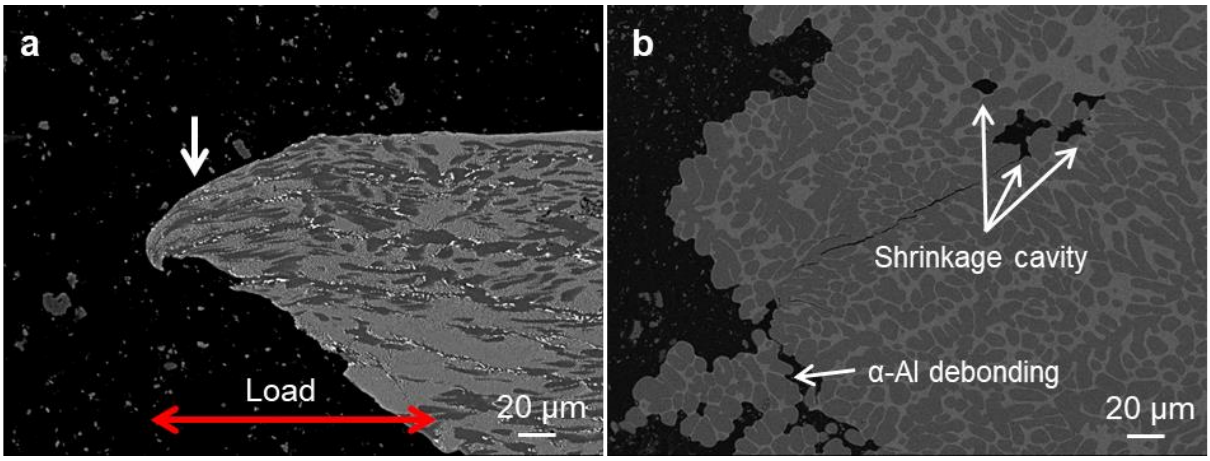

Figure 4.21 SEM micrographs showing microstructure of the Al-4Ni alloy beneath the fracture surface at 250 °C.

Al-4Ni-2Mn alloy also presents a typical cup and cone appearance when examined visually. Figure 4.22(a, b) shows large amount of deformation. The primary α-Al dendrites were stretched. Figure 4.22c shows crack propagation along the eutectic cell boundaries. Observing microstructure far away from fracture surface, crack initiation was found. Some eutectic $Al_9(Ni, Mn)_2$ rods cracked while some $Al_9(Ni, Mn)_2$ rods deboned from the matrix. Observation of fracture surface revealed this phenomenon in Figure 4.23 and eutectic

$Al_9(Ni, Mn)_2$ rods were exposed. However, no debonding of $Al_9(Ni, Mn)_2$ rods was found when testing at ambient temperature. It can be explained that, at elevated temperature, the α-Al became soft and easier to deform. Deformation prevents severe localised stress concentration and hence protect eutectic $Al_9(Ni, Mn)_2$ rods from cracking.

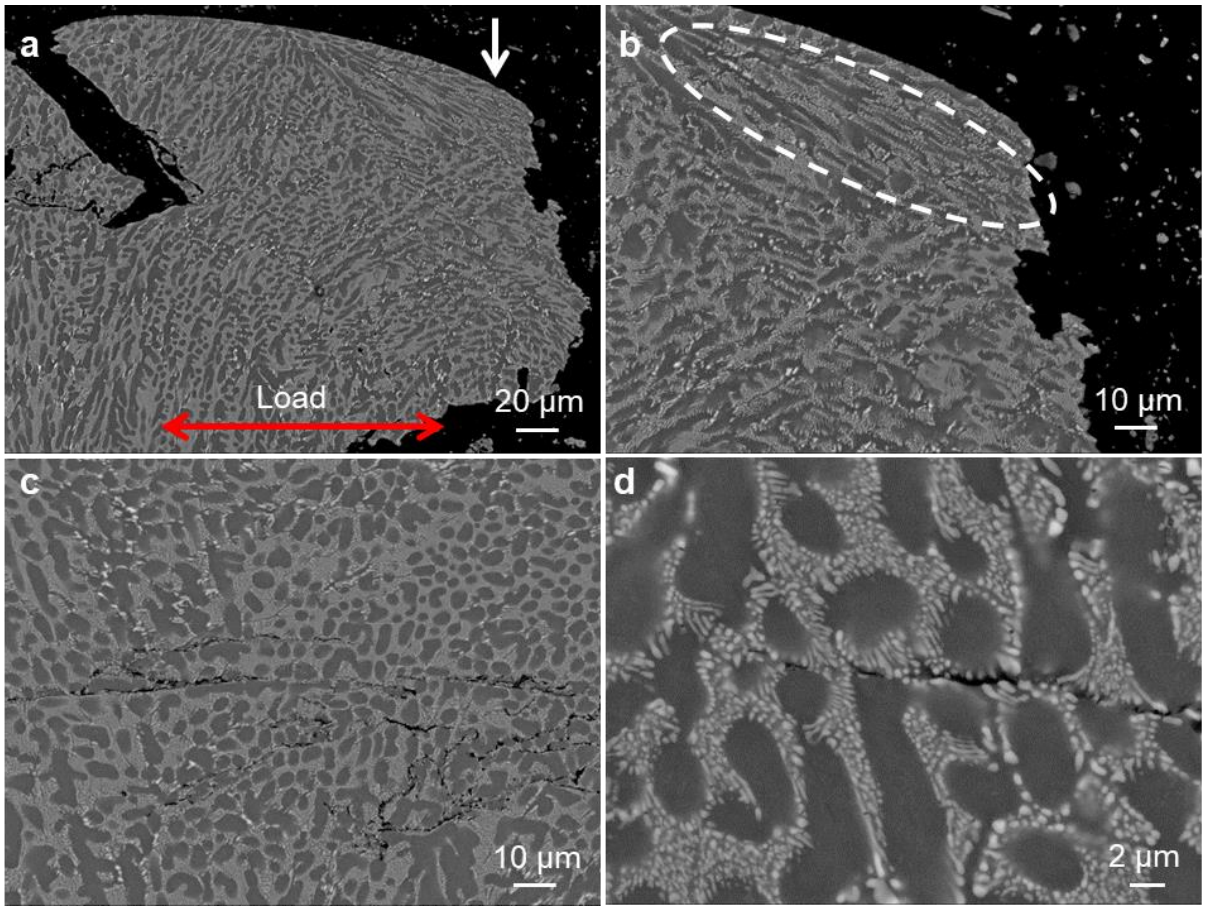

Figure 4.22 SEM micrographs showing microstructure of the Al-4Ni-2Mn beneath the fracture surface after fractured at 250 °C.

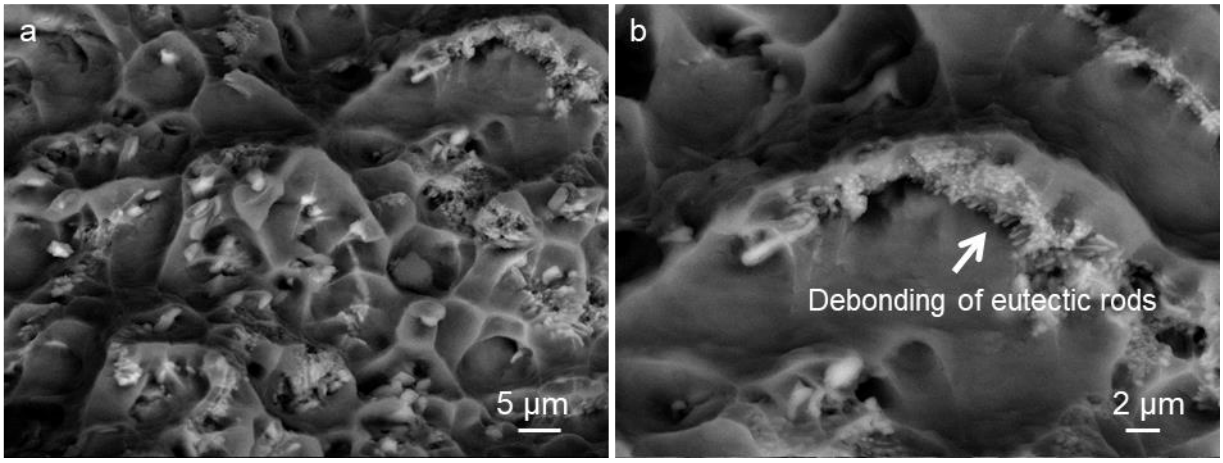

Figure 4.23 Fracture surface observation showing debonding of eutectic $Al_9(Ni, Mn)_2$ rods after fractured at 250 °C.

The microstructure of Al-4Ni-4Mn alloy after tensile test at 250 °C displays in Figure 4.24. Cracked Al_6Mn dendrites and κ-phase were observed, and cracks are mainly normal to tensile direction. When examining at higher magnification, as shown in Figure 4.24b, it is seen that cracked Al_6Mn pieces moved and wrapped closely with matrix leaving no space. It means the matrix continued to deform after Al_6Mn cracked. Therefore, cracked pieces moved and rotated along with deformation of matrix and kill spaces left by cracking.

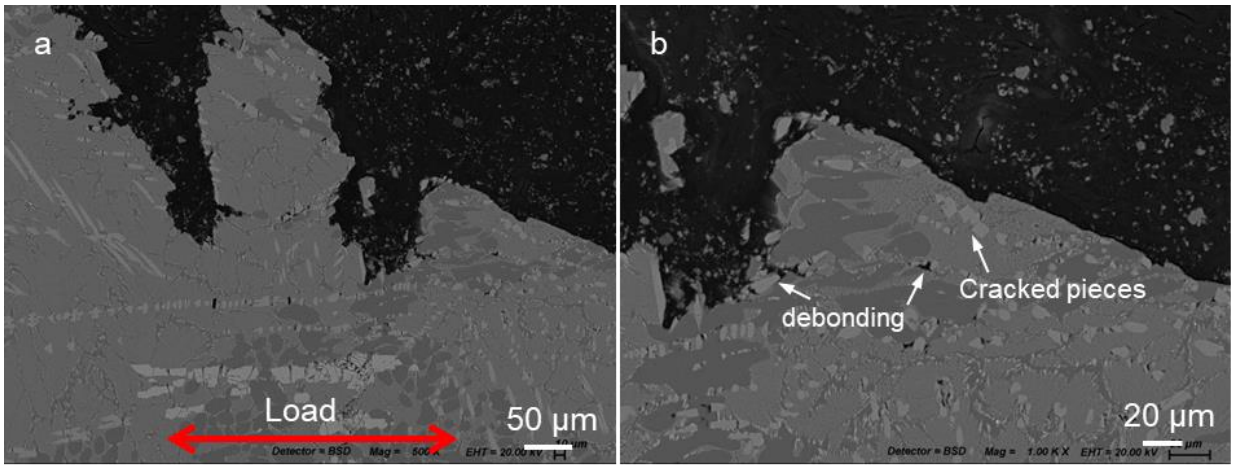

Figure 4.24 SEM micrographs showing microstructure of the Al-4Ni-4Mn beneath the fracture surface after fractured at 250 °C.

Observations of microstructure after fracture at ambient temperature and 250 °C are conducted. The results demonstrate the difference of fracture mode. The Al-4Ni and Al-4Ni-

2Mn alloy present typical ductile fracture mode at ambient temperature. With increasing Mn level, Al-4Ni-4Mn alloy displays a mixed ductile and brittle fracture. In Al-4Ni and Al-4Ni-2Mn alloy, cracks initiate on eutectic rods. While in the Al-4Ni-4Mn alloy, cracks initiate on large size Al_6Mn and κ-phase.

At 250 °C, crack initiation changed. For the Al-4Ni alloy, cracks initiate from shrinkage cavity rather than eutectic Al_3Ni rods. For the Al-4Ni-2Mn alloy, debonding of eutectic $Al_9(Ni, Mn)_2$ rods was observed, which indicates α-Al is soft and easier to deform at 250 °C. Al-4Ni-4Mn alloy presents mixed ductile and brittle fracture mode at 250 °C. Crack initiates on large Al_6Mn and κ-phase, which is similar to ambient temperature. Besides, the eutectic matrix was observed continuing deforming after Al_6Mn cracked. The cracked Al_6Mn pieces moved and rotated along with deformation of matrix.

4.5 Summary

In this Chapter, the effect of Mn on the microstructure and mechanical properties of the Al-4Ni alloy was investigated. SEM, TEM and XRD were applied to characterize microstructure and identify phases. Tensile strength at both ambient temperature and 250 °C were tested.

Mn addition transformed the eutectic intermetallic phase from Al_3Ni to $Al_9(Ni, Mn)_2$ phase. The $Al_9(Ni,Mn)_2$ phase showed rod-like shape. Hence the eutectic structure transformed from α-Al+Al_3Ni to α-Al+$Al_9(Ni, Mn)_2$ with Mn addition. When Mn content increased to 3%, the κ-phase and O-phase appeared. And when Mn content increased to 4%, the dendritic Al_6Mn phase was observed.

Moreover, Mn addition significantly improved the mechanical properties of the as-cast Al-4Ni alloy at both ambient temperature and 250 °C. The yield strength increased significantly from 48 MPa to 117 MPa with 4% Mn at ambient temperature and from 35 MPa to 101 MPa at 250 °C. The improvement is due to the solid solution of Mn in a-Al and the increase amount of eutectic phases and primary intermetallic phases with increasing Mn

content. The softening resistance also showed improvement. Alloys with Mn addition presented less strength loss than the Al-4Ni alloy when temperature increased to 250 °C. It is because the eutectic $Al_9(Ni, Mn)_2$ phase displaying higher softening resistance than the Al_3Ni phase at elevated temperatures.

The fracture mechanism changed with Mn addition. Al-4Ni and Al-4Ni-2Mn alloys present typical ductile fracture at ambient temperature. Whereas the Al-4Ni-4Mn alloy displays a mixed ductile and brittle fracture. In the Al-4Ni and Al-4Ni-2Mn alloy, cracks initiate on eutectic rods. While in the Al-4Ni-4Mn alloy, cracks initiate on large size Al_6Mn and κ-phase. At 250 °C, crack initiation changed. For the Al-4Ni alloy, cracks initiate from shrinkage cavity rather than eutectic Al_3Ni rods. For the Al-4Ni-2Mn alloy, debonding of eutectic $Al_9(Ni, Mn)_2$ rods was observed, which indicates α-Al is soft and easier to deform at 250 °C. In the Al-4Ni-4Mn alloy, the eutectic matrix was observed continuing deforming after Al_6Mn cracked. The cracked pieces moved and rotated along with deformation of matrix.

Chapter 5: The Effect of Mn on Microstructure and Mechanical Properties of Eutectic Al-6Ni alloy and Hyper-eutectic Al-8Ni Alloy

5.1 Introduction

The effect of Mn on hypo-eutectic Al-4Ni alloys was investigated in Chapter 4. The eutectic structure transformation from α-Al+Al_3Ni to α-Al+$Al_9(Ni, Mn)_2$ was observed with 2% Mn addition to hypo-eutectic Al-4Ni alloy. However, it is unclear that whether Mn could transform the eutectic phases from α-Al+Al_3Ni to α-Al+$Al_9(Ni, Mn)_2$ when Ni content increased to 6% and 8%. Moreover, the effect of Mn on the primary Al_3Ni phase in hyper-eutectic A-Ni alloy has not been studied yet. The maximum strength of Al-4Ni-(0-4)Mn alloys was achieved by Al-4Ni-4Mn alloy. It offers yield strength of 117 MPa, UTS of 216 MPa at ambient temperature and yield strength of 101 MPa, UTS of 143 MPa at 250 °C. The strength cannot meet the requirement for application. The Al-6Ni and Al-8Ni alloys are believed to provide better strength. Therefore, the effect of Mn addition on eutectic Al-6Ni and hyper-eutectic Al-8Ni alloy also needs investigation.

This chapter aims at investigating the effect of Mn on eutectic Al-6Ni alloy and hyper-eutectic Al-8Ni alloy. The Al-6Ni-xMn and Al-8Ni-xMn (x=0, 2, 3, 4) alloys were prepared by PMC. The microstructure, especially eutectic phases transformation and new intermetallic phase formation, were characterized. The best performance at ambient temperature and 250 °C were explored.

5.2 Microstructure of as-cast Al-6Ni-(0-4)Mn alloys

The compositions of the experimental alloys obtained by optical emission spectrometry (OES) are listed in Table 5.1. It shows that actual composition is very close to the designed nominal compositions, and the levels of impurity elements such as Si and Fe are controlled at very low.

Table 5.1 The compositions of Al-6Ni-xMn alloys measured by OES.

Alloy	Composition (wt.%)						
	Al	Ni	Mn	Fe	Si	Ti	Zr
Al-6Ni	Bal.	5.92	0.01	0.10	0.12	0.01	0.01
Al-6Ni-2Mn	Bal.	5.89	1.81	0.17	0.13	<0.01	<0.01
Al-6Ni-3Mn	Bal.	5.87	3.19	0.17	0.13	0.1	0.01
Al-6Ni-4Mn	Bal.	5.64	3.81	0.14	0.13	0.01	0.01

Typical microstructures of the Al-6Ni alloy are shown in Figure 5.1(a, b). It is a eutectic alloy and consists of eutectic phases and a very small amount of primary intermetallic phase (<0.5 vol.%). This primary phase was confirmed to be Al_3Ni phase by SEM-EDX. It shows an irregular shape with faceted surfaces, and the size varied from 5-50 μm. The eutectic cell structure was presented in Figure 5.1c. The eutectic Al_3Ni rods at high magnification are shown in Figure 5.1d, which presents the same morphology as in the Al-4Ni alloy.

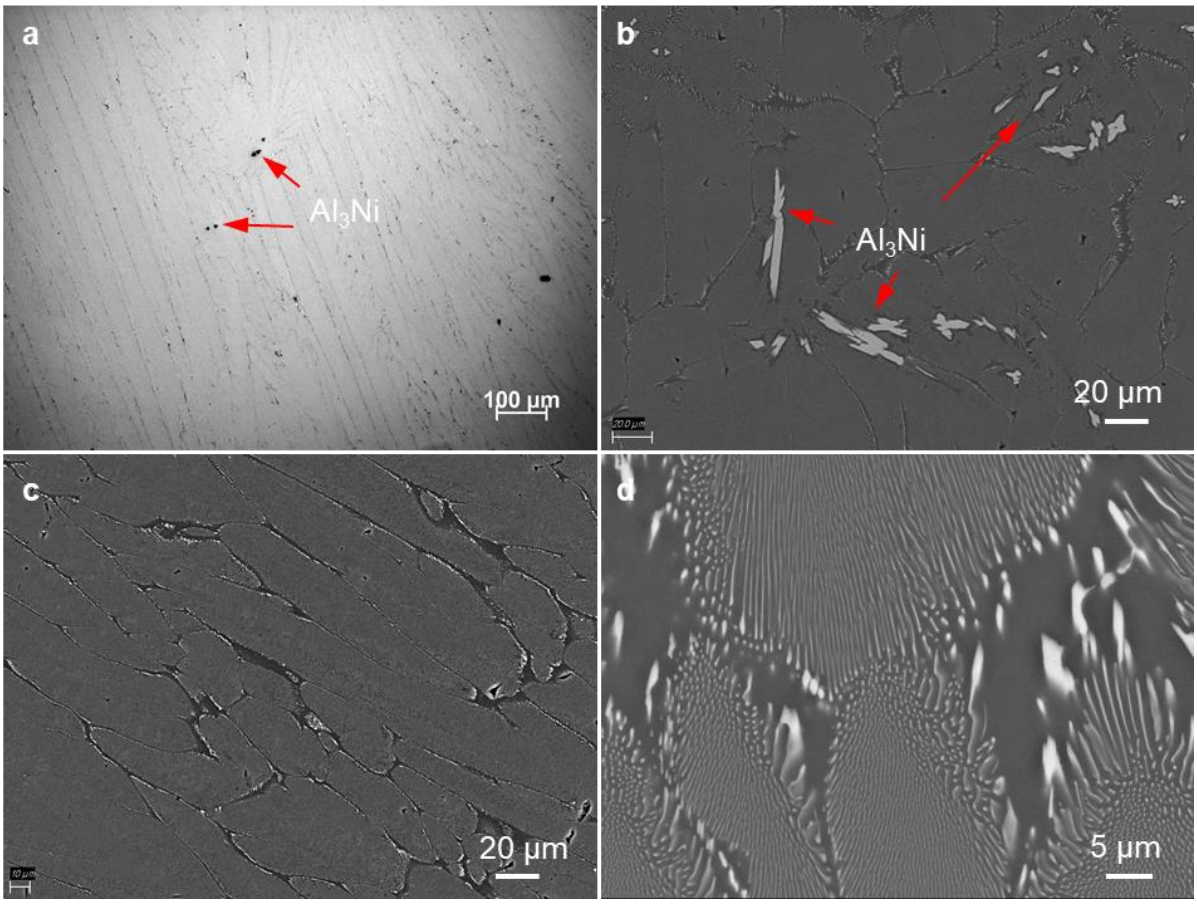

Figure 5.1 Optical image (a) and SEM images (b) showing the typical as-cast microstructure of Al-6Ni alloy. (c) eutectic cells and (d) Al_3Ni phase.

Figure 5.2 presents the SEM images of microstructures of Al-6Ni-2Mn. It shows a similar microstructure as Al-6Ni alloy, which consists of eutectic phases and a small amount of primary intermetallic phases. SEM-EDX result shows that the primary intermetallic phase contains 13.3 at% Ni and 3.3 at.% Mn, which corresponds to $Al_9(Ni, Mn)_2$ phase. Therefore, the primary intermetallic phase in Al-6Ni alloy was transformed to $Al_9(Ni, Mn)_2$ with 2% Mn. The deeply etched image in Figure 5.2c reveals the morphology of the primary $Al_9(Ni, Mn)_2$ phase, which has faceted surfaces and an open hollow. The size of the primary $Al_9(Ni, Mn)_2$ phase varied from 10-60 µm. The eutectic intermetallic phase was also confirmed to be $Al_9(Ni, Mn)_2$ phase. The deeply etched image in Figure 5.2d reveals a rod-shape eutectic $Al_9(Ni, Mn)_2$ phase. Each clump represents a eutectic cell. In brief, Mn addition transformed both the eutectic and primary Al_3Ni phase into $Al_9(Ni, Mn)_2$ phase.

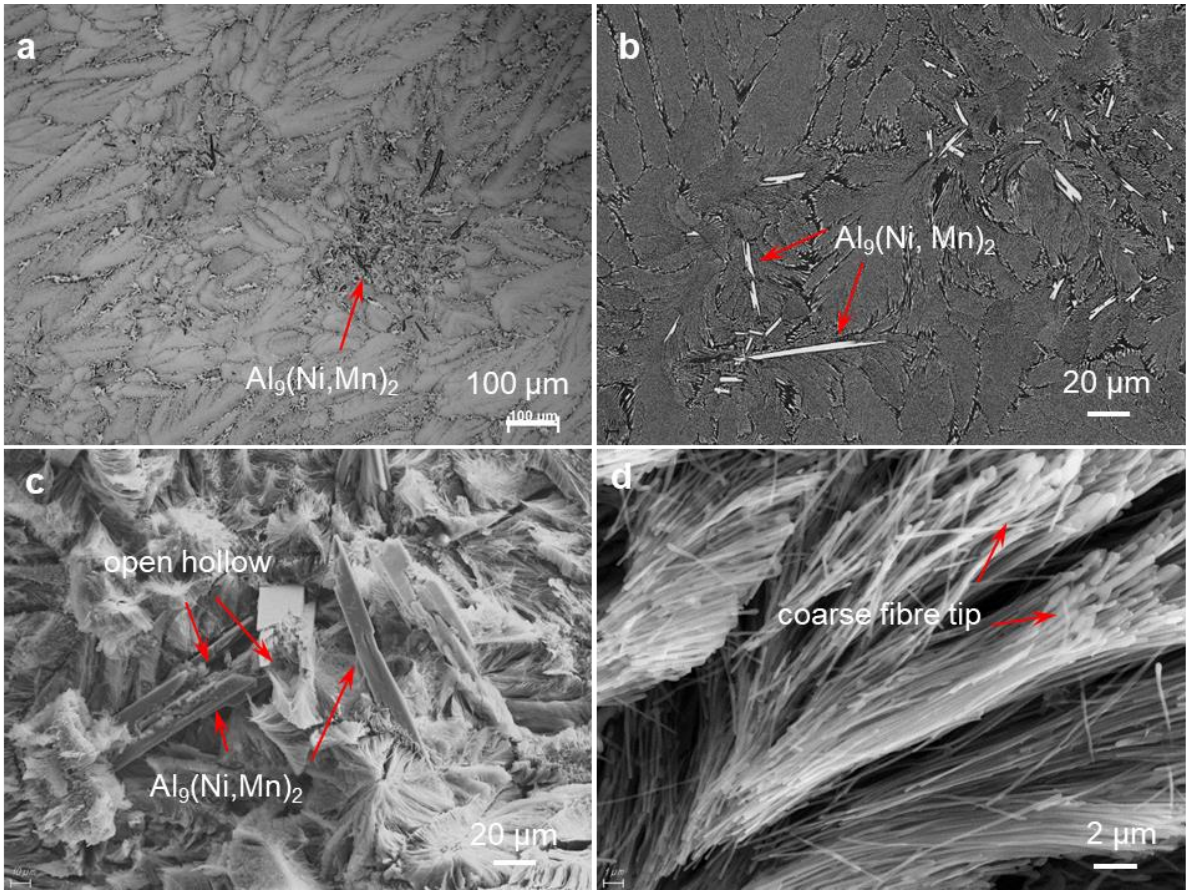

Figure 5.2 Optical image (a) and SEM images (b) showing the typical as-cast microstructure of Al-6Ni-2Mn alloy, and the morphology of the (c) primary $Al_9(Ni, Mn)_2$ phase and (d) eutectic $Al_9(Ni, Mn)_2$ phase revealed by deep etching.

With increasing Mn contents, some intermetallic phases appeared. For the Al-6Ni-3Mn alloy, in addition to the primary $Al_9(Ni, Mn)_2$ phase and eutectic α-Al+$Al_9(Ni, Mn)_2$ phases (Figure 5.3(a, b)), a small amount of intermetallic phase was observed, as shown in Figure 5.3(c, d). SEM-EDX has confirmed that this phase contains 15.6 at.% Mn and 4.8 at.% Ni, which is the κ-phase. It was first observed in the Al-4Ni-3Mn alloy in Chapter 4, which was a hexagonal prism with a hollow inside.

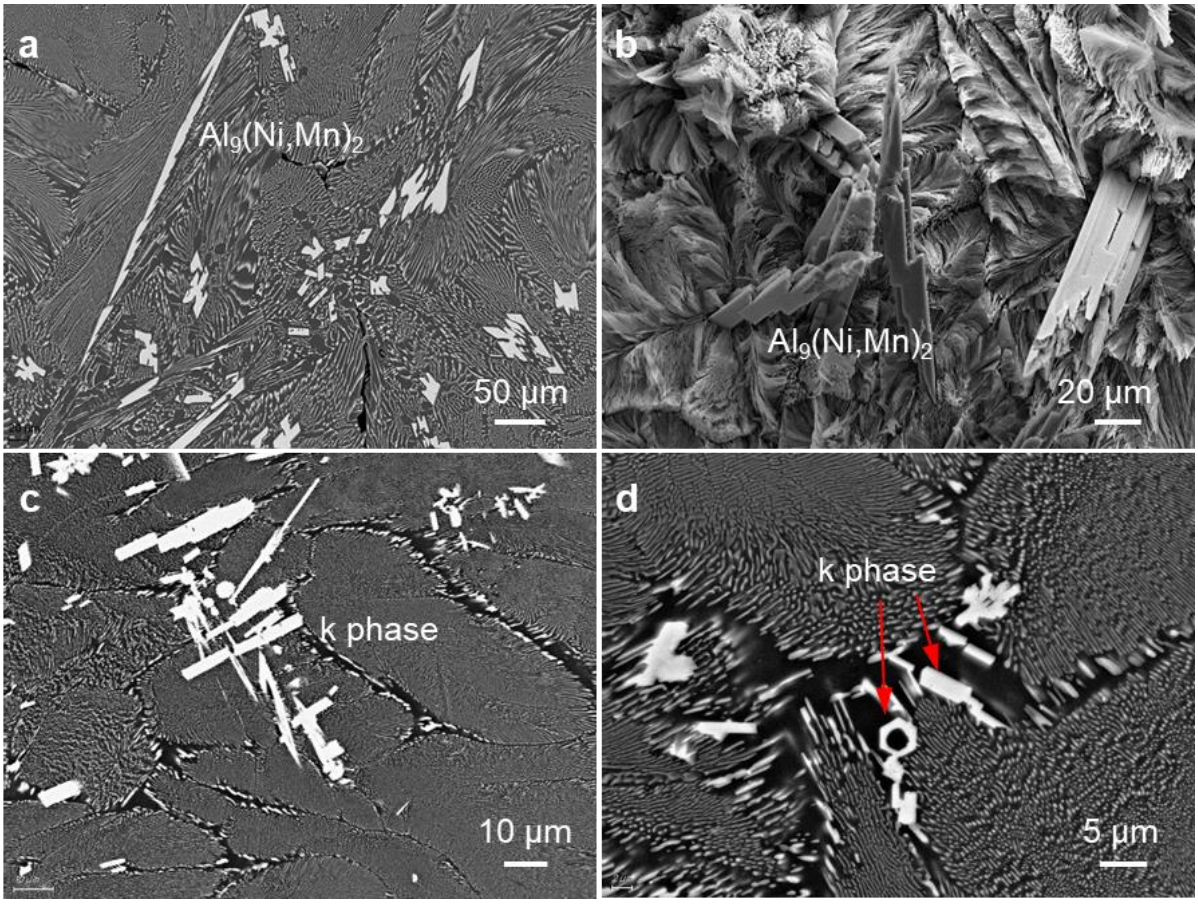

Figure 5.3 SEM images showing (a, b) the primary $Al_9(Ni, Mn)_2$ phase and its morphology and (c, d) κ-phase in as-cast Al-6Ni-3Mn alloy.

When Mn content increased to 4%, the amount of primary $Al_9(Ni, Mn)_2$ and κ-phase. increased. Figure 5.4 provides more details -of the κ-phase, displaying a more complex dendritic morphology. Branches were observed on a central spine. And the central spine in Figure 5.4d showed a hexagonal shape.

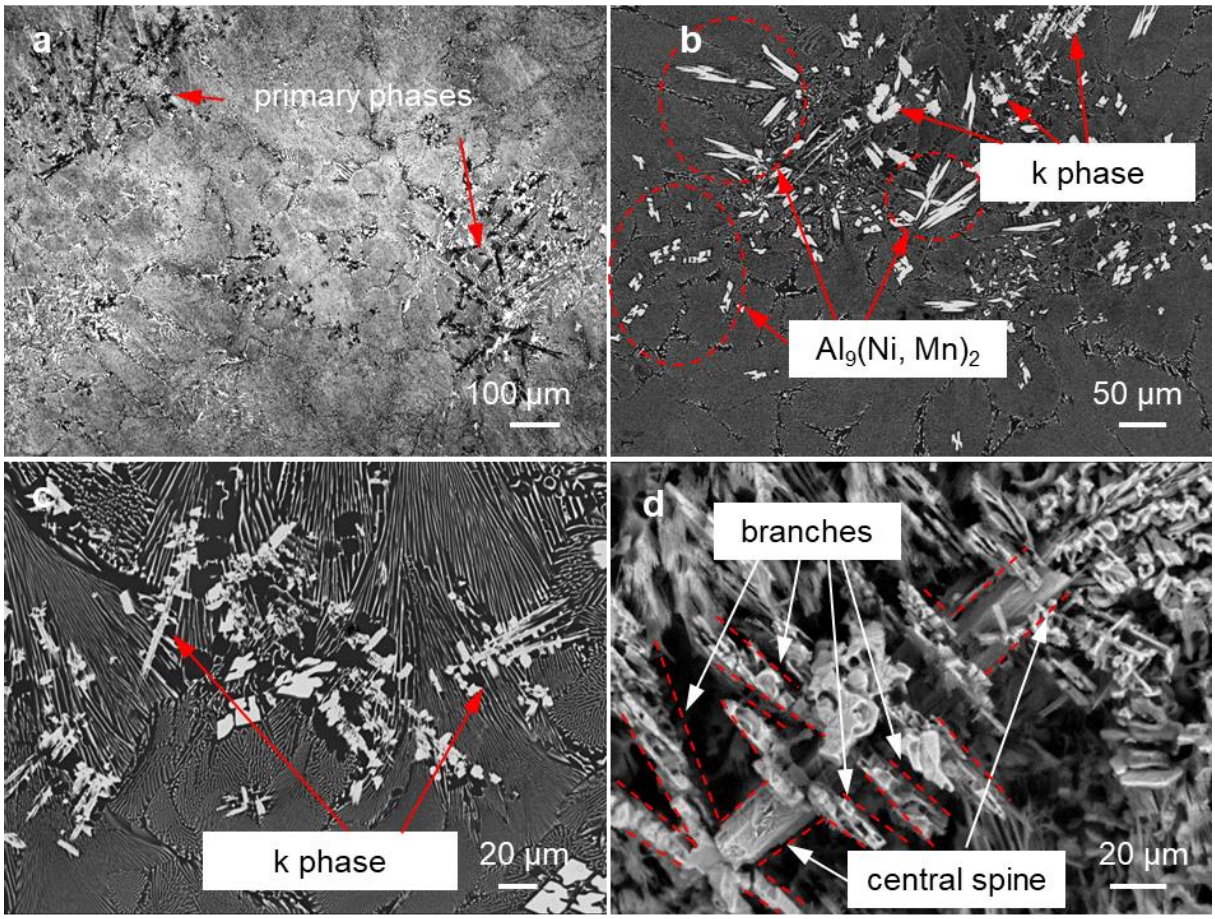

Figure 5.4 (a) Optical image showing the primary phases in the Al-6Ni-4Mn alloy, (b) SEM image showing the primary $Al_9(Ni, Mn)_2$ and κ-phase. (c, d) details of the primary κ-phase.

Microstructural evolution with increasing Mn addition to the Al-6Ni alloy was revealed. The microstructure of Al-6Ni alloy consists of eutectic α-Al+Al_3Ni phases and a very small amount of primary Al_3Ni phase. With 2% Mn addition, the eutectic structure transformed from α-Al+Al_3Ni to α-Al+$Al_9(Ni, Mn)_2$. More significantly, the primary intermetallic phase also transformed from Al_3Ni to $Al_9(Ni, Mn)_2$ phase. With increasing Mn content, the κ-phase appeared and its morphology became a more complex shape with branches.

5.3 Mechanical property of Al-6Ni-(0-4)Mn alloys

5.3.1 Hardness

Figure 5.5 shows the Vickers hardness of the as-cast Al-6Ni-(0-4)Mn alloys. The hardness displays a constant increase with increasing Mn levels. The Al-6Ni alloy presents a hardness of 59.8 HV10, while the hardness of Al-6Ni-2Mn alloy shows an increase of 20% to 71.9

HV10. With increasing the Mn level to 3% and 4%, the hardness increased to 75.9 HV10 and 88.5 HV10, respectively, showing a respective improvement of 28% and 48%, compared to the Al-6Ni alloy. These results have confirmed that the hardness of Al-6Ni-xMn alloys can be increased by increasing the Mn levels.

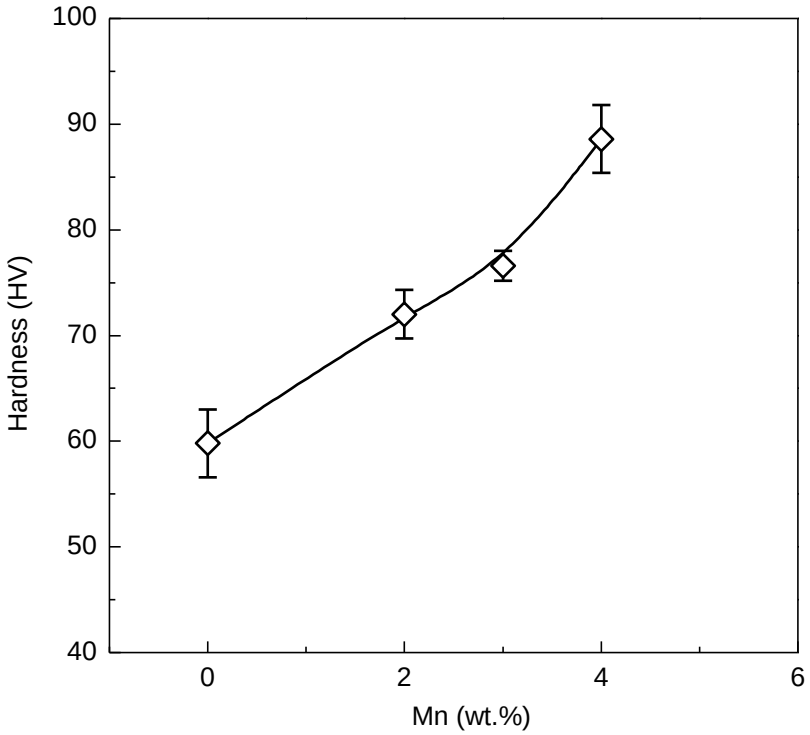

Figure 5.5 Effect of Mn contents on the Vickers hardness of the as-cast Al-6Ni alloy.

Since both the Al-6Ni and Al-6Ni-2Mn alloys are eutectic alloys and only a tiny amount of primary Al_3Ni or $Al_9(Ni, Mn)_2$ phase (<1 vol.%) displays in the microstructure, the hardness of Al-6Ni and Al-6Ni-2Mn alloys generally represent the difference between the eutectic α-Al+Al_3Ni phases and α-Al+$Al_9(Ni, Mn)_2$ phases. The Al-6Ni-2Mn alloy shows 12 HV10 higher than the Al-6Ni alloy in hardness. Therefore, the eutectic α-Al+$Al_9(Ni, Mn)_2$ phases in Al-6Ni-2Mn is stronger than the eutectic α-Al+Al_3Ni phases in Al-6Ni alloy. An improvement of tensile strength can be expected in the eutectic Al-6Ni alloy with additions of Mn element.

5.3.2 Tensile properties at ambient temperature

Figure 5.6 presents the tensile test results of Al-6Ni-(0-4)Mn alloys at ambient temperature. It is seen that both the yield strength and the UTS exhibit significant improvements with Mn addition. The yield strength of the Al-6Ni alloy was 89 MPa, while the yield strength of the Al-6Ni-2Mn was 127 MPa, which increased significantly by 43%. With increasing Mn levels to 3% and 4%, the yield strength constantly increased to 138 MPa for Al-6Ni-3Mn and 164 MPa for Al-6Ni-4Mn alloy, which presents significant improvements. Meanwhile, the UTS also shows an increase by 26% from 182 MPa for Al-6Ni alloy to 230 MPa for Al-6Ni-2 Mn alloy, and that is further increased to 256 MPa for the Al-6Ni-3Mn alloy and 248 MPa for the Al-6Ni-4Mn alloy. However, the elongation shows a dramatic decrease with the increase of Mn levels in the eutectic Al-6Ni alloy. The elongation was 8.8% for the Al-6Ni alloy, but it dropped dramatically to 3.2% for the Al-6Ni-2Mn alloy and then decreased to 2.5% for the Al-6Ni-3Mn alloy and 1.1% for the Al-6Ni-4Mn alloy.

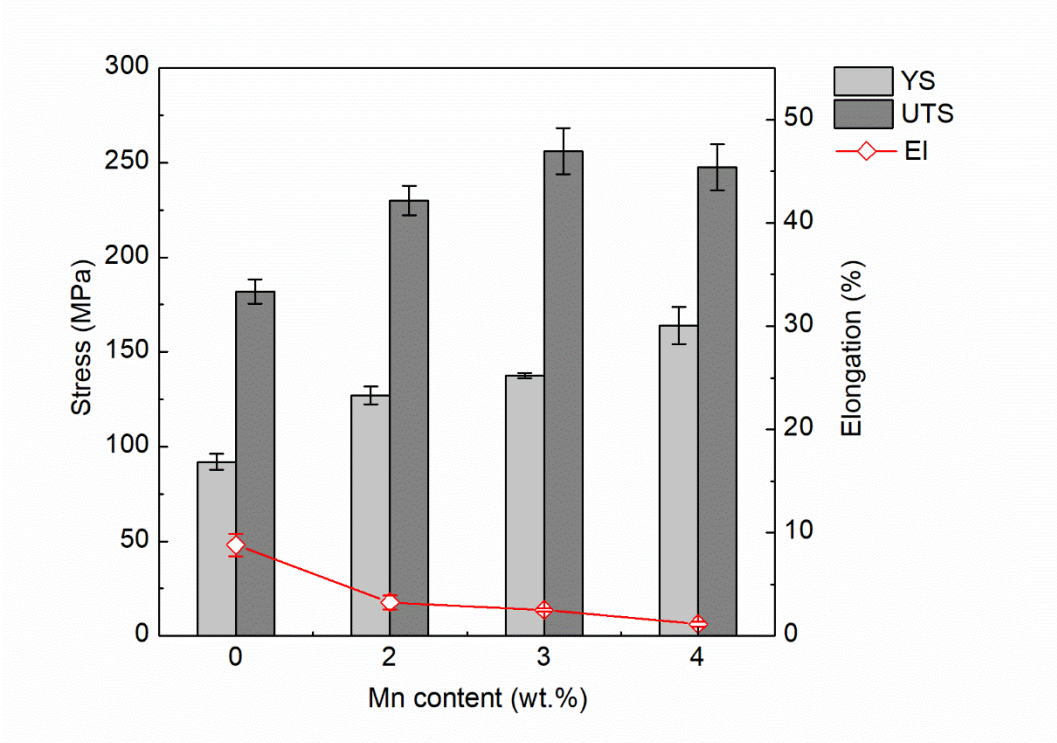

Figure 5.6 Effects of Mn contents on the tensile properties of as-cast Al-6Ni alloy at ambient temperature.

To understand the effect of Mn on the mechanical properties of the Al-6Ni alloy, the microstructural evolution with increasing Mn content was analysed. As mentioned in Chapter 4, the $Al_9(Ni, Mn)_2$ phase showed higher hardness than the Al_3Ni phase. Therefore, the transformation from α-Al+Al_3Ni phases to α-Al+$Al_9(Ni, Mn)_2$ phases with 2% Mn provide better strength. Additionally, the κ-phase appeared in the Al-6Ni-3Mn alloy, and the amount increased with increasing Mn content. The measured volume fractions of different phases in Al-6Ni-(0-4)Mn alloys are listed in Table 5.2. It can be seen that the amount of primary intermetallic phases increased with increasing Mn. The Al-6Ni alloy contained less than 0.5% primary Al_3Ni phase, while the Al-6Ni-2Mn alloy contained 1% primary $Al_9(Ni, Mn)_2$. When Mn content increased to 3% and 4%, the amount of κ-phase increased. The total amount of primary intermetallic phases constantly increased from less than 0.5% for the Al-6Ni alloy to 4% for the Al-6Ni-4Mn alloy. The increased amount of primary intermetallic phases improved strength and decreased elongation.

Table 5.2 The volume fraction of different phases in Al-6Ni-(0-4)Mn alloys

Alloy	Volume Fraction		
	Eutectic Phases	$Al_9(Ni, Mn)_2$	κ-phase
Al-6Ni	99.5%	<0.5%	0
Al-6Ni-2Mn	99%	1%	0
Al-6Ni-3Mn	98%	1%	1%
Al-6Ni-4Mn	95%	2%	3%

5.3.3 Tensile properties at 250 °C

Figure 5.7 shows the tensile results of the Al-6Ni-(0-4)Mn alloys tested at 250 °C. It is seen that Mn addition improved the yield strength and UTS of Al-6Ni alloy at 250 °C. The Al-6Ni alloy presented yield strength of 40 MPa, while the Al-6Ni-2Mn alloy showed a yield

strength of 106 MPa, which was a significant increase of 165%. The yield strength experienced further increases in the Al-6Ni-3Mn and Al-6Ni-4Mn alloys, reaching 116 MPa and 134 MPa, respectively. Meanwhile, the UTS also increased by 146%, from 58 MPa for the Al-6Ni alloy to 138 MPa for the Al-6Ni-2Mn alloy. It then increased to 176 MPa for the Al-6Ni-3Mn and 164 MPa for the Al-6Ni-4Mn alloy.

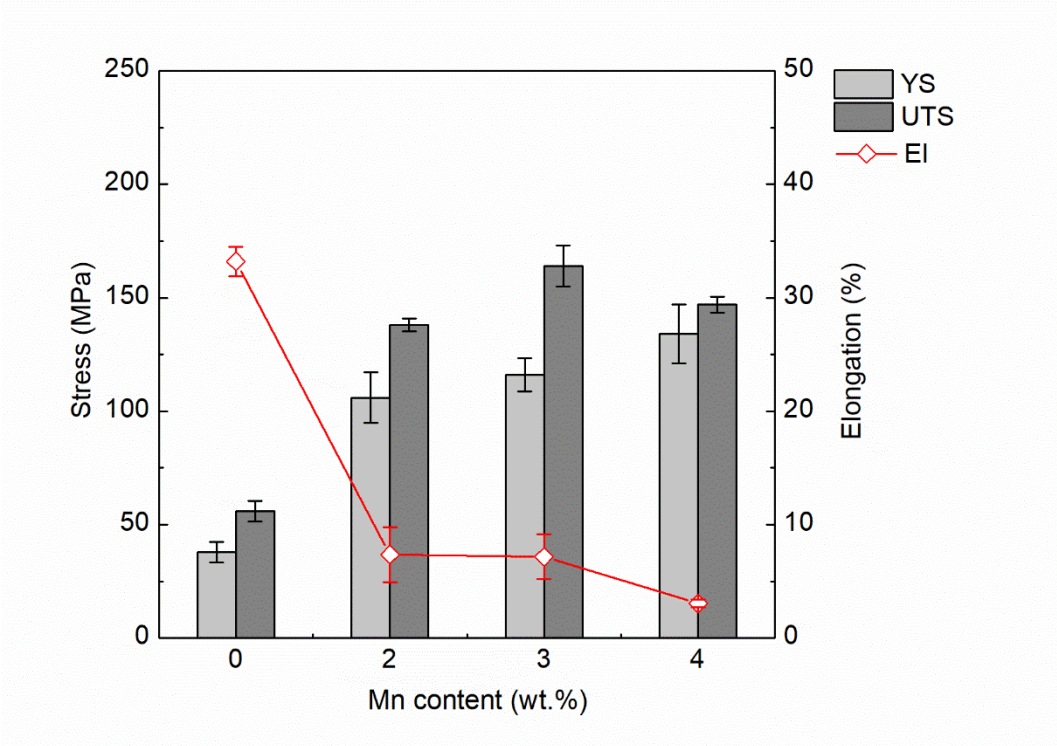

Figure 5.7 Effect of Mn contents on the tensile properties of as-cast Al-6Ni alloy at 250 °C.

Table 5.3 demonstrates the effect of Mn on strength loss of the Al-6Ni alloy at 250 °C. It shows clearly that alloys with Mn addition experienced much less strength loss. The Al-6Ni alloy displayed 59% yield strength loss and 69% UTS loss at 250 °C. The Al-6Ni-2Mn alloy, however, displayed 17% yield strength loss and 40% UTS loss, which were significantly decreased. The Al-6Ni-3Mn and Al-6Ni-4Mn alloys showed similar strength loss with the Al-6Ni-2Mn alloy. Therefore, Mn addition improved softening resistance at 250 °C.

The Al-6Ni and Al-6Ni-2Mn alloys only contain a tiny amount of primary Al_3Ni or $Al_9(Ni, Mn)_2$ phase (<1 vol.%). Hence, the difference of strength loss between the Al-6Ni and Al-6Ni-2Mn alloys at 250 °C reflects the softening resistance of the eutectic α-Al+Al_3Ni

structure and the α-Al+$Al_9(Ni, Mn)_2$ structure. It was confirmed in Chapter 4 that the eutectic α-Al+$Al_9(Ni, Mn)_2$ structure displayed better softening resistance than the α-Al+Al_3Ni structure. Therefore, Mn addition transformed the eutectic structure in Al-6Ni alloy from α-Al+Al_3Ni to α-Al+$Al_9(Ni, Mn)_2$ and consequently improved heat resistance at elevated temperatures. Based on this, alloys with Mn addition are capable of retaining higher strength at 250 °C.

Table 5.3 The strength loss of the Al-6Ni-xMn alloys at 250 °C.

Alloy	Strength Loss	
	Yield Strength	Ultimate Tensile Strength
Al-6Ni	59%	69%
Al-6Ni-2Mn	17%	40%
Al-6Ni-3Mn	16%	36%
Al-6Ni-4Mn	18%	41%

The Al-6Ni-4Mn alloy displayed a yield strength of 164 MPa, UTS of 248 MPa at ambient temperature and yield strength of 134 MPa, UTS of 176 MPa at 250 °C. The tensile strength was promising and competitive. Moreover, the $Al_9(Ni, Mn)_2$ phase presented superior softening resistance. The newly developed Al-Cu-Mn-Zr alloys mentioned in Chapter 2, such as RR350 and ACMZ01 alloys, provide about 170 to 200 MPa at ambient temperature and 100 MPa at 300 °C. These alloys retained less than 60% yield strength at 300 °C. While the Al-6Ni-4Mn alloy retained 82% yield strength at 250 °C. Therefore, the Al-6Ni-4Mn alloy showed comparable tensile strength and superior softening resistance, which demonstrated the potential for application at elevated temperatures.

5.4 Microstructure of as-cast Al-8Ni-(0-4)Mn alloys

The compositions of the experimental alloys obtained by optical emission spectrometry (OES) are listed in Table 5.4. It shows that actual composition is very close to designed

nominal compositions, and the levels of impurity elements such as Si and Fe are controlled at very low.

Table 5.4 The compositions of Al-8Ni-(0-4)Mn alloys measured by OES.

Alloy	Composition (wt.%)						
	Al	Ni	Mn	Fe	Si	Ti	Zr
Al-8Ni	Bal.	8.08	0.01	0.12	0.20	0.01	0.01
Al-8Ni-2Mn	Bal.	8.01	2.01	0.15	0.18	0.01	0.01
Al-8Ni-3Mn	Bal.	8.01	3.15	0.18	0.21	0.01	0.02
Al-8Ni-4Mn	Bal.	8.00	3.99	0.2	0.23	0.01	0.02

Typical microstructures of the Al-8Ni alloy are shown in Figure 5.8. It consists of eutectic phases and the primary Al_3Ni phase. The primary Al_3Ni varied in size and shape. It showed a size range from 2 μm to 100 μm. The large sized primary Al_3Ni phase shows faceted surfaces while the very small Al_3Ni phase shows non-faceted surfaces. Besides, the α-Al cores were observed inside the primary Al_3Ni phase, as indicated with arrows in Figure 5.8b.

Figure 5.9a reveals the morphology of the primary Al_3Ni phase after deep etching. The elongated particles presented. The hollows were observed. Some were open hollows, and some e hollows were inside the primary Al_3Ni phase. The deeply etched image in Figure 5.9b reveals rod-like shape eutectic Al_3Ni phase, which is the same as in Al-6Ni alloy while different from the net-shape structure in Al-4Ni alloy.

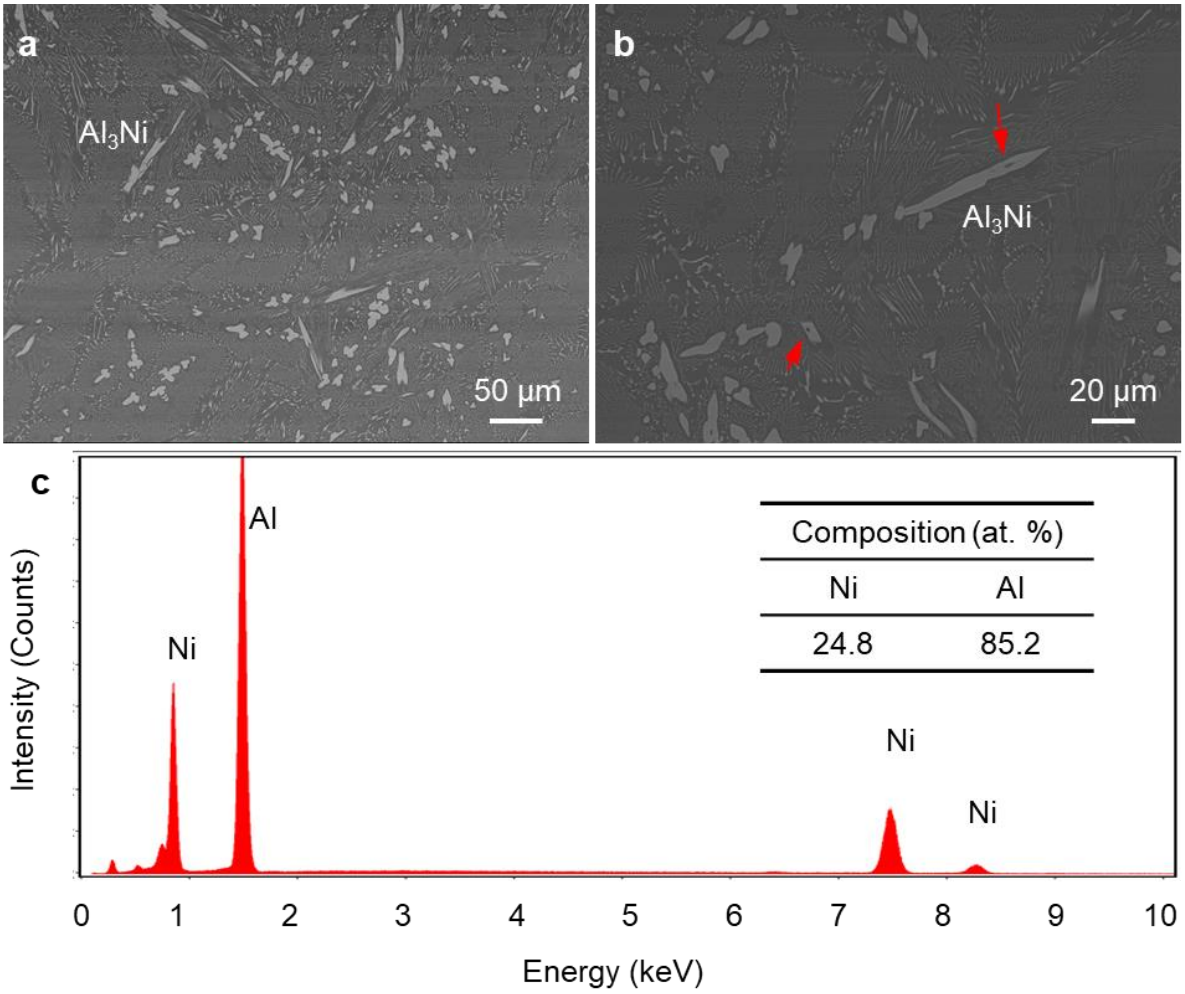

Figure 5.8 SEM images showing (a) the typical as-cast microstructure of Al-8Ni alloy and (b) primary Al_3Ni phase. (c) composition of Al_3Ni obtained by EDX.

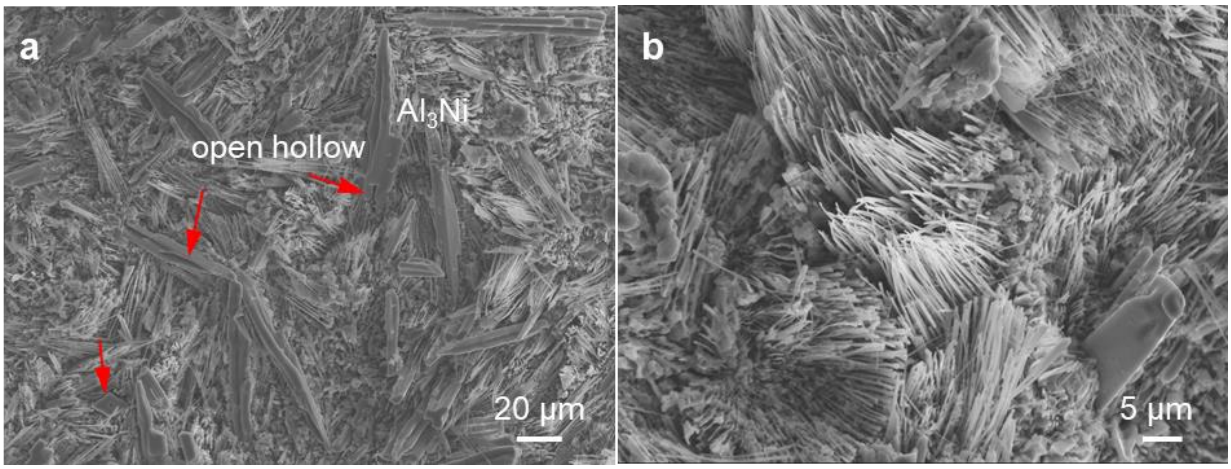

Figure 5.9 Morphologies of (a) primary Al_3Ni phase and (b) eutectic structure in Al-8Ni alloy revealed by deep etching.

Typical microstructures of the Al-8Ni-2Mn alloy are shown in Figure 5.10a. It consists of eutectic phases and large primary phases. EPMA results confirmed that this primary phase contains 14.4 at.% Ni and 3.7 at.% Mn, which corresponds to $Al_9(Ni, Mn)_2$. Hence, in the Al-8Ni-2Mn alloy, the primary phase is $Al_9(Ni, Mn)_2$ rather than the Al_3Ni phase. The deeply etched image in Figure 5.10b reveals that the primary $Al_9(Ni, Mn)_2$ phase is dendritic morphology and has a size of several hundred micrometres. The morphology shows central spine, secondary dendrites and ternary dendrites.

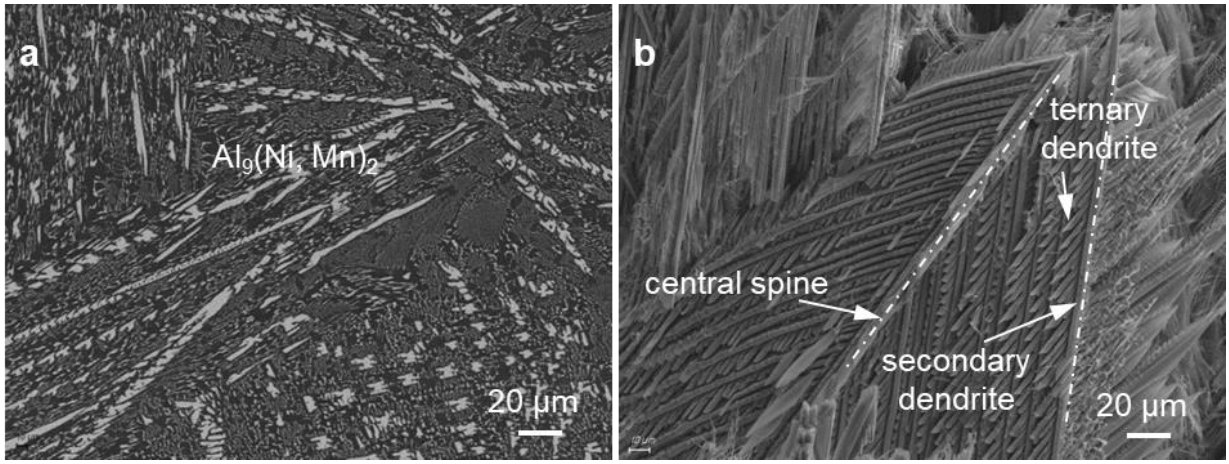

Figure 5.10 SEM images showing (a) the typical as-cast microstructure of Al-8Ni-2Mn alloy and (b) dendritic primary $Al_9(Ni, Mn)_2$ phase.

With increasing Mn content, the morphology of the primary $Al_9(Ni, Mn)_2$ phase changed in Al-8Ni-3Mn alloy. As shown in 5.11a, faceted surfaces were observed. Deep etched images in Figure 5.11(b, c) reveal a clear dendritic morphology. Moreover, faceted surfaces were observed both on the central spine and secondary dendrites. The cross-section of secondary dendrites in Figure 5.11d shows parallel surfaces. The size of the primary $Al_9(Ni, Mn)_2$ phase reached several millimetres.

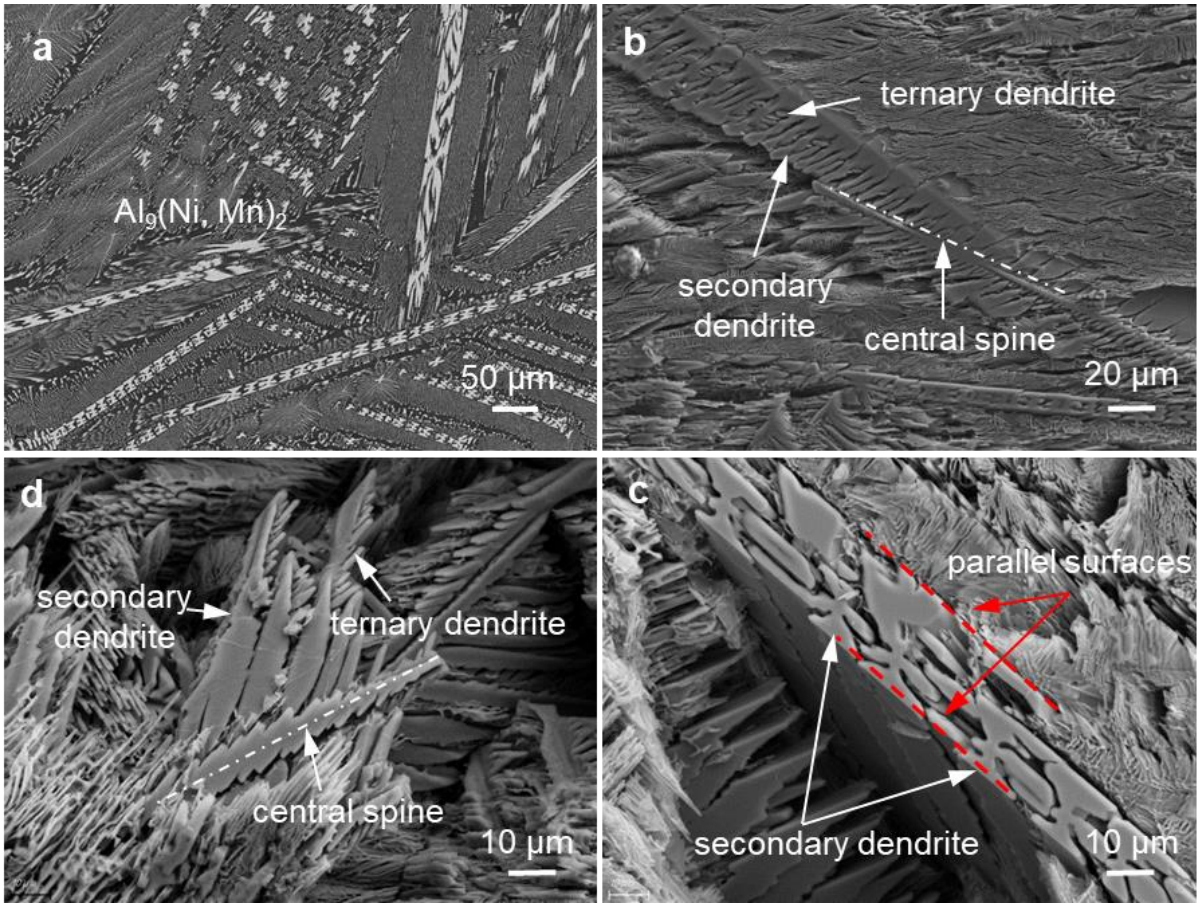

Figure 5.11 SEM images showing (a) the typical as-cast microstructure of Al-8Ni-3Mn alloy and (b, c, d) morphology details of dendritic primary $Al_9(Ni, Mn)_2$ phase.

Figure 5.12 displays the typical microstructure of as-cast Al-8Ni-4Mn alloy. In addition to the dendritic primary $Al_9(Ni, Mn)_2$ phase and eutectic phases, a small amount of acicular phase was observed. The details of this acicular phase are shown in Figure 5.12(c, d). SEM-EDX result showed that this phase contained 12.6 at.% Mn and 8.0 at.% Ni, which was identified as O-phase according to the information given in Chapter 4.

Microstructural evolution with increasing Mn addition to hyper-eutectic Al-8Ni alloy was revealed above. The eutectic structure transformed from α-Al+Al_3Ni to α-Al+$Al_9(Ni, Mn)_2$ with 2% Mn. Moreover, the primary Al_3Ni phase also transformed to $Al_9(Ni, Mn)_2$ phase. The size of primary Al_3Ni phase was about 100 μm while the primary $Al_9(Ni, Mn)_2$ phase reached several millimetres. When Mn content increased to 4%, a small amount of acicular O-phase was observed.

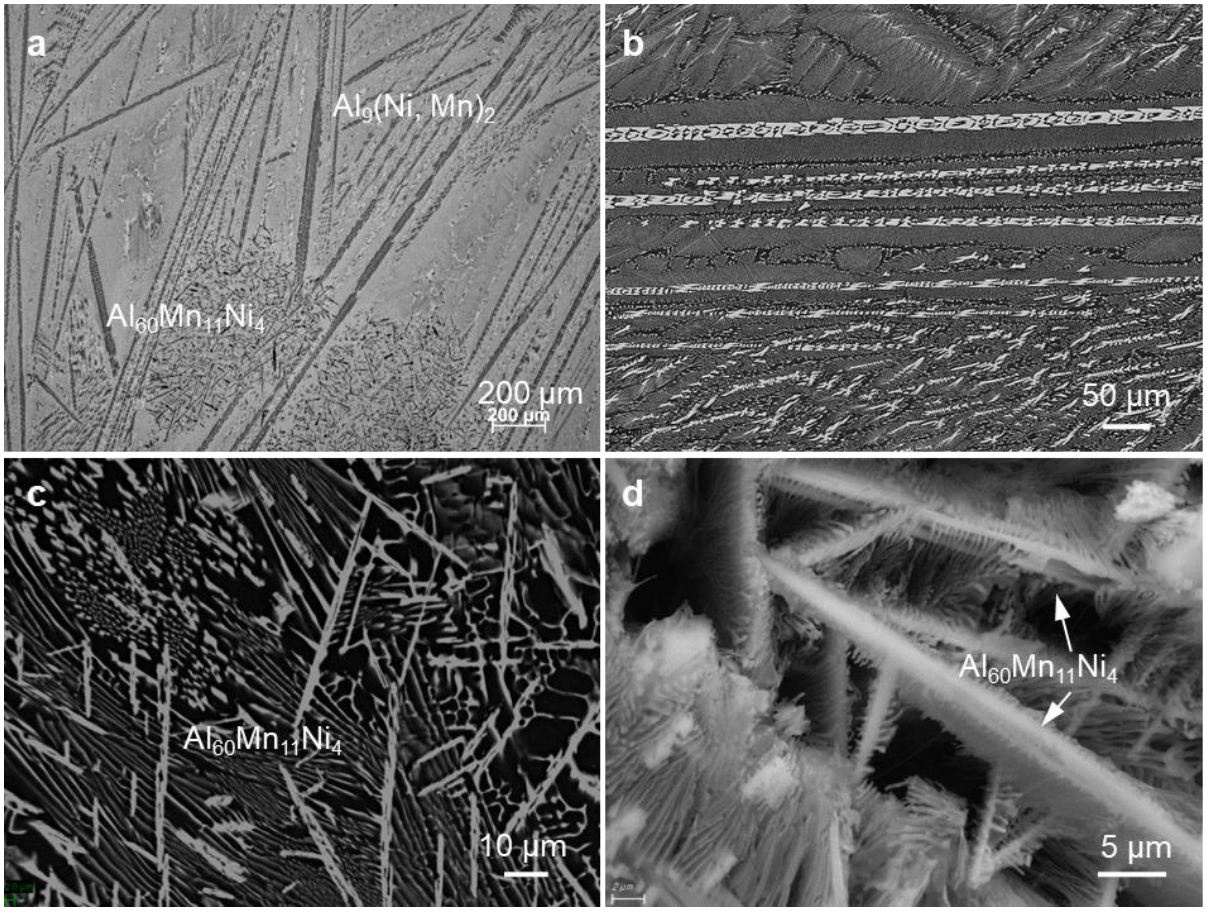

Figure 5.12 (a) Optical image showing the typical as-cast microstructure of Al-8Ni-4Mn alloy, (b) SEM image showing dendritic primary $Al_9(Ni, Mn)_2$ phase, (c) the acicular O-phase and (d) morphology revealed by deep etching.

5.5 Mechanical property of Al-8Ni-(0-4)Mn alloys

5.5.1 Hardness

Figure 5.13 shows the Vickers hardness of as-cast Al-8Ni-(0-4)Mn alloys. The hardness increased with increasing Mn level. The Al-8Ni alloy presented a hardness of 65.0 HV10, while the Al-8Ni-2Mn alloy showed an increase to 70.3 HV10. With increasing the Mn level to 3%, the hardness increased to 85.5 HV10. The Al-8Ni-4Mn alloy displayed a hardness of 82.7 HV10. These results confirmed that the hardness of Al-8Ni-xMn alloys can be increased by increasing the Mn levels, and 3% Mn achieved the maximum hardness.

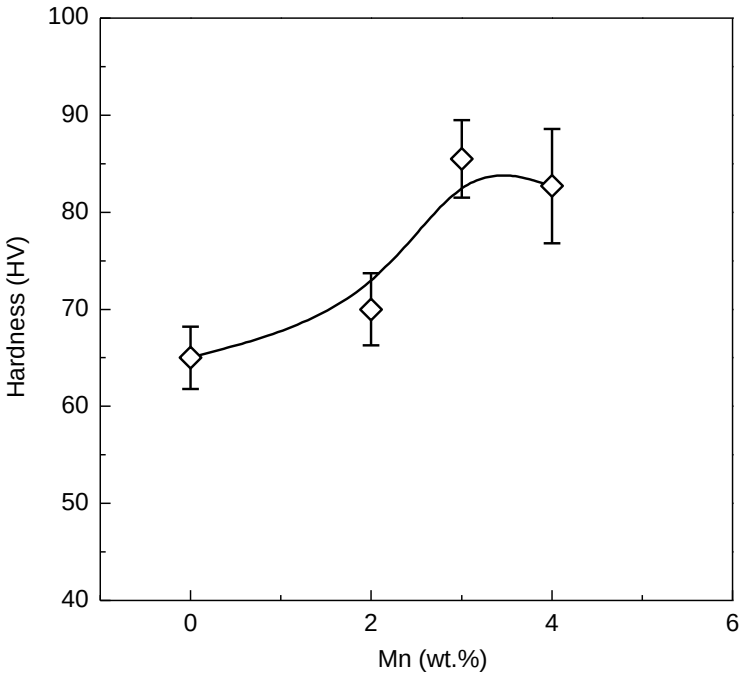

Figure 5.13 Effect of Mn contents on the Vickers hardness of the as-cast Al-8NiMn alloy.

5.5.2 Tensile properties at ambient temperature

Figure 5.14 presents the tensile results of Al-8Ni-(0-4)Mn alloys at ambient temperature. It is seen that the yield strength exhibited significant improvements with Mn addition increasing to 3%. The yield strength of the Al-8Ni alloy was 72 MPa, while that of the Al-8Ni-2Mn and Al-8Ni-3Mn alloys were 114 and 134 MPa, respectively, which presented a significant improvement. With 4% Mn addition, the yield strength slightly decreased to 103 MPa.

The UTS, however, showed a significant decrease with increasing Mn addition. The Al-8Ni alloy displayed UTS of 189 MPa. It was then further decreased to 159 MPa for the Al-8Ni-2Mn alloy, 147 MPa for the Al-8Ni-3Mn alloy and 126 MPa for the Al-8Ni-4Mn alloy. The elongation also showed a dramatic decrease with increasing Mn. The elongation was 8% for the Al-8Ni alloy, while it was less than 1% for the Al-8Ni-2Mn, Al-8Ni-3Mn, and Al-8Ni-4Mn alloys.

The increase of yield strength is mainly associate with the eutectic transformation from α-Al+Al_3Ni to α-Al+$Al_9(Ni, Mn)_2$ and the appearance of O-phase. Moreover, the decrease of

UTS with increasing Mn is because the huge size primary $Al_9(Ni, Mn)_2$ phase, which reached several millimetres. For this type of tough and large size intermetallic phase, the localized stress increases quickly and accelerates fracture of material. Therefore, the UTS decreased with increasing Mn content. Similarly, alloys with Mn addition present extremely low elongations because of the huge size primary $Al_9(Ni, Mn)_2$ phase.

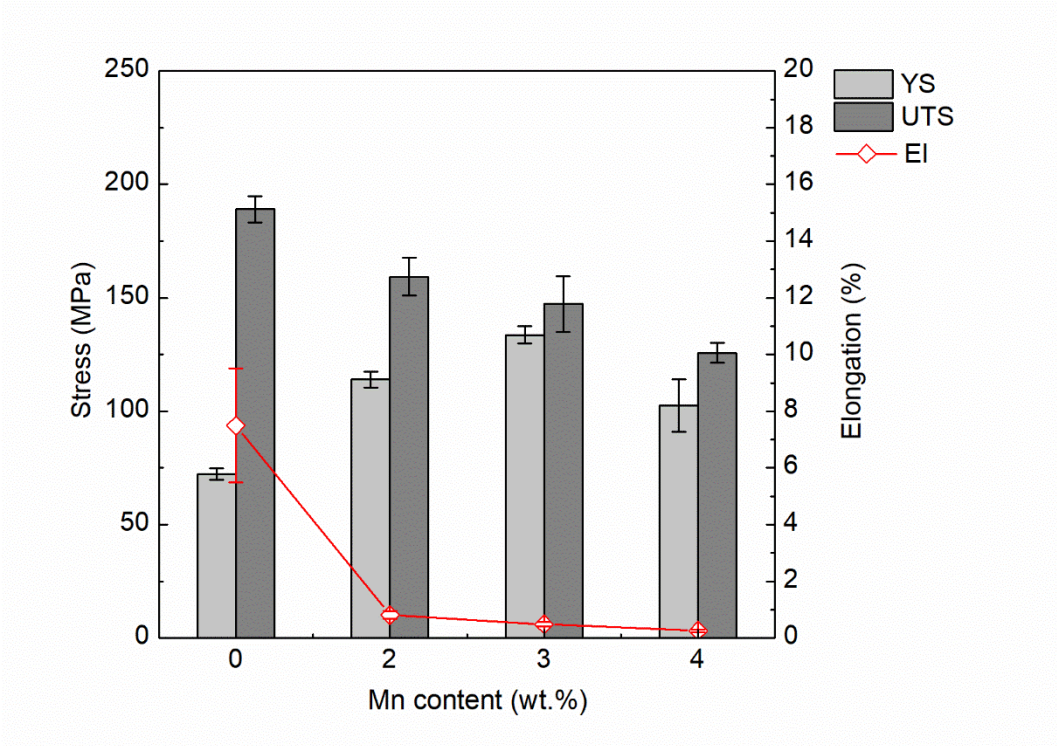

Figure 5.14 Effect of Mn contents on the tensile properties of as-cast Al-8Ni alloy at ambient temperature.

5.5.3 Tensile properties at 250 °C

Figure 5.15 shows the tensile results at 250 °C. It is seen that Mn addition improved both the yield strength and the UTS of Al-8Ni-(0-4)Mn alloys. The Al-8Ni alloy presented a yield strength of 47 MPa, while the Al-8Ni-2Mn alloy showed a yield strength of 106 MPa, which was an increase of 126%. The yield strength then increased to 112 MPa with 3% Mn. When Mn content reached 4%, however, the yield strength decreased to 103 MPa. Moreover, the UTS also increased by 69%, from 71 MPa to 120 MPa with 2% Mn. It then increased to 130 MPa with 3% Mn and decreased slightly to 125 MPa with 4% Mn. The Al-

8Ni alloy showed elongation of 7.5% at 250 °C, while alloys with Mn addition showed extremely low elongation (<1%).

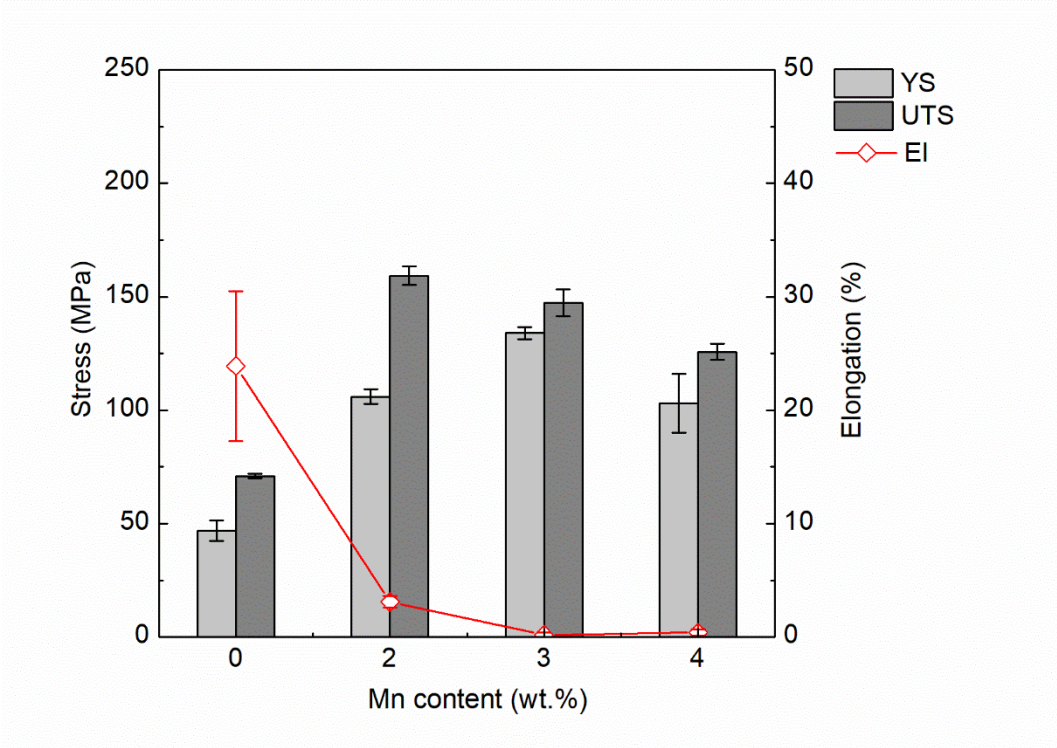

Figure 5.15 Effect of Mn contents on the tensile properties of as-cast Al-8Ni alloy at 250 °C.

Notably, the Al-8Ni-xMn alloys presents lower tensile strength and elongations than the Al-6Ni-xMn alloys. It mainly because of the huge size primary $Al_9(Ni, Mn)_2$ phase. The extremely low levels of elongation of the Al-8Ni-xMn alloys are not acceptable for application.

5.6 Summary

In this chapter, the effect of Mn on the microstructure and the mechanical properties of the Al-6Ni and Al-8Ni alloys were investigated. Microstructures were characterized using SEM. Tensile strength was tested at ambient temperature and 250 °C.

Mn additions transformed the eutectic structure from α-Al+Al_3Ni to α-Al+$Al_9(Ni, Mn)_2$ in both Al-6Ni alloy and Al-8Ni alloy. More significantly, the primary Al_3Ni phase was also transformed to primary $Al_9(Ni, Mn)_2$ phase in both Al-6Ni and Al-8Ni alloys with the

addition of 2% Mn. When Mn content increased to 3% and 4%, κ-phase appeared and the amount increased with Mn additions.

Mn increased tensile strength of Al-6Ni and Al-8Ni alloys at both ambient temperature and 250 °C. Especially, the Al-6Ni-xMn alloys presented a higher strength than Al-8Ni-xMn and Al-4Ni-xMn alloys. Moreover, the elongations of Al-8Ni-xMn alloys were very low (<1%), which is not satisfied in industrial applications. The best strength of experimental Al-Ni-Mn alloys was achieved by the Al-6Ni-4Mn alloy. It offered the yield strength of 164 MPa, UTS of 248 MPa at ambient temperature and the yield strength of 134 MPa, UTS of 176 MPa at 250 °C. The tensile strength of the Al-6Ni-4Mn alloy was promising and competitive. Moreover, the $Al_9(Ni, Mn)_2$ phase presented a superior softening resistance. The newly developed Al-Cu-Mn-Zr alloys mentioned in Chapter 2, such as RR350 and ACMZ01 alloys, provided about 170 to 200 MPa at ambient temperature and 100 MPa at 300 °C. These alloys retained less than 60% of the yield strength at 300 °C. While the Al-6Ni-4Mn alloy retained 82% of the yield strength at 250 °C. Therefore, the Al-6Ni-4Mn alloy showed comparable tensile strength and superior softening resistance, which demonstrated the potential of Al-Ni-Mn alloys for elevated temperature applications.

Chapter 6: The Effect of Cooling Rates on Microstructure of Al-Ni-Mn alloys

6.1 Introduction

In Chapter 4, it was confirmed that the eutectic intermetallic phase in Al-Ni-Mn alloys was $Al_9(Ni, Mn)_2$ rather than Al_3Ni phase. Moreover, the primary phase in hypereutectic Al-Ni alloy also transformed from Al_3Ni into $Al_9(Ni, Mn)_2$ phase with Mn additions. However, no $Al_9(Ni, Mn)_2$ phase is found in the equilibrium Al-Ni-Mn phase diagram. Therefore, the actual solidified microstructure differed from the equilibrium microstructure. This difference is due to the high cooling rates during actual solidification. Normally, the cooling rates can be affected by several factors, such as mould material, mould temperature and pouring temperature. In this chapter, the microstructural evolution under different cooling rates, which are controlled accurately by DSC machine, is studied for the first time and the phase transformation mechanism is discussed. Moreover, the effect of different pouring temperatures on microstructural evolution is studied.

6.2 The equilibrium solidification of Al-Ni-Mn alloy

The Al-4Ni-2Mn alloy was chosen because its microstructure typically consists of primary α-Al and eutectic phases; no other intermetallic phases exist. The effect of cooling rates on the formation of eutectic phases will be more clear to observe. The equilibrium solidification (Lever Rule) path of the Al-4Ni-2Mn alloy is calculated by Pandat (Figure 6.1a). The solidification begins with the formation of primary Al_6Mn at 659 °C. Then $Al \rightarrow \alpha\text{-}Al + Al_6Mn$ eutectic reaction occurs when the temperature drops to 647 °C. The last eutectic reaction, $Al \rightarrow \alpha\text{-}Al + Al_6Mn + Al_3Ni$, occurs at 645 °C. The equilibrium solidification process of Al-4Ni-2Mn alloy ends at this temperature. Non-equilibrium solidification (Scheil model) calculation by Pandat presents the same solidification path as equilibrium

solidification (not shown here) because there are no sufficient experimental data to support non-equilibrium simulation.

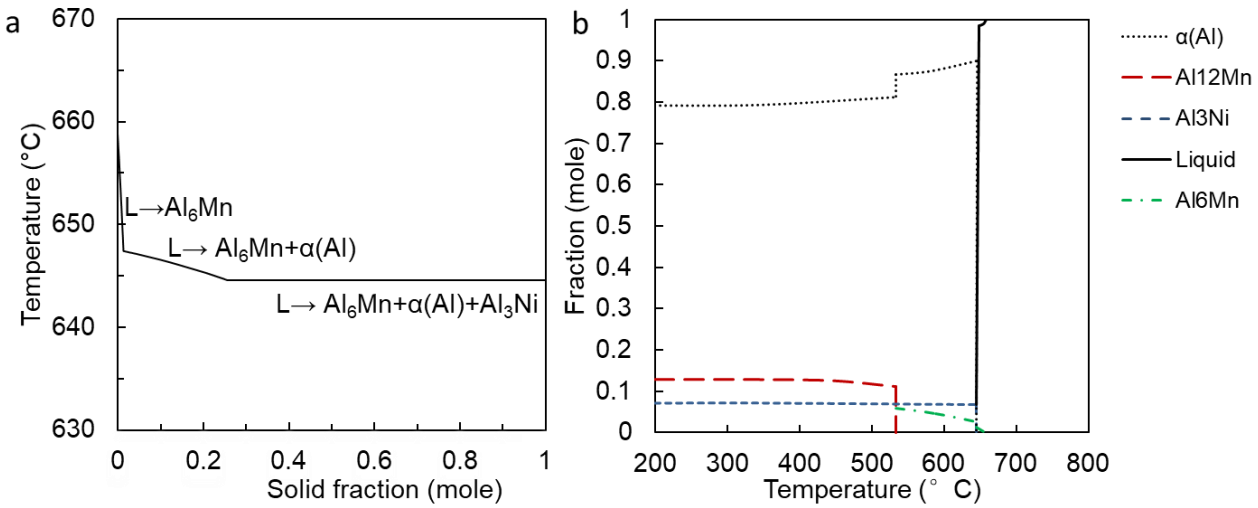

Figure 6.1 Thermodynamic calculation of Al-4Ni-2Mn alloy by Pandat (a) equilibrium solidification sequences. (b) calculated mole fractions of phases as a function of temperature.

Figure 6.1b presents the calculated mole fractions of equilibrium phases in the Al-4Ni-2Mn alloy as a function of temperature. The solidified microstructure is predicted to consist of the primary Al_6Mn intermetallic phase, α-Al+Al_6Mn eutectic phases and eutectic α-Al+Al_3Ni+Al_6Mn phases and the $Al_{12}Mn$ phase. The $Al_{12}Mn$ phase is predicted to form by the solid transformation reaction: α-Al + Al_6Mn → $Al_{12}Mn$ at 533.4 °C. All the reactions are listed in Table 6.1. In summary, equilibrium solidification calculations indicate the existence of Al_6Mn, $Al_{12}Mn$, α-Al and Al_3Ni phases in the Al-4Ni-2Mn alloy.

However, the as-cast microstructure of Al-4Ni-2Mn alloy in Chapter 4 demonstrates existence of α-Al and $Al_9(Ni, Mn)_2$ phases; the Al_3Ni, Al_6Mn and $Al_{12}Mn$ phases were not observed. The difference is due to the high cooling rates during actual solidification process. Hence a series of cooling rates from 20 K/min to 0.2 K/min controlled by DSC machine were set to investigate the phase formation.

Table 6.1 Equilibrium reactions and corresponding temperatures of the Al-4Ni-2Mn alloy.

Reaction	Temperature (°C)
$L \rightarrow Al_6Mn$	658.7 ~ 647.4 °C
$L \rightarrow \alpha\text{-}Al + Al_6Mn$	647.3 ~ 644.6 °C
$L \rightarrow \alpha\text{-}Al + Al_6Mn + Al_3Ni$	644.6 °C
$Al_6Mn + \alpha\text{-}Al \rightarrow Al_{12}Mn$	533.4 °C

6.3 Microstructures of Al-4Ni-2Mn alloy under different cooling rates

6.3.1 The DSC curves

The Al-4Ni-2Mn alloy was heated to 850 °C at a heating rate of 5 °C/min and the DSC heating curve is plotted in Figure 6.2. The solidus (T_{SOL}) is usually determined by the onset temperature on the heating curves. Closer observation of the peak area demonstrates that there are two peaks overlapping. Considering that the microstructure of Al-4Ni-2Mn consists of primary α-Al phase and eutectic phases, the peak at lower temperature indicates the eutectic temperature (T_{EU}) while the peak at higher temperature indicates liquidus (T_{LIQ}). For the Al-4Ni-2Mn alloy, the first peak was at 636.5 °C and the last peak was at 653.5 °C. Therefore, the liquidus and solidus were obtained.

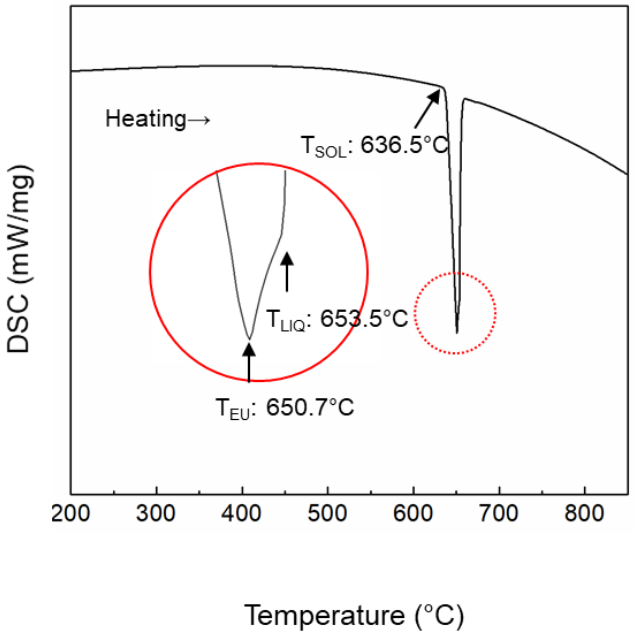

Figure 6.2 DSC heating curve of the Al-4Ni-2Mn alloy at 5 °C/min.

To investigate the effect of cooling rates on microstructure, samples were heated to 750 °C and then cooled at controlled cooling rates between 20 K/min and 0.2 K/min. Figure 6.3 displays the DSC curves with decreasing the cooling rates. On the cooling curves, the onset temperature is determined as the liquidus temperature (T_{LIQ}), which is also the start temperature for the formation of the primary phase (T_P). The peak at the lowest temperature represents the solidus temperature (T_{SOL}).

Two main peaks were observed. The first peak appeared at higher temperature indicates the formation of primary α-Al phase (T_{AL}) while the second peak indicates the eutectic temperature (T_{EU}). As expected, both T_{AL} and T_{EU} were shifted toward higher temperatures with decreasing the cooling rates. The T_{AL} increased from 629.5 °C to 639.4 °C and the T_{EU} increased from 618.7 °C to 634.8 °C, when cooling rates decreased from 20 K/min to 0.2 K/min.

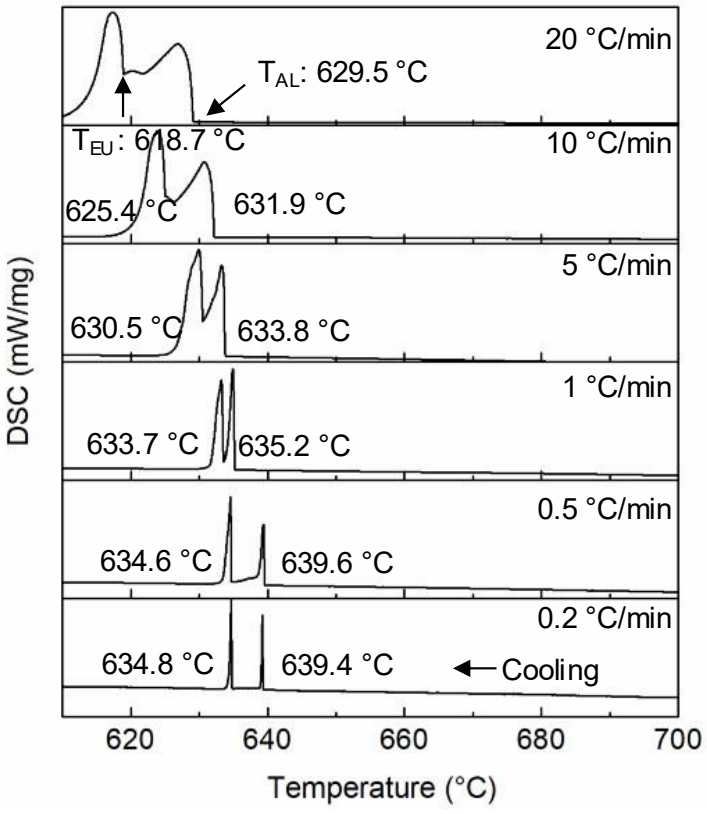

Figure 6.3 DSC curves of the Al-4Ni-2Mn alloy with different cooling rates.

6.3.2 Microstructure solidified under cooling rates between 10-20 K/min

Figure 6.4 presents the microstructures of the Al-4Ni-2Mn alloy solidified at 20 K/. It consists of the primary α-Al phase and two eutectic intermetallic phases. One is the fine eutectic $Al_9(Ni, Mn)_2$ phase. The other phase has an average composition of Al-4.5Ni-15.7Mn (at.%) (Figure 6.5). It is very close to the formula of O-phase ($Al_{60}Mn_{11}Ni_4$). Figure 6.6 displays the diffraction patterns of this phase. They were indexed as zone axis [101] and [312] of the Orthorhombic O-phase. Therefore, the other eutectic phase was confirmed to be the O-phase. The eutectic structure is α-Al+$Al_9(Ni, Mn)_2$+O-phase under a cooling rate of

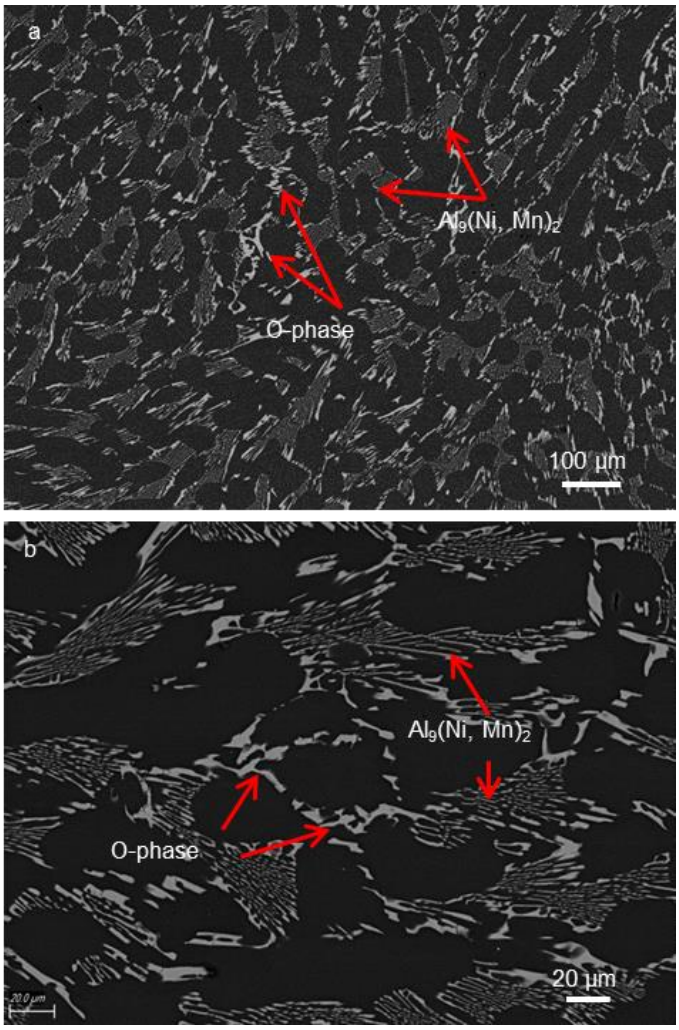

Figure 6.4 Backscattered SEM micrographs for the samples cooled at 20 K/min. (a) the eutectic O-phase and $Al_9(Ni, Mn)_2$ phase, (b) high magnification microstructure.

20 K/min. However, as described in Chapter 4, the eutectic structure is α-Al+$Al_9(Ni, Mn)_2$ after PMC (cooling rate between 4~7 K/s). In brief, the eutectic structure transformed from α-Al+$Al_9(Ni, Mn)_2$ to α-Al+$Al_9(Ni, Mn)_2$+O-phase when the cooling rates decreased from 4~7 K/s to 20 K/min.

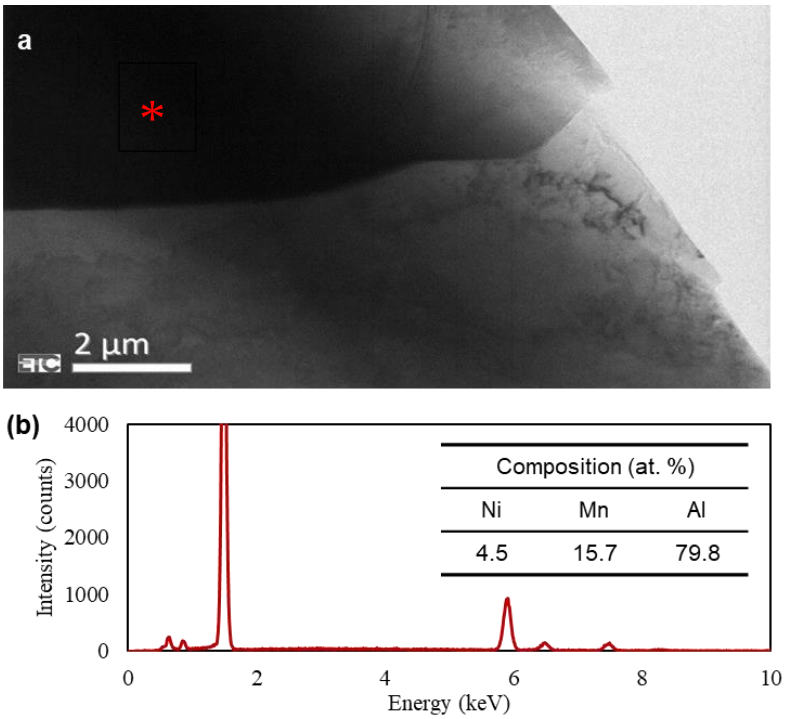

Figure 6.5 Transmission electron micrograph of O-phase and composition obtained by TEM-EDS.

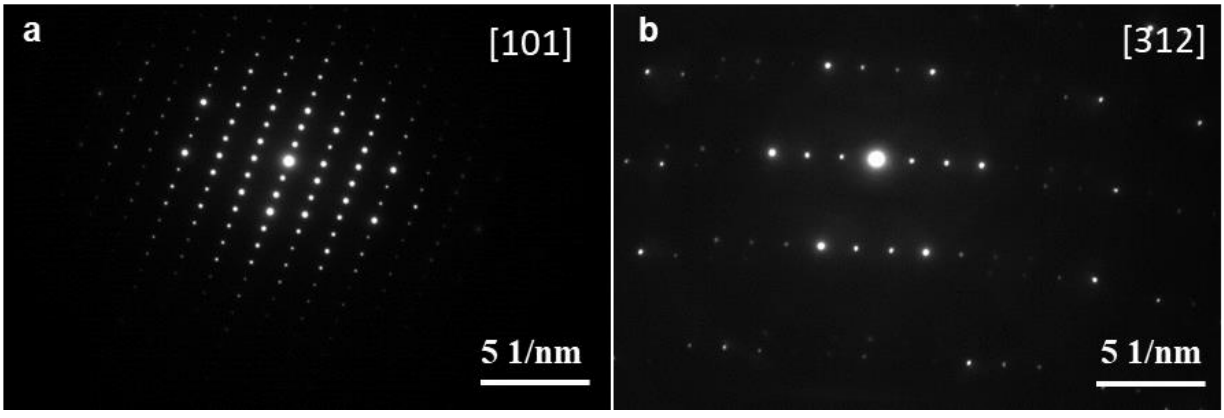

Figure 6.6 Electron diffraction pattern recorded along (a) zone axis [101], and (b) zone axis [312].

Figure 6.7 shows the microstructure of the Al-4Ni-2Mn alloy solidified at a cooling rate of 10 K/, which is similar to the microstructure solidified at a cooling rate of 20 K/min. It consists of primary α-Al phase and eutectic α-Al+$Al_9(Ni, Mn)_2$+O phases.

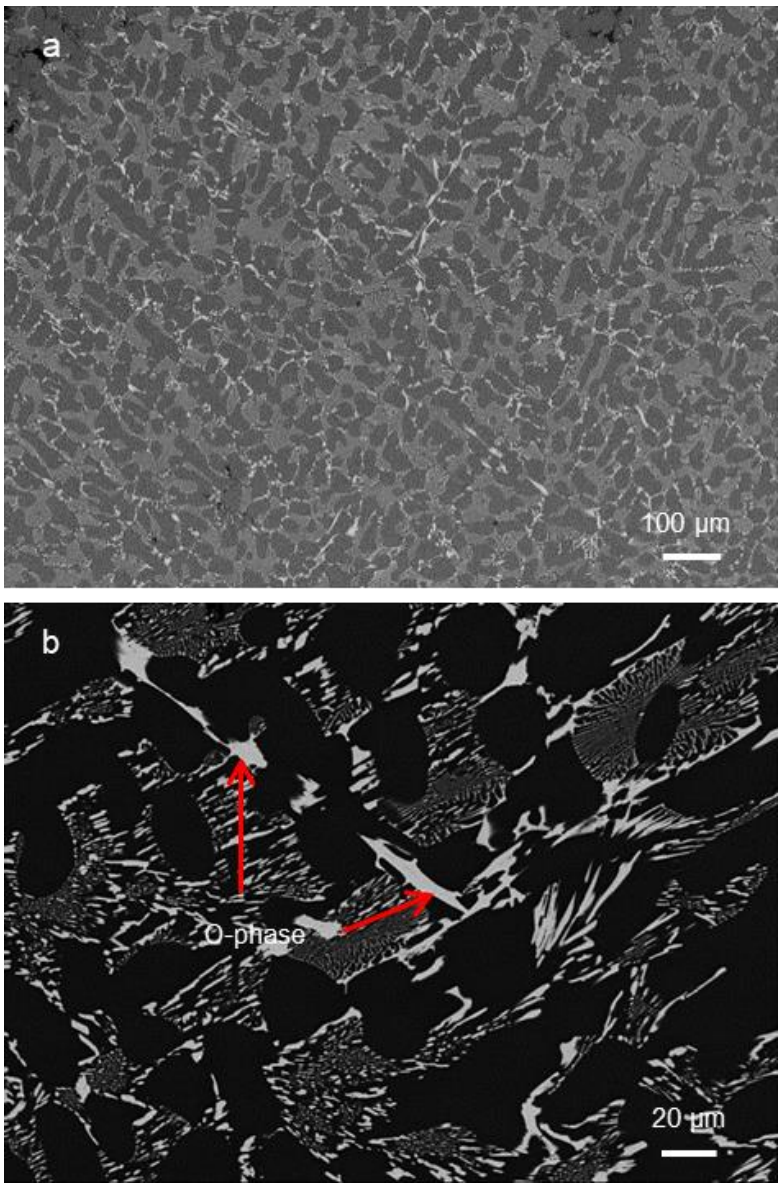

Figure 6.7 Backscattered SEM images showing microstructure solidified at 10 K/min.

6.3.3 Microstructure solidified under cooling rates between 1-5 K /min

A primary intermetallic phase formed when the cooling rate decreased to 5 K/min,, as shown in Figure 6.8. SEM-EDX revealed an average composition of Al-5.1Ni-13.9Mn (at. %), which was confirmed as the O-phase. The eutectic structure remained the same,

containing the eutectic $Al_9(Ni, Mn)_2$ phase and O-phase. Figure 6.9 shows the microstructure of the Al-4Ni-2Mn alloy solidified at a cooling rate of 1 K/min. The primary intermetallic phase was the O-phase and the eutectic structure was α-Al+$Al_9(Ni, Mn)_2$+O.

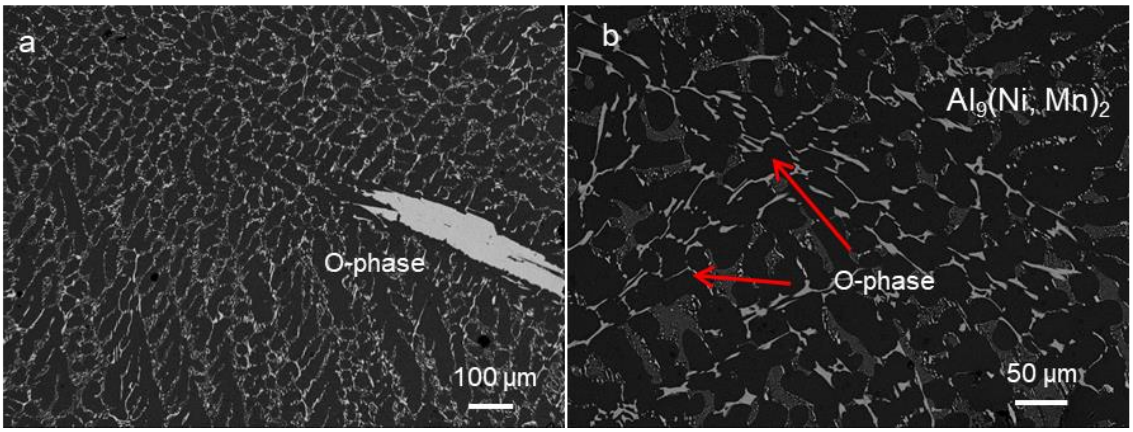

Figure 6.8 Backscattered SEM images showing microstructure solidified at 5 K/min.

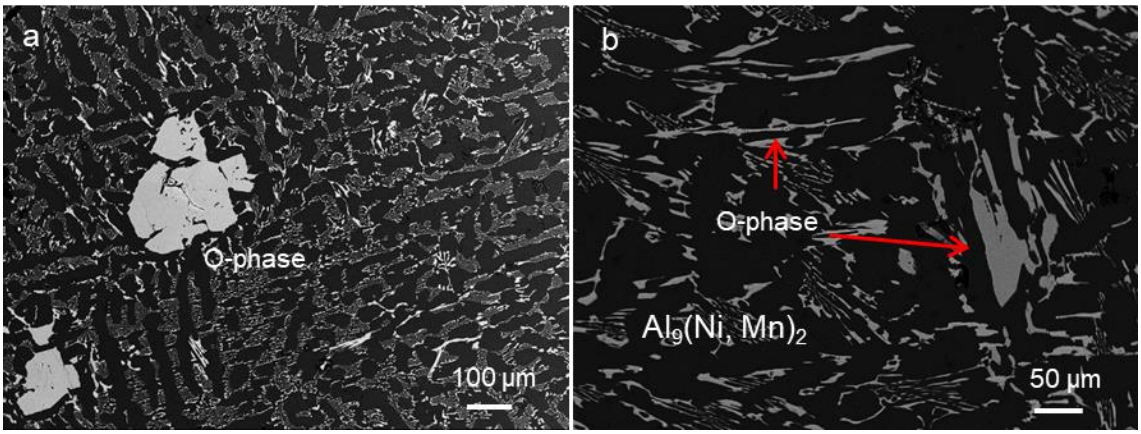

Figure 6.9 Backscattered SEM images showing microstructure solidified at 1 K/min.

6.3.4 Microstructure solidified under cooling rates between 0.2-0.5 K/min

Figure 6.10 shows the microstructure of the A-4Ni-2Mn alloy when cooling rate decreased to 0.5 K/min. tThe primary intermetallic phase remained to be the O-phase. Specially, the eutectic Al_3Ni phase was observed for the first time. Figure 6.10c shows the contrast difference between the Al_3Ni (lighter) and $Al_9(Ni, Mn)_2$ phase (darker) under back scattered

electron mode. Therefore, the eutectic structure experienced another transformation, from α-Al+Al_9(Ni, Mn)$_2$+O to α-Al+Al_9(Ni, Mn)$_2$+O+Al_3Ni phases at 0.5 K/min.

Figure 6.11 presents the microstructure at the slowest cooling condition of 0.2 K/min. Two primary phases with different contrast under back scattered electron mode were observed in Figure 6.11(a). The larger and lighter phase is O-phase. Figure 6.11(b) displays the details of the darker phase. SEM-EDX result showed a composition of Al-12.9Mn (at. %), which was Al_6Mn phase. The primary Al_6Mn phase was observed for the first time and enveloped with O-phase. The eutectic structure at 0.2 K/min was α-Al+Al_9(Ni, Mn)$_2$+O+Al_3Ni phases, which is the same as solidified at 0.5 K/min. In brief, when cooling rates decreased to 0.2 K/min, the primary Al_6Mn phase appeared.

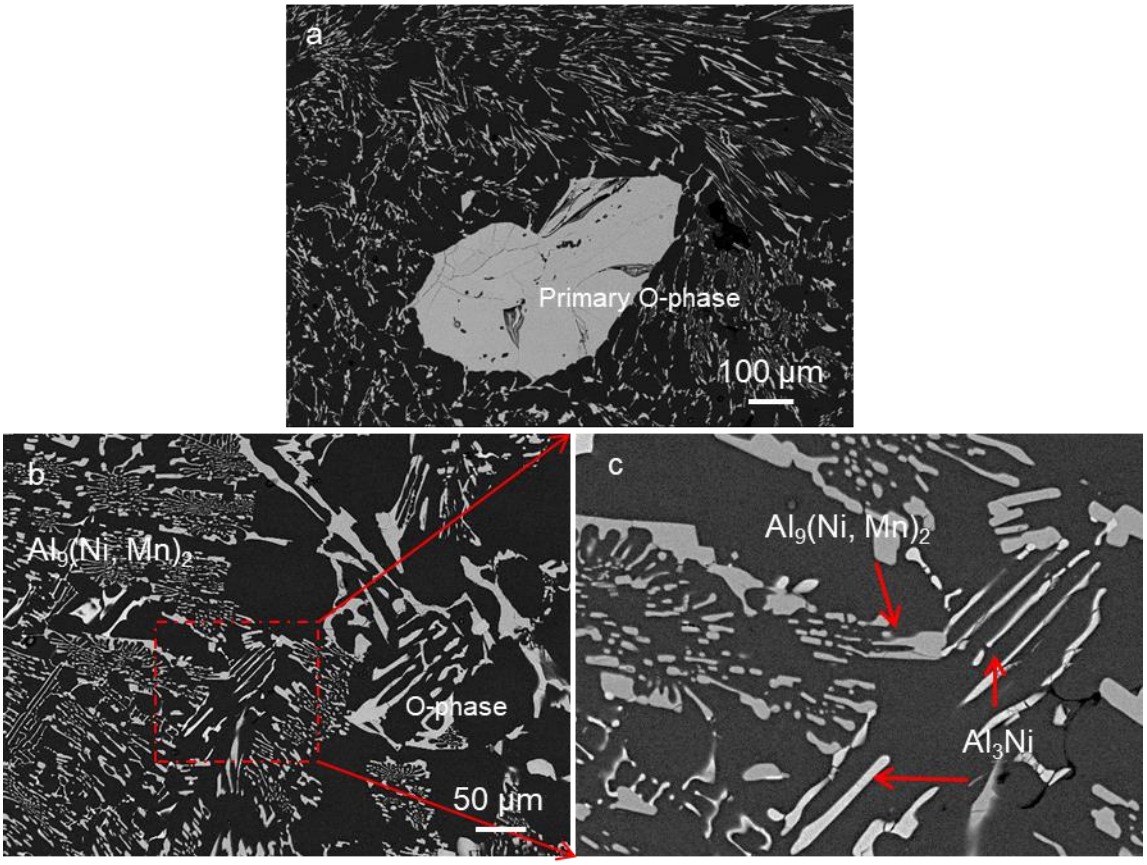

Figure 6.10 Backscattered SEM micrographs showing microstructure at 0.5 K/min. (a) primary O-phase, (b) eutectic Al_9(Ni, Mn)$_2$ and O-phase, (c) eutectic Al_3Ni phase.

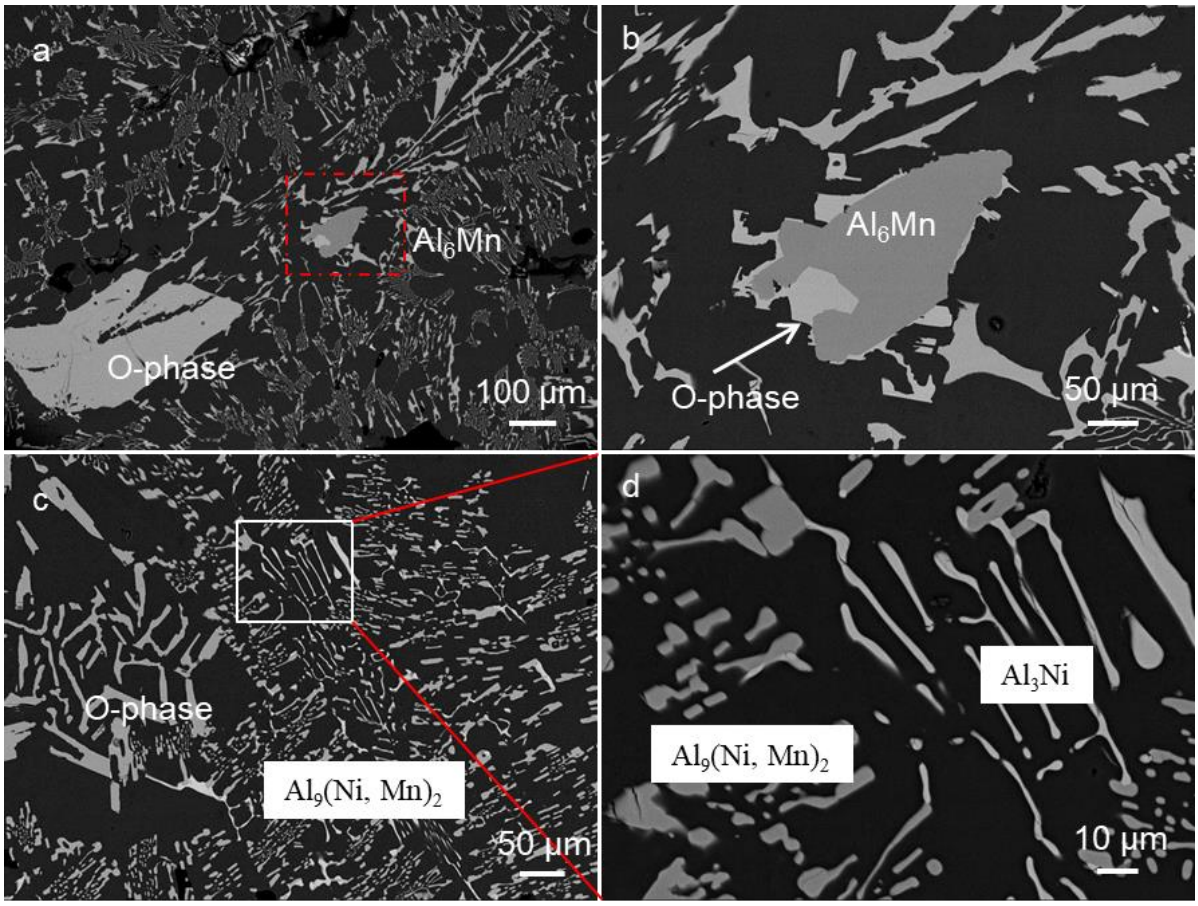

Figure 6.11 Backscattered SEM micrographs showing microstructure at 0.2 K/min. (a) primary O-phase and Al_6Mn phases, (b) high magnification of Al_6Mn phase, (c) eutectic $Al_9(Ni, Mn)_2$ and O-phase and (d) eutectic Al_3Ni phase.

In summary, the microstructural evolution of Al-4Ni-2Mn alloy with decreasing cooling rates was revealed. Firstly, the eutectic structure transformed from α-Al+$Al_9(Ni, Mn)_2$ to α-Al+$Al_9(Ni, Mn)_2$+O phases at 20 K/min. Secondly, the primary O-phase appeared at 5 K/min. Thirdly, the eutectic structure transformed from α-Al+$Al_9(Ni, Mn)_2$+O phases to α-Al+$Al_9(Ni, Mn)_2$+O+Al_3Ni phases at 0.5 K/min. Finally, the primary Al_6Mn phase appeared when solidified at 0.2 K/min.

6.4 The analysis of phase transformation at different cooling rates

It is well-established that higher cooling rates increases the supercooling of the melt and then triggers the formation of metastable phases. Both $Al_9(Ni, Mn)_2$ and O-phase are referred to as metastable phases since they do not exist in the equilibrium ternary Al-Ni-Mn

phase diagram [140]. The transition of primary and eutectic phases is discussed according to kinetic and thermodynamic of phase nucleation and growth. According to the equilibrium solidification simulation of the Al-4Ni-2Mn alloy, the predicted equilibrium microstructure consists of primary Al_6Mn phase, eutectic α-Al+Al_3Ni+Al_6Mn phases. However, no primary intermetallic phase was observed until the cooling rate dropped to 5 K/min. Generally, a higher cooling rate is likely to lead to a metastable phase. The diffusion coefficients of Mn and Ni in liquid Al are 1.93×10^{-7} m^2/s and 9.54×10^{-8} m^2/s in the range between 650-750 °C, respectively [128]. When solidification occurs quickly, atom migration is limited. Since the Al_6Mn phase is so enriched with Mn, the composition is far away from the liquid. Therefore, there is no sufficient time for Mn to cluster and form the Al_6Mn phase during PMC. The formation of the primary intermetallic phase was then suppressed at higher cooling rates. It is noticeable that the primary phase in the Al-4Ni-2Mn alloy was suppressed at cooling rates above 5 K/min. Based on this, the primary Al_6Mn intermetallic phase in the Al-4Ni-2Mn alloy will be suppressed in most conventional casting processes such as HPDC, PMC and even sand casting (cooling rate between 0.75-1.2 K/s) [157].

When the cooling rate decreased to 5 K/min, the primary O-phase appeared. Decreasing cooling rates provide more time for diffusion and atomic clustering, which facilitates intermetallic phase formation. However, the O-phase appeared rather than the Al_6Mn, which is predicted to be the primary phase during equilibrium solidification. The crystal structures of the O-phase and Al_6Mn are both orthorhombic structures; hence nucleation possibility of these two phases based on the crystal structure cannot be distinguished. Phase nucleation and growth will reject other elements into the remaining melt. The solubility of Ni in Al_6Mn is less than 0.05% [138], so the formation of Al_6Mn needs to reject all Ni into the remaining melt. It would encounter huge obstruction considering the slow diffusion coefficient of Ni in Al and the fact that the Ni concentration is twice the Mn concentration in the melt. While the O-phase contains about 5.5% Ni, which indicates less hindrance in rejecting Ni. Therefore, the primary O-phase is preferable to form than the Al_6Mn phase under a such

non-equilibrium condition. When the cooling rate decreased to 0.2 K/min, the primary Al_6Mn phase was observed. This cooling rate is very close to equilibrium solidification. There is sufficient time for long-range diffusion, and the controlling factor of phase formation is moving more close to thermodynamic. The Al_6Mn is an equilibrium phase and has lower Gibbs free energy than the O-phase; thus, is able to nucleate and grow under a low cooling rate of 0.2 K/min.

As mentioned above, the eutectic intermetallic phase in the Al-4Ni-2Mn alloy was $Al_9(Ni, Mn)_2$ after PMC and the primary phase was α-Al. So all the remaining liquid turned into eutectic phases after the primary α-Al phase. The concentrations of Ni and Mn in the remaining liquid will markedly increase because a large amount of Al was consumed when producing α-Al (52 vol.% by PMC). The Ni to Mn ratio also increased and became greater than two since Mn can dissolve in the primary α-Al (1.6% by PMC) while Ni solubility in Al is negligible [129]. Consequently, the composition of the remaining liquid is closer to the $Al_9(Ni, Mn)_2$ phase (14.7% Ni, 3.0% Mn) than the Al_3Ni phase. The importance of composition match on phase formation was studied by Malakhov [158]. It is reported that a phase with composition close to the remaining liquid has the greatest likelihood to form because nucleation and growth do not necessitate long-range diffusion. In this case, the $Al_9(Ni, Mn)_2$ has a composition much closer to the remaining liquid than the Al_3Ni, which explains appearance of the eutectic $Al_9(Ni, Mn)_2$ phase after PMC.

When cooling rate decreased, the eutectic structure transformed from α-Al+$Al_9(Ni, Mn)_2$ to α-Al+$Al_9(Ni, Mn)_2$+O phase and then to α-Al+$Al_9(Ni, Mn)_2$+O+Al_3Ni. This will be discussed from both diffusion and thermodynamic stability aspects. Total atomic percentages of Ni and Mn in the $Al_9(Ni, Mn)_2$ phase, O-phase and Al_3Ni phase are about 18%, 20% and 25%, respectively. Phase with higher concentrations of Ni and Mn need more time for diffusion, which can be achieved by slowing the solidification process. When cooling rate decreases to 0.5 K/min, the solidification process is more closer to equilibrium than non-equilibrium solidification. Atomic diffusion is sufficient, and hence

thermodynamic factor dominates phase nucleation and growth. Al_3Ni is an equilibrium phase with lower Gibbs free energy comparing to the $Al_9(Ni, Mn)_2$ and O-phase. Therefore, the Al_3Ni phase is able to nucleate and grow. It should be noted that the eutectic Al_3Ni phase co-exists with the O-phase and $Al_9(Ni, Mn)_2$ phases. The transition was partially completed at 0.2 K/min. But from a thermodynamic viewpoint, Al_3Ni will take over the other two phases when the solidification process approaches equilibrium solidification.

In addition to the transition of primary and eutectic phases, the size and morphology of the eutectic phase changed as well. Figure. 6.12 shows the morphology of eutectic phase under different cooling rates. The size of the eutectic O-phase increased markedly with decreasing cooling rates. Besides, the O-phase presented a regular fibrous structure at a cooling rate of 5 K/min. When the cooling rate decreased to 1 K/min, it became irregular and faceted Chinese script. At cooling rates of 0.5 K/min and 0.2 K/min, the eutectic O-phase became huge irregular and faceted fish bone structure. Figure 6.13 demonstrates the effect of the cooling rates on the secondary dendrite arm spacing (SDAS). The cooling rate is between 4~7 k/s for PMC, hence a cooling rate of 500 k/min can be determined to represent PMC. The SDAS increased with decreasing cooling rates. It was 14 μm after PMC and increased to 32 μm at cooling rate of 20 K/min and 69 μm at cooling rate of 0.5 K/min.

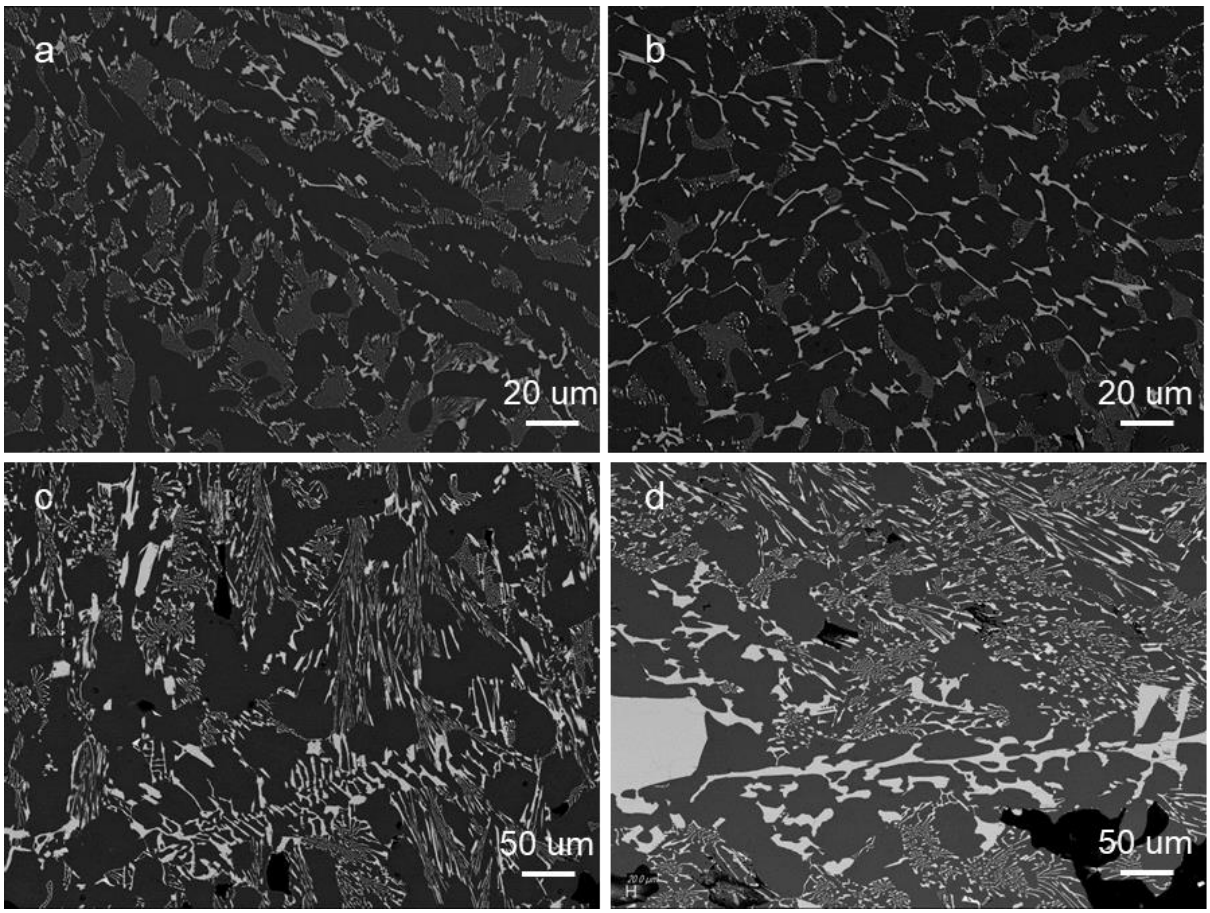

Figure 6.12 Backscattered SEM images showing the morphology evolution of eutectic O-phase solidified at (a) 20 K/min, (b) 5 K/min, (c) 0.5 K/min, (d) 0.2 K/min.

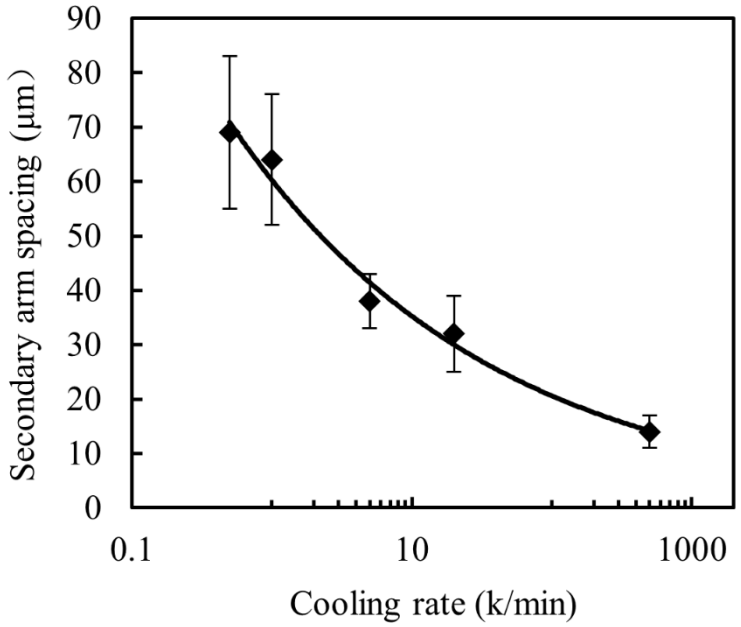

Figure 6.13 Effect of cooling rates on SDAS of Al-4Ni-2Mn alloy

6.5 The effect of pouring temperatures on microstructure

The distribution and size of the intermetallic phase strongly affect mechanical properties. However, the primary O-phase and $Al_9(Ni, Mn)_2$ phases in the Al-6Ni-4Mn alloy were non-uniformly distributed. A microstructure with uniformly distributed fine intermetallic phases is desired for good performance at both ambient temperature and elevated temperatures.

Considering the PMC is applied in the present study, the pouring temperature and mould temperature are two key factors affecting solidification process and consequently changes the distribution of the primary phases. The size and distribution of primary phases can affect the hardness and tensile strength of aluminium alloys [159–163]. The mould temperature was preheated to 400 ℃ prior casting to ensure the fluidity of the melt. Here the effect of pouring temperatures on the size and distribution of the primary phases in the Al-6Ni-4Mn alloy was investigated. The pouring temperatures varied between 780 ℃ and 740 ℃.

Samples were cut from the middle part of tensile bars, as illustrated in Figure 6.14. Plates with a diameter of 10 mm and thickness of 10 mm were obtained. They were divided into

several areas under OM, and an image for each area was taken. Then a panorama for the cross-section was obtained by stitching all images.

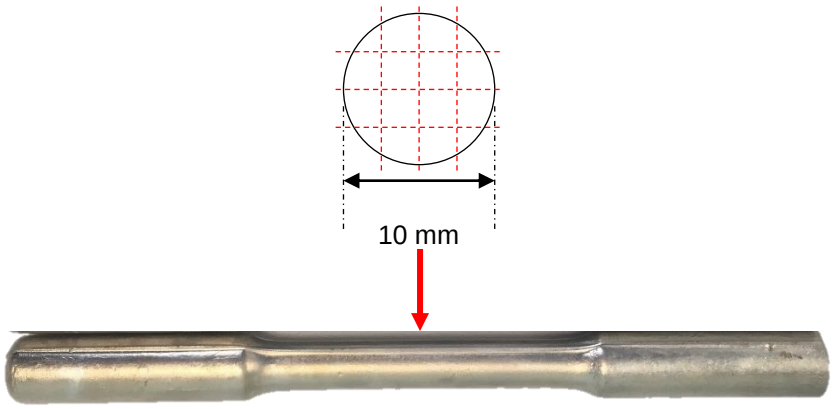

Figure 6.14 Illustration of one plate sample which was obtained from the middle of tensile bars and it was divided into 16 areas under the optical microscope.

Figure 6.15 shows the panoramas of the Al-6Ni-4Mn alloy with different pouring temperatures. It showed clearly that the pouring temperatures strongly affected the distribution of the primary phases. When poured at 780 °C, the primary phases showed a highly non-uniform distribution, which were observed only in the central area of the sample. When the pouring temperature dropped to 765 °C, the primary phases were mainly observed within the central 1/2 radius circle. A decrease of 15 °C in pouring temperature significantly improved the primary phase distribution. When the pouring temperature decreased to 750 °C, the primary phases distributed within the central 4/5 radius circle. And when the pouring temperature decreased to 740 °C, the primary phases uniformly distributed in the whole area of the sample.

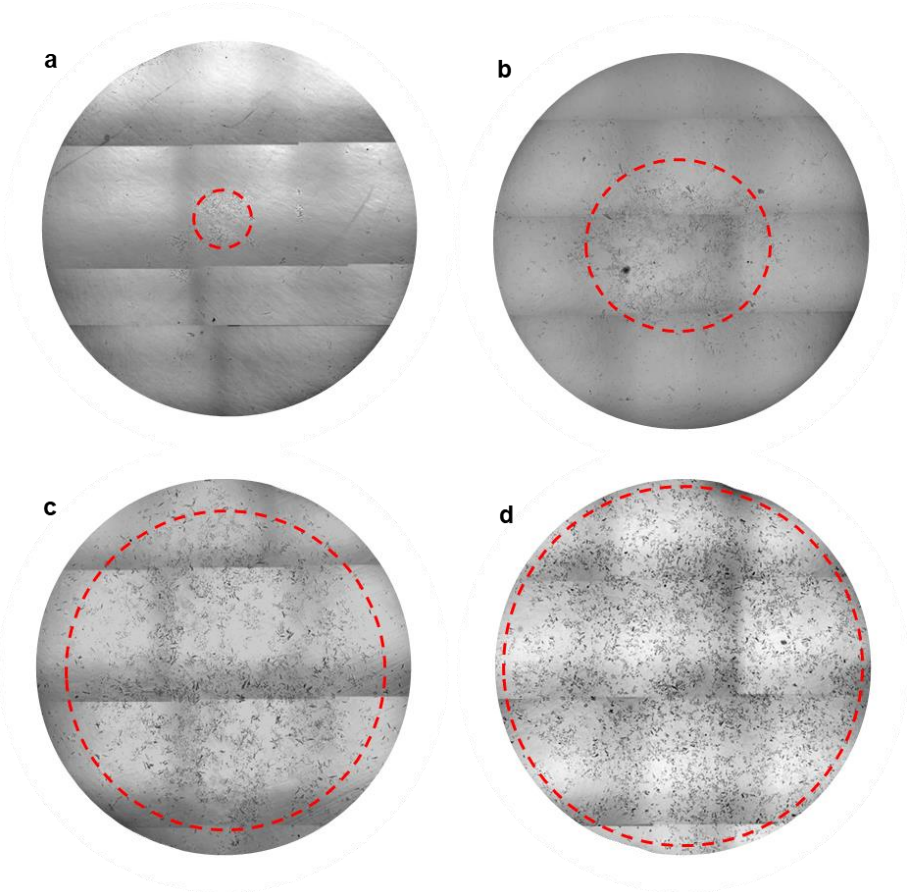

Figure 6.15 The microstructure of Al-6Ni-4Mn alloy with different pouring temperatures. (a) 780 °C; (b) 765 °C, (c) 750 °C and (d) 740 °C.

The difference of distribution under different pouring temperature is associate with cooling rates. Pouring temperature has a significant effect on solidification process. Generally, higher pouring temperature provides more heat to the mould and results in smaller cooling rate [163]. The solidification time thereby decreases with decreasing pouring temperature. Subsequently, decreasing solidification time improves solute segregation during the solidification process. The primary phases in Figure 6.15a distributed non-uniformly in the scale of several millimetres, which demonstrated a macro-segregation. Macro-segregation is based on the micro-segregation or partitioning of solute elements between liquid and solid phases during the solidification process [164], which depends on the partition coefficient, K. Both the Ni and Mn present $K<1$, just like other alloying elements (Cu, Mg, Zn, Li, Si, Fe) in aluminium alloys [164,165]. The negative segregation of Ni and Mn in aluminium

indicates that the concentrations of Ni and Mn in the remaining melt increase during solidification. Consequently, the primary phases rich in Ni and Mn formed in the centre of the samples, which is the last stage of solidification. In brief, for negative segregation solute elements (Ni, Mn), the centre part of the sample is richer in solute elements. And higher pouring temperatures exacerbate element segregation. It thus explained the non-uniform primary phase distribution at a pouring temperature of 780 °C. When pouring temperature decreases, the cooling rate increases. The undercooling then increases and subsequently increase the nucleation rates of the primary phases. More primary phases will form, and the distribution will be more uniform.

The size of primary phases also decreases because there is no sufficient time for diffusion and growth. Figure 6.16 presents the primary phases with different pouring temperatures. The size of the primary phases poured at 740 °C was smaller than that poured at 780 °C.

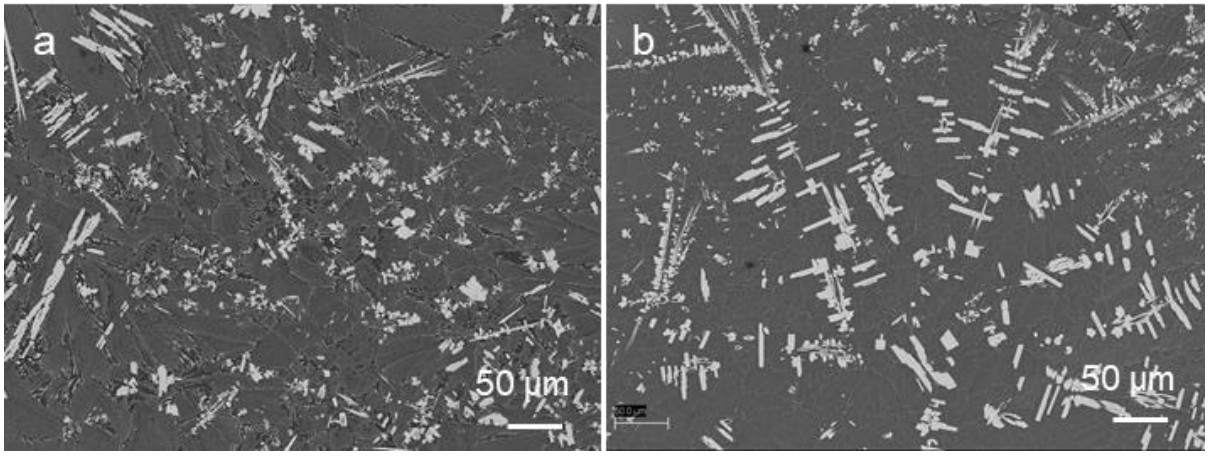

Figure 6.16 The primary phases with pouring temperatures at (a) 740 °C, (b) 780 °C.

To evaluate the size of the primary phases, more than 200 particles were measured for each sample. Figure 6.17 displays the statistical size of the primary phases at pouring temperatures of 740 °C and 780 °C. The size of primary phases decreased with decreasing pouring temperature. When poured at 740 °C, the size ranged between 0-150 μm, and the average size was 39.5 μm. When poured at 780 °C, the average size increased to 65.0 μm. And some primary κ-phase reached 150 μm and above.

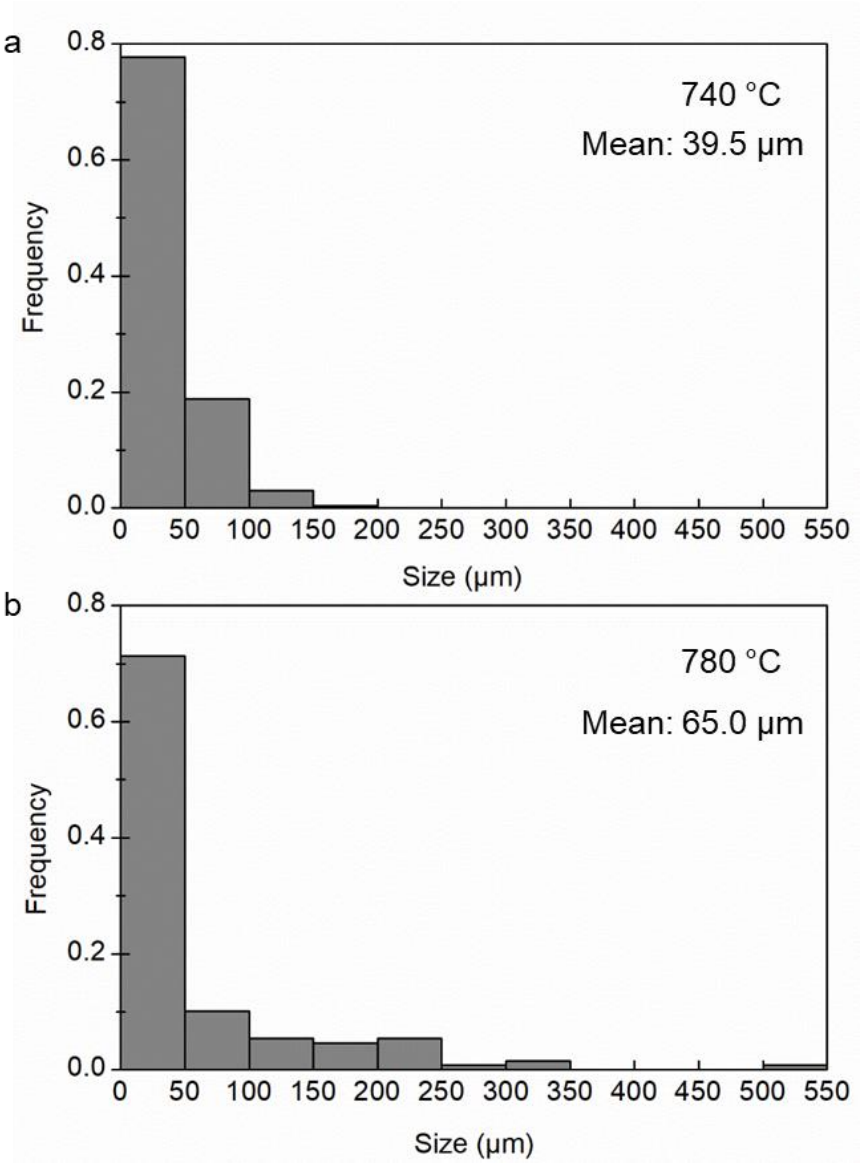

Figure 6.17 The size distribution of the primary phases in Al-6Ni-4Mn alloy at pouring temperatures of (a) 740 °C, (b) 780 °C.

6.6 Summary

In this chapter, the microstructures of Al-4Ni-2Mn alloy under different cooling rates have been studied using DSC. The size and distribution of the primary phases in the Al-6Ni-4Mn alloy with different pouring temperatures were also investigated.

Both the eutectic and primary phases in the Al-4Ni-2Mn alloy changed with the variation of cooling rates. The eutectic structure was α-Al+Al_9(Ni, Mn)$_2$ phases in PMC and then became α-Al+Al_9(Ni, Mn)$_2$+O phases and a mixture of α-Al+Al_9(Ni, Mn)$_2$+ O+Al_3Ni as the cooling rates decreased to 20 K/min and 0.5 K/min, respectively. As for the primary phases, α-Al phase was the only primary phase in PMC. When the cooling rate decreased to 5 K/min and 0.2 K/min, the O-phase and Al_6Mn phase began to form, respectively.

Moreover, pouring temperature affected the size and distribution of the primary phases in the Al-6Ni-4Mn alloy. The primary phases distributed more uniformly and became smaller as pouring temperature decreased.

Chapter 7: Microstructural Evolution of Al-4Ni-2Mn Alloy at Elevated Temperatures

7.1 Introduction

The eutectic structure in the Al-Ni-Mn alloys obtained through PMC is α-Al+$Al_9(Ni, Mn)_2$ and shows a very good softening resistance at 250 °C, indicating a good potential for their applications at elevated temperatures. However, significant strength degradation may happen when serves at elevated temperatures due to phase coarsening. Therefore, long term microstructural stability needs to be assessed and the suitable service temperature needs to be determined. However, there is almost no reported research on this issue so far. Our study, for the first time, aims at revealing the thermal stability of eutectic phases and investigating the microstructural evolution at elevated temperatures.

The Al-4Ni-2Mn alloy consists of primary α-Al phase and eutectic α-Al+$Al_9(Ni, Mn)_2$ phases. The microstructure is suitable for observing eutectic structure evolution during long-term service at elevated temperatures. On the other hand, the α-Al phase contained 1.6% Mn, which might produce precipitates at elevated temperatures, which making it suitable to characterize both the eutectic structure evolution and precipitates. The Al-4Ni-2Mn alloy was holding at 250 °C, 300 °C, 400 °C for different time. Microstructural evolution was investigated using SEM and TEM. Hardness with different isothermal holding time at each temperature was tested. TEM was also applied to characterize size and morphology of precipitates.

7.2 Microstructural evolution during isothermal holding

7.2.1 Isothermal holding at 250 °C

Figure 7.1 shows the microstructure of the Al-4Ni-2Mn alloy after held at 250 °C for different time. The eutectic $Al_9(Ni, Mn)_2$ rods showed no change after isothermal holding at 250 °C. It maintained a rod-like shape even after 2000 h. The TEM images in Figure 7. 2

shows the morphologies of the as-cast eutectic $Al_9(Ni, Mn)_2$ rods and eutectic $Al_9(Ni, Mn)_2$ rods after 1000 h at 250 °C. The eutectic morphologies remained rod-like shape; no coarsening of the eutectic rods was observed. Moreover, the thickness of eutectic rods after 1000 h at 250 °C is more uniform than the as-cast sample, which indicates short-term diffusion at 250 °C.

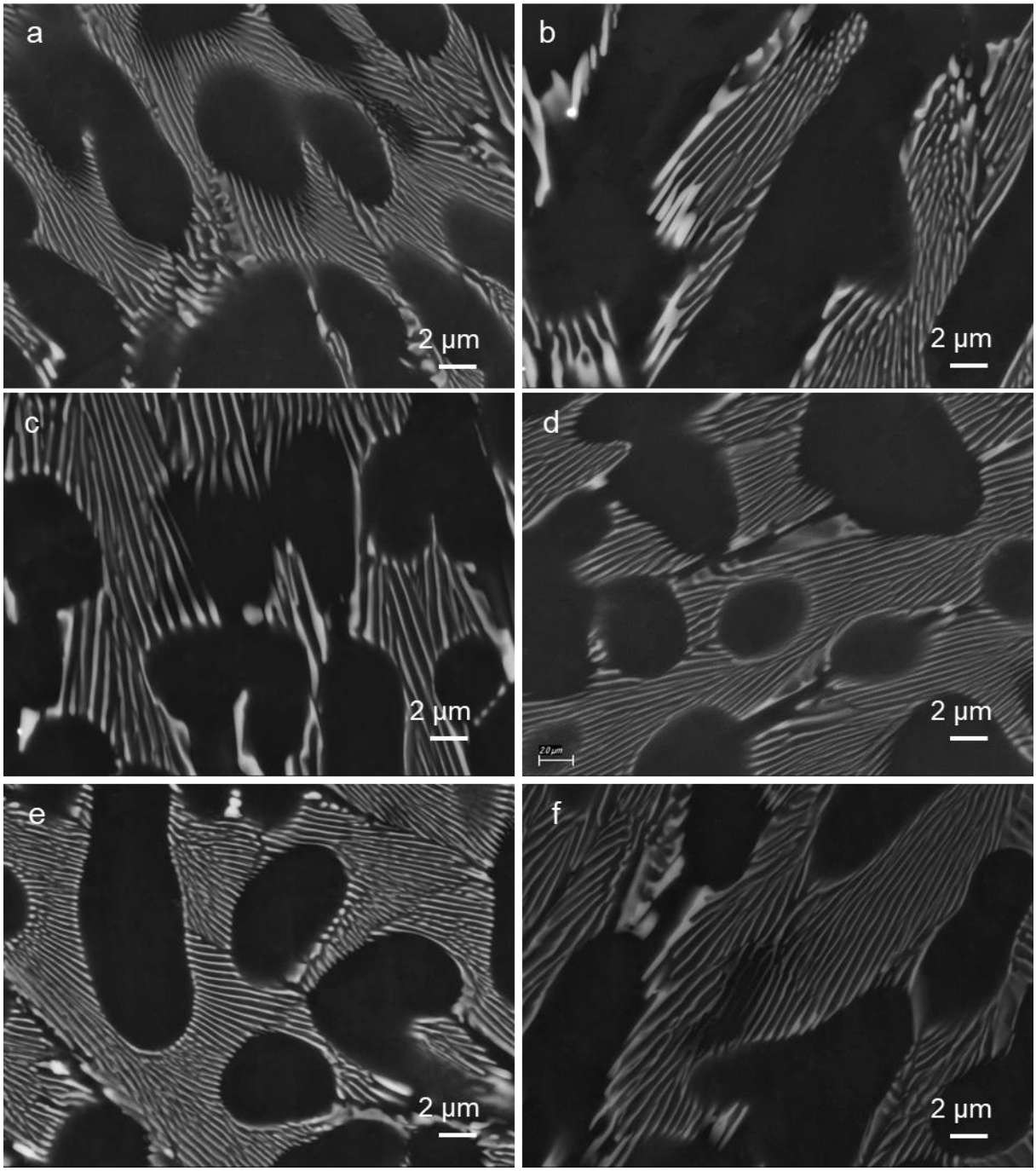

Figure 7.1 Backscattered images showing eutectic $Al_9(Ni, Mn)_2$ rods after isothermal holding at 250 °C for (a) 100 h, (b) 360 h, (c) 540 h, (d) 720 h, (e)1000 h, (f) 2000 h.

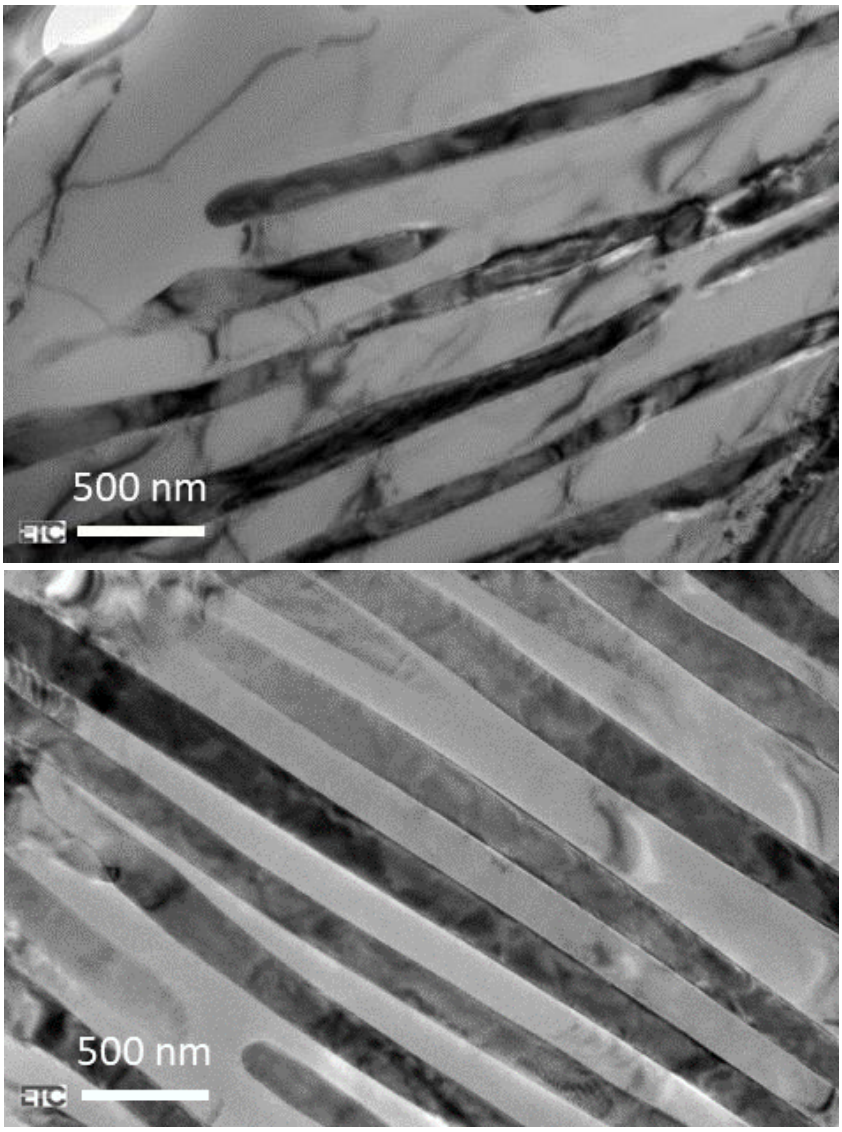

Figure 7.2 TEM image showing the eutectic $Al_9(Ni, Mn)_2$ phase after (a) solidified and (b) isothermal holding at 250 °C for 1000 h.

Figure 7.3 presents the Vickers hardness of the Al-4Ni-2Mn alloy after isothermal holding at 250 °C for different time. The hardness showed no obvious change, and fluctuation was within a very narrow range. The hardness of the as-cast sample increased slightly from 64.5 HV10 to 69.0 HV10 after 540 h at 250 °C. The hardness remained at a similar level of 68.1

HV10 after 2000 h. The results indicate that the hardness remained at a similar level to that observed at room temperature. The hardness results are in strong agreement with the stable eutectic $Al_9(Ni, Mn)_2$ phase at 250 °C.

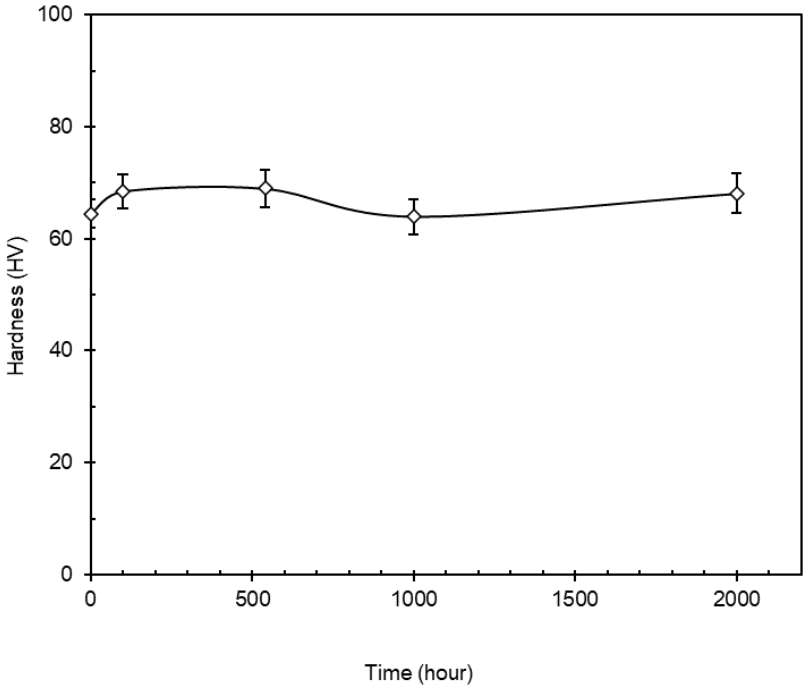

Figure 7.3 Room temperature Vickers hardness evolution after different isothermal holding time at 250 °C.

The eutectic $Al_9(Ni, Mn)_2$ phase presents superior thermal stability at 250 °C. This is mainly due to the low diffusion rate of Ni and Mn in Al. Generally, the coarsening process is controlled by volume diffusion, as solute atoms are transferred through the matrix. The diffusion rate of Mn is much lower than that of Si, Mg and Cu. At 400 °C, the diffusion rate of Mn is 5.20×10^{-19} m^2/s, while for Cu it is 2.31×10^{-15} m^2/s, for Mg it is 1.1×10^{-14} m^2/s, and for Si it is 3.68×10^{-15} m^2/s [129]. The coarsening of eutectic $Al_9(Ni, Mn)_2$ phase was likely impeded by slow diffusion rate.

7.2.2 Isothermal holding at 300 °C

The Al-4Ni-2Mn alloy was also held at 300 °C for 100 h, 360 h, 540 h, 720 h and 1000 h. The microstructures are displayed in Figure 7.4. Morphology of eutectic $Al_9(Ni, Mn)_2$ phase maintained a rod-like shape after 1000 h at 300 °C. However, some small particles were

observed in the sample after isothermal holding. Figure 7.4f presents an enlarged view of the eutectic area marked by a rectangle in Figure 7.4e. Particles are clearly seen in the eutectic area. Microstructure at higher magnification at 300 °C after 1000 h is presented in Figure 7.5. Eutectic rods segments were also observed in the eutectic area and are indicated by red arrows. This new particle was analysed using TEM in a later section.

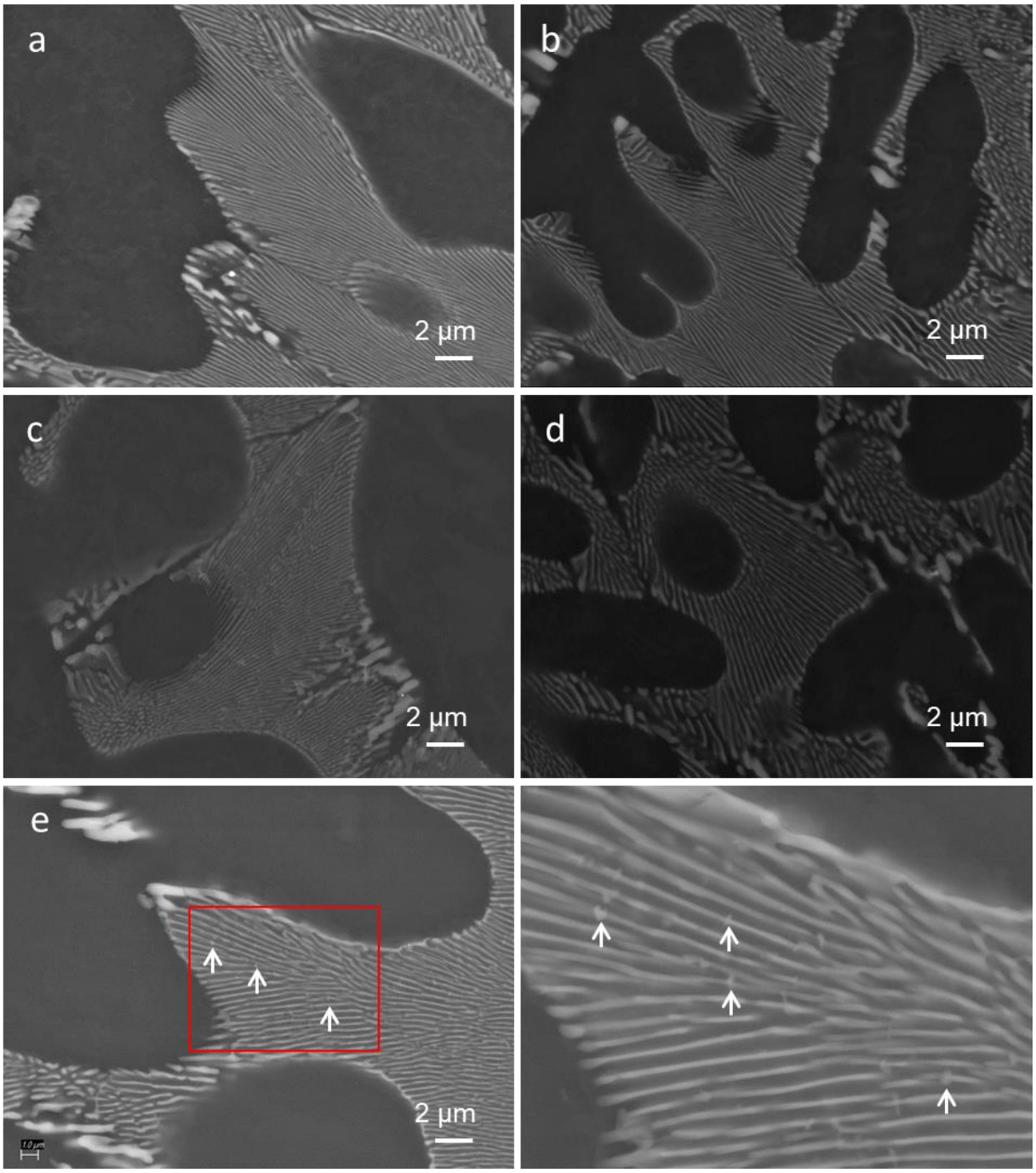

Figure 7.4 Backscattered images showing eutectic phase after isothermal holding at 300 °C for (a) 100 h, (b) 360 h, (c) 540 h, (d) 720 h, (e)1000 h, (f) enlarged area in Figure 7.4e.

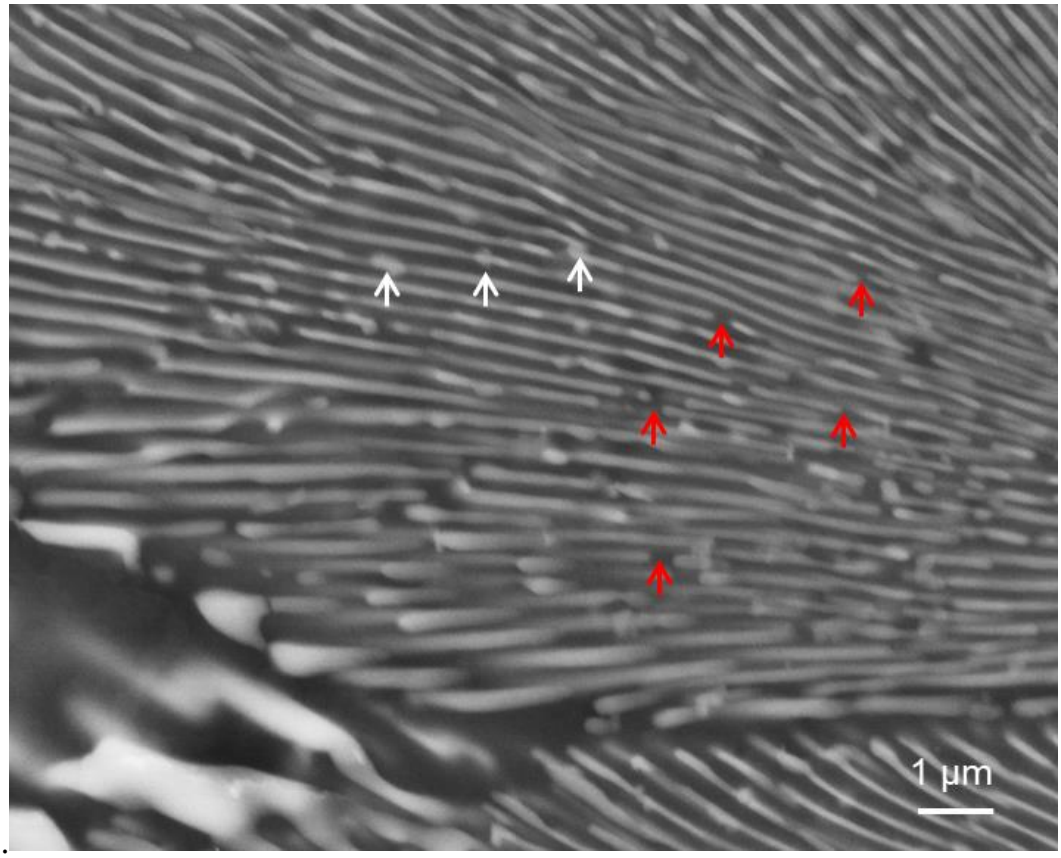

Figure 7.5 The eutectic rods break into segments at 300 °C after 1000 h.

Figure 7.6 presents the Vickers hardness of the Al-4Ni-2Mn alloy after isothermal holding at 300 °C for different time. The hardness did not show a significant decrease at 300 °C even after 1000 h. The fluctuation was within a very narrow range. The hardness of the as-cast sample slightly increased from 64.5 HV10 to 68.4 HV10 after 20 h at 300 °C. And then it dropped back down to the as-cast level after 100 h. The hardness still remained at a level of 62.6 HV10 after 1000 h at 300 °C, which is nearly the same level as that for the as-cast sample.

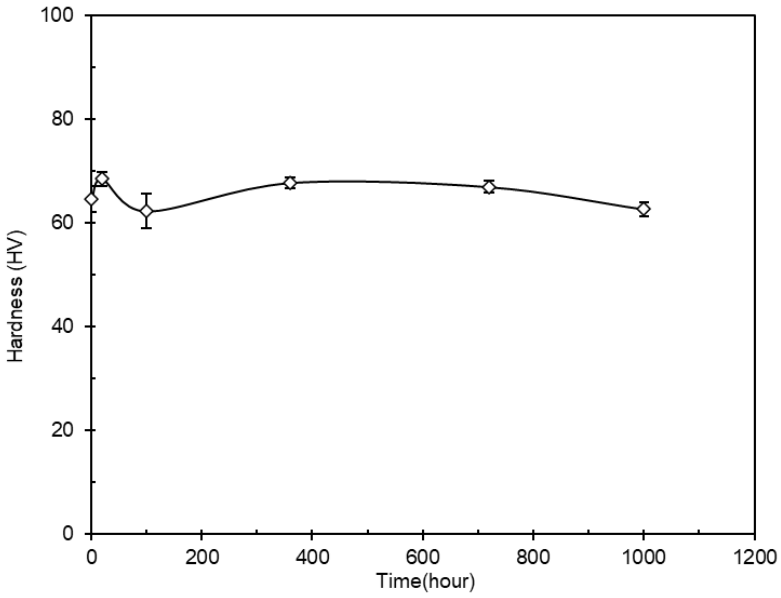

Figure 7.6 Room temperature Vickers hardness evolution during isothermal holding at 300 °C.

7.2.3 Isothermal holding at 400 °C

Figure 7.7 displays the microstructures of Al-4Ni-2Mn alloy after holding at 400 °C for 20 h, 120 h, 540 h and 720 h separately. The eutectic structure remained the same after 20 h at 400 °C. As shown in Figure. 7.7(b), there are some particles observed in the eutectic area after 120 h. Moreover, when isothermal holding time increased up to 540 h and 720 h, particles formed on the eutectic $Al_9(Ni, Mn)_2$ rods, as indicated by the arrows. Furthermore, some acicular precipitates were observed in the α-Al phase, and the size of precipitates increased over time. TEM was used to investigate the new particle observed in the eutectic area and the precipitates in α-Al.

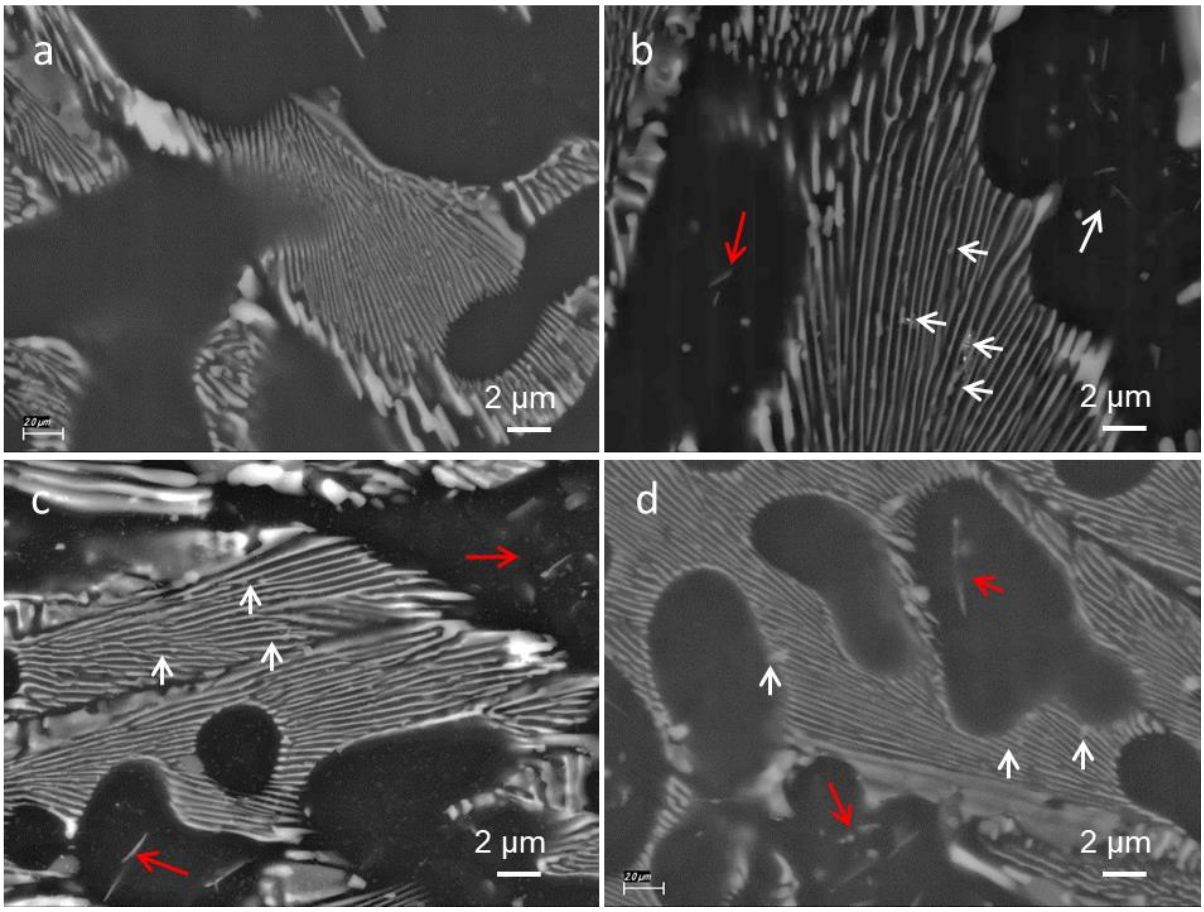

Figure 7.7 SEM images showing microstructure at 400 °C for (a) 20 h, (b) 120 h, (c) 540 h, (d) 720 h.

Figure 7.8 presents the Vickers hardness of the Al-4Ni-2Mn alloy after isothermal holding at 400 °C for different time. The hardness markedly decreased during the first 120 h. It decreased from 64.5 HV10 for the as-cast sample to 62.3 HV10 after 20 h and to 57.5 HV10 after 120 h. Then the hardness remained at the same level over time. For example, it was 58.4 HV10 after 720 h at 400 °C.

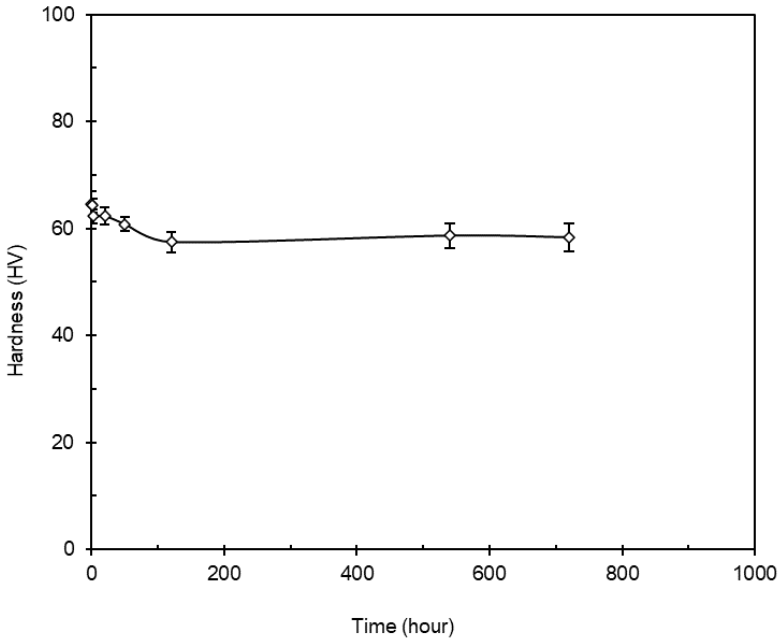

Figure 7.8 Room temperature Vickers hardness evolution during isothermal holding at 400 ℃.

7.3 TEM characterization

7.3.1 New phase in eutectic area

As mentioned above, some particles were observed in the eutectic area by SEM after isothermal ageing at 300 ℃ for 1000 h and 400 ℃ for 120 h, suggesting a solid phase transformation. Since the particles are very small, under 0.5 μm, it is beyond the characterization capability of SEM; TEM was therefore used to characterize it. Figure 7.9 presents TEM images of the samples after 20 h and 540 h at 400 ℃. A new phase appears to have formed at the α-Al/$Al_9(Ni, Mn)_2$ interphase boundaries. Figure 7.10 displays this new phase, the $Al_9(Ni, Mn)_2$ phase and their compositions by TEM-EDS. P1 is a Mn-rich phase with a composition of Al-13.1 Mn-3.1 Ni (at.%).. The composition is very close to the κ-phase in the Al-Ni-Mn alloys [140,141,166]. Recently, Yu [166] reported this κ-phase. The κ-phase is a hexagonal phase with lattice parameters: a= 1.7625 nm, c = 1.2516 nm. It has the same structure as k-$Al_{14.4}Cr_{3.4}Ni_{1.1}$ in the Al-Cr-Ni system [142–144]. The TEM results

indicate that nucleation of this new phase occurs heterogeneously on interphase boundaries. The morphology of this new phase is shown in Figure 7.9 (red arrows), which is tetrahedral with the base of the tetrahedron on the α-Al/Al_9(Ni, Mn)$_2$ interphase boundaries. After holding for 540 h at 400 °C, the new particles grew large and broke the eutectic Al_9(Ni, Mn)$_2$ rods into several segments. It is also noticeable that the size of this new phase did not show an obvious increase when the time was increased from 20 h to 540 h at 400 °C, indicating that the transformation from Al_9(Ni, Mn)$_2$ into κ-phase appears to be slow at 400 °C.

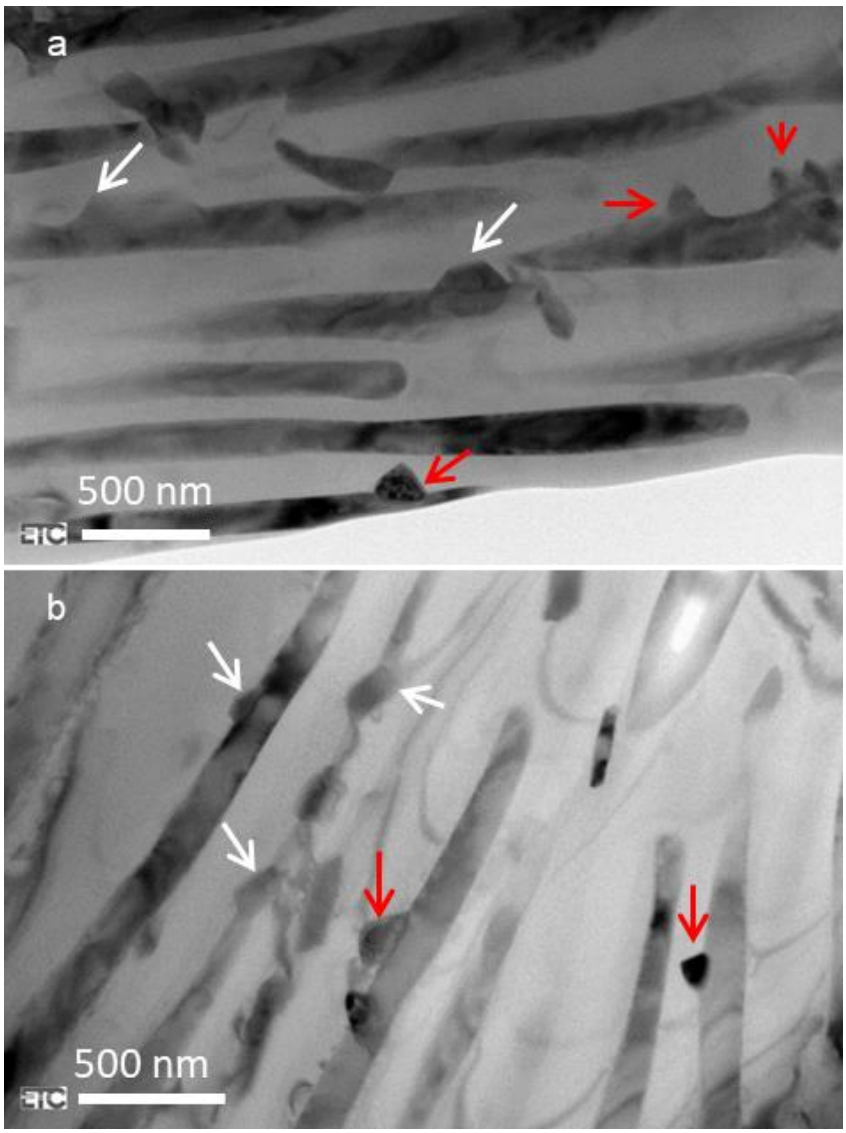

Figure 7.9 TEM images showing the eutectic phase transition product after (a) 20 h and (b) 540 h at 400 °C.

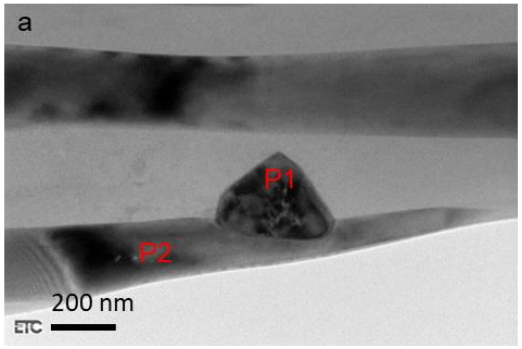

b

	Composition (at.%)		
	Ni	Mn	Al
P1	3.1	13.1	83.8
P2	12.4	2.5	85.1

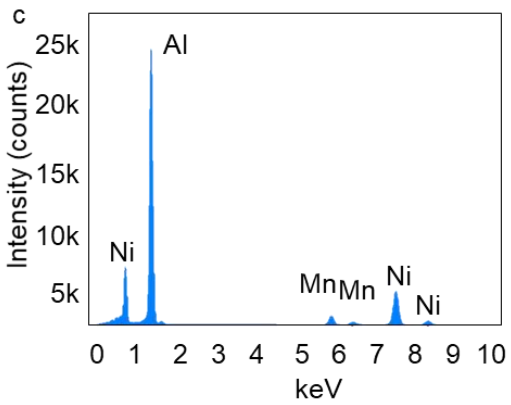

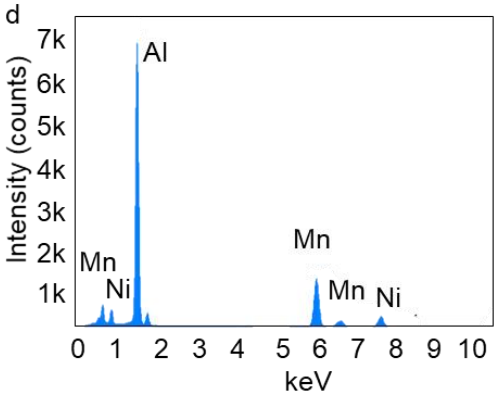

Figure 7.10 TEM image showing a new phase (P1) and eutectic $Al_9(Ni, Mn)_2$ phase (P2) and their compositions by TEM-EDX.

7.3.2 Precipitates in α-Al matrix

Apart from the formation of κ-phase, some precipitates were also observed in α-Al matrix when isothermal holding at 400 °C. Figure 7.11 presents the microstructure after isothermal holding at 400 °C for 50 h and 120 h. Precipitates appeared in the primary α-Al and their size and density increased over time at 400 °C.

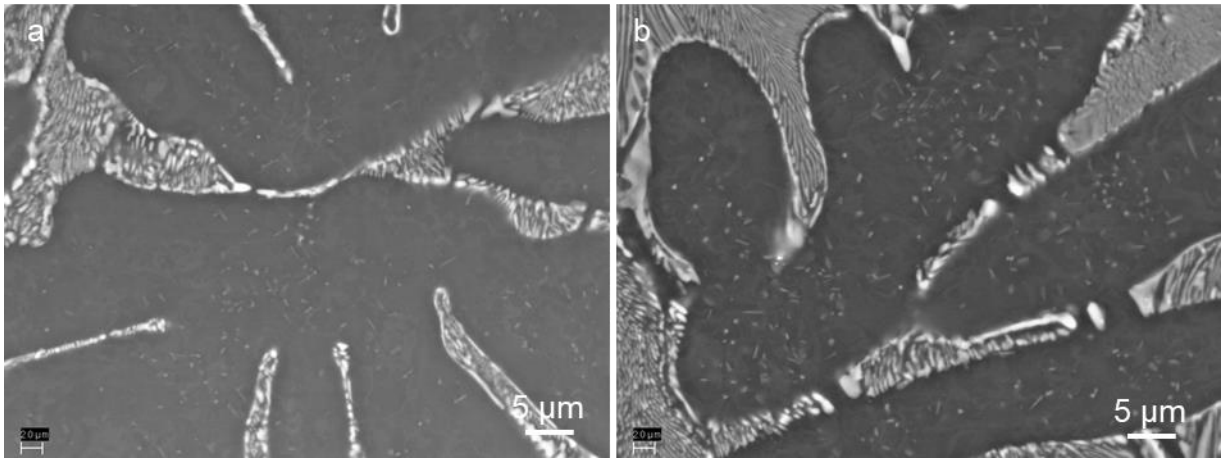

Figure 7.11 Microstructure of the Al-4Ni-2Mn alloy after holding at 400 °C for (a) 50 h and (b) 120 h.

TEM images in Figure 7.12 present the precipitates in Al-4Ni-2Mn alloy. TEM-EDS revealed that this phase contained 11.0-12.5 at.% Mn and about 1.0 at% Ni. It was identified as the Al_6Mn phase. The primary α-Al in Al-4Ni-2Mn alloy contained 1.6% Mn and 0.43% Ni. Hence, the Al_6Mn is the only possible precipitate in the Al-4Ni-2Mn alloy. The Al_6Mn phase displayed different morphologies, for instance, some are acicular, and some are cuboids.

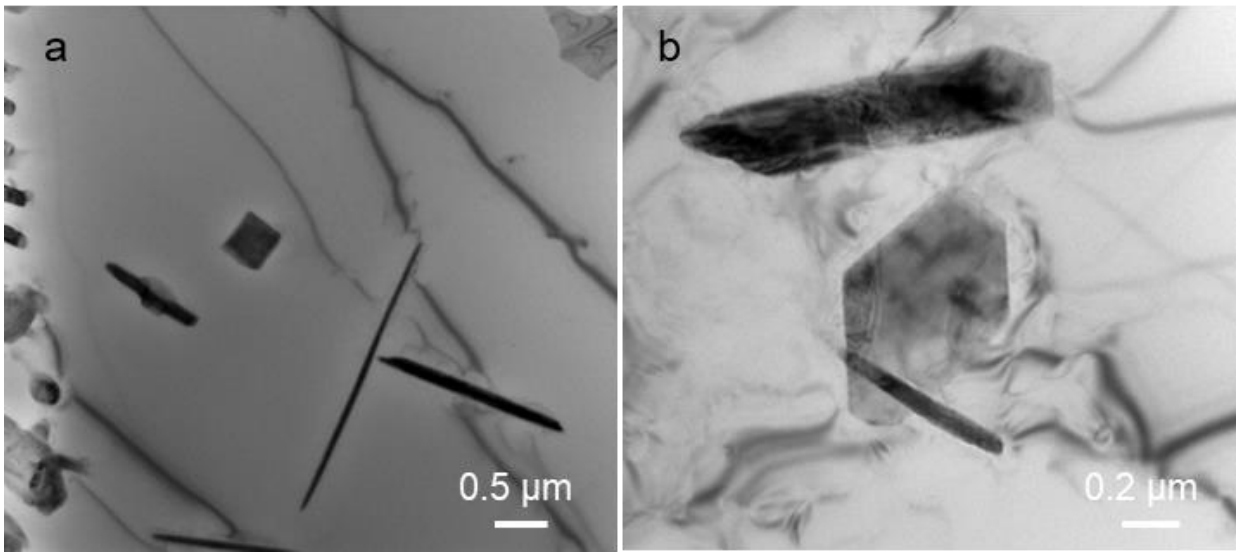

Figure 7.12 TEM images showing morphologies of the Al_6Mn precipitates.

The size of Al_6Mn precipitates increased over time at 400 °C. To evaluate the precipitate size, more than 200 precipitates were measured for each sample. Figure 7.13 displays the statistical results of precipitates length. T average precipitate size was 489 nm, and the peak interval was between 200-400 nm after holding at 400 °C for 50 h. Moreover, a large portion of the precipitates were under 200 nm. When holding time increased to 120 h, the average precipitate size increased to 605 nm, and the peak interval moved to 400 -600 nm. When holding time increased to 540 h and 720 h, the average precipitate size increased to 1.258 μm and 1.407 μm, respectively. Especially, some precipitates even reached 2 μm and 4 μm.

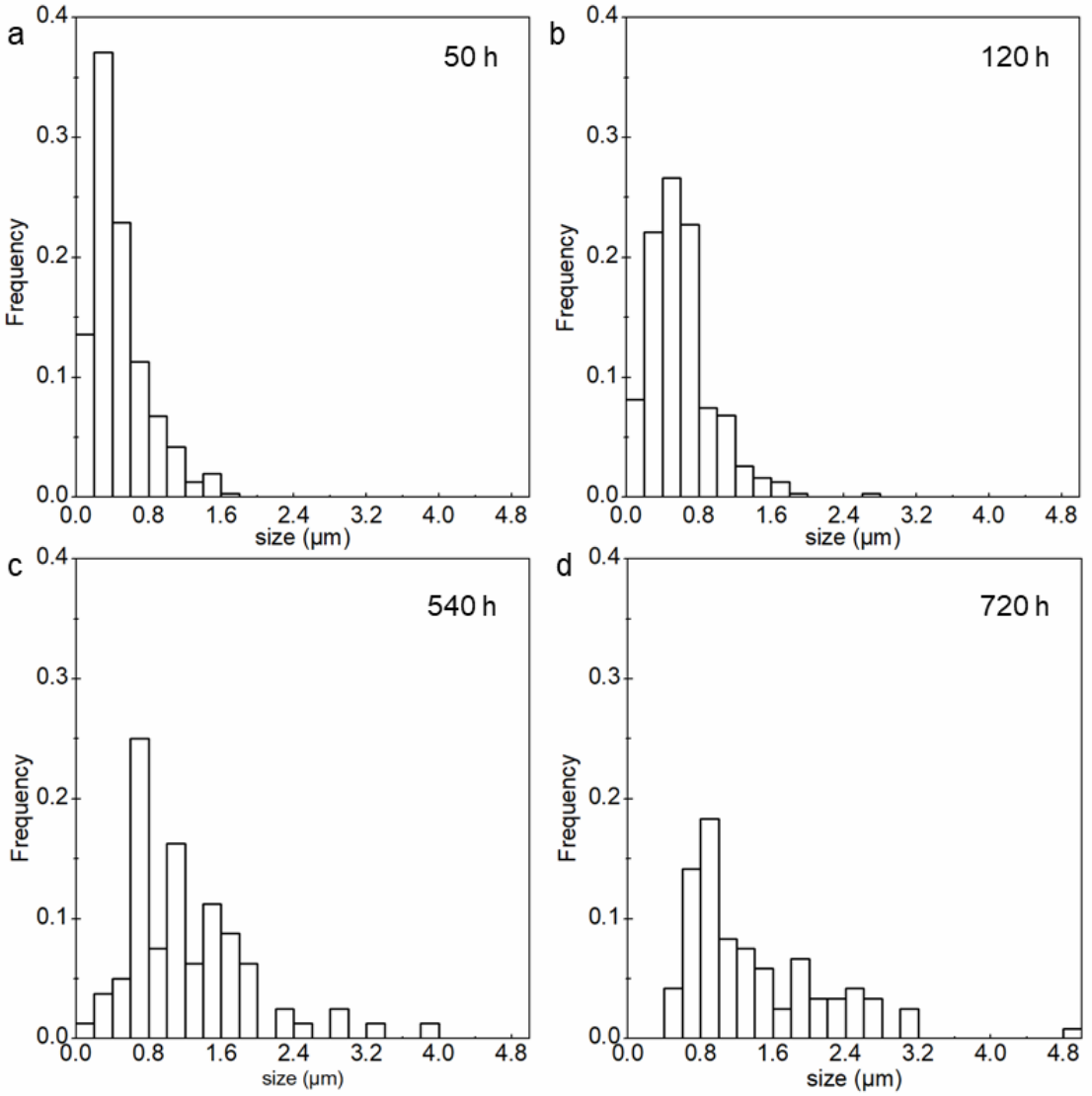

Figure 7.13 The statistic graphs showing precipitate size in the Al-4Ni-2Mn alloy after holding at 400 °C for (a) 50 h, (b) 120 h, (c) 540 h and (d) 720 h.

7.4 Summary

In the present chapter, thermal stability of the eutectic $Al_9(Ni, Mn)_2$ phase was investigated. The microstructural evolution and hardness response at 250 °C, 300 °C and 400 °C were characterized.

The eutectic $Al_9(Ni, Mn)_2$ phase demonstrated good thermal stability at 250 °C. No coarsening of eutectic rods was observed and the hardness remained the same level in the as-cast sample even after isothermal holding for 2000 h at 250 °C. After isothermal holding at 300 °C and 400 °C, a solid phase transformation from $Al_9(Ni, Mn)_2$ into κ-phase was observed. The κ-phase appeared at the α-Al/$Al_9(Ni, Mn)_2$ interphase boundaries and broke the eutectic $Al_9(Ni, Mn)_2$ rods into several segments. The transformation from $Al_9(Ni, Mn)_2$ into κ-phase was notably slow at 400 °C. Al_6Mn precipitates were also observed in the α-Al matrix at 400 °C. The average size of the Al_6Mn precipitates was measured to be 1.258 μm after 540 h at 400 °C. The results in this chapter confirmed the good stability of the eutectic $Al_9(Ni, Mn)_2$ phase at 250 °C. The Al-Ni-Mn alloys are believed to be suitable for applications at 250 °C.

Chapter 8: The Effect of Alloying Elements (Cu, Ce) on Microstructure and Mechanical Properties of Al-Ni-Mn Alloys

8.1 Introduction

Previous chapters showed that the Al-Ni-Mn alloys have good softening resistance and microstructural stability at elevated temperatures, which demonstrates potential for commercial applications. However, the maximum strength achieved by Al-Ni-Mn alloys is still unsatisfactory. Therefore, effective approaches to further strengthening Al-Ni-Mn alloys are needed. In this chapter, the effect of alloying additions on the microstructure and mechanical properties of Al-Ni-Mn alloys are investigated. Cu is widely used in Al-Si alloys as an effective strengthening element. The metastable θ′ (tetragonal Al_2Cu) precipitates provide a strong strengthening effect and lead to a high strength. Notably, the Cu addition to Al-Ni-Mn alloys have not been studied yet. Similarly, Ce was reported being capable of improving elevated temperature strength by introducing heat resistant intermetallic phases [80,103,115,117], but no related research has been carried out for Al-Ni-Mn alloys yet. In this chapter, for the first time we sought to investigate the effect of Cu and Ce on the microstructure and mechanical properties of the Al-5Ni-2Mn alloy. Tensile tests were performed at both ambient temperature and 250 °C

8.2 Effect of Cu on the microstructure and mechanical properties

8.2.1 Microstructures of Al-5Ni-2Mn-(0-2)Cu alloys

Figure 8.1 displays the microstructures of the Al-5Ni-2Mn, Al-5Ni-2Mn-1Cu and Al-5Ni-2Mn-2Cu alloys. The Al-5Ni-2Mn alloy consists of primary α-Al and eutectic α-Al+$Al_9(Ni, Mn)_2$ structure, which is also confirmed by XRD in Figure 8.2. From Figure 8.1 (c, d) and Figure 8.2, 1% Cu addition did not induce an microstructural change and the formation of Cu-rich phase. When Cu content was increased to 2.0%, a very small amount of Al_2Cu

phase was observed by SEM, as indicated by arrows in Figure 8.1 (f). However, these Al_2Cu particles were not detected by XRD due to its small amount.

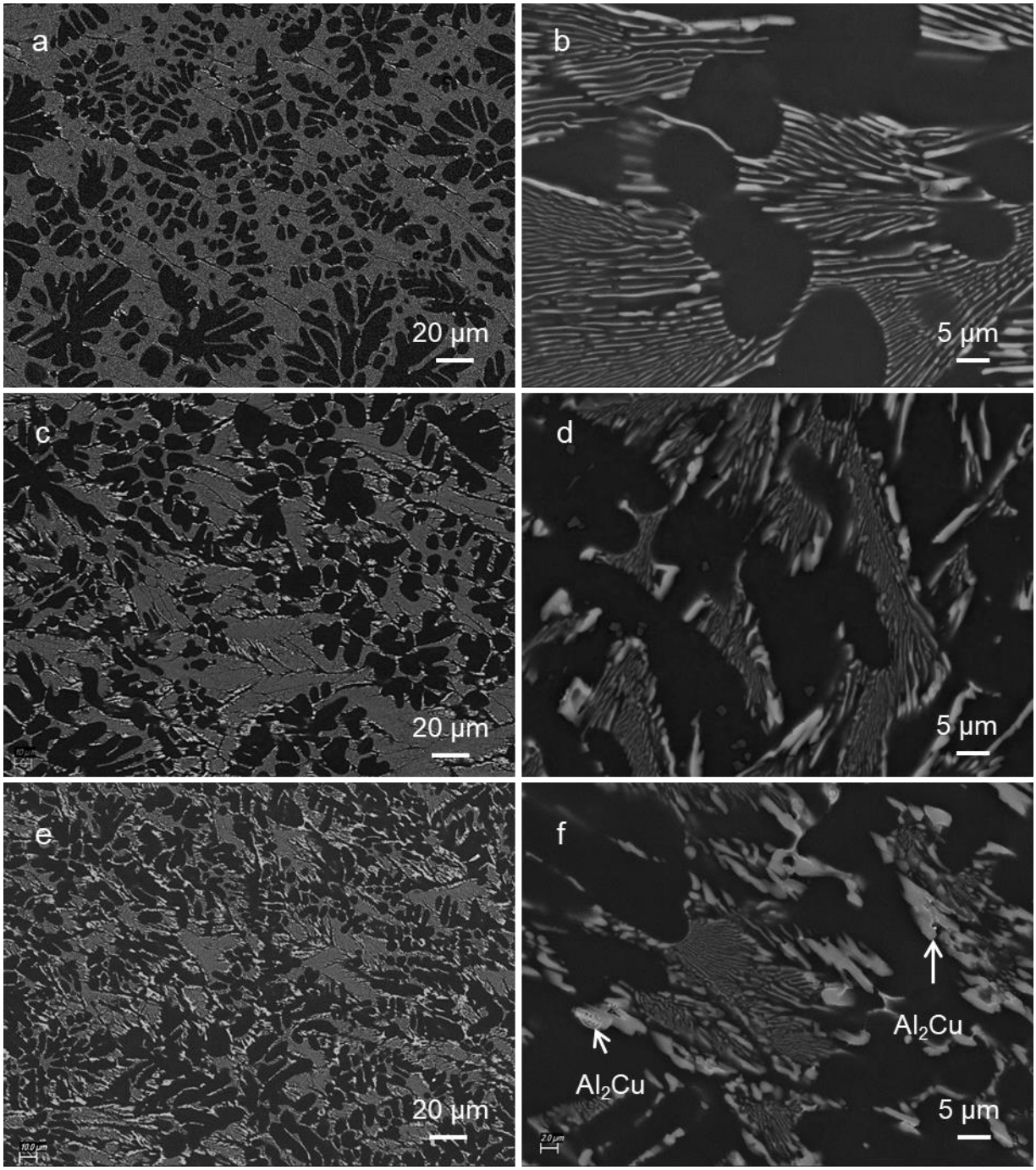

Figure 8.1 SEM micrographs showing the microstructures of (a, b)Al-5Ni-2Mn, (c, d) Al-5Ni-2Mn-1Cu, (e, f) Al-5Ni-2Mn-2Cu.

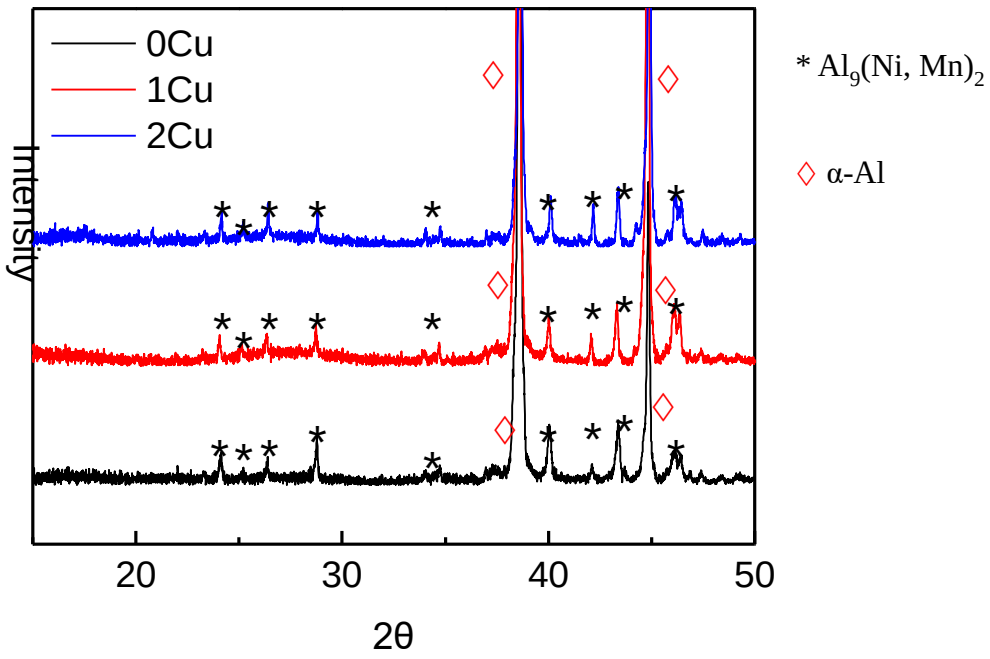

Figure 8.2 XRD patterns for the Al-5Ni-2Mn, Al-5Ni-2Mn-1Cu, and Al-5Ni-2Mn-2Cu alloys.

8.2.2 Mechanical properties of Al-5Ni-2Mn-(0-2)Cu alloys

Figure 8.3 shows the effect of Cu on the room temperature tensile properties of the as-cast Al-5Ni-2Mn alloy. Cu additions improved both yield strength and UTS. The Al-5Ni-2Mn alloy presents a yield strength of 109 MPa while Al-5Ni-2Mn-1Cu and Al-5Ni-2Mn-2Cu show yield strength of 115 MPa and 130 MPa, respectively. The Al-5Ni-2Mn alloy displays a UTS of 228 MPa while Al-5Ni-2Mn-1Cu and Al-5Ni-2Mn-2Cu alloy show UTS of 254 MPa and 248 MPa, respectively. Moreover, the elongation decreased significantly with increasing Cu content. It dropped continuously from 7.6% for the Al-5Ni-2Mn alloy to 4.8% for the Al-5Ni-2Mn-1Cu and 2.0% for the Al-5Ni-2Mn-2Cu alloy.

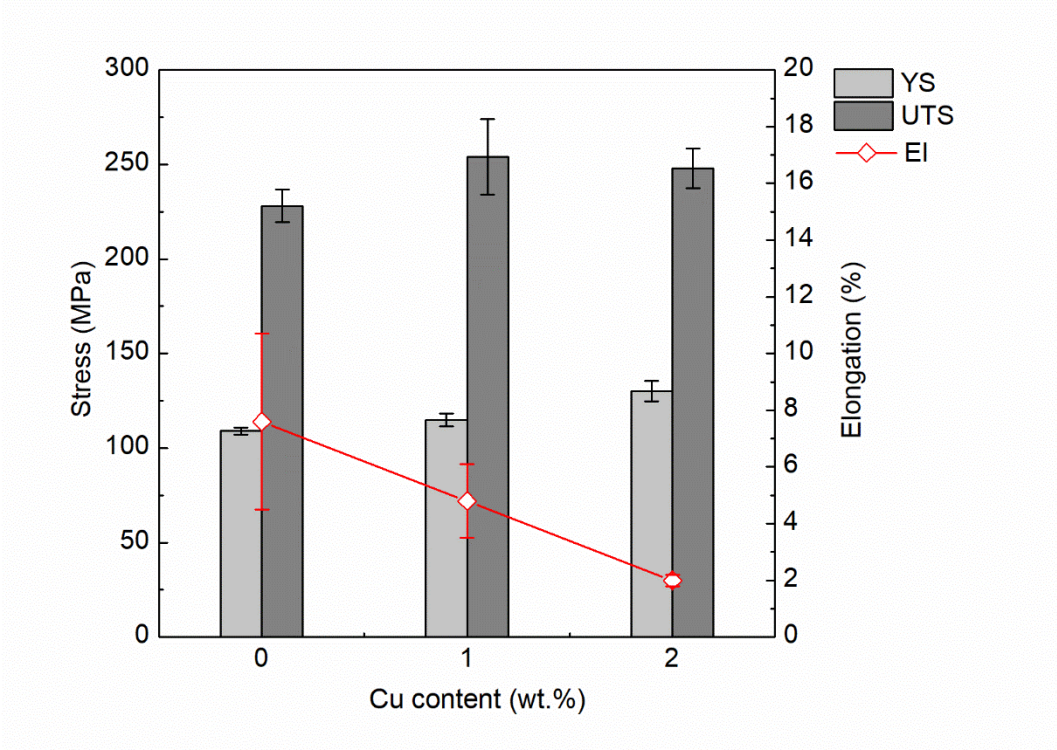

Figure 8.3 Effect of Cu contents on tensile properties of the as-cast Al-5Ni-2Mn alloy at room temperature.

Figure 8.4 presents the effect of Cu on the tensile properties of Al-5Ni-2Mn alloy at 250 °C. Cu additions slightly improves the yield strength. The Al-5Ni-2Mn alloy presented a yield strength of 90 MPa at 250 °C. The Al-5Ni-2Mn-1Cu and the Al-5Ni-2Mn-2Cu alloys showed 94 MPa and 102 MPa, respectively, at 250 °C. However, Cu additions did not induce an improvement on UTS as expected. On the contrary, Cu slightly decreased the UTS at 250 °C. The Al-5Ni-2Mn alloy presented a UTS of 140 MPa while the Al-5Ni-2Mn-1Cu and Al-5Ni-2Mn-2Cu alloys displayed 128 and 134 MPa, respectively.

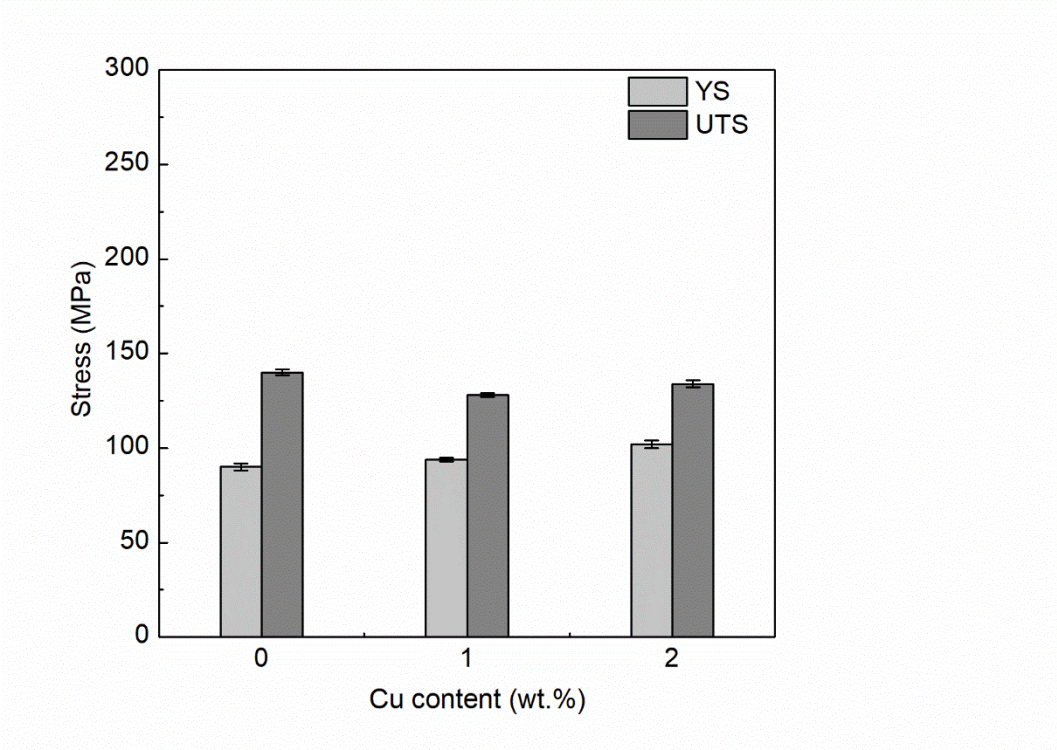

Figure 8.4 The effect of Cu contents on tensile strength of as-cast Al-5Ni-2Mn alloys at 250 °C.

The Cu was found in three phases. Firstly, Cu dissolved in the primary α-Al phase during solidification. According to the Al-Cu binary phase diagram [167], the maximum solubility of Cu in Al is 5.65%. The compositions of α-Al were obtained by EDS. The α-Al contained 1.1% Cu in the Al-5Ni-2Mn-1Cu alloy and it contained 2.1% Cu in the Al-5Ni-2Mn-2Cu alloy. The Cu atoms dissolved in the α-Al provide solid solution strengthening. Secondly, Cu atoms also dissolved in the $Al_9(Ni, Mn)_2$ phase. In the Al-5Ni-2Mn-2Cu alloy, the $Al_9(Ni, Mn)_2$ phase contained 1.0% Cu. Thirdly, the Cu provides the formation of the Al_2Cu phase, providing secondary phase strengthening. To sum up, the Cu additions could strengthen the Al-Ni-Mn alloys by both solid solution strengthening and secondary phase strengthening.

Figure 8.5 shows the effect of Cu contents on Vickers hardness of the Al-5Ni-2Mn alloy. The Al-5Ni-2Mn alloy exhibited a hardness of 62.2 HV10, while the Al-5Ni-2Mn-1Cu alloy showed a hardness of 70.5 HV10. When Cu content increased to 2%, the hardness increased

to 83.3 HV10. The Vickers hardness confirmed the expected improvement in hardness with increasing Cu contents.

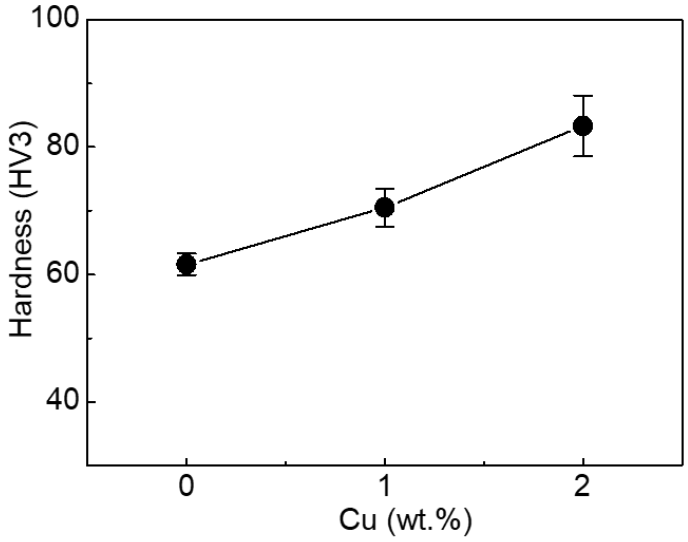

Figure 8.5 The effect of Cu contents on the Vickers hardness of the Al-5Ni-2Mn alloy.

8.2.3 Heat treatment exploration

Cu improved tensile strength and Vickers hardness of the as-cast Al-5Ni-2Mn alloy. Normally, Cu can produce precipitates, which further improve tensile strength and hardness by heat treatment. Here suitable heat treatment is explored. Since the Cu-containing phases start to melt at above 530 °C [80,168,169], the solution temperature for the Cu-containing Al-Si alloys is usually set at 530 °C and below [79,171,172]. Moreover, as mentioned in Chapter 7, the acicular Al_6Mn phase within α-Al matrix appeared after 120 h at 400 °C and grew to 1.258 μm after 540 h. Based on these, the solution temperature for the Al-5Ni-2Mn-1Cu alloy is determined to be 450 °C.

Figure 8.6 displays the microstructure of Al-5Ni-2Mn-1Cu alloy after solution treatment at 450 °C for different time: 2 h, 6 h and 12 h. No precipitates were observed after 2 h solution treatment at 450 °C. When the solution time was increased to 6 h, fine acicular precipitates were observed in the primary α-Al phase. These precipitates were identified to be the Al_6Mn

precipitates with size varying from 100 nm to 1000 nm. As the solution time increased to 12 h, Al_6Mn precipitates grew up to 2 to 5 μm and the precipitate density decreased.

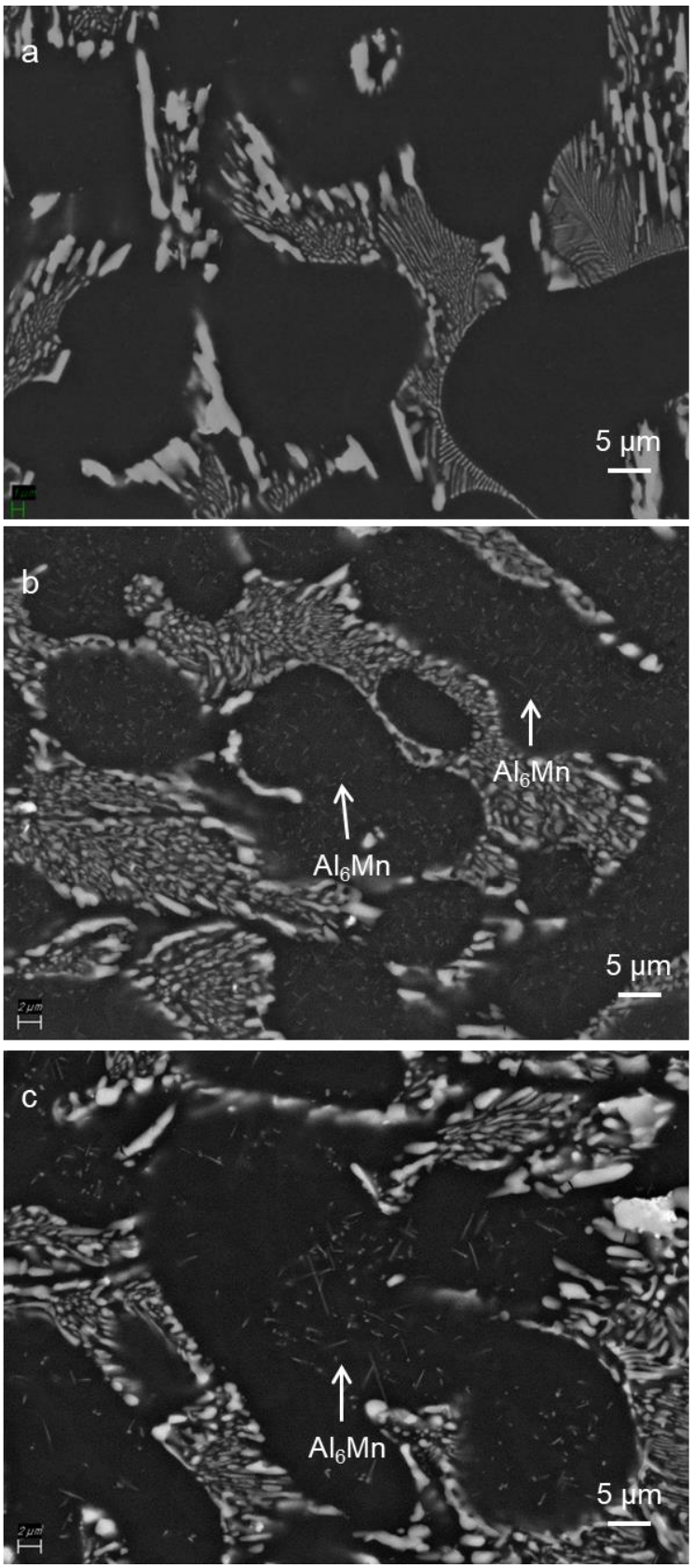

Figure. 8.6 Microstructure of the Al-5Ni-2Mn-1Cu alloy after solution treatment at 450 °C for (a) 2 h, (b) 6 h and (c) 12 h.

Apart from the appearance of Al_6Mn precipitates, the eutectic $Al_9(Ni, Mn)_2$ phase changed during solution treatment as well. When solution time increased to 6 h, as can be seen in Figure 8.6b, the eutectic $Al_9(Ni, Mn)_2$ rods were broken up into segments. And when solution time increased to 12 h, spheroidization and coarsening of the $Al_9(Ni, Mn)_2$ segments were observed.

The ageing procedure was set at 170 °C for 12 h, which is widely used in Cu containing Al-Si alloys [170–172]. The microstructures are displayed in Figure. 8.7. No precipitates were observed after 12 h ageing for sample with 2 h solution treatment by SEM. After 6 h solution treatment and 12 h ageing, fine precipitates were observed. The precipitates were examined and confirmed to be a mixture of Al_6Mn and Al_2Cu. After ageing with 12 h solution treatment, the amount of precipitates increased. The proportion of Al_2Cu precipitates also increased.

Figure 8.8 presents the Vickers hardness response of the Al-5Ni-2Mn-1Cu alloy after solution as well as ageing. During solution, the hardness slightly decreased with increasing solution time. It decreased from 70.5 HV10 to 65.5 HV10 after 6 h solution and to 64.0 HV10 after 12 h solution, respectively. The decrease of hardness during solution is common, which is usually associated with dissolving of the secondary phases, such as the Al_2Cu phase in this alloy. Breaking-up of the eutectic $Al_9(Ni, Mn)_2$ rods during solution is another factor decreases the hardness.

The hardness of the as-cast Al-5Ni-2Mn-1Cu alloy increased after ageing. It increased from 70.5 HV10 to 71.6 HV10 after 2 h solution treatment and ageing, and 77.7 HV10 after 6 h solution treatment and 12 h ageing, respectively. It then remained at the same level after 12 h solution treatment and 12 h ageing. The maximum hardness obtained through heat treatment was 77.7 HV10, provided by a combination of 6 h solution treatment at 450 °C and 12 h ageing at 170 °C. In comparison with the as-cast sample, heat treatment only

provided 7.2 HV10 increase. To sum up, the hardness of Al-Ni-Mn-Cu alloys was not improved effectively by heat treatment. The limited improvement with Cu addition could be explained by two factors. Firstly, the distribution of Cu may provide a clue. There was no Al_2Cu phase observed in Al-5Ni-2Mn-1Cu alloy. The Cu was found in the α-Al and eutectic $Al_9(Ni, Mn)_2$ phase. The α-Al phase contains 1.1% Cu and the $Al_9(Ni, Mn)_2$ also contains about 1.0% Cu. Thus, some of the Cu is not free to strengthen the alloy since it goes into the eutectic $Al_9(Ni, Mn)_2$ phase, which was not able to produce Al_2Cu precipitates. Secondly, the breaking-up of eutectic $Al_9(Ni, Mn)_2$ rods during solution treatment decreases hardness. The well aligned eutectic rods broke into segments after 6 h at 450 °C. When solution time increased to 12 h, spheroidization and coarsening of the $Al_9(Ni, Mn)_2$ segments were observed. Breaking-up and coarsening of eutectic $Al_9(Ni, Mn)_2$ rods decrease hardness. Particularly, large Al_6Mn precipitates were observed after solution treatment. As mentioned before, after 6 h solution treatment at 450 °C, Al_6Mn precipitates formed with a size of 100 nm to 1000 nm. The size of these precipitates increased to 2 to 5 μm after 12 h solution treatment. Large Al_6Mn precipitates may not decrease hardness but definitely harm strength and elongation. Therefore, Cu additions to Al-5Ni-2Mn was not able to provide effective improvement.

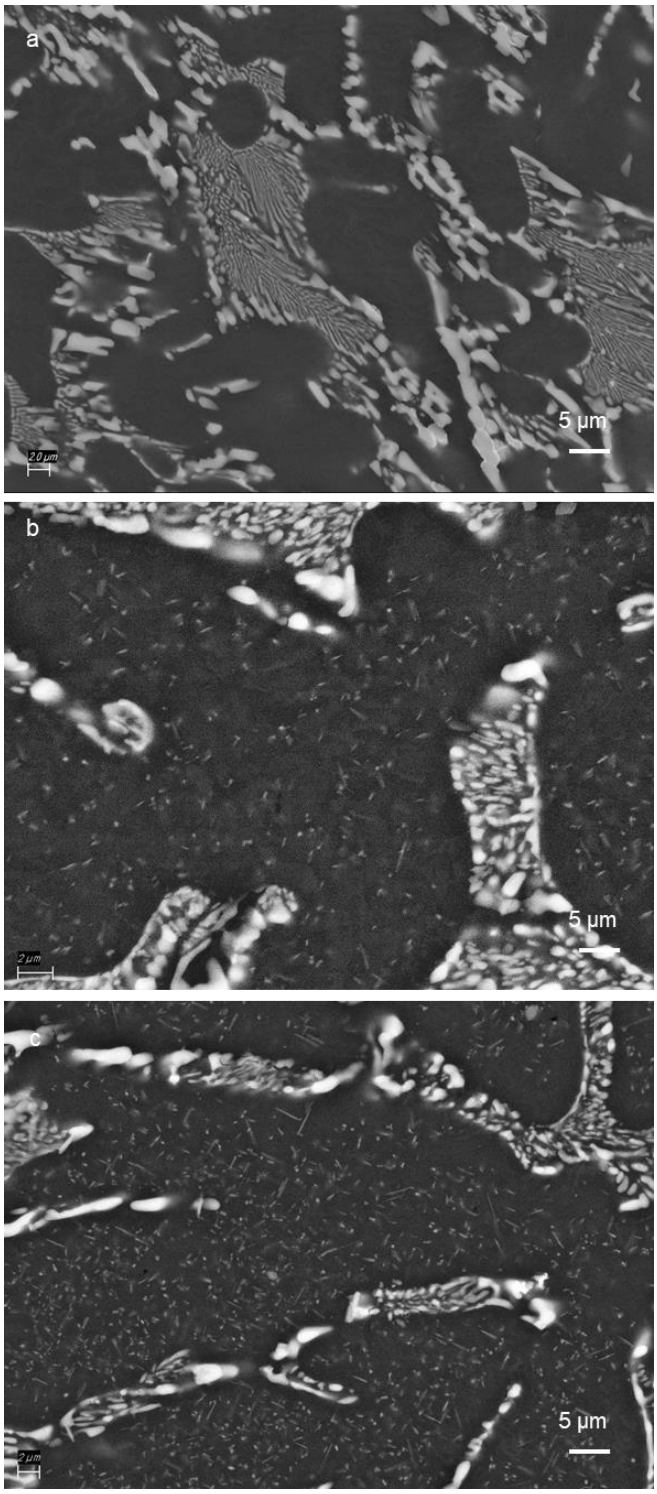

Figure 8.7 Precipitates in Al-5Ni-2Mn-1Cu alloy after ageing for samples solutioned at 450 °C for (a) 2 h, (b) 6 h, and (c) 12 h.

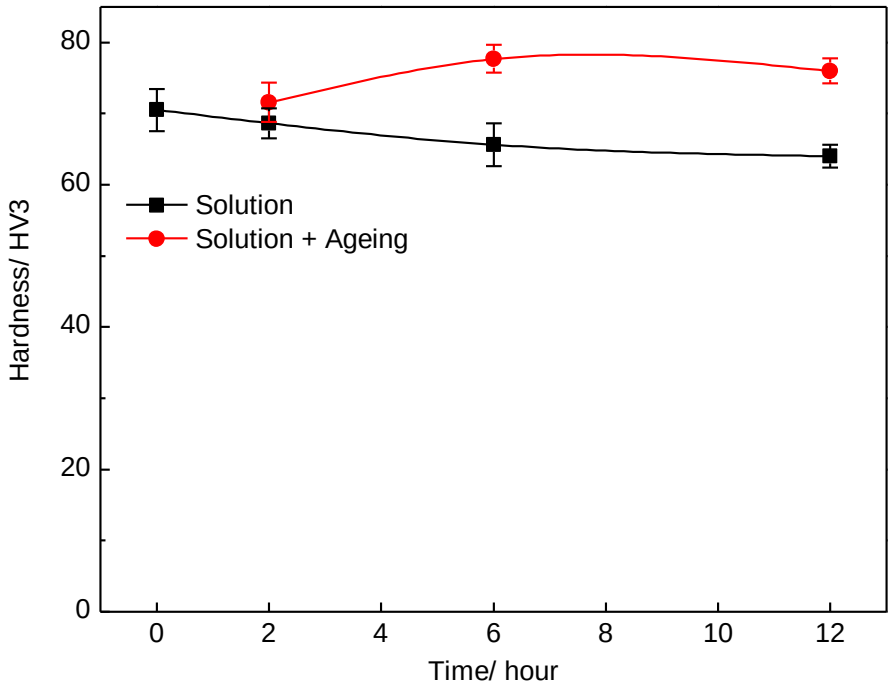

Figure 8.8 Vickers hardness of the Al-5Ni-2Mn-1Cu alloy after solution and ageing.

8.3 Effect of Ce on Microstructure and mechanical properties

8.3.1 Microstructure of Al-5Ni-2Mn-(0-4)Ce alloys

The Ce element was widely studied to modify the eutectic silicon phase in Al-Si alloys [19,173] and its effect on improving elevated temperature strength was also reported [80,103,115,117]. However, no related research has been done in Al-Ni-Mn alloy yet. Three levels of Ce addition (0.5%, 2.0% and 4.0%) were added to Al-5Ni-2Mn alloy. The effect of Ce on microstructure and mechanical properties was investigated in the present work.

Figure 8.9 displays the microstructures of Al-5Ni-2Mn alloy with different levels of Ce contents. When 0.5% Ce was added, apart from primary α-Al phase and the eutectic $Al_9(Ni, Mn)_2$ phase, a small amount of bright eutectic phase was observed, as indicated by the arrows in Figure 8.9b. XRD patterns of the Al-5Ni-2Mn alloys with Ce additions were also tested and displayed in Figure 8.10. Comparing the peaks of Al-5Ni-2Mn-0.5Ce alloy with existing PDF cards of different AlCe compounds, the Ce-rich phase in experimental alloys was identified as $Al_{11}Ce_3$ phase (PDF Card: 04-002-7472). When Ce content increased to

2.0%, the eutectic $Al_9(Ni, Mn)_2$ changed from rod-like to fibrous. The amount of eutectic $Al_{11}Ce_3$ phase also increased. When the Ce content increased to 4.0%, a primary intermetallic phase appeared. It has a composition of Al-16.4Ce-11.8Mn-1.3Ni, and was identified as $Al_{10}Mn_2Ce$ phase. The XRD pattern in Figure 8.10 confirmed the existence of $Al_{10}Mn_2Ce$ (PDF Card: 51-1052). Furthermore, the amount of eutectic $Al_{11}Ce_3$ phase in Al-5Ni-2Mn-4Ce alloy increased. In summary, eutectic $Al_{11}Ce_3$ phase and primary $Al_{10}Mn_2Ce$ phase successively formed with increasing Ce contents.

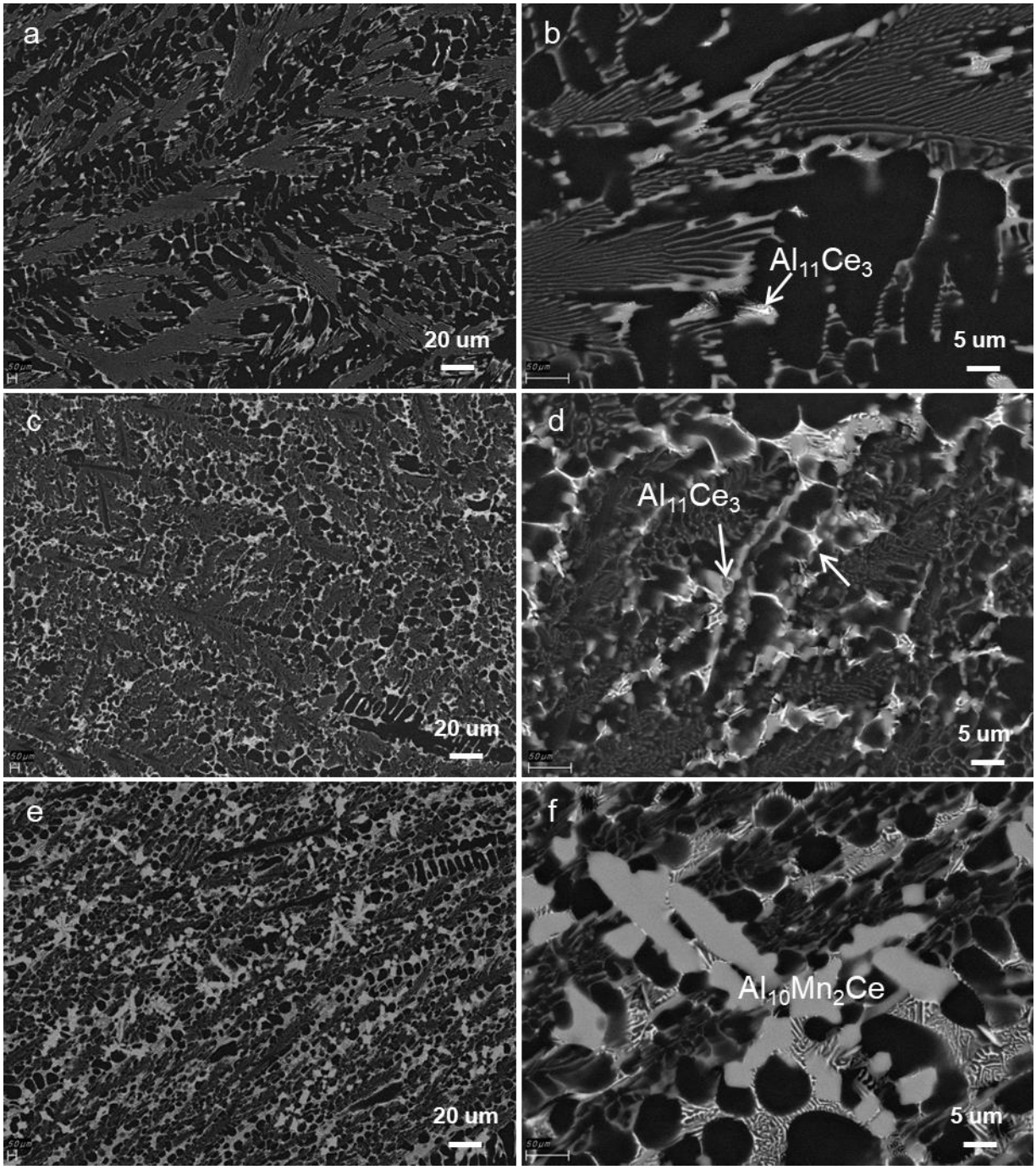

Figure 8.9 SEM images showing typical microstructure of (a, b) Al-5Ni-2Mn-0.5Ce, (c, d) Al-5Ni-2Mn-2Ce, (e, f) Al-5Ni-2Mn-4Ce.

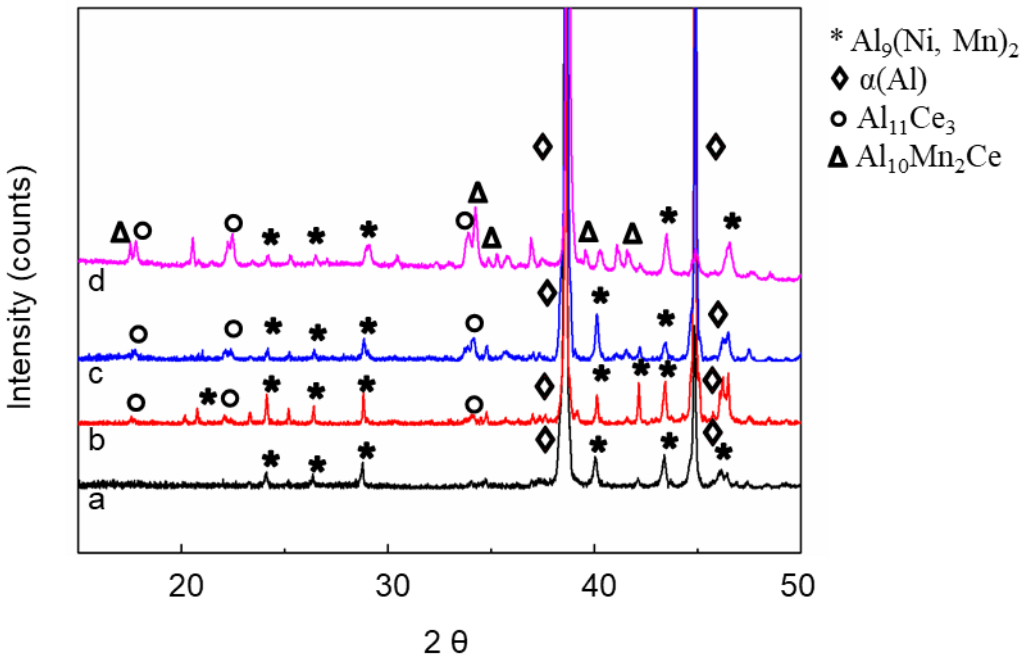

Figure 8.10 XRD patterns for the (a) Al-5Ni-2Mn alloy, (b) Al-5Ni-2Mn-0.5Ce alloy, (c) Al-5Ni-2Mn-2Ce alloy, (d) Al-5Ni-2Mn-4Ce alloy.

Figure 8.11 displays the Al-Ce binary phase diagram. In the Al-rich corner, the eutectic point is about 11% Ce, and the eutectic intermetallic phase is $Al_{11}Ce_3$ phase. Hence an alloy with Ce content below 11% is a hypoeutectic Al-Ce alloy. The calculated phase diagram of Al-5Ni-2Mn-Ce by Pandat is shown in Figure 8.12. According to the calculation results, for Al-5Ni-2Mn-Ce (Ce<5%), the primary intermetallic phases are Al_6Mn, Al_3Ni phases, and the eutectic structure is ternary α-Al+Al3Ni+$Al_{11}Ce_3$ phases. The only Ce-containing phase is the eutectic $Al_{11}Ce_3$ phase. There are some differences between the experimental outcomes and the calculated results. Firstly, primary $Al_{10}Mn_2Ce$ was observed in the Al-5Ni-2Mn-4Ce alloy, but it does not exist in the calculated equilibrium phase diagram. Secondly, the eutectic phases observed are α-Al+$Al_{11}Ce_3$+Al_9(Ni, Mn)$_2$ phases, while they were α-Al+Al_6Mn+Al_3Ni+$Al_{11}Ce_3$ in the calculations. The absence of the Al_3Ni and Al_6Mn was already discussed in Chapter 4.

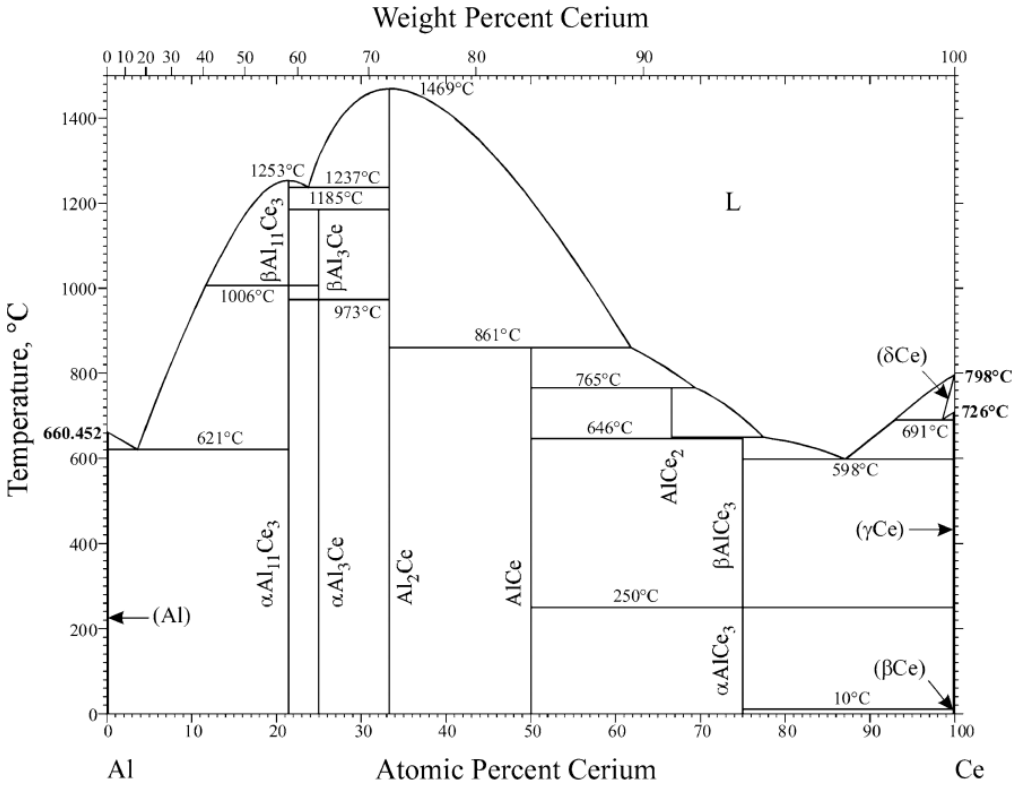

Figure 8.11 Al-Ce phase diagram[174]

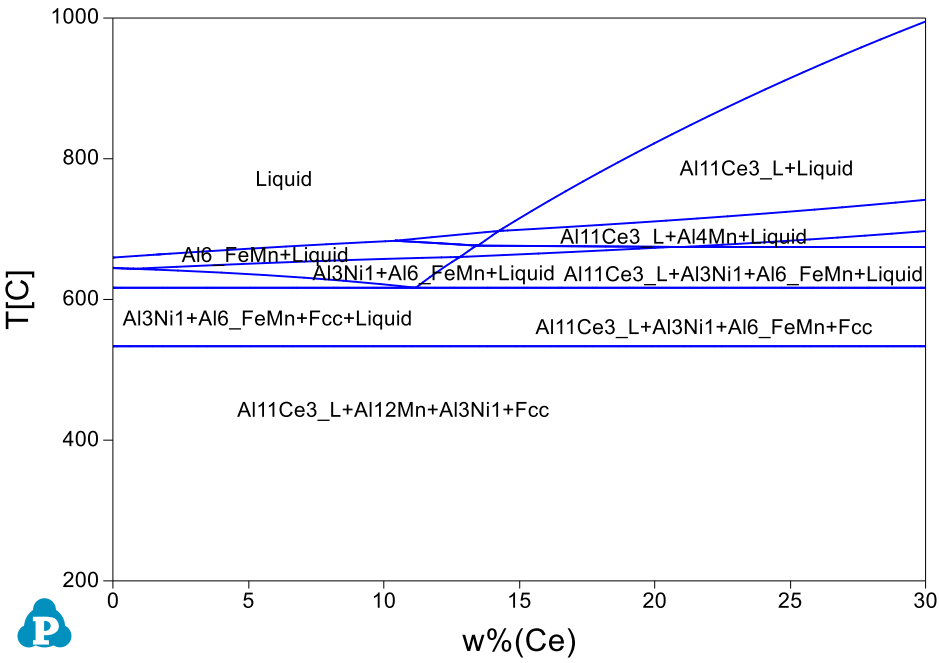

Figure 8.12 Calculated equilibrium phase diagram of Al-5Ni-2Mn-Ce by Pandat.

8.3.2 Mechanical properties of Al-5Ni-2Mn-(0-4)Ce alloys

Figure 8.13 displays the effect of Ce on the Vickers hardness of the Al-5Ni-2Mn alloy. It is seen that Ce addition significantly improves hardness. The Al-5Ni-2Mn alloy showed a hardness of 62.2 HV10, while the Al-5Ni-2Mn-0.5Ce alloy showed 73.3 HV10, which was a 18% improvement. The hardness then increased to 89.3 HV10 for the Al-5Ni-2Mn-2Ce alloy and to 91.1 HV10 for the Al-5Ni-2Mn-4Ce alloy. The hardness increase is mainly associated with appearance of the eutectic $Al_{11}Ce_3$ and primary $Al_{10}Mn_2Ce$ phases. Additionally, the amount of soft primary α-Al phase decreased with Ce addition. In contrast, the amount of eutectic phases and primary $Al_{10}Mn_2Ce$ phase increased. This explains the hardness increase with increasing Ce contents.

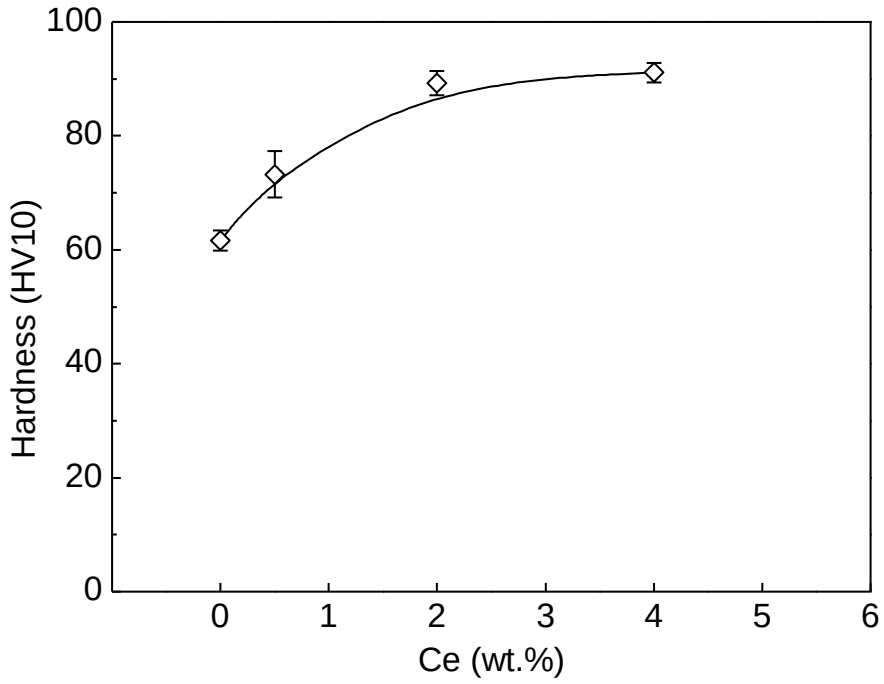

Figure 8.13 Effect of Ce contents on the Vickers hardness of the Al-5Ni-2Mn alloy.

Figure 8.14 presents the effect of Ce on tensile properties of Al-5Ni-2Mn alloy at ambient temperature. Notably, Ce addition did not improve yield strength or UTS. The strength firstly decreased with 0.5% Ce and then slightly increased when Ce content further increased to 2.0% and 4.0%. The Al-5Ni-2Mn alloy displayed a yield strength of 108 MPa; it then slightly decreased to 98 MPa and 99 MPa, respectively, for the Al-5Ni-2Mn-0.5Ce

alloy and Al-5Ni-2Mn-2Ce alloy. When Ce content increased to 4%, the yield strength slightly increased to 104 MPa. Moreover, the elongation decreased remarkably with increasing Ce content. It decreased from 7.6% for the Al-5Ni-2Mn alloy to 3.3% for the Al-5Ni-2Mn-4Ce.

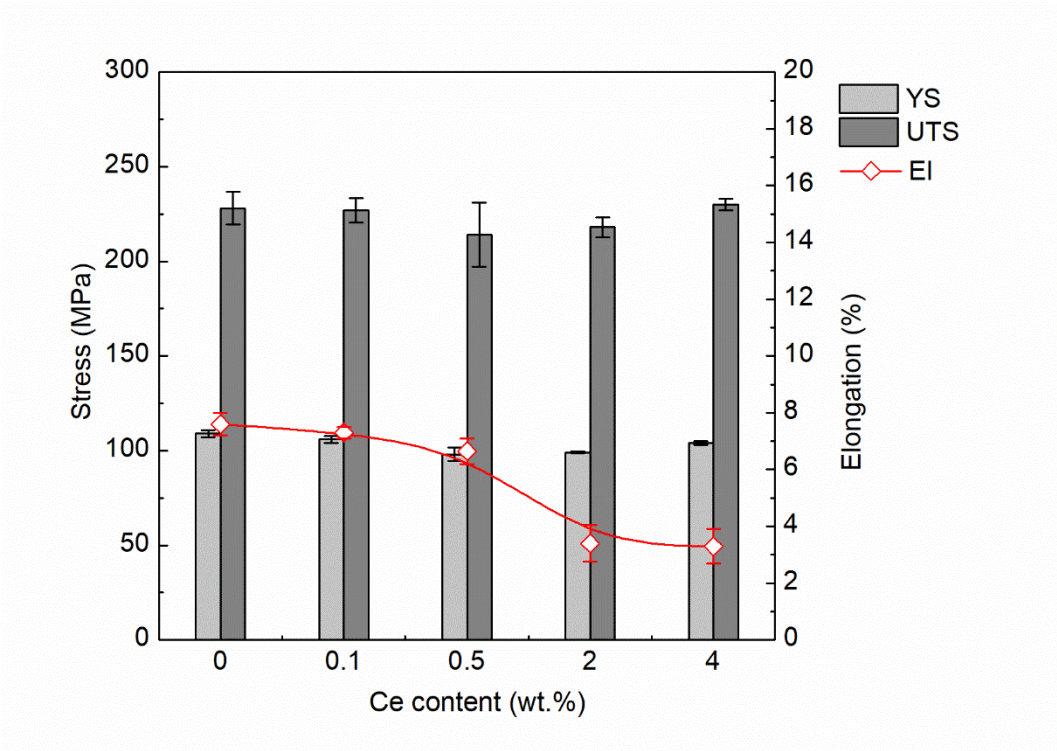

Figure 8.14 Effect of Ce contents on tensile properties of the Al-5Ni-2Mn alloy at ambient temperature.

Figure 8.15 presents the effect of Ce on tensile strength at 250 °C. It can be seen that Ce did not show an improvement on tensile strength at 250 °C. Alloys with Ce addition presented a similar level of tensile strength as the Al-5Ni-2Mn alloy.

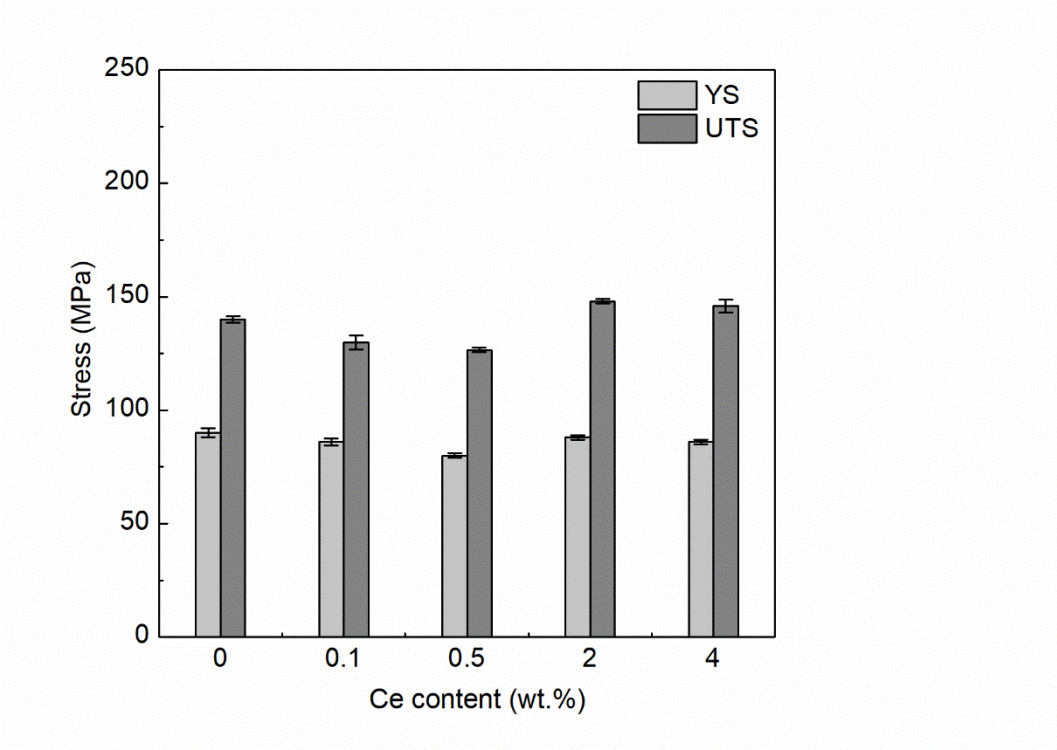

Figure 8.15 Effect of Ce contents on tensile properties of the Al-5Ni-2Mn alloy at 250 °C.

According to the results above, Ce additions have no improvement on the strength of the Al-5Ni-2Mn alloy. It is mainly associated with the morphological change of the eutectic $Al_9(Ni, Mn)_2$ phase. Figure 8.16 displays the effect of Ce on the morphology of $Al_9(Ni, Mn)_2$ phase in the Al-5Ni-2Mn alloy. The morphology changed from well aligned rods to fibrous structure with increasing Ce contents. Obviously, the well aligned rods provide better strength. The limited strength increment by eutectic $Al_{11}Ce_3$ phase is another reason for Ce addition presented no improvement on tensile strength. As reported in ref [175], the strength increment by the eutectic $Al_{11}Ce_3$ phase was measured to be 67±20 MP. It was much smaller than that of Al_3Ni phase (150±10 MPa) and Si phase (153±10 MPa). Moreover, the eutectic $Al_9(Ni, Mn)_2$ phase provides better strength than the Al_3Ni phase. Therefore, the eutectic $Al_{11}Ce_3$ phase introduced by Ce addition is weaker than the $Al_9(Ni, Mn)_2$ phase, which offers a negative effect on tensile strength of the Al-5Ni-2Mn alloy.

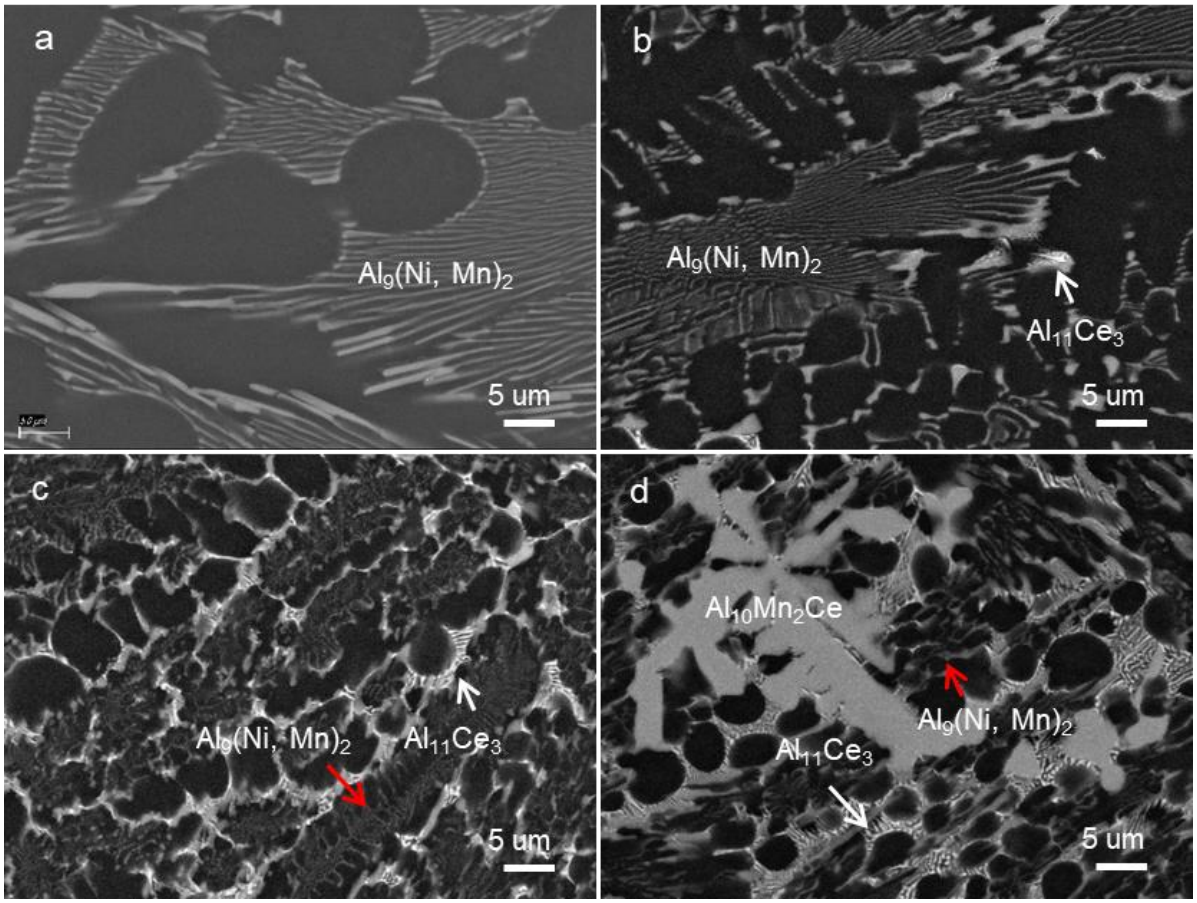

Figure 8.16 SEM images showing the eutectic $Al_9(Ni, Mn)_2$ phase in Al-5Ni-2Mn alloy with different Ce content. (a) 0%, (b) 0.5%, (c) 2.0%, (d) 4.0%

8.4 Summary

In this chapter, the effects of Cu (1.0%, 2.0%) and Ce (0.1%, 0.5%, 2.0%, 4.0%) on the microstructure and mechanical properties of the Al-5Ni-2Mn alloy were investigated.

No Cu-containing phase was observed in the alloys with 1.0% Cu. When Cu content increased to 2.0%, a very small amount of eutectic Al_2Cu phase was observed. Cu additions improved the yield strength from 109 MPa to 130 MPa and the UTS increased from to 228 MPa to 248 MPa at ambient temperature. At 250 °C, the yield strength increased from 90 MPa to 102 MPa, and the UTS showed no viable increase. While T6 heat treatment just induced a very slight strengthening effect (a hardness increasement of 7 HV10), because of the dissolution of Cu-rich phases into the $Al_9(Ni, Mn)_2$ phase and the segmentation of eutectic $Al_9(Ni, Mn)_2$ rods during solution treatment at 450 °C.

Ce addition to the Al-5Ni-2Mn alloy introduced the formation of eutectic $Al_{11}Ce_3$ phase and primary $Al_{10}Mn_2Ce$ phase. The hardness significantly increased with increasing the Ce content. However, the tensile strength was not improved at both ambient temperature and 250 °C. It is mainly due to the morphological change of the eutectic $Al_9(Ni, Mn)_2$ phase from well aligned rods to fibrous structure and the weak strengthening effect of the eutectic $Al_{11}Ce_3$ phase compared with the $Al_9(Ni, Mn)_2$ phase.

Chapter 9: Conclusions

Six objectives including (1) the effect of Mn on the microstructure and mechanical properties of Al-4Ni, Al-6Ni, and Al-8Ni alloys, (2) relationship between the microstructure and the mechanical properties of Al-Ni-Mn alloys, (3) the effect of cooling rates on the microstructure, (4) the size and distribution of primary intermetallic phases at different pouring temperatures, (5) the thermal stability of eutectic $Al_9(Ni, Mn)_2$ phase at 250 °C, 300 °C, and 400 °C, (6) minor additions of alloying elements (Cu, Ce) are achieved. This thesis provide a comprehensive understanding of Al-Ni-Mn alloys. The main conclusions are as follows:

1) Mn in the Al-4Ni alloy could transform the eutectic structure from α-Al+Al_3Ni to α-Al+$Al_9(Ni, Mn)_2$. The eutectic $Al_9(Ni,Mn)_2$ phase showed rod-like shapes. The κ-phase and O-phase was seen in the alloy with 3% Mn, and the Al_6Mn phase appeared in the alloy with 4% Mn. The tensile strength showed a significant improvement in the Al-Ni alloy with Mn additions. The yield strength increased by 69 MPa at room temperature and 66 MPa at 250 °C, respectively. This improvement was mainly attributed to the solid solution of Mn in α-Al, the increase amount of eutectic phases and the primary intermetallic phases in the alloys with increased Mn contents. Moreover, Mn additions also led to a change in fractural mechanism. The Al-4Ni alloy and Al-4Ni-2Mn alloy presented a typical ductile fracture at ambient temperature, while the Al-4Ni-4Mn alloy displayed a mixed ductile and brittle fracture. More significantly, Mn additions improved softening resistance at 250 °C. The alloys with Mn addition presented less strength loss than the Al-4Ni alloy when temperature was increased to 250 °C. It was because that Mn additions transformed the eutectic structure from α-Al+Al_3Ni to α-Al+$Al_9(Ni, Mn)_2$. The $Al_9(Ni, Mn)_2$ phase displayed better softening resistance than the Al_3Ni phase at elevated temperatures.

2) Mn additions in Al-6Ni and Al-8Ni alloys transformed the eutectic structure from α-Al+Al_3Ni to α-Al+$Al_9(Ni, Mn)_2$. Additionally, the primary Al_3Ni phase in Al-6Ni and Al-

8Ni alloys could be transformed into $Al_9(Ni, Mn)_2$ phase with 2% Mn. When the Mn content increased to 3% and 4%, κ-phase appeared. Mn addition increased the tensile strength of Al-6Ni and Al-8Ni alloys at both ambient temperature and 250 °C. Specifically, the Al-6Ni-xMn alloys presented higher strength than Al-8Ni-xMn and Al-4Ni-xMn alloys.

3) The best strength of the experimental Al-Ni-Mn alloys studied in Chapter 4 and Chapter 5 was achieved by the Al-6Ni-4Mn alloy. It offered the yield strength of 164 MPa and UTS of 248 MPa at ambient temperature. At 250 °C, the yield strength was 134 MPa and the UTS was 176 MPa. More significantly, the $Al_9(Ni, Mn)_2$ phase presented superior softening resistance. The Al-6Ni-4Mn alloy could still retain 82% of the yield strength at 250 °C. However, the Al-Cu-Mn-Zr alloys from literature, such as RR350 and ACMZ01 alloys, retain less than 60% of the yield strength at 300 °C, providing 170 to 200 MPa at ambient temperature and 100 MPa at 300 °C. Therefore, the Al-6Ni-4Mn alloy showed comparable tensile strength, which demonstrated the potential of Al-Ni-Mn alloys for elevated temperature applications.

4) The study on cooling rates showed that both the eutectic phases and primary phases in the Al-4Ni-2Mn alloy changed with decreasing cooling rates. The eutectic structure was α-Al+Al9(Ni, Mn)2 phases in PMC alloy and then became α-Al+$Al_9(Ni, Mn)_2$+O and a mixture of α-Al+$Al_9(Ni, Mn)_2$+O+Al_3Ni as the cooling rates decreased to 20 K/min and 0.5 K/min, respectively. Primary α-Al phase was the only primary phase in PMC alloy. When cooling rate decreased to 5 K/min and 0.2 K/min, the O-phase and Al_6Mn phase began to form, respectively. Moreover, the pouring temperature affected the size and distribution of primary phases. The primary phases distributed more uniformly and became smaller as pouring temperature decreased.

5) The eutectic $Al_9(Ni, Mn)_2$ phase demonstrated good thermal stability, and the Al-Ni-Mn alloys were suitable for applications at 250 °C. No coarsening of eutectic rods was observed and the hardness remained the same level as as-cast samples after holding 2000

h at 250 °C. However, when the alloy was isothermal held at 300 °C and 400 °C, the solid phase transformation from $Al_9(Ni, Mn)_2$ into κ-phase was observed. The κ-phase appeared at the α-Al/$Al_9(Ni, Mn)_2$ interphase boundaries and broke the eutectic $Al_9(Ni, Mn)_2$ rods into several segments. The transformation from $Al_9(Ni, Mn)_2$ into κ-phase was notably slow at 400 °C. Moreover, the Al_6Mn precipitates were found in the α-Al matrix at 400 °C. The average size of the Al_6Mn precipitates was measured to be 1.258 μm after 540 h at 400 °C.

6) The minor elements alloying study revealed the effects of Cu and Ce on the microstructure and mechanical properties of Al-Ni-Mn alloys. A small amount of eutectic Al_2Cu phase was observed with 2.0% Cu in Al-Ni-Mn alloys. The yield strength under as-cast condition increased from 109 MPa to 130 MPa with 2.0% Cu at ambient temperature. At 250 °C, the yield strength increased from 90 MPa to 102 MPa. However, the following T6 heat treatment only induced a very slight strengthening effect (a hardness increasement of 7 HV10), because of partial dissolution of Cu in the $Al_9(Ni, Mn)_2$ phase and the segmentation of eutectic $Al_9(Ni, Mn)_2$ rods during solution.

7) Ce addition in the Al-5Ni-2Mn alloy introduced eutectic $Al_{11}Ce_3$ phase and primary $Al_{10}Mn_2Ce$. The hardness increased significantly with increasing the Ce content, while the tensile strength was not improved at both ambient temperature and 250 °C. It is mainly due to the morphological change of the eutectic $Al_9(Ni, Mn)_2$ phase from well aligned rods to fibrous structure and the weaker strengthening effect of the eutectic $Al_{11}Ce_3$ phase compared with the $Al_9(Ni, Mn)_2$ phase.

Chapter 10: Suggestions for Future Work

In the present study, a comprehensive understanding of Al-Ni-Mn alloys was presented. The microstructure and mechanical properties with different Ni and Mn contents were obtained and tensile strength was tested for the Al-6Ni-4Mn alloy. The Al-Ni-Mn alloys showed good thermal stability at 250 °C. The cooling rates was found to be able to change the primary phases and eutectic phases. The pouring temperature affected the distribution and size of primary intermetallic phases. Whereas for better evaluating the application potential of Al-Ni-Mn alloys and for further improvement of mechanical properties of Al-Ni-Mn alloys, several suggestions are proposed for future works.

(1) High resolution TEM characterization on the eutectic $Al_9(Ni, Mn)_2$ phase and the κ-phase during holding at 300 °C and above. Phase transformation in solids always follows specific orientation relationships (ORs), which helps to understand the nucleation and growth of κ-phase.

(2) The tensile strength of Al-Ni-Mn alloys needs to be tested at more temperatures such as 280 °C, 300 °C and 350 °C. The holding time prior to tensile test at these temperatures also need to vary from 1 h to 1000 h. These results will offer detailed information to determine the application temperatures for Al-Ni-Mn alloys.

(3) The exploration of the addition of minor elements to Al-Ni-Mn alloys for further improvement of mechanical properties is essential. The solubility of Ni and Mn in Al alloys is limited and therefore the strengthening is not significant. The further study using minor elements to strengthen the alloy at ambient temperature and at high temperature is essential to make the alloy practically useful in future.

(4) The manufacturing process is another area for further study. Currently we used gravity casting. It has been found that the cooling rate is significant for the microstructural evolution and mechanical properties. Therefore, the optimisation of casting process and the use of alternatives to achieve optimised mechanical

properties in association with excellent process flexibility are huge tasks for the applications of these alloys.

(5) The fundamental of dataset for equilibrium phase diagrams for Al-Ni-Mn based alloys are missing in the literature. The works in setting up the dataset are very necessary for understanding the solidification and microstructural evolution. This can be an important direction for future work.

References

[1] K.E. Knipling, D.C. Dunand, D.N. Seidman, Criteria for developing castable, creep-resistant aluminium-based alloys - A review, Zeitschrift Für Metallkunde. 97 (2006) 246–265.

[2] M. Arfan, X. Cong, X. Wang, H. Shuji, Y. Hiroshi, R. Li, C. Ma, High strength aluminium cast alloy: A Sc modification of a standard Al-Si-Mg cast alloy, Materials Science and Engineering A. 604 (2014) 122–126.

[3] J. Røyset, N. Ryum, Scandium in aluminium alloys, International Materials Reviews. 50 (2005) 19–44.

[4] S. Riva, K.V. Yusenko, N.P. Lavery, D.J. Jarvis, S.G.R. Brown, The scandium effect in multicomponent alloys, International Materials Reviews. 61 (2016) 203–228.

[5] C.B. Fuller, D.N. Seidman, Temporal evolution of the nanostructure of Al(Sc,Zr) alloys: Part II-coarsening of Al3(Sc1-xZrx) precipitates, Acta Materialia. 53 (2005) 5415–5428.

[6] T. Gao, X. Zhu, Q. Sun, X. Liu, Morphological evolution of ZrAlSi phase and its impact on the elevated-temperature properties of Al–Si piston alloy, Journal of Alloys and Compounds. 567 (2013) 82–88.

[7] A.M.A. Mohamed, F.H. Samuel, S.A. Kahtani, Microstructure, tensile properties and fracture behaviour of high temperature Al–Si–Mg–Cu cast alloys, Materials Science and Engineering: A. 577 (2013) 64–72.

[8] M.H. Abdelaziz, E.A. Elsharkawi, H.W. Doty, F.H. Samuel, Mechanical performance of Zr-containing 354-type Al-Si-Cu-Mg cast alloy: Role of geometrical discontinuities, Journal of Materials Engineering and Performance. 29 (2018) 6640–6651.

[9] G. Liu, P. Blake, S. Ji, Effect of Zr on the high cycle fatigue and mechanical properties of Al–Si–Cu–Mg alloys at elevated temperatures, Journal of Alloys and Compounds. 809 (2019) 151795.

[10] K. Wang, P. Tang, Y. Huang, Y. Zhao, W. Li, J. Tian, Characterization of microstructures and tensile properties of recycled Al-Si-Cu-Fe-Mn alloys with individual and combined addition of titanium and cerium, Scanning. 2018 (2018).

[11] M. Jaradeh, T. Carlberg, Effect of titanium additions on the microstructure of DC-cast aluminium alloys, Materials Science and Engineering: A. 413–414 (2005) 277–282.

[12] R.S. Rana, R. Purohit, S. Das, Reviews on the influences of alloying elements on the microstructure and mechanical properties of aluminium alloys and aluminium alloy composites, International Journal of Scientific and Research Publications. 2 (2012) 1–7.

[13] Y. Meng, J. Cui, Z. Zhao, Y. Zuo, Effect of vanadium on the microstructures and mechanical properties of an Al-Mg-Si-Cu-Cr-Ti alloy of 6XXX series, Journal of Alloys and Compounds. 573 (2013) 102–111.

[14] S.K. Shaha, F. Czerwinski, W. Kasprzak, J. Friedman, D.L. Chen, Microstructure and mechanical properties of Al-Si cast alloy with additions of Zr-V-Ti, Materials and Design. 83 (2015) 801–812.

[15] J. Hernandez-Sandoval, G.H. Garza-Elizondo, A.M. Samuel, S. Valtiierra, F.H. Samuel, The ambient and high temperature deformation behaviour of Al–Si–Cu–Mg alloy with minor Ti, Zr, Ni additions, Materials and Design. 58 (2014) 89–101.

[16] Z. Nie, T. Jim, J. Fu, G. Xu, J. Yang, J. Zhou, T. Zuo, Research on Rare earth in Aluminium, Materials Forum. 396–402 (2002) 1731–1736.

[17] X. Hu, F. Jiang, F. Ai, H. Yan, Effects of rare earth Er additions on microstructure development and mechanical properties of die-cast ADC12 aluminium alloy, Journal of Alloys and Compounds. 538 (2012) 21–27.

[18] E.A. de la Torre, R. Pérez-Bustamante, J. Camarillo-Cisneros, C.D. Gómez-Esparza, H.M. Medrano-Prieto, R. Martínez-Sánchez, Mechanical properties of the A356 aluminium alloy modified with La/Ce, Journal of Rare Earths. 31 (2013) 811–816.

[19] K. Nogita, S.D. McDonald, A.K. Dahle, Eutectic modification of Al-Si alloys with rare earth metals, Materials Transactions. 45 (2004) 323–326.

[20] F. Mao, Y. Qiao, P. Zhang, L. Ou, C. Chen, C. Zhang, Y. Wang, Modification mechanism of rare earth Eu on eutectic Si in hypoeutectic Al-Si alloy, International Journal of Metalcasting 2021. (2021) 1–12.

[21] R.A. Karnesky, M.E. van Dalen, D.C. Dunand, D.N. Seidman, Effects of substituting rare-earth elements for scandium in a precipitation-strengthened Al-0.08 at. %Sc alloy, Scripta Materialia. 55 (2006) 437–440.

[22] Y. Harada, D.C. Dunand, Microstructure of Al3Sc with ternary rare-earth additions, Intermetallics. 17 (2009) 17–24.

[23] S.A. Alkahtani, E.M. Elgallad, M.M. Tash, A.M. Samuel, F.H. Samuel, Effect of rare earth metals on the microstructure of Al-Si Based alloys, Materials. 9 (2016) 45–57.

[24] R.E. Franck, J.A. Hawk, Effect of very high temperatures on the mechanical properties of Al-Fe-V-Si alloy, Scripta Metallurgica. 23 (1989) 113–118.

[25] G.J. Shiflet, Y. He, S.J. Poon, Mechanical properties of aluminium-rich AlFeGd metallic glass, Scripta Metallurgica. 22 (1988) 1661–1664.

[26] L. Rogal, Z. Szklarz, P. Bobrowski, D. Kalita, G. Garzel, A. Tarasek, M. Kot, M. Szlezynger, Microstructure and mechanical properties of Al–Co–Cr–Fe–Ni base high entropy alloys obtained using powder metallurgy, Metals and Materials International. 25 (2019) 930–945.

[27] P. Biswas, S. Patra, H. Roy, C.S. Tiwary, M. Paliwal, M.K. Mondal, Effect of Mn addition on the mechanical properties of Al–12.6Si alloy: Role of Al15(MnFe)3Si2 intermetallic and microstructure modification, Metals and Materials International. 27 (2021) 1713–1727.

[28] Y. Fan, K. Huang, M.M. Makhlouf, Precipitation strengthening in Al-Ni-Mn alloys, Metallurgical and Materials Transactions A: Physical Metallurgy and Materials Science. 46 (2015) 5830–5841.

[29] W. Yu, Q. Hao, L. Fan, J. Li, Eutectic solidification microstructure of an Al-4Ni-2Mn alloy, Journal of Alloys and Compounds. 688 (2016) 798–803.

[30] J. Lin, V. Zolotorevsky, M. Glazoff, S. Murtha, N. Belov, Dispersion hardenable Al-Ni-Mn casting alloys for automotive and aerospace structural components., 2004.

[31] W.S. Miller, L. Zhuang, J. Bottema, A.J. Wittebrood, P. de Smet, A. Haszler, A. Vieregge, Recent development in aluminium alloys for the automotive industry, Materials Science and Engineering: A. 280 (2000) 37–49.

[32] M. Javidani, D. Larouche, Application of cast Al-Si alloys in internal combustion engine components, International Materials Reviews. 59 (2014) 132–158.

[33] H.N. Bogart, Automotive cylinder block materials - cast iron, SAE Technical Papers. (1961).

[34] S.H. Choo, S. Lee, S.J. Kwon, Surface hardening of a grey cast iron used for a diesel engine cylinder block using high-energy electron beam irradiation, Metallurgical and Materials Transactions A. 30 (1999) 1211–1221.

[35] European Aluminium Association, Applications – Power train – Cylinder heads, The Aluminium Automotive Manual. (2011) 1–11.

[36] Adroit Market Research, Global engine block market size, share and industry forecast 2018-2025, 2018.

[37] D. Weiss, High performance aluminium casting alloys for engine applications, SAE Technical Papers. 32 (2016) 1–19.

[38] R. Torres, J. Esparza, E. Velasco, S. García-Luna, R. Colás, Characterisation of an aluminium engine block, International Journal of Microstructure and Materials Properties. 1 (2006) 129–138.

[39] L. Kerni, A. Raina, M.I.U. Haq, Performance evaluation of aluminium alloys for piston and cylinder applications, Materials Today: Proceedings. 5 (2018) 18170–18175.

[40] S. Roy, L.F. Allard, A. Rodriguez, T.R. Watkins, A. Shyam, Comparative evaluation of cast aluminium alloys for automotive cylinder heads: Part I—microstructure evolution, Metallurgical and Materials Transactions A. 48 (2017) 2529–2542.

[41] R. Jahn, W.T. Donlon, J.E. Allison, Characterization of age hardening in a 319 Al alloy, Microscopy and Microanalysis. 4 (1998) 514–515.

[42] A.M. Samuel, F.H. Samuel, H.W. Doty, Observations on the formation of β-Al5FeSi phase in 319 type Al-Si alloys, Journal of Materials Science. 31 (1996) 5529–5539.

[43] J. Espinoza-Cuadra, G. García-García, H. Mancha-Molinar, Influence of defects on strength of industrial aluminium alloy Al–Si 319, Materials and Design. 28 (2007) 1038–1044.

[44] J. Espinoza-Cuadra, P. Gallegos-Acevedo, H. Mancha-Molinar, A. Picado, Effect of Sr and solidification conditions on characteristics of intermetallic in Al–Si 319 industrial alloys, Materials and Design. 31 (2010) 343–356.

[45] A. Lombardi, C. Ravindran, R. MacKay, Improvements in mechanical properties of 319 Al alloy engine blocks through cost-effective solution heat treatment, Journal of Materials Engineering and Performance. 23 (2014) 2766–2771.

[46] S.M. Miresmaeili, S.G. Shabestari, S.M.A. Boutorabi, The effect of Sr-modification treatment on porosity formation of reduced pressure 319 Al alloy castings, Canadian Metallurgical Quarterly. 42 (2003) 245–252.

[47] M.M. Makhlouf, D. Apelian, Casting characteristics of aluminium die casting alloys, Idaho Falls, 2002.

[48] M. Karamouz, M. Azarbarmas, M. Emamy, M. Alipour, Microstructure, hardness and tensile properties of A380 aluminium alloy with and without Li additions, Materials Science and Engineering: A. 582 (2013) 409–414.

[49] K.N. Obiekea, S.Y. Aku, D.S. Yawas, Effects of pressure on the mechanical properties and microstructure of die cast aluminium A380 alloy, Journal of Minerals and Materials Characterization and Engineering. 2 (2014) 248–258.

[50] M. Wang, W. Xu, Q. Han, The influence of Sr addition on the microstructure of A380 alloy, International Journal of Metalcasting. 11 (2016) 321–327.

[51] S. Toschi, Optimization of A354 Al-Si-Cu-Mg alloy heat treatment: Effect on microstructure, hardness, and tensile properties of peak aged and overaged alloy, Metals, 8 (2018) 961-976.

[52] A. Morri, L. Ceschini, S. Messieri, E. Cerri, S. Toschi, Mo Addition to the A354 (Al–Si–Cu–Mg) Casting Alloy: Effects on Microstructure and Mechanical Properties at Room and High Temperature, Metals 2018, Vol. 8, Page 393. 8 (2018) 393.

[53] C.L. Chen, G.D. West, R.C. Thomson, Characterisation of intermetallic phases in multicomponent Al-Si casting alloys for engineering applications, Materials Science Forum. 519–521 (2006) 359–364.

[54] S. Manasijevic, R. Radisa, S. Markovic, Z. Acimovic-Pavlovic, K. Raic, Thermal analysis and microscopic characterization of the piston alloy AlSi13Cu4Ni2Mg, Intermetallics. 19 (2011) 486–492.

[55] S. Manasijevic, Z. Pavlovic-Acimovic, K. Raic, R. Radisa, V. Kvrgić, Optimisation of cast pistons made of Al-Si piston alloy, International Journal of Cast Metals Research. 26 (2013) 255–261.

[56] Y. Yang, K. Yu, Y. Li, D. Zhao, X. Liu, Evolution of nickel-rich phases in Al-Si-Cu-Ni-Mg piston alloys with different Cu additions, Materials and Design. 33 (2012) 220–225.

[57] A. Humbertjean, T. Beck, Effect of the casting process on microstructure and lifetime of the Al-piston-alloy AlSi12Cu4Ni3 under thermo-mechanical fatigue with superimposed high-cycle fatigue loading, International Journal of Fatigue. 53 (2013) 67–74.

[58] K. Pratheesh, M. Ravi, A. Kanjirathinkal, M.A. Joseph, Effects of Sr and pressure on microstructure, mechanical and wear properties of near eutectic Al–Si piston alloys, International Journal of Cast Metals Research. 28 (2015) 301–309.

[59] P. Krishnankutty, A. Kanjirathinkal, M.A. Joseph, M. Ravi, Effect of aging time on mechanical properties and wear characteristics of near eutectic Al–Si–Cu–Mg–Ni piston alloy, Transactions of the Indian Institute of Metals. 68 (2015) 25–30.

[60] R. Ahmad, M.B.A. Asmael, Influence of Cerium on microstructure and solidification of eutectic Al–Si piston alloy, Materials and Manufacturing Processes. 31 (2016) 1948–1957.

[61] J. Jorstad, D. Apelian, Hypereutectic Al-Si alloys: Practical casting considerations, International Journal of Metalcasting. 3 (2009) 13–36.

[62] S. Hegde, K.N. Prabhu, Modification of eutectic silicon in Al–Si alloys, Journal of Materials Science. 43 (2008) 3009–3027.

[63] R. Ahmad, M.B.A. Asmael, N.R. Shahizan, S. Gandouz, Reduction in secondary dendrite arm spacing in cast eutectic Al–Si piston alloys by cerium addition, International Journal of Minerals, Metallurgy and Materials. 24 (2017) 91–101.

[64] G.H. Zhang, J.X. Zhang, B.C. Li, W. Cai, Characterization of tensile fracture in heavily alloyed Al-Si piston alloy, Progress in Natural Science: Materials International. 21 (2011) 380–385.

[65] H. Fujii, T. Oka, Development of lightweight forged piston material by optimizing size of needle-type intermetallic compound, SAE International Journal of Materials and Manufacturing. 1 (2009) 450–458.

[66] L. Ceschini, A. Morri, E. Balducci, N. Cavina, N. Rojo, L. Calogero, L. Poggio, Experimental observations of engine piston damage induced by knocking combustion, Materials and Design. 114 (2017) 312–325.

[67] J. il Choi, J.H. Park, J.H. Kim, S.K. Kim, Y.H. Kim, J.H. Lee, A study on manufacturing of aluminium automotive piston by thixoforging, The International Journal of Advanced Manufacturing Technology. 32 (2006) 280–287.

[68] J.G. Kaufman, Properties of aluminium alloys: tensile, creep, and fatigue data at high and low temperatures, ASM International. (2006).

[69] A. Thirugnanam, K. Sukumaran, U.T.S. Pillai, K. Raghukandan, B.C. Pai, Effect of Mg on the fracture characteristics of cast Al–7Si–Mg alloys, Materials Science and Engineering: A. 445–446 (2007) 405–414.

[70] M.Z. Wu, J.W. Zhang, Y. bin Zhang, H.Q. Wang, Effects of Mg content on the fatigue strength and fracture behaviour of Al-Si-Mg casting alloys, Journal of Materials Engineering and Performance. 27 (2018) 5992–6003.

[71] P. Ouellet, F.H. Samuel, Effect of Mg on the ageing behaviour of Al-Si-Cu 319 type aluminium casting alloys, Journal of Materials Science. 34 (1999) 4671–4697.

[72] J. Røyset, N. Ryum, Scandium in aluminium alloys, International Materials Reviews. 50 (2005) 19–44.

[73] A.F. Norman, P.B. Prangnell, R.S. McEwen, The solidification behaviour of dilute aluminium-scandium alloys, Acta Materialia. 46 (1998) 5715–5732.

[74] J. Taendl, A. Orthacker, H. Amenitsch, G. Kothleitner, C. Poletti, Influence of the degree of scandium supersaturation on the precipitation kinetics of rapidly solidified Al-Mg-Sc-Zr alloys, Acta Materialia. 117 (2016) 43–50.

[75] J. Hyung-Ho, Kinetics of precipitation in Al-Sc alloys and low temperature solid solubility of scandium in aluminium studied by electrical resistivity measurements, Materials Science and Engineering. 171 (1993) 151–161.

[76] C.B. Fuller, D.N. Seidman, D.C. Dunand, Mechanical properties of Al(Sc,Zr) alloys at ambient and elevated temperatures, Acta Materialia. 51 (2003) 4803–4814.

[77] M. Wang, X. Du, Y. Li, Z. Zhang, H. Su, Y. Wu, Effect of Sc on as-cast microstructures and mechanical properties of Al-Si-Mg-Cu-Ti alloys, Key Engineering Materials. 732 (2017) 32–37.

[78] H.K. Govindaraju, T. Jayaraj, P.R. Sadanandarao, C.S. Venkatesha, Evaluation of mechanical properties of as-cast Al-Zn-Ce alloy, Materials and Design. 31 (2010) S24–S29.

[79] M. Vončina, S. Kores, P. Mrvar, J. Medved, Effect of Ce on solidification and mechanical properties of A360 alloy, Journal of Alloys and Compounds. 509 (2011) 7349–7355.

[80] W.L. Bevilaqua, A.R. Stadtlander, A.R. Froehlich, G.V.B. Lemos, A. Reguly, High-temperature mechanical properties of cast Al-Si-Cu-Mg alloy by combined additions of cerium and zirconium, Materials Research Express. 7 (2020) 0–12.

[81] M. Zamani, S. Toschi, A. Morri, L. Ceschini, S. Seifeddine, Effect of Mo addition on room and high temperature tensile behaviour of Al-Si-Cu-Mg alloy in as-cast and heat-treated conditions, Advanced Materials Research. 1155 (2019) 71–79.

[82] W. Kasprzak, B.S. Amirkhiz, M. Niewczas, Structure and properties of cast Al–Si based alloy with Zr–V–Ti additions and its evaluation of high temperature performance, Journal of Alloys and Compounds. 595 (2014) 67–79.

[83] S.K. Shaha, F. Czerwinski, W. Kasprzak, J. Friedman, D.L. Chen, Microstructure and mechanical properties of Al-Si cast alloy with additions of Zr-V-Ti, Materials and Design. 83 (2015) 801–812.

[84] S.K. Shaha, F. Czerwinski, W. Kasprzak, J. Friedman, D.L. Chen, Thermal stability of (AlSi)x(ZrVTi) intermetallic phases in the Al-Si-Cu-Mg cast alloy with additions of Ti, V, and Zr, Thermochimica Acta. 595 (2014) 11–16.

[85] S.K. Shaha, F. Czerwinski, W. Kasprzak, J. Friedman, D.L. Chen, Improving high-temperature tensile and low-Cycle fatigue behaviour of Al-Si-Cu-Mg alloys through micro-additions of Ti, V, and Zr, Metallurgical and Materials Transactions A: Physical Metallurgy and Materials Science. 46 (2015) 3063–3078.

[86] F. Czerwinski, S.K. Shaha, W. Kasprzak, J. Friedman, D.L. Chen, Thermal stability of Al-Si-Cu-Mg cast alloys modified with transition metals Zr, V and Ti, Materials Science Forum. 828–829 (2015) 29–34.

[87] J. Murray, A. Peruzzi, J.P. Abriata, The Al-Zr (aluminium-zirconium) system, Journal of Phase Equilibria. 13 (1992) 277–291.

[88] Roger. Reed, The superalloys: fundamentals and applications, Cambridge University Press, Cambridge, 2006.

[89] K.E. Knipling, D.C. Dunand, D.N. Seidman, Precipitation evolution in Al-Zr and Al-Zr-Ti alloys during isothermal aging at 375-425 °C, Acta Materialia. 56 (2008) 114–127.

[90] U. Patakham, J. Kajornchaiyakul, C. Limmaneevichitr, Grain refinement mechanism in an Al–Si–Mg alloy with scandium, Journal of Alloys and Compounds. 542 (2012) 177–186.

[91] E.A. Marquis, D.N. Seidman, Nanoscale structural evolution of Al 3 Sc precipitates in Al(Sc) alloys, Acta Materialia. 49 (2001) 1909–1919.

[92] S. Iwamura, Y. Miura, Loss in coherency and coarsening behaviour of Al3Sc precipitates, Acta Materialia. 52 (2004) 591–600.

[93] L.S. Toropova, D.G. Eskin, M.L. Kharakterovam, T.V. Dobatkina, Advanced aluminium alloys containing scandium: structure and properties, Gordon and Breach Science Publishers, Amsterdam, 1998.

[94] J.L. Murray, The Al-Sc (Aluminium-Scandium) system, Journal of Phase Equilibria. 19 (1998) 380–384.

[95] R.R. Sawtell, C.L. Jensen, Mechanical properties and microstructures of Al-Mg-Sc alloys, Metallurgical Transactions A. 21 (1990) 421–430.

[96] C.B. Fuller, J.L. Murray, D.N. Seidman, Temporal evolution of the nanostructure of Al(Sc,Zr) alloys: Part I – Chemical compositions of Al(ScZr) precipitates, Acta Materialia. 53 (2005) 5401–5413.

[97] J. Røyset, N. Ryum, Kinetics and mechanisms of precipitation in an Al-0.2 wt.% Sc alloy, Materials Science and Engineering: A. 396 (2005) 409–422.

[98] K.E. Knipling, D.N. Seidman, D.C. Dunand, Ambient-and high-temperature mechanical properties of isochronally aged Al–0.06 Sc, Al–0.06 Zr and Al–0.06 Sc–0.06 Zr (at.%) alloys, Acta Materialia. 59 (2011) 943–954.

[99] R. Ramli, M.K. Talari, A.Z. Omar Arawi, Microstructure and mechanical properties of Al-Si cast alloy grain refined with Ti-B-Sr-Sc-Mg, in: 2011 IEEE Colloquium on Humanities, Science and Engineering, Chuser, (2011) 692–695.

[100] E.A. Marquis, D.C. Dunand, Model for creep threshold stress in precipitation-strengthened alloys with coherent particles, Scripta Materialia. 47 (2002) 503–508.

[101] E.P. George, D.P. Pope, C.L. Fu, J.H. Schneibel, Deformation and fracture of L12 trialuminides, ISIJ International. 31 (1991) 1063–1075.

[102] H.K. Govindaraju, T. Jayaraj, P.R. Sadanandarao, C.S. Venkatesha, Evaluation of mechanical properties of as-cast Al–Zn–Ce alloy, Materials and Design. 31 (2010) S24–S29.

[103] D.H. Xiao, J.N. Wang, D.Y. Ding, H.L. Yang, Effect of rare earth Ce addition on the microstructure and mechanical properties of an Al-Cu-Mg-Ag alloy, Journal of Alloys and Compounds. 352 (2003) 84–88.

[104] F. Cverna, Thermal properties of metals, conductivity, thermal expansion, specific heat, ASM International, Ohio, 2002.

[105] C. Wolverton, V. Ozoliņš, Entropically favoured ordering: The metallurgy of Al2Cu revisited, Physical Review Letters. 86 (2001) 5518–5521.

[106] V. Vaithyanathan, C. Wolverton, L.Q. Chen, Multiscale modelling of θ′ precipitation in Al–Cu binary alloys, Acta Materialia. 52 (2004) 2973–2987.

[107] A. Shyam, S. Roy, D. Shin, J.D. Poplawsky, L.F. Allard, Y. Yamamoto, J.R. Morris, B. Mazumder, J.C. Idrobo, A. Rodriguez, T.R. Watkins, J.A. Haynes, Elevated temperature microstructural stability in cast AlCuMnZr alloys through solute segregation, Materials Science and Engineering A. 765 (2019) 138279.

[108] B.K. Milligan, S. Roy, C.S. Hawkins, L.F. Allard, A. Shyam, Impact of microstructural stability on the creep behaviour of cast Al–Cu alloys, Materials Science and Engineering: A. 772 (2020) 138697.

[109] P. Shower, S. Roy, C.S. Hawkins, A. Shyam, The effects of microstructural stability on the compressive response of two cast aluminium alloys up to 300 °C, Materials Science and Engineering: A. 700 (2017) 519–529.

[110] P. Shower, J.R. Morris, D. Shin, B. Radhakrishnan, L.F. Allard, A. Shyam, Temperature-dependent stability of θ′-Al2Cu precipitates investigated with phase field simulations and experiments, Materialia. 5 (2019) 100185.

[111] S.K. M, S. Mondol, S. Kumar, S. Suwas, K. Chattopadhyay, Aluminium based alloys for high temperature applications and method of producing such alloys, 2014.

[112] A. Shyam, J.A. Haynes, G. Black, J. Talamantes, High performance cast aluminium alloys for next generation passenger vehicle engines, 2018.

[113] Z.C. Sims, D. Weiss, S.K. McCall, M.A. McGuire, R.T. Ott, T. Geer, O. Rios, P.A.E. Turchi, Cerium-based, intermetallic-strengthened aluminium casting alloy: High-volume Co-product development, JOM. 68 (2016) 1940–1947.

[114] N.A. Belov, E.A. Naumova, D.G. Eskin, Casting alloys of the Al–Ce–Ni system: microstructural approach to alloy design, Materials Science and Engineering: A. 271 (1999) 134–142.

[115] Z.C. Sims, O.R. Rios, D. Weiss, P.E.A. Turchi, A. Perron, J.R.I. Lee, T.T. Li, J.A. Hammons, M. Bagge-Hansen, T.M. Willey, K. An, Y. Chen, A.H. King, S.K. McCall, High performance aluminium–cerium alloys for high-temperature applications, Materials Horizons. 4 (2017) 1070–1078.

[116] Y. Liu, R.A. Michi, D.C. Dunand, Cast near-eutectic Al-12.5 wt.% Ce alloy with high coarsening and creep resistance, Materials Science and Engineering: A. 767 (2019) 138440.

[117] D. Weiss, Improved high-temperature aluminium alloys containing Cerium, Journal of Materials Engineering and Performance. 28 (2019) 1903–1908.

[118] Ø. Ryen, O. Nijs, E. Sjölander, B. Holmedal, H.E. Ekström, E. Nes, Strengthening mechanisms in solid solution aluminium alloys, Metallurgical and Materials Transactions A. 37 (2006) 1999–2006.

[119] Y.G. Nakagawa, G.C. Weatherly, The thermal stability of the rod Al3Ni-Al eutectic, Acta Metallurgica. 20 (1972) 345–350.

[120] V.S. Zolotorevsky, N.A. Belov, M.V. Glazoff, Casting aluminium alloys, Elsevier, Amsterdam, 2007.

[121] Y.H. Cho, H.W. Kim, J.M. Lee, M.S. Kim, A new approach to the design of a low Si-added Al-Si casting alloy for optimising thermal conductivity and fluidity, Journal of Materials Science. 50 (2015) 7271–7281.

[122] H. Kaya, U. Böyük, E. Çadirli, N. Maraşli, Measurements of the microhardness, electrical and thermal properties of the Al-Ni eutectic alloy, Materials and Design. 34 (2012) 707–712.

[123] H. Okamoto, Al-Ni (aluminium-nickel), Journal of Phase Equilibria and Diffusion. 25 (2004) 394–394.

[124] W.R. Osório, L.C. Peixoto, M.V. Canté, A. Garcia, Microstructure features affecting mechanical properties and corrosion behaviour of a hypoeutectic Al-Ni alloy, Materials and Design. 31 (2010) 4485–4489.

[125] C. Suwanpreecha, P. Pandee, U. Patakham, C. Limmaneevichitr, New generation of eutectic Al-Ni casting alloys for elevated temperature services, Materials Science and Engineering: A. 709 (2018) 46–54.

[126] G.B. Olson, W. Tang, C. Qiu, H.J. Jou, High-temperature high-strength aluminium alloys processed through the amorphous state, 2007.

[127] J.C. Lin, J.R. Fields, A.L. Askin, X. Yan, R.R. Sawtell, S.P. Sullivan, J.L. Abbott, Aluminium alloys, aluminium alloy products and methods for making the same, 2010.

[128] E.R. Wang, X.D. Hui, G.L. Chen, Eutectic Al–Si–Cu–Fe–Mn alloys with enhanced mechanical properties at room and elevated temperature, Materials and Design. 32 (2011) 4333–4340.

[129] Y. Du, Y.A. Chang, B. Huang, W. Gong, Z. Jin, H. Xu, Z. Yuan, Y. Liu, Y. He, F.Y. Xie, Diffusion coefficients of some solutes in fcc and liquid Al: critical evaluation and correlation, Materials Science and Engineering: A. 363 (2003) 140–151.

[130] R. Kainuma, M. Ise, K. Ishikawa, I. Ohnuma, K. Ishida, Phase equilibria and stability of the B2 phase in the Ni–Mn–Al and Co–Mn–Al systems, Journal of Alloys and Compounds. 269 (1998) 173–180.

[131] A. Singh, S. Ranganathan, Rational approximants to the decagonal phase in Al-Mn-M (M = Ni, Cu, Zn) systems, Materials Science and Engineering: A. 181–182 (1994) 754–757.

[132] V. Raghavan, Al-Mn-Ni (aluminium-manganese-nickel), Journal of Phase Equilibria and Diffusion. 27 (2006) 493–496.

[133] M. Naoya, T. Takayuki, I. Osamu, K. Hisami, Phase diagram of the pseudo binary Ni3Al-Ni3Mn system, Materials Research and Advanced Techniques. 77 (1986) 212–217.

[134] G.V. Raynor, The constitution of the Aluminium-rich Aluminium-Manganese-Nickel alloys, The Journal of the Institute of Metals. 70 (1944) 507–529.

[135] K. Robinson, The determination of the crystal structure of Ni4Mn11Al60, Acta Crystallographica. 7 (1954) 494–497.

[136] P.I. Kripyakebich, Structural types of intermetallic compounds, Nauk, Moscow, 1977.

[137] L.F. Mondolfo, Aluminium alloys: structure and properties, Butterworths, London, 1976.

[138] N.A. Belov, D.G. Eskin, A.A. Aksenov, Multicomponent phase diagrams: applications for commercial aluminium alloys, Elsevier, Oxford, 2005.

[139] H.X. Sui, K. Sun, K.H. Kuo, A structural model of the orthorhombic C-31-Al60Mn11Ni4 approximant, Philosophical Magazine A. 75 (1997) 379–393.

[140] S. Balanetskyy, G. Meisterernst, M. Feuerbacher, The Al-rich region of the Al-Mn-Ni alloy system. Part I: Ternary phases at 750-950 °C, Journal of Alloys and Compounds. 509 (2011) 3787–3794.

[141] S. Balanetskyy, G. Meisterernst, B. Grushko, M. Feuerbacher, The Al-rich region of the Al-Mn-Ni alloy system. Part II. Phase equilibria at 620-1000 °C, Journal of Alloys and Compounds. 509 (2011) 3795–3805.

[142] B. Grushko, W. Kowalski, D. Pavlyuchkov, B. Przepiórzyński, M. Surowiec, A contribution to the Al–Ni–Cr phase diagram, Journal of Alloys and Compounds. 460 (2008) 299–304.

[143] A. Sato, A. Yamamoto, X.Z. Li, K. Hiraga, T. Haibach, W. Steurer, A new hexagonal κ phase of Al–Cr–Ni, Acta Crystallographica Section C Crystal Structure Communications. 53 (1997) 1531–1533.

[144] R.E. Marsh, Concerning the κ Phase of Al-Cr-Ni, Acta Crystallographica Section B: Structural Science. 54 (1998) 925–926.

[145] V. Raghavan, Al-Cr-Cu (Aluminium-Chromium-Copper), Journal of Phase Equilibria and Diffusion. 33 (2012) 53–54.

[146] K. Sugiyama, H. Saito, K. Hiraga, On the crystal structures of the Al-Cu-Cr alloy system, Journal of Alloys and Compounds. 342 (2002) 148–152.

[147] S. Balanetskyy, D. Pavlyuchkov, T. Velikanova, B. Grushko, The Al-rich region of the Al-Fe-Mn alloy system, Journal of Alloys and Compounds. 619 (2015) 211–220.

[148] N.A. Belov, A.N. Alabin, Assessment of the Al–Ni–Mn–Fe–Si–Zr phase diagram for new–generation heat–resistant casting aluminium alloys, 13th International Conference on Aluminium Alloys. (2012) 123–128.

[149] S.A. Villaseca, J. Ledieu, L.N.S. Loli, M.C. de Weerd, P. Gille, V. Fournée, J.M. Dubois, É. Gaudry, Structural investigation of the (001) surface of the Al9Co2 complex metallic alloy, Journal of Physical Chemistry C. 115 (2011) 14922–14932.

[150] S.G. Men'Shikova, I.G. Shirinkina, I.G. Brodova, V.I. Lad'Yanov, A.A. Suslov, Structure of thin ribbons from an Al – Co alloy under rapid cooling, Metal Science and Heat Treatment. 58 (2016) 393–399.

[151] M. Warmuzek, Chemical composition of the Ni-containing intermetallic phases in the multicomponent Al alloys, Journal of Alloys and Compounds. 604 (2014) 245–252.

[152] X.Z. Li, K.H. Kuo, Decagonal quasicrystals with different periodicities along the tenfold axis in rapidly solidified Al-Ni alloys, Journal of Materials Science Letters. 58 (2006) 167–171.

[153] I. Chumak, K.W. Richter, H. Ipser, The Fe-Ni-Al phase diagram in the Al-rich (>50 at.% Al) corner, Intermetallics. 15 (2007) 1416–1424.

[154] S. Mi, B. Grushko, C. Dong, K. Urban, Ternary Al–Ni–Ru phases, Journal of Alloys and Compounds. 351 (2003) L1–L5.

[155] Å. Jansson, A thermodynamic evaluation of the Al-Mn system, Metallurgical Transactions A. 23 (1992) 2953–2962.

[156] J.C. Slater, Atomic radii in crystals, The Journal of Chemical Physics. 41 (1964) 3199–3204.

[157] L. Han, X. Nie, D. Northwood, H. Hu, Effect of cooling rates on the microstructure evolution and eutectic formation of as-cast Mg-Al-Ca alloys, SAE World Congress and Exhibition. 1 (2010) 1–9.

[158] D.V. Malakhov, D. Panahi, M. Gallerneault, On the formation of intermetallics in rapidly solidifying Al-Fe-Si alloys, Calphad: Computer Coupling of Phase Diagrams and Thermochemistry. 34 (2010) 159–166.

[159] M. Singh, M. Bajwa, R. Sharma, H. Arora, Behaviour of aluminium alloy casting with the variation of pouring temperature and permeability of sand, International Journal of Scientific and Engineering Research. 4 (2013) 1497–1503.

[160] A. Hasan, Suyitno, Effect pouring temperature on casting defect susceptibility of hot tearing in metal alloy Al-Si, Applied Mechanics and Materials. 758 (2015) 95–99.

[161] A. Jahangiri, S.P.H. Marashi, M. Mohammadaliha, V. Ashofte, The effect of pressure and pouring temperature on the porosity, microstructure, hardness and yield stress of AA2024 aluminium alloy during the squeeze casting process, Journal of Materials Processing Technology. C (2017) 1–6.

[162] L.A. de S. Baptista, A.F. Ferreira, K.G. Paradela, D.M. da Silva, J.A. de Castro, Experimental investigation of ternary Al-Si-Cu Alloy solidified with unsteady-State heat flow conditions, Materials Research. 21 (2018) 565–571.

[163] A.F. Ferreira, W.B. Chrisóstimo, R.C. Sales, W.J.L. Garção, N. de Paula Sousa, Effect of pouring temperature on microstructure and micro segregation of as-cast

aluminium alloy, International Journal of Advanced Manufacturing Technology. 104 (2019) 957–965.

[164] R. Nadella, D.G. Eskin, Q. Du, L. Katgerman, Macro segregation in direct-chill casting of aluminium alloys, Progress in Materials Science. 53 (2008) 421–480.

[165] V.I. Dobatkin, N.F. Anoshkin, Comparison of macro segregation in titanium and aluminium alloy ingots, Materials Science and Engineering: A. 263 (1999) 224–229.

[166] W. Yu, Q. Hao, The phase transformation of Al9(Mn, Ni)2 eutectic phase in an Al-4Ni-2Mn alloy during heat treatment, Materials Characterization. 129 (2017) 53–59.

[167] J.L. Murray, The aluminium-copper system, International Metals Reviews. 30 (1985) 211–233.

[168] S. Toschi, Optimization of a354 al-si-cu-mg alloy heat treatment: Effect on microstructure, hardness, and tensile properties of peak aged and overaged alloy, Metals. 8 (2018) 961–976.

[169] S. Saxena, C.H. Tyagi, S. Kumar, Heat treatment of Al-Si-Cu-Mg casting alloys for the manufacturing of light weight machines/ vehicle parts with increased strength, International Journal of Mechanical Engineering and Robotics Research. 3 (2014) 706–715.

[170] F.J. Tavitas-Medrano, A.M.A. Mohamed, J.E. Gruzleski, F.H. Samuel, H.W. Doty, Precipitation-hardening in cast AL–Si–Cu–Mg alloys, Journal of Materials Science. 45 (2010) 641–651.

[171] A. Wiengmoon, P. Apichai, J.T.H. Pearce, T. Chairuangsri, Effects of T6 age hardening on microstructure and mechanical properties of Al-Si-Cu Cast aluminium alloy, Advanced Materials Research. 770 (2013) 88–91.

[172] W. Yu, H. Zhao, L. Wang, Z. Guo, S. Xiong, The influence of T6 treatment on fracture behaviour of hypereutectic Al-Si HPDC casting alloy, Journal of Alloys and Compounds. 731 (2018) 444–451.

[173] S.A. Alkahtani, E.M. Elgallad, M.M. Tash, A.M. Samuel, F.H. Samuel, Effect of Rare Earth Metals on the Microstructure of Al-Si Based Alloys, Materials 2016, Vol. 9, Page 45. 9 (2016) 45.

[174] H. Okamoto, Al-Ce (Aluminium-Cerium), The Journal of Phase Equilibria and Diffusion. 19 (1998) 396.

[175] Y. Li, Y. Yang, Y. Wu, L. Wang, X. Liu, Quantitative comparison of three Ni-containing phases to the elevated-temperature properties of Al–Si piston alloys, Materials Science and Engineering: A. 527 (2010) 7132–7137.